Analysis of a methane/air flame propagating in a two-dimensional small-scale channel with consideration of the conjugate heat transfer

Kévin Bioche

Normandie Université

THÈSE

Pour obtenir le diplôme de doctorat

Spécialité Mécanique des Fluides

Préparée à l'INSA Rouen Normandie

ANALYSE DE LA PROPAGATION D'UNE FLAMME MÉTHANE/AIR DANS UN CANAL ÉTROIT BI-DIMENSIONNEL AVEC PRISE EN COMPTE DES COUPLAGES THERMIQUES

présentée et soutenue par

KÉVIN BIOCHE

Thèse soutenue publiquement le 27 Novembre 2018 devant le jury composé de		
G. DAYMA	Professeur à l'Université d'Orléans, ICARE-CNRS	Rapporteur
B. DENET	Professeur à l'Université d'Aix-Marseille, IRPHE-CNRS	Rapporteur
P. GARCIA-YBARRA	Professeur à l'Université Nationale d'Éducation à Distance de Madrid	Examinateur
F. RICHECOEUR	Professeur à l'École CentraleSupelec, EM2C-CNRS	Examinateur
P. DOMINGO	Directrice de Recherche, CORIA-CNRS	Examinateur
G. RIBERT	Maître de Conférences à l'INSA Rouen Normandie, CORIA-CNRS	Directeur de thèse
L. VERVISCH	Professeur à l'INSA Rouen Normandie, CORIA-CNRS	Co-Directeur de thèse

Thèse dirigée par Luc VERVISCH et Guillaume RIBERT, laboratoire CORIA (UMR 6614 CNRS)

INSA ROUEN NORMANDIE

ED PSIME

UMR 6614 CORIA COMPLEXE DE RECHERCHE INTERPROFESSIONNEL EN AEROTHERMOCHIMIE

Résumé : Analyse de la propagation d'une flamme méthane-air dans un canal étroit bi-dimensionnel avec prise en compte des couplages thermiques

La stabilisation et la propagation d'une flamme laminaire pré-mélangée méthane/air dans un canal étroit, sont revisitées à partir de simulations numériques. La combustion est modélisée à l'aide d'une chimie et de propriétés de transport complexes, ainsi que du couplage des transferts thermiques à l'interface et dans les parois. Premièrement, une procédure de réduction des mécanismes chimiques adaptée à cette application est mise en œuvre. Deuxièmement, la réponse de la forme de flamme, lorsque soumise à diverses conditions thermiques, est analysée en termes de vitesse de propagation et de topologie de l'écoulement au voisinage du front de réaction. Troisièmement, le mécanisme de transfert thermique déclenchant la propagation de flamme lorsque celle-ci est soumise à un préchauffage est montré être principalement convectif. Pour finir, le rôle prépondérant de la gravité, via l'action du moment barocline, sur l'asymétrie des flammes se propageant dans des canaux étroits, est démontré.

Mots-clés : simulation numérique directe de la combustion, écoulements laminaires, transferts flamme-paroi, combustion à petite échelle, réduction de schéma cinétique

Abstract: Analysis of methane-air flame propagation in a narrow channel with conjugate heat transfer accounting

The flow physics controlling the stabilization and propagation of a methane/air laminar premixed flame in a narrow channel is revisited from numerical simulations. Combustion is described with complex chemistry and transport properties, along with a coupled simulation of heat transfer at and within the wall. First, a chemistry mechanism reduction procedure fitted to this application is applied. Second, the response of the premixed flame shape to various heat transfer conditions is analysed in terms of flame propagation velocity and flow topology in the vicinity of the reactive front. Third, the heat transfer mechanism triggering the flame movement when this last is submitted to an upstream wall preheating is revealed to be mainly convective. To finish, the preponderant role of gravity, via an impact on the baroclinic torque, in the symmetry breaking of small-scale channel flames is demonstrated.

Keywords: direct numerical simulation of combustion, laminar flows, flame-wall transfers, small-scale combustion, kinetic mechanism reduction

Remerciement

Mes travaux de thèse sont le fruit d'un travail personnel mais aussi de nombreuses interactions, je tiens ici à remercier les personnes qui ont compté dans leur accomplissement.

Je remercie les membres de mon jury, Guillaume Dayma, Bruno Denet, Pedro Garcia-Ybarra, Frank Richecoeur et Pascale Domingo pour le temps consacré à la lecture de mon manuscrit ainsi que les commentaires enrichissants formulés et discutés lors de ma soutenance.

Cette thèse, financée par l'Agence National de la Recherche dans le cadre du projet ANR-14-CE05-0030-MAPEE: 'Microcombustion Assistée par Plasma et Excès d'Enthalpie', et a été menée au sein du laboratoire CORIA. Je remercie ses directeurs successifs, Mourad Boukhalfa et Armelle Cessou de m'avoir accueilli dans leurs locaux.

Je remercie chaleureusement mes directeurs de thèse, Guillaume Ribert et Luc Vervisch, de m'avoir encadré et fait confiance pour ce projet. Merci pour votre investissement particulièrement remarquable dans l'ensemble de mes travaux, votre disponibilité et le plaisir que vous mettez à discuter de science. Merci de m'avoir montré comment communiquer des résultats scientifiques, et merci de votre approche positive.

Je remercie les autres permanents de l'équipe: Ghislain, pour les conseils et le support info au top du top; Vincent, pour les discussions scientifiques intéressantes et Guido pour les échanges sur les méthodes pseudo-spectrales.

Merci aux anciens, partis trop tôt à mon avis (trop tard au leur peut-être). Bastien (en parlant de tard) pour ton guidage lors de mes premiers pas avec SiTCom. JB pour nos sessions musicales saveur stoner. Umut pour tes citations complexes, voire abyssales mais toujours pleines de fraicheur, qui ont définitivement marqué le bureau. Loic pour tes généreuses gamelles-traiteurs (j'admets que le tofu c'est bon en fait). Pierre pour l'accueil en territoire hostile bas-Normand. Nico L. et Yann pour les soirées Halloween et les sorties au bar, ce toujours en concervant un certain standing (voir un standing incertain). Nico J. pour les soirées à la coloc et la rhythm guitar. Dorian, "franchement je reste une demie-heure, ma copine m'attend à l'appart", merci pour ça entre autres. Eurielle pour ta bonne humeur. Geogeo l'affreux, ah mais qu'est-ce que tu es affreux... Alex pour les discussions qui élèvent le niveau, et les caïpi qui l'abaissent. Francis pour la bricole et les jeux du dimanche. Andréa pour les échanges musicaux. Patricia pour

les cours linguistiques. Felix, Romain, Hakim et Lancelot pour les pauses et sorties en ville. Deewakar, Huu-tri et Camille pour la bonne prise en main de l'ambiance du bureau.

Merci à DD, la Petite Dure, Gourmandine et Digiaud pour les moments décontractés qui font relativiser quand l'un a mal à sa douleur. Ce fut bon d'être un Flanders parmis vous pendant ce début de thèse.

Merci aux copains de longue date, voir de toujours. Que l'on ne se quitte jamais.

Merci à mon frère, ma soeur, mes parents et Peluche pour leur soutien qui rechauffe le coeur.

Jack, merci pour la compagnie (à peine envahissante) pendant la rédaction.

Laura, je t'< 4

Contents

1 Introduction **19**

1.1 Chapter summary . . . 19

1.2 Context of the micro-combustion study . . . 20

1.2.1 Industrial context: The miniaturisation race . . . 20

1.2.2 Limits of miniaturisation: The power source . . . 20

1.2.3 Small-scale combustion as a solution and first achievements . . . 22

1.3 State of the art . . . 23

1.3.1 Definitions . . . 23

1.3.2 Micro-combustion specificities . . . 24

1.3.2.1 Thermal quenching . . . 24

1.3.2.2 Radical quenching . . . 25

1.3.2.3 Diffusion dominated flows . . . 27

1.3.3 Micro-combustion modelling background . . . 28

1.3.3.1 Heat loss modelling . . . 28

1.3.3.2 Surface reactions modelling . . . 29

1.3.3.3 Kinetic mechanism choices . . . 31

1.3.3.4 Soret effect . . . 31

1.3.3.5 Multi-dimensional property of the simulations . . . 32

1.3.3.6 Symmetric and asymmetric flame topologies . . . 32

1.3.3.7 Gravity effect . . . 35

1.3.3.8 Unsteady modes . . . 36

1.3.3.9 Flame front tracking in numerical simulations . . . 36

1.3.4 Managing small-scale combustion . . . 36

1.3.4.1 Excess enthalpy . . . 37

1.3.4.2 Catalytic combustion . . . 38

1.4 Ph. D. thesis objectives and outline . . . 40

1.5 Publications . . . 43

1.5.1 Peer-reviewed international journals . . . 43

1.5.2 Conferences . . . 43

2 Modelling **45**

2.1 Chapter summary . . . 45

2.2 Aerothermochemistry equations . . . 46
2.2.1 Mixture properties . . . 46
2.2.2 Balance equations . . . 47
2.2.2.1 Conservation of momentum . . . 47
2.2.2.2 Conservation of mass . . . 47
2.2.2.3 Conservation of total sensible energy . . . 49
2.2.2.4 Species source term computation . . . 49
2.2.3 Dimensionless numbers . . . 50
2.3 Solid/flow conjugate heat transfer: A solid solver . . . 51
2.3.1 Conservation of energy . . . 52
2.3.2 Numerical resolution . . . 53
2.3.3 Imposition of the boundary conditions . . . 55
2.3.4 Coupling strategy . . . 55
2.3.5 Validation . . . 57
2.3.5.1 Mono-dimensional semi-infinite flat plate . . . 57
2.3.5.2 Three-dimensional diffusion of a Dirac peak . . . 58
2.3.5.3 Infinitely Fast Flame test case . . . 59
2.4 Numerical solving with SiTCom-B . . . 60
2.4.1 Numerical methods . . . 60
2.4.1.1 Space and time integration . . . 60
2.4.1.2 Artificial viscosity . . . 60
2.4.1.3 Boundary conditions . . . 62
2.4.1.4 Kinetics and transport modelling . . . 62
2.4.1.5 Energy equation resolution in the solid . . . 62
2.4.2 Simulations parameters . . . 63
2.4.2.1 Domain dimensions . . . 63
2.4.2.2 Mesh resolution . . . 63
2.4.2.3 Temporal advancement restriction . . . 63
2.4.2.4 Wall characteristics and coupling with the flow solver . . . 65
2.4.2.5 Inlet velocity profile . . . 65
2.4.3 Numerically stabilizing flames in channels . . . 66

3 Kinetic mechanism reduction strategy for small-scale combustion 69
3.1 Preamble . . . 69
3.2 Introduction . . . 70
3.3 Optimised and Reduced Chemistry: ORCh method . . . 70
3.4 Reduction trajectories for small-scale combustion . . . 71
3.5 Results on canonical problems . . . 74
3.5.1 1D premixed flames with and without uniform heat loss . . . 74
3.5.2 Auto-ignition delays . . . 79
3.6 Results on the 2D case of a flame propagating in a small-scale channel . . . 80
3.7 Computational performances . . . 82

4 Premixed flame/wall interaction in a narrow channel under microgravity: Impact of wall thermal conductivity and heat losses 85
4.1 Introduction . . . 86
4.2 Configuration . . . 86
4.3 Analysis of the burning velocity . . . 90
4.3.1 Observations . . . 90
4.3.2 Scaling law . . . 91
4.4 Effect of the sheared flow . . . 93
4.4.1 Quenching . . . 93
4.4.2 Flow deviation . . . 93
4.4.3 Kinetics . . . 95
4.5 Thermal coupling influence . . . 97
4.5.1 Heat transfer at the wall . . . 97
4.5.2 Flow deviation . . . 98
4.5.3 Energy budget on the thermally coupled flame . . . 99
4.5.4 Kinetics . . . 101
4.6 Flame response to wall heat transfer properties in a regime diagram . . . 103
4.6.1 Asymptotic behaviours . . . 103
4.6.2 Competition of the influence of conductivity and convection on the flame characteristics . . . 105

5 Simulating upstream flame propagation in a narrow channel after wall preheating under microgravity 108
5.1 Introduction . . . 108
5.2 Configuration . . . 109
5.2.1 Numerics . . . 109
5.2.2 Heating scenario . . . 110
5.3 Downstream movement by fresh gases dilatation . . . 113
5.4 Flame acceleration from convective heat transfer . . . 114
5.5 Flame translation and final position . . . 116

6 The role of gravity and external heating in the asymmetry of flames stabilized in a narrow combustion chamber 120
6.1 Introduction . . . 120
6.2 Experimental and numerical set-up . . . 121
6.2.1 Experimental configuration . . . 121
6.2.2 Numerical set-up . . . 122
6.3 Analysis of gravity effects . . . 123
6.3.1 Case (i): Flame stabilised with heat-conductive wall . . . 123
6.3.2 Case (ii): Flame propagating over a quasi-isothermal wall . . . 125
6.3.3 Analysis of baroclinic-torque response to gravity . . . 127

6.4 Influence of external heating and channel dimensions on the stability of symmetric flame topologies . . . 132

7 Conclusion and perspectives **137**
7.1 Chapter summary . . . 137
7.2 Conclusion . . . 137
7.2.1 Chemistry modelling . . . 138
7.2.2 Flame/wall interactions . . . 139
7.2.3 Flame response to upstream heating . . . 140
7.2.4 Role of the gravity in the breaking of flame symmetry . . . 140
7.3 Perspectives . . . 141
7.3.1 On-earth intricate boundary layer, heat recirculation and flame coupling 141
7.3.2 Experimental comparisons . . . 141
7.3.3 Low temperature chemistry . . . 141
7.3.4 Thermally optimised and catalytic burners . . . 142

A Reduced mechanisms for small-scale combustion at $\phi = 0.8$ and $\phi = 0.7$ **144**
A.1 17S-53R-0.8 mechanism assessment . . . 147
A.1.1 Flame speed . . . 147
A.1.2 Auto-ignition delays . . . 147
A.1.3 1D flame profiles . . . 147
A.2 17S-53R-0.7 mechanism assessment . . . 151
A.2.1 Flame speed . . . 151
A.2.2 Auto-ignition delays . . . 151
A.2.3 1D flame profiles . . . 151

B Meshing for DNS **156**
B.1 15S-26R . . . 156
B.2 17S-53R-1.0 . . . 159
B.3 GRI-1.2 . . . 162

C Equivalence ratio influence on the flame topology **166**
C.1 Under microgravity . . . 166
C.2 Under the gravitational field of the earth . . . 167

Bibliography **169**

Nomenclature

Abbreviations

Symbol	Description
ANR	Agence Nationale de la Recherche
CFD	Computational Fluid Dynamics
CNC	Computer Numerical Control
CNRS	Centre National de la Recherche Scientifique
CORIA	COmplexe de Recherche Interprofessionel en Aerothermochimie
CPU	Central Processing Unit
DNS	Direct Numerical Simulation
DRGEP	Directed Relation Graph with Error Propagation
D-L	Darrieus-Landau
D-T	Diffusive-Thermal
EDM	Electro-Discharge Machining
EM2C	Energétique Moléculaire et Macroscopique, Combustion
GPS	Global Positioning System
FREI	Flame Repetitive Extinction Ignition
GRI	Gas Research Institute
IBM	Ion Beam Machining
INSA	Institut National des Sciences Appliquées
LBM	Laser Beam Machining
MEMS	Micro-Electro-Mechanical Systems
MIT	Massachusetts Institute of Technology
MPI	Message Passing Interface
NASA	National Aeronautics and Space Administration
NSCBC	Navier-Stokes Characteristic Boundary Condition
ONERA	Office National d'Etudes et de Recherches Aérospatiales

ORCh	Optimised and Reduced Chemistry
QSS	Quasi-Steady State
RK	Runge-Kutta
R-T	Rayleigh-Taylor
SCTP	Standard Conditions for Temperature and Pressure
SiTCom-B	Simulation of Turbulent Combustion with Billion of points
S-T	Saffman-Taylor

Roman letters

Symbol	**Description**	**Unit**
A_j	Pre-exponential factor of the Arrhenius law for reaction j	variable
$A_{\mathrm{f},j}$	Forward pre-exponential factor of the Arrhenius law for reaction j	variable
$A_{\mathrm{b},j}$	Backward pre-exponential factor of the Arrhenius law for reaction j	variable
b	Thermal effusivity	$\mathrm{J.m^{-2}.K^{-1}.s^{-\frac{1}{2}}}$
c	Speed of sound	$\mathrm{m.s^{-1}}$
C_p	Specific heat capacity at constant pressure	$\mathrm{J.kg^{-1}.K^{-1}}$
$C_{p,k}$	Specific heat capacity of species k at constant pressure	$\mathrm{J.kg^{-1}.K^{-1}}$
$C_{v,k}$	Specific heat capacity of species k at constant volume	$\mathrm{J.kg^{-1}.K^{-1}}$
CFL	Courant-Friedrichs-Lewy number	-
$Chem$	Chemical time step restriction number	-
$\mathcal{D}_k$	Diffusion coefficient of species k	$\mathrm{m^2.s^{-1}}$
$\mathcal{D}_{k,j}$	Binary diffusion coefficient of species k into species j	$\mathrm{m^2.s^{-1}}$
E	Specific total sensible or non-chemical energy	$\mathrm{J.kg^{-1}}$
$E_{\mathrm{a},j}$	Molecular activation energy of reaction j	$\mathrm{J.mol^{-1}}$
Fo	Fourier number	-
h	Convective heat transfer coefficient	$\mathrm{W.m^{-2}.K^{-1}}$
h_k	Specific enthalpy of species k	$\mathrm{J.kg^{-1}}$
h_k^{s}	Specific sensible enthalpy of species k	$\mathrm{J.kg^{-1}}$
h_k^{o}	Specific enthalpy of formation of species k	$\mathrm{J.kg^{-1}}$
j_k	Diffusive mass flux	$\mathrm{kg.m^{-2}.s^{-1}}$
k_{w}	Wall heat transfer coefficient inside the channel	$\mathrm{W.m^{-2}.K^{-1}}$
$K_{\mathrm{f},j}$	Forward chemical constant of reaction j	variable

$K_{\mathrm{b},j}$	Backward chemical constant of reaction j	variable
ℓ_{c}	Characteristic length	m
ℓ_{e}	External channel height	m
ℓ_{i}	Internal channel height	m
$\mathcal{M}_k$	Formula of species k	-
m	Overall mass contained in the control volume V	kg
m_k	Mass of species k contained in the control volume V	kg
n	Overall moles contained in the control volume V	mol
n_k	Moles of species k contained in the control volume V	mol
N_{r}	Number of reactions	-
N_{sp}	Number of species	-
N_{var}	Number of transported variables	-
P	Pressure	Pa
$\mathcal{Q}_j$	Reaction rate of reaction j	mol.m^{-3}.s^{-1}
$\mathcal{Q}_{\mathrm{f},j}$	Forward reaction rate of reaction j	mol.m^{-3}.s^{-1}
$\mathcal{Q}_{\mathrm{b},j}$	Backward reaction rate of reaction j	mol.m^{-3}.s^{-1}
r	Reduced ideal gas constant	J.kg^{-1}.K^{-1}
R	Ideal gas constant	J.mol^{-1}.K^{-1}
S_{L}	Flame burning velocity	m.s^{-1}
T	Temperature	K
$\mathbf{u}$	Velocity vector	m.s^{-1}
u	Velocity in the x direction	m.s^{-1}
v	Velocity in the y direction	m.s^{-1}
V	Control volume	m^3
$V_{\mathrm{c},j}$	Correction velocity of species k	m.s^{-1}
$V_{k,j}$	Molecular diffusion velocity of the k-th species in the j-th direction	m.s^{-1}
w	Velocity in the z direction	m.s^{-1}
W	Molecular weight of the mixture	kg.mol^{-1}
W_k	Molecular weight of species k	kg.mol^{-1}
X_k	Molecular fraction of species k	-
$[X_k]$	Molecular concentration of species k	mol.m^{-3}
$\mathbf{Y}$	Species mass fraction vector containing the mass fractions of the N_{sp} species	-

Y_C	Progress variable	-
Y_F	Mass fraction of fuel	-
Y_k	Mass fraction of species k	-
Y_Ox	Mass fraction of oxidizer	-

Greek letters

Symbol	**Description**	**Unit**
α	Thermal diffusion coefficient	$\mathrm{m}^2.\mathrm{s}^{-1}$
α_loss	Heat loss coefficient	$\mathrm{W.m}^{-3}.\mathrm{K}^{-1}$
β_j	Temperature exponent of the Arrhenius law for reaction j	-
$\boldsymbol{\delta}$	Kronecker tensor	-
δ_F	Flame thickness	m
δt	Time step	s
δt_C	Convective time step	s
δt_Ch	Chemical time step	s
δt_D	Diffusive time step	s
δx	Cell size in the direction x	m
ΔH_j^o	Molecular enthalpy change when passing from reactants to products in reaction j	$\mathrm{J.mol}^{-1}$
ΔS_j^o	Molecular entropy change when passing from reactants to products in reaction j	$\mathrm{J.mol}^{-1}.\mathrm{K}^{-1}$
ε	Radiative emission coefficient	-
λ	Thermal conductivity	$\mathrm{W.m}^{-1}.\mathrm{K}^{-1}$
λ_k	Thermal conductivity of pure species k	$\mathrm{W.m}^{-1}.\mathrm{K}^{-1}$
μ	Dynamic viscosity	$\mathrm{kg.m}^{-1}.\mathrm{s}^{-1}$
μ_k	Dynamic viscosity of pure species k	$\mathrm{kg.m}^{-1}.\mathrm{s}^{-1}$
ν	Kinematic viscosity j	$\mathrm{m}^2.\mathrm{s}^{-1}$
$\nu_{k,j}$	Stoichiometric coefficient of species k in reaction j	-
$\nu'_{k,j}$	Reactant stoichiometric coefficient of species k in reaction j	-
$\nu''_{k,j}$	Product stoichiometric coefficient of species k in reaction j	-
ρ	Density	$\mathrm{kg.m}^{-3}$
$\dot{\omega}_k$	Chemical source term of species k	$\mathrm{kg.m}^{-3}.\mathrm{s}^{-1}$
$\dot{\omega}_k^m$	Molar chemical source term of species k	$\mathrm{mol.m}^{-3}.\mathrm{s}^{-1}$

$\dot{\omega}_{\rho Y_k}$	Chemical source term of species k	kg.m^{-3}.s^{-1}
$\dot{\omega}_{\rho E}$	Heat release source term	W.m^{-3}
ϕ	Equivalence ratio	-
σ	Stefan-Boltzmann constant	W.m^{-2}.K^{-4}
$\boldsymbol{\tau}$	Newtonian viscous tensor	kg.m^{-1}.s^{-2}
τ_{conv}	Convection characteristic time	s
τ_{chem}	Chemical characteristic time	s
τ_{diff}	Diffusion characteristic time	s
τ_{ign}	Auto-ignition delay	s

Non dimensional numbers

Symbol	**Description**
Da	Damköhler number
Fr	Froude number
Le$_k$	Lewis number associated to species k
Nu	Nusselt number
Pe	Péclet number
Re	Reynolds number

Superscript and subscript

Symbol	**Description**
$^{\text{o}}$	Adiabatic
$_{\text{f}}$	Fluid
$_{\text{F}}$	Flame
$_{\text{s}}$	Solid
$_{\text{st}}$	Stoichiometric
$_{\text{w}}$	Wall

Chapter 1

Introduction

Contents

1.1 Chapter summary 19
1.2 Context of the micro-combustion study 20
1.2.1 Industrial context: The miniaturisation race 20
1.2.2 Limits of miniaturisation: The power source 20
1.2.3 Small-scale combustion as a solution and first achievements 22
1.3 State of the art 23
1.3.1 Definitions 23
1.3.2 Micro-combustion specificities 24
1.3.3 Micro-combustion modelling background 28
1.3.4 Managing small-scale combustion 36
1.4 Ph. D. thesis objectives and outline 40
1.5 Publications 43
1.5.1 Peer-reviewed international journals 43
1.5.2 Conferences 43

1.1 Chapter summary

Section 1.2 gives a picture of the industrial and technological context of the young micro-combustion field. The recent trend to miniaturise the electrical power sources is depicted in subsection 1.2.1 while subsection 1.2.2 presents the limits of this technology. Subsection 1.2.3 shows that combustion is evoked as an alternative to electrical batteries for embedded low power sources and presents the first technological achievements made by the community in this area.

Section 1.3 is the opportunity to give an overview on the former and ongoing research work on small-scale combustion. First, in subsection 1.3.1, the various definitions for micro-combustion encountered in the literature are recalled and discussed to introduce the present

study framework. Second, subsection 1.3.2 evokes the physics specificities of combustion at small scales. In subsection 1.3.3 an overview of the common modelling strategies is then given with a special attention paid to the analytical and numerical assumptions made in the approach of the physics. The propositions brought by the community to manage this new combustion technology are then presented in subsection 1.3.4. Finally, the Ph. D. thesis objectives are presented and placed within this state of the art in section 1.4 and the communications issued from this work are listed in section 1.5.

1.2 Context of the micro-combustion study

1.2.1 Industrial context: The miniaturisation race

The last decades have been marked by research and industrial efforts in the field of miniaturisation. The recent deep changes in the consumers habits, with the entry in private life of a multitude of portable devices such as the cellular phones, the laptops or the GPS technologies, motivated the downsizing and the weight reduction of electronic devices. In addition, technical fields such as biomedicine or molecular biology, also took advantage of miniaturisation for applications such as the conception of micro-grippers used to manipulate organic cells or tissues [39], or the fabrication of bio-sensors used in the detection of virus [74]. The need for downsizing, issued by these recent applications, motivated the development of small-scale fabrication technologies. Among the current techniques one can count the Electro-Discharge Machining (EDM), the Laser Beam Machining (LBM) and the Ion Beam Machining (IBM) permitting to assemble the so-called Micro-Electro-Mechanical Systems (MEMS). These technologies have been employed with success to decrease dramatically the size of all types of components, from gas separation column of portable chromatograph used in the detection of hazardous gases [56] to inkjet print heads.

1.2.2 Limits of miniaturisation: The power source

In the context of portable devices with embedded low power source, the ability of the evoked techniques in the conception of low-scale mechanisms creates now a gap between the weight constrain of the powered technology and the onboard source powering this technology, typically an electrical battery. Indeed, electrical batteries are currently widely preferred for the powering of small portable devices, creating a market reaching 37 billion dollars per year, in 2005 [35]. The weight and space constrains induced by the low specific energy of electrical batteries are now a limitation for numerous applications. An extreme example can be found in figure 1.1 on which an actuator is displayed on top of its electrical battery. The battery is several times bigger and heavier than the device it is powering. The micro-satellite application offers also quite striking examples. Taking for instance the A62 version of the Ariane 6 rocket [5]: with a mass of 530 tons at lift-off, this rocket can transfer in geostationary orbit a payload of 4,5 tons. Considering the very low payload/mass ratio in this type of application, a gain in mass on the satellite power source would have a significant economical impact. This gives prominence

to microgravity applications in the research for lighter powering sources. Other mechanical devices such as micro-rovers, micro-robots, and micro-airplanes are also limited by the weight of the available power systems.

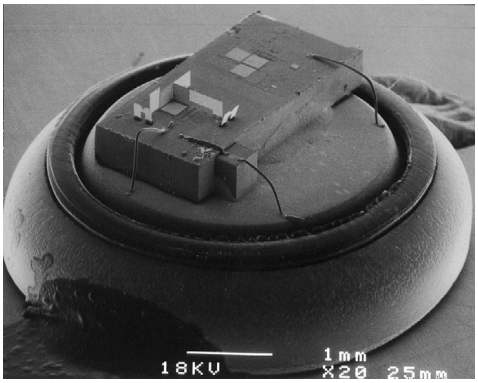

Figure 1.1: Communication component with a MEMS optics chip and a hearing aid battery for power [155].

Source	Energy density [MJ/kg]
Lead acid batteries	0.0792
Nickel cadmium (NiCad) batteries	0.158
Lithium ion batteries	0.468
Lithium sulfur batteries	0.792
Methanol combustion	22.7
Ethanol combustion	30.5
Heating oil combustion	42.5
Diesel combustion	45.3
Gasoline combustion	45.8
n-Octane combustion	48.2
n-Butane combustion	49.6
Propane combustion	50.3
Methane combustion	55.5
Hydrogen combustion	142

Figure 1.2: Energy densities of various sources, extracted from [68].

Globally, the number of components hosted in portable devices grows with the improvement of miniaturisation techniques, leading to an increase in energy consumption and the necessity for adapted power sources. An example of this type of limitation is found in the current smart-phones. On one hand, smart-phones now carry a computational power comparable to the computers of last decade, extending the range of utility brought by these devices at the same occasion. On the other hand, the associated increase in power consumption has led to a considerable decrease in the practical autonomy of such devices, requiring for more regular recharge than before. Besides, some niche areas such as cellular phones for soldiers can be limited by the necessity for instantly rechargeable power supplies when in mission. Generally, improvements of the power source are now required to further reduce the weight while ensuring a sufficient autonomy of portable devices.

Further, electrical batteries suffer from their low lifetime due to the lost in capacity subsequent to regular reloads and from the use of toxic products, whose recycling is still an environmental concern. Ongoing research incentives aim at reducing the electrochemical cell size [126], but a considerable breakthrough would be necessary to compensate the current difference in specific energy with other technologies. The objective to reduce the powering systems weight and increase their lifetime pushes the communities to look for other sources. Micro- and meso-scale combustion are now seen as a potential technology for embedded low power sources, as reviewed by Ju *et al.* [63], Kaisare *et al.* [68] and Walther *et al.* [153]. Figure 1.2 points out the tremendous difference in energy density of combustion and electrical batteries. The high energy density of hydrocarbon fuels, which is about 60 times larger than that of most efficient lithium-ion electrical batteries once considered the burner mass, presently motivates the development of small- or micro-scale combustion devices.

1.2.3 Small-scale combustion as a solution and first achievements

The recent improvements of the small-scale fabrication techniques such as EDM, LBM and IBM, have made possible the conception of complex MEMS, that can be assembled into micro-scale burners. As for their macro-scale counterparts, various strategies are considered to extract useful power from the chemical energy released in micro-burners:

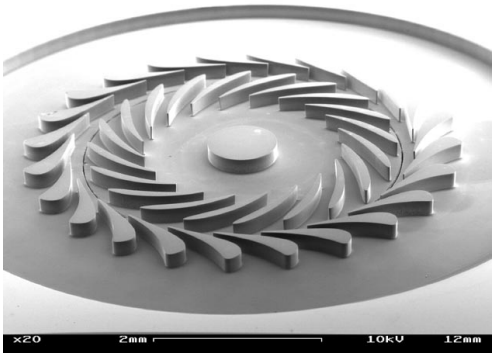

Figure 1.3: 50 watt microturbine from MIT [38].

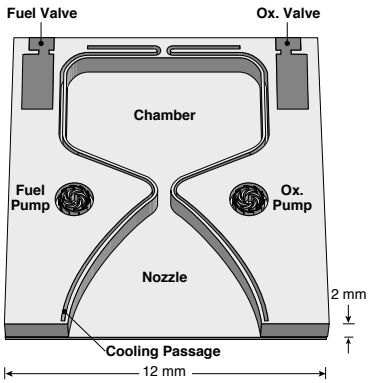

Figure 1.4: Bipropellant from MIT [38].

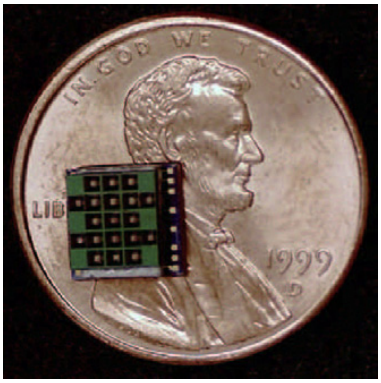

Figure 1.5: Digital Micro-Propulsion "rocket chip" [88]. Figure extracted from [63].

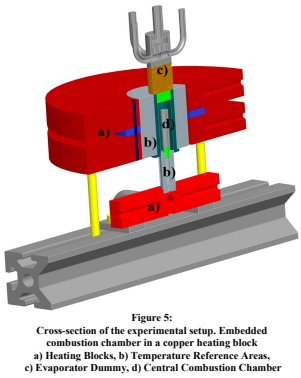

Figure 1.6: Experimental set-up of a micro-combustion chamber for a thermoelectric energy converter [70].

- The mechanical power can be obtained through mobile parts, actioned by the gas expansion due to combustion. Several concepts of micro-turbines have been studied at the university of Leuven [109], the university of Tohoku [55], the french aerospace lab ONERA [51] and the university of Auckland [150]. The first to achieve such a conception was the MIT, where deep reactive ion etching was used to produce the micro-turbine delivering 50 W [38] (see figure 1.3). This project was largely compromised by combustion instabilities, exhibiting the difficulties in running a stable combustion at micro-scale. Other concepts than turbines have also been considered such as a meso-scale stirling engine [36] or a free piston engine [3].

- Micro-combustion can be adapted to rocket-type propulsion systems. This technology could be interesting for the propulsion of micro-satellites [19] during orbital control. This leaves microgravity conditions in a central position in the list of small-scale combustion applications. Among the concepts under study, one can find the MIT micro-bipropellant regenerative rocket engine displayed in figure 1.4 [38], mono-propellant micro-rocket [54] or solid fuel concepts [88] (see figure 1.5).

- Thermoelectric converter can be used to transform the heat released into electricity [156]. Work from the university of Darmstadt [70] claims the feasibility of a micro-thermoelectric energy converter that can compete with state-of-the-art lithium-ion batteries (figure 1.6).

Eventually, micro-combustion should permit to produce power ranging from a few Watt to a couple of hundreds of Watt, in a volume of the order of magnitude of the current batteries hosted in modern mobile devices. To advance this new technology, the development at micro-scale of three techniques is required: the high temperature material manufacturing, the rotating machinery conception and the mastery of combustion. In micro-combustion, whatever the strategy employed, the flame sits in a narrow channel leading to a specific interaction between the flame and the combustion chamber. Currently, research is needed to understand the flame propagation mechanisms in such small-scale environment and propose ways to handle stable micro-combustion. The present work is along these lines.

1.3 State of the art

1.3.1 Definitions

The present work addresses the physics of small-scale combustion. The term small-scale stands in opposition to traditional bigger combustion system, such as the ones found in the automotive or the aviation sectors, referred to as macro-scale combustion. Macro-combustion is beyond the scope of the present work. Small-scale combustion is commonly divided in two ranges, micro- and meso-scale combustion. To delineate between these two ranges, various criteria exist and are based on [63]:

- The absolute **burner dimensions**. It is commonly mentioned as micro-combustors, burners with a characteristic length between 1 µm and 1 mm and as meso-combustors, burners of characteristic length from 1 mm to 1 cm [40]. Beyond 1 cm is the category of macro-combustors. Figure 1.7 gives some examples of representative powering systems while associating the scale category and power generated. Note that, as previously mentioned, micro-combustion is an appealing powering system for microgravity satellite applications.

- The **flammability range**. Following this definition, micro-combustion is the combustion occurring below the quenching diameter [28]. The quenching diameter is the burner dimension below which, in the absence of external energy supply, combustion cannot

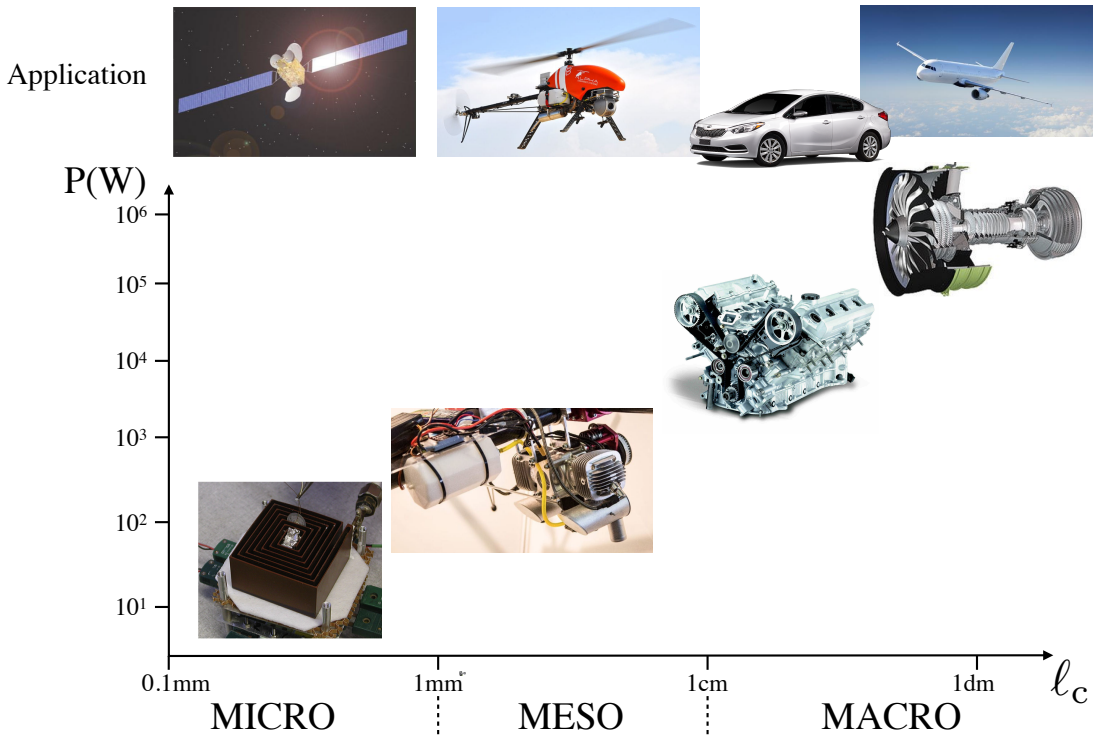

Figure 1.7: Classical definition of combustion type with respect to the burner characteristic dimension following the criterion from Fernandez-Pello [40] and corresponding application examples.

occur. This definition requires to know the quenching diameter which depends on a lot of parameters such as the fuel composition, the equivalence ratio, the initial temperature, the pressure and the heat loss undergone by the system among others. The multiplicity of the parameters influencing the quenching makes it sensible to the configuration and hard to evaluate a priori. The difficulty in the quenching diameter evaluation makes this definition more sensitive to use, even though its physical basis is appealing.

- The **global system qualification** that the energy source is powering. For example the power source propelling a micro-rover (called this way in opposition to the conventional large scale models) will be called micro-propeller even though its characteristic length may not respect one of the two previous definitions [160].

1.3.2 Micro-combustion specificities

1.3.2.1 Thermal quenching

In micro-burners, flammability limits, quenching distance and flame propagation speed are controlled by phenomena which differ from that of large-scale devices. The early highlights of Davy [28] showed the presence of extinction and flammability limits when flames propagate in narrow environments. This discovery resulted in the conception of the first safety lamp (named after him [157]) used in the mines to prevent for gas blast. This foundation stone was later

supported by experimental investigation by Andrews *et al.* [4] and Jarosinski [59] on flame quenching in small channels. Indeed, continuum theory, which still applies at this scales, predicts that below a critical distance, heat loss to the wall overtakes the heat generation from the chemical reaction leading to thermal quenching [87]. A simple thermal model can be considered to evaluate the heat loss to heat generated ratio. Assuming that the heat loss are directly proportional to the exchange surface and that the heat generated evolves with the volume occupied by the flame, the heat loss (Q_{loss}) to heat generated (Q_{gen}) ratio should evolve as

$$\frac{Q_{\text{loss}}}{Q_{\text{gen}}} \propto \frac{S}{V} \propto \frac{\ell_c^2}{\ell_c^3} \propto \frac{1}{\ell_c}, \tag{1.1}$$

In this small-scale problem the invasive presence of the wall, because of the high surface to volume ratio, leads thus to an enhanced heat loss to heat production ratio when compared to its macro-scale counterpart. Furthermore, the reduction of the burning volume available for the flame forces this last to evolve in the wall vicinity, leading to an increase of the thermal gradients at this last and to enhanced thermal transfer.

1.3.2.2 Radical quenching

Reactions	Pre-Exponential (s^{-1}) or Sticking Coefficient
$CH_3 + {}^a \rightarrow CH_3{}^a$	0-1
$H + {}^a \rightarrow H^a$	0-1
$OH + {}^a \rightarrow OH^a$	0-1
$O + {}^a \rightarrow O^a$	0-1
$2CH_3{}^a \rightarrow C_2H_6 + 2^a$	10^{13}
$2H^a \rightarrow H_2 + 2^a$	10^{13}
$2OH^a \rightarrow H_2O + O^a + {}^a$	10^{13}
$2O^a \rightarrow O_2 + 2^a$	10^{13}
$CH_3{}^a + H^a \rightarrow CH_4 + 2^a$	10^{13}
$OH^a + H^a \rightarrow H_2O + 2^a$	10^{13}

Table 1.1: Examples of radical recombination reactions on surfaces. X^a Denotes a surface adsorbed species and ^{a} a vacant surface site. Table extracted from [121].

It is well known that most material are not inert, in the sense that surface reactions occur at their interface with gas or liquid. In the case of close wall combustion these reactions lead to radical adsorption, desorption and recombination, and can weaken the flame down to extinction. This is called radical quenching. This phenomenon has been very few studied at macro-scale as the flame is mostly far from the wall and the surface to volume ratio is low. But in small-scale configurations, the increase of the surface to volume ratio reinforces the role of surface reactions both by increasing the wall temperature and by forcing a closer cohabitation between the wall and the flame. Table 1.1 gives an example of reactions typical of this process

for methane/air combustion. As explained by Raimondeau *et al.* [121], the sticking coefficients of the Langmuir-Hinshelwood mechanisms describes the probability of a colliding molecule to stick to the surface and the probability of a radical to meet an empty active wall site. When this coefficient tends to zero the wall is inert while the fastest possible removal rate of radicals corresponds to a coefficient of one. As it will be discussed in § 1.3.3.2 the modelling and understanding of surface reactions still needs to be fuelled by the community research. Generally, the thermal quenching mechanism is considered to be dominant in front of the radical quenching. Nevertheless, the influence ratio between these two phenomena is shown to be sensible to three main parameters:

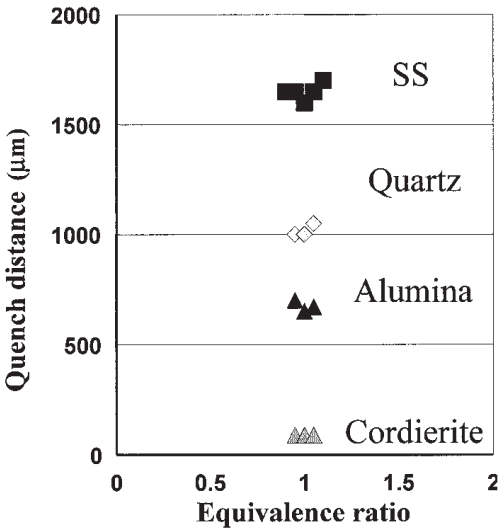

Figure 1.8: Quenching distances measured for a series of wall materials as a function of methane/oxygen ratio when the walls were insulated to give inside wall temperatures near 1300K. SS: stainless stell. Figure extracted from [100].

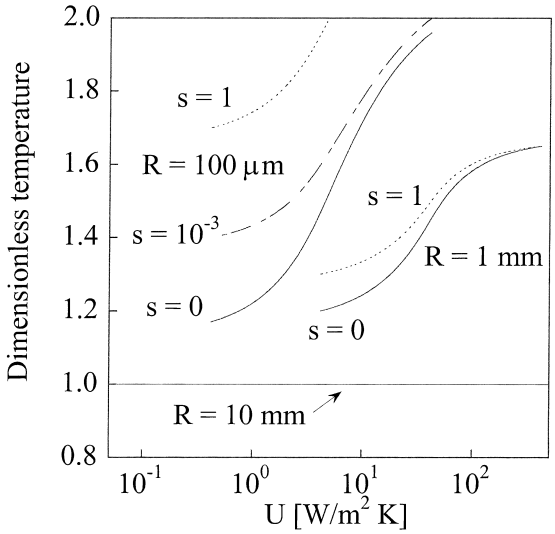

Figure 1.9: Stability map of premixed methane/air mixtures in terms of preheat temperature vs. coefficient of heat loss for flame propagation in a cylindrical tube. The tube radius R and the sticking coefficient, s, of key radicals are indicated in panel. The region under each curve indicates no propagation; conversely, the region above each curve indicates that the flame propagates. Figure extracted from [121].

- The **wall material**. Dealing with an active surface, the recombination of H radicals at the wall surface induces sharper consumption of radical compared to an inert wall. Kaisare *et al.* [68] indicate that surface reactions, depending on the wall material, can lead to enhanced radical quenching. Indeed, experiments from Miesse *et al.* [100] show that even when the walls are insulated, the quenching distance varies considerably with wall material (see figure 1.8). This study shows that materials with very stable properties in front a thermal stress, such as cordierite, exhibit far lower quenching distance than materials well known to be receptive to adsorption phenomena such as stainless steel.

- The **burner dimension**. Raimondeau *et al.* [121] performed an analytical study, varying the burner dimension. They used a boundary layer approximation of the governing equation and a simple radical recombination mechanism, on their cylindrical configuration. As increasing the inlet temperature favours the flame stability, they found the minimum inlet temperature necessary to stabilise the flame while varying the tube radius for given heat loss coefficient and sticking coefficient of key radicals (see figure 1.9). The work investigated three characteristic burner scales. First, with a radius of 1 cm, both the heat loss coefficient and the sticking coefficient of key radicals have no influence on the flame stability since the flame is far from the wall. Second, when decreasing the radius to 1 mm and reaching the micro-scale, the heat loss have a strong effect while the chemical quenching plays a secondary role. Indeed the sticking coefficient influences weakly the flame stability compared to the heat loss coefficient. Finally, the role played by the radical quenching further increases with the radius reduction, up to a domination of this mechanism in front of the thermal quenching under the micro-scale (radius of 0.1 mm).

- The **wall temperature**. Xie *et al.* [158] investigated numerically the influence of radical quenching in a 1 mm high 2D channel and found that, as the temperature increases, the radical removal in the vicinity of the wall becomes more effective. In this case, surface reactions were shown to modify the temperature distribution at the wall. Measurements by Kim *et al.* [75] indicated that the quenching distances are independent of the surface characteristics such as oxygen vacancy, grain boundary, or impurities at low temperatures. At high temperatures, however, the surface characteristics were shown to strongly affect the quenching distance, implying that radical removal at the wall plays a significant role in the quenching process. For lower temperature, H radicals recombine in the gas phase, their concentration being reduced close to the wall, thermal quenching becomes the dominant flame inhibitor [66].

In conclusion, the radical quenching can become a dominant phenomenon on flame extinction if the burner dimension is bellow the millimetre-scale, the walls are hot and their surface is not inert.

1.3.2.3 Diffusion dominated flows

The pioneering work of Karlovitz *et al.* [71] showed the importance of the sheared flow/flame interactions on combustion. This is especially true in the case of small-scale burners where the flame is placed exclusively within boundary layers [78]. The sheared flows in these highly confined configurations are very sensitive to density variations, making the thermal expansion an additional key ingredient of the problem [134]. In opposition to their macro-scale counterparts, the micro-scale burners promote the viscous and diffusive effects in front of the convective ones, since exhibiting low Reynolds (Re$= u_c \ell_c / \nu$) and Peclet (Pe$= u_c \ell_c / \alpha$) numbers, where u_c is the characteristic flow velocity, ν the kinematic viscosity and α the thermal diffusivity. This leads generally to laminar flow conditions. As the characteristic length diminishes, the diffusive effects can control the flow, as the characteristic diffusion time τ_{diff} (expressed here for unity

Prandtl and Lewis numbers) is lower than the residence time linked to convective effects τ_{conv},

$$\tau_{\text{diff}} = \frac{\ell_{\text{c}}^2}{\alpha} \quad < \quad \tau_{\text{conv}} = \frac{\ell_{\text{c}}}{u_{\text{c}}} \,. \tag{1.2}$$

Fernandez-Pello [40] pointed out that in non-premixed combustion situations, as the turbulent mixing is absent, the mixing time will be controlled by the diffusive effects. Besides, when the viscous effects and the surface to volume increase, the frictional loss will require more pumping. Nevertheless, Fernandez-Pello [40] specifies that this rise in viscous force could have a positive impact on technical issues such as the leakage of gases through joints or through moving surfaces, usually being a limitation of internal combustion engines efficiency. When considering micro-scale burners, the residence time of the fuel depends on the characteristic length in the propagation direction. If the combustion chamber is to short, the convective residence time can get smaller than the chemical time τ_{chem}, leading to low Damköhler number (Da$= \tau_{\text{c}}/\tau_{\text{chem}}$). The reduction of the Damköhler number should be considered as it may lead to incomplete combustion and impact both efficiency and pollutant emissions.

1.3.3 Micro-combustion modelling background

In this subsection, common strategies and assumptions made while modelling small-scale combustion, are gathered. As the parameters controlling the modelling are numerous, works issued by the community are analysed to point out the aspect requiring further study. This review is a key point in the construction of the modelling strategy used in this Ph. D. thesis work.

1.3.3.1 Heat loss modelling

The governing role of the wall on small-scale combustion requires to account for the flame/wall interactions (see § 1.3.2.1). Following the low order analysis by Ronney [123], the extinction limits captured are very sensible to the wall modelling. In micro-scale combustion, most of the heat transfer is driven by the conduction within the wall. Boehman [12] points out that the heat transfer through conduction in the fresh gases along with the radiative transfer play a much lower role. Several studies attended to account for the heat loss [44, 64, 66, 85, 89, 96, 151]. In some 1D simulations [44] and theoretical work [64, 96], models account for interface heat transfer via the Newton's law of cooling based on a Nusselt number (Nu$= h\ell_{\text{c}}/\lambda$),

$$\dot{Q}_{\text{w}} = \frac{\lambda \text{Nu}}{r_{\text{w}}}(T - T_{\text{w}}) \,. \tag{1.3}$$

This Nusselt number is fixed following an analytical solution of fully developed flow. A value of Nu=4 is typically assumed in a channel. As pointed out by Gauthier *et al.* [44], this assumption permits to recover global flame dynamics trends [96, 101, 147]. Yet, studies by Norton *et al.* [107] and Veeraragavan *et al.* [151], who performed an analysis of the Nusselt number, showed that this last varies along the channel axis, especially at the flame location (see figure 1.10). This approximation should thus be avoided to produce quantitative results.

Besides, the heat exchange between the external wall surface and the ambient is often neglected, as in the work of Kurdyumov *et al.* [85], where the wall is modelled by assuming that the external surface of the wall is maintained at the temperature of the fresh mixture. Simultaneously, the temperature evolution across the wall is taken linear by supposing that the wall thickness is very small compared to the channel height. Hypothesis which might not be always valid in such a configuration.

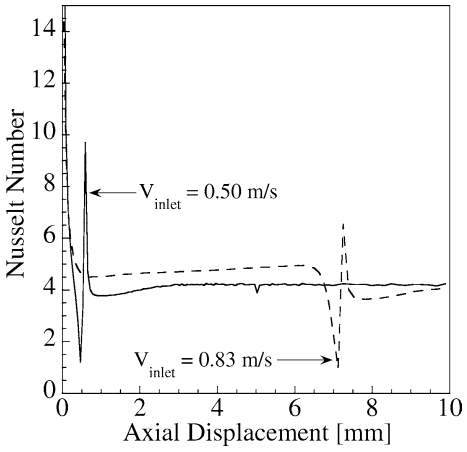

Figure 1.10: Nusselt number vs axial displacement for two inlet flow velocities indicated. The Nusselt number strongly varies at the flame position. Figure extracted from [107].

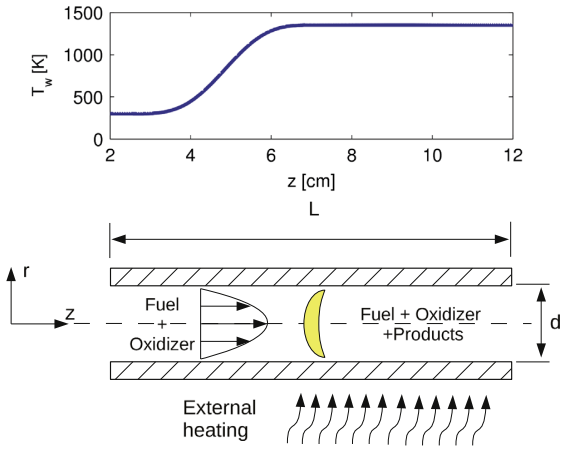

Figure 1.11: Schematic of the configuration investigated. The evolution along the channel's axis of the temperature $T_{\mathrm{w}}(z)$ imposed at the wall is shown at the top. Figure extracted from [7].

In addition, experimental [147] and numerical [7] studies avoid the coupling between the flame and the solid by imposing a temperature profile in the solid (figure 1.11). Fixed temperature studies provide useful informations on transient instabilities. Still, the often-used hyperbolic tangent temperature profile might not be representative of a realistic burner. In this case, the channel temperature does not correspond to any preheating by the flame and forces enhanced heat losses when approaching the channel inlet (low temperature imposed). Similarly, if the inlet velocity is high and pushes the flame further downstream the transition to high wall temperature, the reactants will be preheated although in practice the walls would have no reason to be hot at this location. Finally, in the literature, few studies were found to model the conduction in the solid by solving therein the conservation of energy and to model heat loss from the wall exterior surface to the surrounding environment [43, 66, 89, 106]. This realistic modelling requires more focus and a specific attention will be brought to this point in the following.

1.3.3.2 Surface reactions modelling

In § 1.3.2.2 the role of surface reactions was discussed. This phenomenon is the subject of very few studies in combustion, as usually the surface-to-volume ratio allows for neglecting it. However, the radical quenching can become an essential flame inhibitor when passing from meso to

micro-scale combustion, while exhibiting non-inert materials and high wall temperatures. The modelling of this phenomenon is very complex and not well understood yet. In their study, Bai *et al.* [6] investigated the radical wall quenching with a single surface reaction modelling in a quasi-one-dimensional theoretical model. They concluded that the influence of the radical quenching increases with the wall temperature, as observed by Ju *et al.* [66]. Nevertheless, in this low-order model, the radical to heat loss quenching coefficients ratio was setted not to vary with the channel diameter, in opposition to the conclusions of Raimondeau *et al.* [121], exhibiting the difficulty in finding a simple modelling strategy.

Substantial efforts on chemistry modelling both in the flow and at the surface have been offered by Raimondeau *et al.* [121]. In particular the use a complex surface mechanism for methane/air flames radical quenching, which was displayed in table 1.1. They notably showed that, in their configuration, the wall effect of radical quenching is significant due to the fast mass transfer between the walls and the bulk flow. Comparing their results to experimental data involving a quartz wall, Kizaki *et al.* [79] considered the same surface kinetic mechanism and found that, for a unity sticking coefficient, no-modelling of the radical quenching exhibited results closer from experiment than using the aforementioned mechanism. This was noted e.g. for the CO concentration of the exhaust gas, in fuel-rich configuration. They concluded that the model in table 1.1 overestimates the effect of radical quenching in this case. They reduced the sticking coefficient and found that the CO concentration the closet to the experiments was obtained for $5 \cdot 10^{-4}$. Finally, they stated that the quenching mechanism is negligible at atmospheric pressure but activates when decreasing the operating pressure. The lack of quantitative experimental/numerical comparison limits the confidence that one can place in the modelling strategies employed so far. Besides, conclusion drawn on the effect of surface reactions were shown to vary. It was also evoked when discussing figure 1.8 that experiments show a great

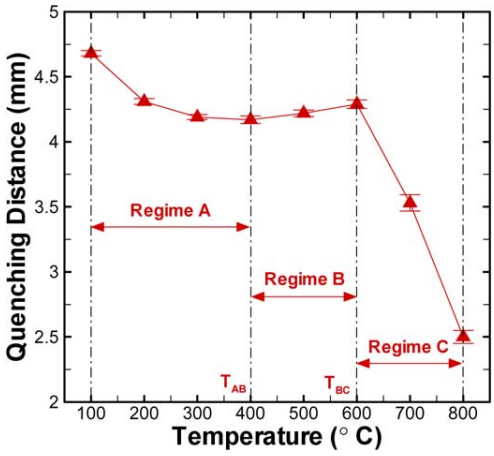

Figure 1.12: Different regimes driving flame quenching. Regime A is dominted by thermal effects, regime B by heterogeneous surface reactions and C by homogeneous chemical reactions. Figure extracted from [75].

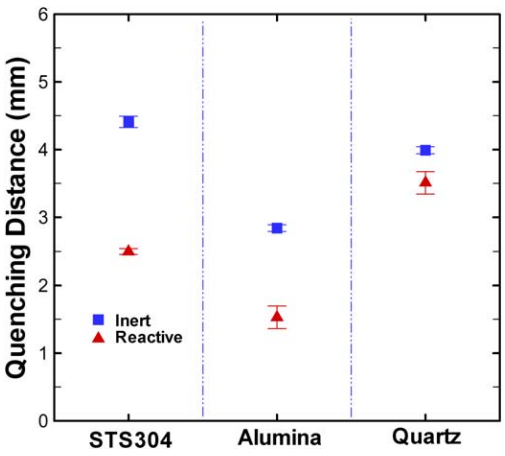

Figure 1.13: Quenching distances from reactive and inert plates at wall temperature of 1100K. Figure extracted from [75].

variability of radical quenching influence with the wall material, effect which should thus be accounted in the modelling to produce thoughtful results. Notably, Kim *et al.* [75] measured experimentally the quenching distance for a methane/air flame between two plates, for various plate temperatures, material and both reactive and inert versions of each material. They concluded that for a plate temperature of 1100 K, the rapid chain-branching reaction results in excessive production of OH, O and H radicals, dominating the radical removal surface reactions and resulted in a strong decrease of the quenching distance (figure 1.12). At this temperature, and for material exhibiting naturally low surface reactivity such as quartz, it results in low discrepancies between reactive and inert version of the material (figure 1.13). To finish, Saiki *et al.* [128] analysed experimentally the effect of wall material on a methane-air premixed flame formed in 5 mm wide channel. In a numerical simulation, the sticking coefficient of a surface reaction model was estimated to reproduce the OH mole fractions measured experimentally. A coefficient of 0.01 was determined for the quartz wall case. This led to a 1.5% variation, on the global flame heat release, compared to no accounting of surface reactions.

From the evoked experimental observations and the fact that the coming study exhibits a 5 mm high quartz channel, the surface reactions will be neglected in the present work.

1.3.3.3 Kinetic mechanism choices

Because of the numerous couplings between chemistry, heat transfer and flame propagation in flame/wall interaction [42, 117], the complexity level of chemistry introduced in the simulation of small-scale combustion is usually in line with the physical phenomena under study. Focusing on wide parametric analysis, global single- or multi-step chemical schemes have been used [7, 66, 78, 106, 146]. Skeletal mechanism for methane/air mixtures were also employed, e.g. 16 species and 25 reactions by Li *et al.* [89] and 19 species and 84 reactions by Gauthier *et al.* [44]. Hydrogen/air flames have been modelled with detailed schemes by Pizza *et al.* [114], also to examine the impact of the Soret effect in the study of Jimenez *et al.* [60]. Besides, Nakamura *et al.* [103] pointed out that the simulation of combustion instabilities in small-scale systems may require a refined description of chemistry. Further in the case of methane/air flames, Kizaki *et al.* [79] reported two-dimensional simulations in a low-Mach number formalism with the detailed GRI-3.0 mechanism [137], with a good agreement against experiments on a quenched flame stabilised after imposing a temperature profile. This Ph. D. thesis work will stress that, when considering a fully thermally coupled confined flow problem, the kinetic mechanism has a preponderant influence on the flame topology and dynamics. In consequence, an important effort will be devoted to this point in the present work.

1.3.3.4 Soret effect

The transport of light species toward high temperature areas and of heavy species toward low temperature areas, known as the Soret effect, and its conterpart Dufour effect, are known to modify the burning rate when considering combustion with fuel Lewis number different from unity. This was observed by Jimenez *et al.* [60] for hydrogen/air combustion, where combustion is enhanced by the transport of hydrogen into the reaction zone. Because of the close

to unity Lewis number, it is usually admitted that this effect is negligible when considering methane/air combustion. Hypothesis widely followed in the micro-combustion community [7, 44, 66, 78, 79, 89, 106, 146]. Accordingly, these effects are neglected in the present work. Nevertheless, when considering confined combustion, Popp *et al.* [120] and Hasse *et al.* [52] point out that pressure and temperature gradient at the wall might increase the Soret and Dufour effects, weakening the hypothesis.

1.3.3.5 Multi-dimensional property of the simulations

Gauthier *et al.* [44] and Bai *et al.* [6] point out that, under adiabatic conditions and with a tube diameter or a channel height below the millimetre scale, a stretched flame surface can hardly develop and the problem is reduced to a single direction. In opposition, heat losses with wall-quenching [44] impose at least two-dimensional simulations, as does larger channel height, because of the flow redirection by the flame [78]. Studies by Kurdyumov *et al.* [84], Tsai [146] and Pizza *et al.* [114] display three-dimensional simulations of flames in tubes, either to study relatively large tube diameters or lower than unity Lewis number flames. Indeed some specific configurations may require to seize azimuthal effects. The present configuration is a planar channel, and will be modelled with 2D simulations.

1.3.3.6 Symmetric and asymmetric flame topologies

In small-scale combustion, a vast amount of studies consider the problem as symmetric, either with respect to the middle plane in a flat channel or to the centreline in a tube [43, 44, 66, 78, 79, 89, 106, 107, 121, 123, 134, 158]. Recent numerical [60, 83, 114, 146] and experimental [65, 161] studies show the apparition of asymmetric flame shapes for various conditions, making notably rare to observe tulip-shaped flames. Depending on the configuration, the phys-

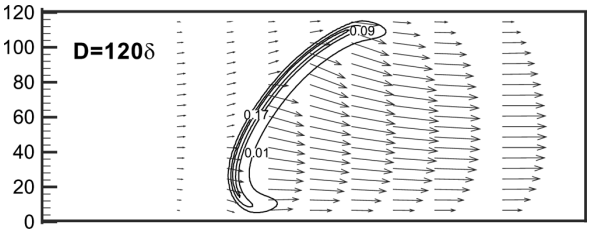

Figure 1.14: Contours of the dimensionless fuel mass reaction rate and the velocity vectors, for the slanted flame in 2-D channel without symmetry assumption, $D = 120\delta_F$. Figure extracted from [146].

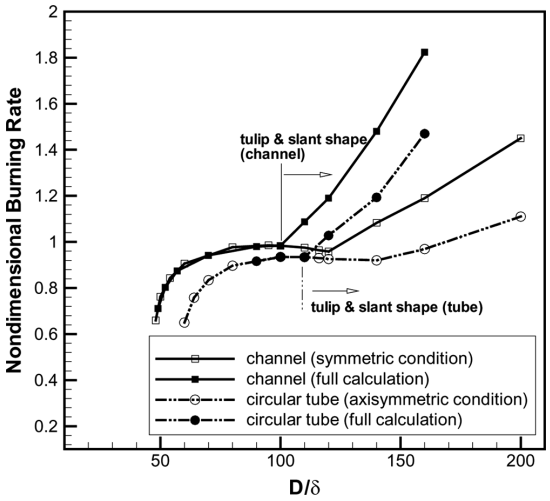

Figure 1.15: The variation of the flame burning rate with the duct width for the stationary flame in ducts. Figure extracted from [146].

ical phenomena susceptible to break symmetry are numerous and various parameters need ones attention when formulating a symmetry assumption:

- First, a focus is made on the streamline deformation due to thermal expansion, referred to as hydrodynamic **Darrieus-Landau** (D-L) instabilities [27, 86]. The numerical study by Tsai [146] points out the predominance of slanted flames against tulip-shaped flames for a tube diameter exceeding a hundred times the flame thickness δ_F (around 5 cm in this case) due to D-L instabilities (figure 1.14). In these simulations of methane/air flames with fixed unity Lewis number, such an asymmetry is not observed for lower diameters, as it is well known that D-L instabilities require a minimal characteristic length to develop (figure 1.15). In the present work, where the channel transverse characteristic length does not exceed $15\delta_F$, such instability should not experience sufficient space to develop. This point will be the object of a verification.

- Second, the viscosity-induced **Saffman-Taylor** (S-T) instabilities [127] are typical of combustion in narrow channels. Indeed, this instability is due to the viscous-induced pressure gradients (favored by small channel dimensions, as pointed out by Joulin *et al.* [61]) in the case specific to flames, momentum loss being shown to contribute to flame instability. Kang *et al.* [69] specify that this effect is not correlated with the Lewis number and is reduced in presence of heat loss, which typically occurs in small-scale combustion, since based on viscosity variations.

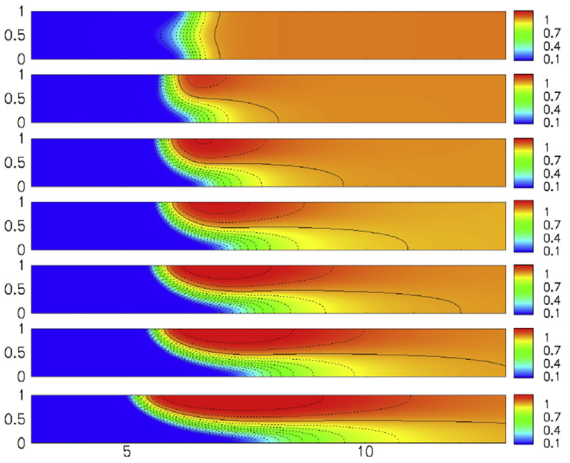

Figure 1.16: The reduced temperature of the steady flame solution obtained when symmetry about the axis is relaxed for different reactant non-dimensional flow rates -4, -2, 0, 2, 4, 6 and 10 (top to bottom) for this hydrogen flame. Figure extracted from [60].

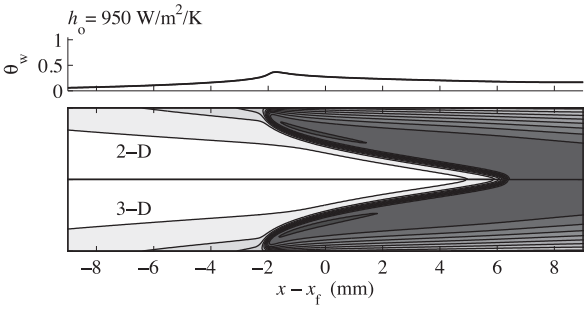

Figure 1.17: Contour plots of normalized fluid temperature θ, obtained with both 2- D and 3-D models of a methane flame, for an inner tube diameter of $D = 5.0$ mm. Isocontours are shown at intervals of 0.1 of θ. The wall temperature profile imposed at the wall interface, obtained from the conjugate heat transfer results at $h_o = 950$ W.m^{-2}.K^{-1} is shown above the contour plots. Figure extracted from [43].

- Third, numerous numerical studies on flame symmetry breaking focus on **Diffusive-Thermal** (D-T) instabilities [136, 149], making the Lewis number (Le) a key parameter.

This instability is due to the growth in curvature of flame fronts when the fuel presents light chemical species, quickly diffused into the flame front. For Le < 1, the existence of non-symmetric flames is discussed in various studies [60, 83, 114, 130, 131, 161], pointing out the instability of symmetric flames in front of their non-symmetric counterparts (figure 1.16). Consequently, when studying fuel exhibiting Le < 1, such as hydrogen, one must systematically consider non-symmetric effects in the modeling. In addition, in the context of a thermo-diffusive model, Le > 1 flames with low mass flow rate are found asymmetric by Kurdyumov [83]. Clavin et al. [24] stress that, for Lewis number larger than unity, vibratory instability of the planar flame in the tube can develop. Besides, unity Le flames have been found symmetric when approaching the micro-combustion scale. A study by Gauthier *et al.* [43] performs a comparison of 2-D axi-symmetric and 3-D stoichiometric methane/air flames propagating in a tube of internal diameter 5 mm with unity Lewis number, yielding similar symmetric tulip-shaped flames (figure 1.17). A stability analysis, by Kurdyumov *et al.* [85], of flames submitted to heat loss also stresses that unity Lewis number symmetric flames are stable. It is essential to note that these numerical studies do not consider the gravity.

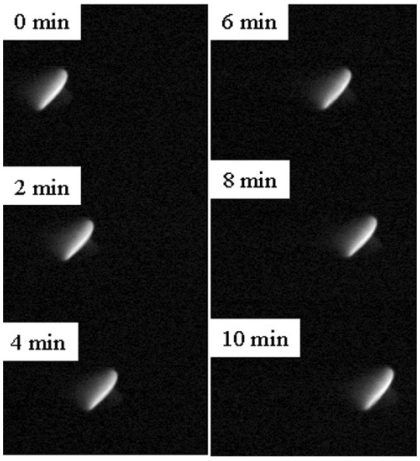

Figure 1.18: The time evolution of a methane-air stoichiometric flame slowly moving in a 5 mm horizontal tube. Note that the reactants flow from the right in these pictures. Figure extracted from [65].

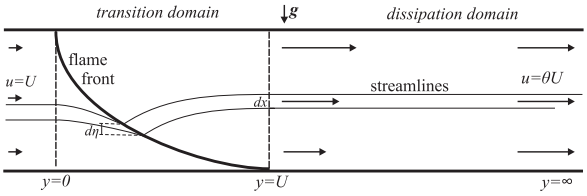

Figure 1.19: Schematics of steady flame propagation in horizontal channel. Horizontal arrows of different lengths qualitatively depict gas velocity profiles in various parts of the channel. Figure extracted from [72].

- Fourth, **body forces** might influence the flame topology. In small-scale combustion numerical studies, gravity is often neglected based on the relatively high Froude number (Fr) associated, this last varying as $1/\ell_c$,

$$\mathrm{Fr} = \frac{u_c^2}{g\ell_c} \simeq 3\,, \tag{1.4}$$

for a characteristic velocity $u_c = 40$ cm.s^{-1} and a characteristic length $\ell_c = 5$ mm. Having a Fr number higher than one yields that gravitational effects do not drive the flame

dynamics but not necessarily that these can be completely neglected. Experiments by Ju *et al.* [65] and Zamashchikov [161], treating the flame propagation in horizontal tubes, show the appearance of slanted flames with a preferential direction, suggesting the role of a directional force (figure 1.18). In these works, symmetry breaking is generally thought to be due to free convection in the air surrounding the hot tube. Several studies [1, 129, 154] show that a thermal and flow plume develops around a heated tube, consequently the Nusselt number decreases toward the top of the cylinder as the boundary layer thickens. In fact, the plume insulates the cylinder from the surrounding air and results in a lower heat transfer coefficient. A temperature difference between the top and bottom wall also results from the establishment of this plume around the tube. This phenomenon is a possible symmetry breaking source, but no complete analysis has been made on this point. Further, in a theoretical study employing a model equation for flame propagation, Kazakov [72] points out that gravity might play a role not only through external free convection but also via buoyant effects inside the channel. The generation of vorticity due to the gravity field would result in asymmetric flames, anchored at the top (figure 1.19). Further numerical and experimental analyses of this point are advanced in the present manuscript.

- Finally, when studying the flame propagation in a vertical tube numerically, Tsai [146] remarks that the symmetry breaking observed (and related to D-L instabilities) occurs for lower tube diameter when gravity is entered with the same direction as the flow, and the Froude number is diminished. This suggests the effect of gravity-driven **Rayleigh-Taylor** (R-T) instabilities [140, 144] on the symmetry breaking, this buoyant instability occurring at the contact of two gases with the denser one on top of the other.

Various parameters are known to influence the aforementioned instabilities such as, the channel dimensions, the nature of the fuel, the wall temperature as well as the application area (micro-gravity, on-earth). From the numerous symmetry breaking sources, stable tulip flames have rarely been observed experimentally. Nevertheless, the observations by Di Stazio *et al.* [29], of a stable tulip-shaped stoichiometric methane/air flame, have been realized for a tube of 2.15 mm inner diameter. Such a configuration was obtained with an imposed high temperature profile, via an intense external heating of the quartz tube (temperature peak at 1600 K), and an inlet flow rate of 1 $m.s^{-1}$. In the work of Brambilla *et al.* [14], while decreasing the artificially high wall temperature, the transition from tulip to slanted flames is observed, suggesting the stabilizing role of the hot walls on the flame, in this syngas combustion experiment. In the present Ph. D. thesis, further numerical investigations are proposed on this point.

1.3.3.7 Gravity effect

Quite generally, the effect of gravity is neglected when modelling flames propagating in small-scale burners, as it is the case in most of the studies presently reviewed. See the work of Raimondeau *et al.* [121], Xie *et al.* [158], Ju *et al.* [62, 66], Kim *et al.* [76, 78], Short *et al.* [134], Ronney [123], Boehman [12], Li *et al.* [89], Gauthier *et al.* [43, 44], Kurdyumov *et al.* [83–85], Minaev *et al.* [101], Norton *et al.* [106, 107], Bai *et al.* [6], Kizaki *et al.* [79],

Ganter *et al.* [42], Pizza *et al.* [114, 115], Jimenez *et al.* [60], Nakamura *et al.* [103], Hasse *et al.* [52], Kang *et al.* [69], Sanchez-Sanz *et al.* [130, 131], Chakraborty *et al.* [17] and Kuo *et al.* [82]. In this manuscript, this assumption is first followed, as it is also coherent with the microgravity conditions often addressed among the micro-combustion applications. Then the effect of gravity will be considered, as it will be revealed to be essential to the comprehension of some phenomena observed experimentally.

1.3.3.8 Unsteady modes

In micro-combustors, the enhanced heat loss and the flame/wall thermal coupling result in various instabilities. In the case of a diverging tube diameter, Xu *et al.* [159] showed the apparition of a so-called spinning flame instability. Another specific unsteady phenomenon called Flame Repetitive Extinction Ignition (FREI) was observed by Maruta *et al.* [96] and Richecoeur *et al.* [122], and simulated by Bucci *et al.* [15] with single-step chemistry and with an imposed external source of heat at the wall. These phenomena might make the conception of micro-combustion chambers more complex and require further study from the community.

1.3.3.9 Flame front tracking in numerical simulations

Stabilizing a flame in a channel or a tube by adjusting the mass flow rate of fresh gases, is experimentally [77] and numerically [78] challenging, mainly because of the difference in characteristic time scales between convection, heat transfer and combustion. To overcome this difficulty, stabilization is sometimes secured by imposing a temperature profile at the wall boundary condition, as applied by Maruta *et al.* [96], Gauthier *et al.* [44] and Sánchez-Sanz *et al.* [131]. Various other options have been discussed in the literature without adding thermal forcing at the wall. The flame front can be tracked in a well-defined reference frame attached to the flame, thus limiting the length of the computational domain [17, 60]. A given radial position and temperature level (i.e. a temperature known to be attained within the flame) is then used as the origin of the reference frame [83–85]. Besides, to the author knowledge, among the few studies which considered the fully coupled problem, with the solving of the heat equation in the solid and accounting for convective heat transfert from the wall exterior surface to the surrounding environment [66, 89, 106], none completely avoided the inlet effect, by ensuring zero gradients in the solid and flow parts, at the entrance. In the following, the proximity of the inlet to the flame front will be shown to impacts strongly the flame propagation, as it modifies the preheating of reactants. A specific attention will be brought to this point during this Ph. D. thesis.

1.3.4 Managing small-scale combustion

For the reasons presented in § 1.3.2, micro-combustion suffers a limitation of the flammability range compared to its macro-scale counterpart. In this section two technological leads, explored to extend the stability range for micro-burners, are presented: the excess of enthalpy and the catalytic combustion.

1.3.4.1 Excess enthalpy

The excess enthalpy principle was first introduced by Lloyd and Weinberg [90] and consists in using the energy of the burnt gases to preheat the reactants. By bringing energy to the reactant mixture, the combustion stability range is extended. One may note that this phenomenon is inherent to realistic micro-burners. At such scale, a non-negligeable heat recirculation from the burnt to the fresh gases via upstream conduction in the solid is observed, as presented in figure 1.20. Part H_o of the energy H, transferred from the burnt gases to the wall, is convected to the ambient while a flux Q is conducted upstream through the wall and preheats the fresh gases. Besides, Boehman [12] points out that backward gas conduction of heat is negligible and internal radiation plays a much lower role in micro-burners than in their conventional-sized counterparts, making the heat transfer by conduction in the wall the main preheating mechanism. In practical configurations, excess enthalpy is thus naturally performed through conduction in the walls, making the wall material one of the influencial concerns for micro-combustion. As example, Norton *et al.* [107] showed the influence of the wall material conductivity on extinction and blow-out (see figure 1.21).

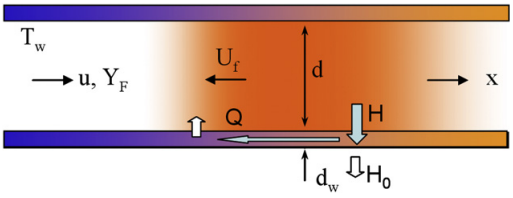

Figure 1.20: Schematic of flame propagation in a mesoscale channel with indirect heat recirculation through flame/wall structure thermal coupling. Figure extracted from [63].

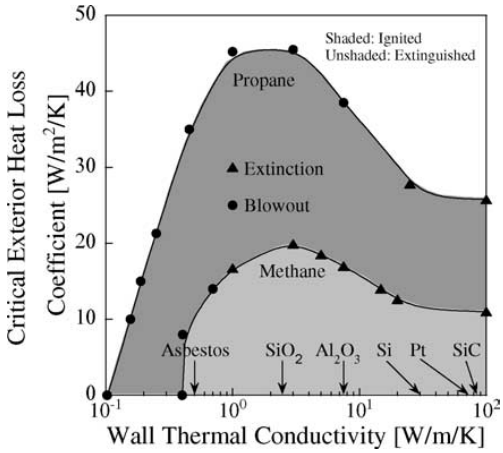

Figure 1.21: Critical external heat loss coefficient vs wall thermal conductivity for propane/air combustion in a 0.6 mm high 2D channel with 0.2 mm thick wall. Figure extracted from [107].

Not only the wall material can be adequately picked, but also the burner geometry can be thought in order to optimise the excess enthalpy phenomenon. Various configurations can be employed to allow the burnt gases to transfer efficiently heat to the reactant mixture (see figure 1.22). Some numerical and experimental studies considered such excess enthalpy configurations. For example, Weinberg *et al.* [156] and Ronney [123] performed an analysis of a U-shaped reactor, with products preheating reactants. Ju *et al.* [62] analysed two flames propagating in opposite directions in parallel channels. Recently some paper investigated more complicated configurations: Vican *et al.* [152], Kim *et al.* [76] and Cho *et al.* [20] (see figure 1.23) studied experimentally and analytically a swiss-roll burner configuration while Kuo *et*

al. [82] developed a two-dimensional numerical model of a similar spiral configuration. These thermal optimisations will most likely be employed in realistic burners. It is thus mandatory to understand the influence of excess enthalpy on the flame propagation and stabilisation.

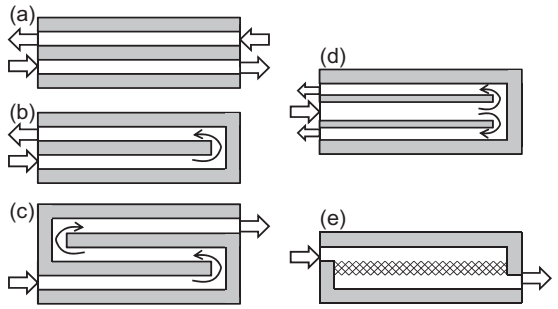

Figure 1.22: Various geometries of 'excess enthalpy' microburners: (a) combustion in counter-current heat exchanger, (b) heat recirculation geometry, (c) serpentine geometry, (d) symmetric heat recirculating geometry, and (e) porous co-current geometry. Shaded regions are solid walls and blank regions are flow channels. Figure extracted from [68].

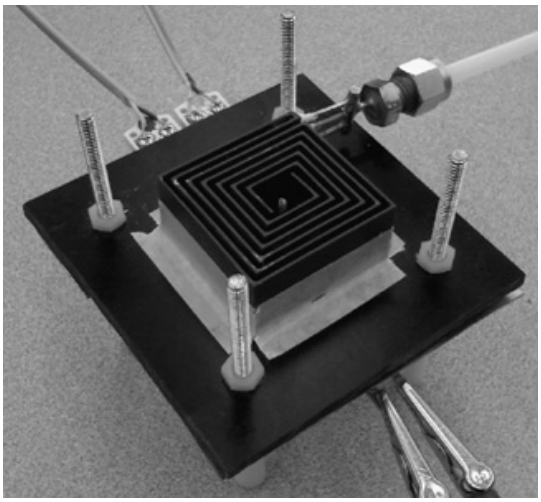

Figure 1.23: CNC-milled Vespel Swiss roll combustor in experimental stand. The top plate is removed for clarity. Figure extracted from [20].

1.3.4.2 Catalytic combustion

Although it will not be studied in this Ph. D. thesis work, the highlights of catalytic combustion are now shown. The high surface-to-volume ratio has been presented as a disadvantage for small-scale combustion, due to the enhanced heat and mass transfer to the wall leading to thermal and radical quenching, respectively. On the contrary, when a catalyst layer is deposited on the wall surface, the combustion can take advantage of the flame/wall proximity. In this context, catalytic combustion, by improving the thermal efficiency of the system, allows for an extension of the burner flammability limits, as pointed out in the pionneering work of Pfefferle *et al.* [113]. Figure 1.24, from Kaisare *et al.* [68], depicts the mechanism occurring in catalytic combustion. The reactants diffuse from the bulk flow to the catalyst layer, where reactions take place with lower activation energies than in the gas phase, before the products diffuse back in the flow channel. These exothermic catalytic reactions participate to the flame stabilisation by heating both the wall and the bulk flow and locating the combustion area. In addition, an appropriate catalytic material reduce the pollutant emissions.

Catalytic reactions impact strongly the flame stabilisation, including its location. The experiment by Norton *et al.* [108], focusing on the behavior of a platinum/alumina catalytic microburner, shows that the flowing hydrogen/air mixture self-ignites at the channel entrance. This trend is recovered from stoichiometric to extermely fuel lean ($\phi = 0.29$) equivalence ratio, although in this last case combustion exhibits quite low (400 K) maximal temperature. As

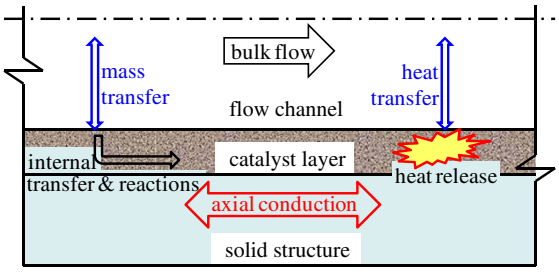

Figure 1.24: Schematic of various processes within a catalytic microburner. The mass and thermal processes are shown on left and right ends, respectively, for clarity: these processes indeed take place at the same location in a microburner. Figure extracted from [68].

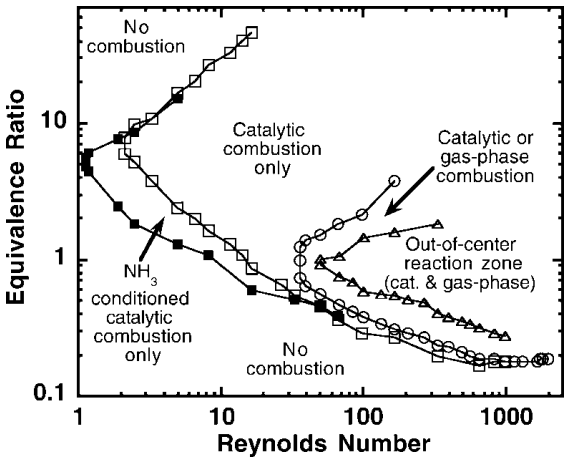

Figure 1.25: Extinction limit map for catalytic and gas-phase combustion in the inconel Swiss roll. Figure extracted from [2].

pointed out by Kaisare *et al.* [67], the reaction area can be widespread when considering catalytic combustion in channels, in opposition to pure gas-phase combustion where flame fronts of the order of the adiabatic flame thickness are more usual. This can lead to a different stabilisation strategy when compared to gas-phase combustion only. When reaching high velocities in catalytic burners, the reaction zone might spread all along the reactor length, leading to incomplete combustion. The low flow conversion can be risen by using highly conductive walls to enhance the preheating of the reactants and favour reactions at the channel entrance. Comparisons of catalytic and non-catalytic (gas-phase) combustion stability can be found in the literature. Although it prevents from radical quenching, catalyst combustion does not suppress the thermal loss from the wall and is meant to be used conjointly with other methods such as excess enthalpy configuration, see e.g. the work of Ahn *et al.* [2] on a Swiss roll catalytic burner. Figure 1.25 shows, in this case, the drastic extension of rich stability limits in presence of catalytic combustion, allowing for stable combustion down to unity Reynolds number flows.

It was pointed out in § 1.3.3.6 that the imposition of a high thermal profile allows to stabilise symmetric tulip-shaped flames where slanted flames are usually observed. In the same way, catalytic walls allow a stronger stability of such flames. Dogwiler *et al.* [30] studied experimentally methane/air flames stabilised between two horizontal plates spaced 7 mm apart. The flow is preheated at 700 K and propagates along uniformly hot walls at 1300 K, at an equivalence ratio of 0.35. They pointed out that slanted flames which could not be predicted by their model, are observed when experimenting with inert walls (figure 1.26(a)), while catalytically active walls yield stable tulip-shaped flames (figure 1.26(b)). Similar conclusions were drawn in the numerical study of hydrogen/air flames in a 1 mm channel by Pizza *et al.* [115], in which the intensity of surface reactions is progressively raised, leading to enhanced stability of the tulip-shaped flame along with the suppression of some combustion instabilities.

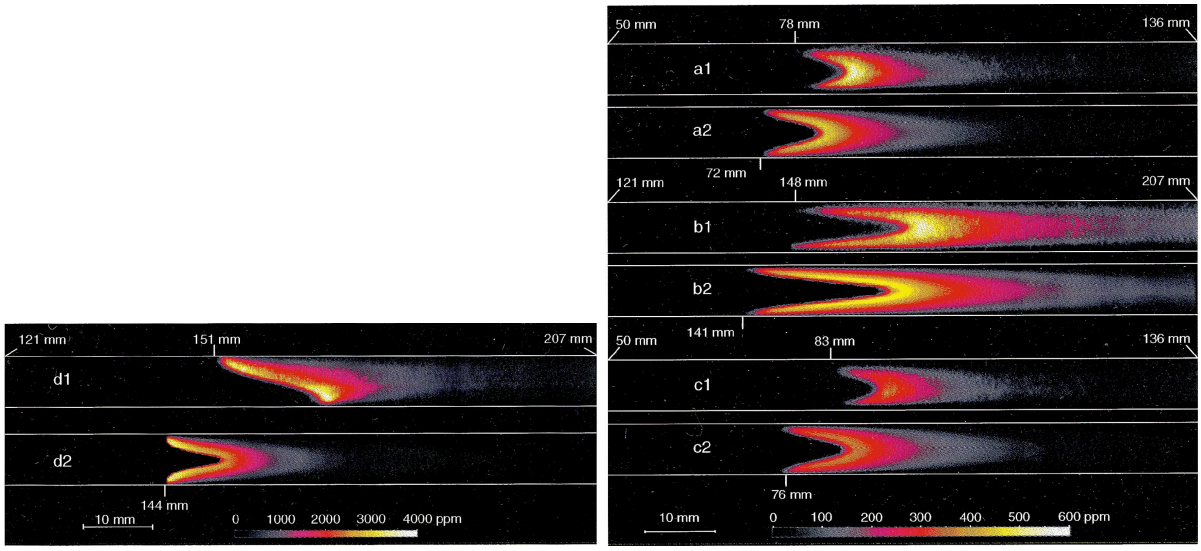

(a) Inert surface (b) Active surface

Figure 1.26: Measured (1) and predicted (2) OH concentration maps (in ppm) for the non-catalytic and catalytic cases. Figure extracted from [30].

1.4 Ph. D. thesis objectives and outline

This Ph. D. thesis is part of the project ANR-14-CE05-0030-MAPEE: 'Microcombustion Assistée par Plasma et Excès d'Enthalpie', by the Agence Nationale de la Recherche (ANR). The project is conjointly piloted with a team from EM2C-CNRS-UPR288 laboratory, composed of Amanda Pieyre, Franck Richecoeur and Nasser Darabiha.

For micro-combustion to become a widespread power source for portable devices, deep progress are still to be made in the comprehension of flame propagation in narrow environments. Physical phenomena at play in the flame propagation need to be mastered to ensure stable combustion. In this context, this manuscript treats of the modelling and the understanding of fundamental physics phenomenology applied to micro-combustion. To build on previous works about flame/wall interactions, flames topology, flames dynamics and interactions with the surrounding environment, the most simple configuration of a two dimensional planar channel is considered. Keeping in mind the industrial objective of building energy producing small-scale burners, the present Ph. D. thesis is organised around the problem of flame stabilisation in such devices. In order to allow for self-sustained combustion in the absence of supplementary energy source such as heating, excess enthalpy or catalytic walls, the characteristic dimension of the studied channel is chosen slightly above the quenching distance of methane/air flames at $\phi = 0.8$, i.e. 3 mm [59]. A channel of internal height 5 mm is thus studied, as it allows for flame stabilisation while exhibiting similar mechanisms as in micro-scale combustion.

To build up on previous numerical works, a specific attention is brought to the modelling of key phenomena. As the literature review revealed, in small-scale burners, the flame suffers specific stress including enhanced heat loss. The modelling of kinetics in this precise context

was few discussed by the community, calling for deeper insight on this aspect. Besides, as the thermal conditions were shown to influence actively the flame propagation, further analysis is needed on the thermal coupling between the flame and the wall.

Aside from modelling aspects, this work intends to bring understanding on various physical phenomena, typical of micro-combustion. First, in the absence of gravity effects, various analyses are driven. The flame interactions with the flow boundary layer and wall thermal coupling are studied. The influence of the wall thermal characteristics on the flame behaviour is analysed. The flame behaviour when submitted to a thermal stress is considered. Finally, the on-earth breaking of flame symmetry observed in small-scale channels is explained. To present these results, the manuscript is organised as follows.

Chapter 1: Introduction
This chapter depicted how the miniaturisation of portable devices progressively leads to an industrial context favourable to the study of micro-scale combustion for embedded low power sources. Subsequently, a literature review, treating from the specificities of micro-combustion to the modelling strategies in numerical studies and the potential method for managing combustion at small-scale, was provided. Finally, the Ph. D. thesis objectives were positioned in the light of the literature review.

Chapter 2: Modelling
First, the aerothermochemistry equations are displayed. The balance equations, variables and dimensionless number employed to model and describe reactive flows are given along with details on the combustion reactions modelling. The construction of a solid solver is then detailed and assessed. The function of this solid solver is to model the heat transfer in the solid and to couple these last with the reactive flow. Finally, the numerical methods and simulations parameters used in this Ph. D. thesis, with the code SiTCom-B, are listed.

Chapter 3: Kinetic reduction strategy for small-scale combustion
The quality of the flames dynamics predictions depends strongly on the kinetics modelling. This chapter is thus dedicated to the building of skeleton mechanisms fitted to small-scale combustion study. The reduction method ORCh (Optimised and Reduced Chemistry) [58] is employed while determining reference trajectories, for the reduction and optimisation processes, tailored to small-scale combustion. The comparison of skeleton mechanisms derived with and without considering these adapted trajectories is provided with respect to the reference detailed GRI-1.2 mechanism. The 17 species skeleton mechanism, reduced while accounting for trajectories tailored to small-scale combustion, is shown to replicate with fidelity results from the reference mechanism.

Chapter 4: Premixed flame/wall interaction in a narrow channel under microgravity: Impact of wall thermal conductivity and heat losses
In this chapter, a methane/air flame stabilized in a 5 mm high channel is studied under microgravity conditions. The response of the premixed flame shape to various operating conditions is

analysed in terms of flame propagation velocity and flow topology in the vicinity of the reactive front. A focus is made on the interrelations between the flame speed, the configuration taken by the flame surface, the flow deviation induced by the heat released and the fluxes at the wall. The flame couplings with the boundary layer and the thermal exchanges with the channel walls are highlighted. The influence of the channel thermal properties and heat losses to the ambient, on the flame dynamics and topology, is then discussed. A regime diagram is proposed to delineate between flame shapes in order to build a classification versus heat transfer properties.

Chapter 5: Simulating upstream flame propagation in a narrow channel after wall preheating under microgravity
The response of the premixed flame not submitted to gravity effects and initially stabilised in the narrow channel, is investigated for an amount of heat supplied upstream through the wall. Various heating intensities are considered and a minimum heating supply is found necessary to initiate a complete upstream flame translation. A specific attention is paid on the relative contributions of heat convection in the flow and heat conduction in the solid. The heat transfer mechanism triggering the flame movement is revealed to be mainly convective. The flame translation is found to be organised in two stages, with first a downstream movement due to fresh gases expansion because of heating by the wall, followed by the upstream propagation due to the enhancement of the burning rate by the mixture preheating. The shape, the flash back speed, and the final position of the flame vary with the amplitude of the heat flux brought to an external surface of the wall.

Chapter 6: Symmetry of flames stabilized in small-scale channels : Impact of gravity, external heating and channel dimensions
The symmetry breaking of methane/air flames, propagating in the horizontal narrow channel, is investigated experimentally (EM2C results), theoretically and numerically. Indeed, in place of a symmetric flame, EM2C experiments show the stability of a slanted flame with a preferential anchoring at the top. This result is recovered both when the flame propagates along cold walls and when it is stabilized and thermally coupled with the channel walls. Numerically, physical phenomena at play are incorporated progressively to finally show the preponderant role played by gravity in the symmetry breaking. Theoretical analysis of the configuration predicts that gravity acts on the flame topology via a modification of the baroclinic term at the flame crossing, resulting in a deviation of the incoming streamlines in a coherent manner with the experimental observations. This analysis is supported by the post-processing of a series of simulations. The methane/air flame numerical simulations performed include complex molecular transport and the fully coupled solving of heat transfer at and within the wall. Finally, further investigations show and comment the stabilizing effect of wall heating and flame/wall proximity on the flame symmetric form, as observed in previous experiments.

Chapter 7: Conclusion and perspectives
First, the conclusion is the occasion for gathering the highlights of this Ph. D. thesis. Then the

limits of the accomplished work are drawn and a discussion is provided on improvements and further work to bring to this thesis.

1.5 Publications

1.5.1 Peer-reviewed international journals

This thesis work led to the publication of three peer-reviewed articles.

- K. Bioche, A. Pieyre, G. Ribert, F. Richecoeur, and L. Vervisch. The role of gravity in the asymmetry of flames in narrow combustion chambers. *Combustion and Flame*, 203:238-246, 2019
- K. Bioche, G. Ribert, and L. Vervisch. Simulating upstream flame propagation in a narrow channel after wall preheating: Flame analysis and chemistry reduction strategy. *Combustion and Flame*, 200:219-231, 2019
- K. Bioche, L. Vervisch, and G. Ribert. Premixed flame-wall interaction in a narrow channel: Impact of wall thermal conductivity and heat losses. *Journal of Fluid Mechanics*, 856:5-35, 2018

1.5.2 Conferences

- K. Bioche, G. Ribert and L. Vervisch, *Flame stabilisation and propagation in a narrow channel after wall preheating*, in 12$^{\text{th}}$ International ERCOFTAC Symposium on Engineering Turbulence Modelling and Measurements, Montpellier, France (2018).
- K. Bioche, G. Ribert and L. Vervisch, *DNS analysis of flame propagation in a boundary layer: A classification diagram of flame shapes versus wall thermal properties* , in 4$^{\text{th}}$ INitiative en Combustion Avancée, Safran Paris Saclay, France (2017).
- K. Bioche, G. Ribert and L. Vervisch, *Premixed flame propagation in a boundary layer*, in 16$^{\text{th}}$ International Conference on Numerical Combustion, Orlando, USA (2017).

Chapter 2

Modelling

Contents

2.1 Chapter summary 45

2.2 Aerothermochemistry equations 46

2.2.1 Mixture properties 46

2.2.2 Balance equations 47

2.2.3 Dimensionless numbers 50

2.3 Solid/flow conjugate heat transfer: A solid solver 51

2.3.1 Conservation of energy 52

2.3.2 Numerical resolution 53

2.3.3 Imposition of the boundary conditions 55

2.3.4 Coupling strategy 55

2.3.5 Validation 57

2.4 Numerical solving with SiTCom-B 60

2.4.1 Numerical methods 60

2.4.2 Simulations parameters 63

2.4.3 Numerically stabilizing flames in channels 66

2.1 Chapter summary

This chapter gathers various modelling aspects of the physics under study. Section 2.2 introduces the governing equations of the aerothermochemistry as well as the variables used to describe the reacting flow. Then, the solver developed and employed to model the thermal transfer in the channel walls is presented in section 2.3, along with the coupling strategy applied between the flow and the solid solvers. The solid solver and its coupling with the code

SiTCom-B are then validated against canonical tests. Finally, section 2.4 describes the numerics used in the code SiTCom-B, from the integration schemes to the simulations parameters and the method used to stabilise the flames in the channel.

2.2 Aerothermochemistry equations

2.2.1 Mixture properties

Various quantities are useful to describe the composition and state of a reactive mixture. Mass fraction Y_k of a species k is defined as the mass of this species over the overall mass contained in a control volume V,

$$Y_k = \frac{m_k}{m}\,, \tag{2.1}$$

while the molecular fraction is defined in an analogous manner based on moles,

$$X_k = \frac{n_k}{n}\,. \tag{2.2}$$

The molecular weight of species k is noted W_k and gives the molecular weight of the mixture W, composed of N_{sp} species, in combination with the molecular fraction,

$$W = \sum_{k=1}^{N_{\text{sp}}} X_k W_k\,. \tag{2.3}$$

Mass and molecular fractions are linked by the relation

$$Y_k = \frac{W_k}{W} X_k\,. \tag{2.4}$$

The mixture density ρ is defined as

$$\rho = \frac{m}{V}\,, \tag{2.5}$$

and is linked to the temperature T and the pressure P through the state equation for ideal gas,

$$P = \rho r T\,, \tag{2.6}$$

with r the reduced ideal gas constant, defined from the ideal gas constant $R = 8.3144621$ J.mol^{-1}.K^{-1} via

$$r = \frac{R}{W}\,. \tag{2.7}$$

Finally, the equivalence ratio ϕ is a relevant mixture property when studying reactive flows. For premixed flames, this data is sufficient to quantify the relative concentrations in fuel and oxidizer. It is built to yield unity when fuel and oxidizer are present in concentrations such that they should theoretically be fully consumed across the flame, the mixture is then said stoichiometric (st),

$$\phi = \frac{Y_{\text{F}}/Y_{\text{Ox}}}{(Y_{\text{F}}/Y_{\text{Ox}})_{\text{st}}}, \tag{2.8}$$

with Y_{F} and Y_{Ox} the mass fractions in fuel and oxidant, respectively. When the equivalent ratio is less (resp. greater) to one, the mixture is said lean (resp. rich).

2.2.2 Balance equations

In the following, the transport equations employed to model the flow are recalled. They can be derived based on the fact that, in a continuous medium, extensive quantities are conserved. In the case of a reacting flow, typical conservative quantities are $\rho\mathbf{u}$, $\rho\mathbf{Y}$ and ρE with $\mathbf{u}$ the velocity vector, $\mathbf{Y}$ the species mass fraction vector containing the mass fractions of the N_{sp} species and E the specific total sensible or non-chemical energy. Their derivation may be found in standard books such as the ones by Candel [16] or Poinsot and Veynante [116].

2.2.2.1 Conservation of momentum

In a reacting flow, in the absence of other external body forces than gravity (such as an electromagnetic field), the three momentum conservation equations yield for the i-th direction

$$\frac{\partial \rho u_i}{\partial t} + \frac{\partial}{\partial x_j}\left(\rho u_j u_i\right) = -\frac{\partial P}{\partial x_i} + \frac{\partial \tau_{ij}}{\partial x_j} + \rho g_i \,, \tag{2.9}$$

where u_i are the components of the velocity vector, τ_{ij} are the components of the Newtonian viscous tensor and g_i are the components of the gravity acceleration vector. The Newtonian viscous tensor is written [37]

$$\tau_{ij} = -\frac{2}{3}\mu\frac{\partial u_k}{\partial x_k}\delta_{ij} + \mu\left(\frac{\partial u_i}{\partial x_j} + \frac{\partial u_j}{\partial x_i}\right) \,, \tag{2.10}$$

with μ the dynamic viscosity and δ_{ij} the components of the Kronecker tensor. This equation is directly issued from the Navier-Stokes equations [104, 139].

2.2.2.2 Conservation of mass

Unlike the typical mass conservation equation, part of the Navier-Stokes equations,

$$\frac{\partial \rho}{\partial t} + \frac{\partial}{\partial x_j}\left(\rho u_j\right) = 0 \,, \tag{2.11}$$

multi-species reacting flows require for the solving of the mass conservation equation of each species. This leads to the solving of N_{sp} mass transport equations of species k, of the form

$$\frac{\partial \rho Y_k}{\partial t} + \frac{\partial}{\partial x_j}\left(\rho(u_j + V_{k,j})Y_k\right) = \dot{\omega}_k \,, \tag{2.12}$$

with $V_{k,j}$ the molecular diffusion velocity of the k-th species in the j-th direction and $\dot{\omega}_k$ the chemical source term standing for the production or destruction of species k. In the following chapters, the chemical source terms will be noted $\dot{\omega}_{\rho Y_k}$. Besides, remarking that

$$\sum_{k=1}^{N_{\text{sp}}} V_{k,j} Y_k = 0 \,, \tag{2.13}$$

and

$$\sum_{k=1}^{N_{\text{sp}}} \dot{\omega}_k = 0\,, \tag{2.14}$$

one finds that the set of transport equations for ρY_k, equation (2.12), ensures the mass conservation, from its summing reduces to the mass conservation equation (2.11). To compute the molecular diffusion velocity, the approximation of Curtiss and Hirschfelder is employed [26],

$$V_{k,j} X_k = -\mathcal{D}_k \frac{\partial X_k}{\partial x_j} \tag{2.15}$$

with $\mathcal{D}_k$ the diffusion coefficient of species k. It is determined as

$$\mathcal{D}_k = \frac{1 - Y_k}{\sum\limits_{j=1, j\neq k}^{N_{\text{sp}}} (X_j / \mathcal{D}_{k,j})} \tag{2.16}$$

with $\mathcal{D}_{k,j}$ the binary diffusion coefficient of species k into species j. Nevertheless, this approximation does not verify the continuity equation, thus a correction velocity is introduced to secure the mass conservation [45]. In the direction j, the correction velocity $V_{\text{c},j}$ reads

$$V_{\text{c},j} = \sum_{k=1}^{N_{\text{sp}}} \mathcal{D}_k \frac{W_k}{W} \frac{\partial X_k}{\partial x_j}\,. \tag{2.17}$$

Reformulating equation (2.12) from equation (2.15) and adding the correction velocity, the N_{sp} species mass transport equations solved yields

$$\frac{\partial \rho Y_k}{\partial t} + \frac{\partial}{\partial x_j}\left(\rho (u_j + V_{\text{c},j}) Y_k\right) = \frac{\partial}{\partial x_j}\left(\rho \mathcal{D}_k \frac{W_k}{W} \frac{\partial X_k}{\partial x_j}\right) + \dot{\omega}_k\,. \tag{2.18}$$

The Curtiss and Hirschfelder approximation on the molecular diffusion velocity is part of the mixture-averaged model employed to compute the diffusion properties of the transported species. In this context, the dynamic viscosity μ for momentum diffusion and the thermal conductivity λ for thermal diffusion, are averaged in the mixture. These mixture properties are deduced from the pure species properties. The dynamic viscosity is given by [11]

$$\mu = \sum_{k=1}^{N_{\text{sp}}} \frac{X_k}{\sum\limits_{j=1}^{N_{\text{sp}}} X_j \Phi_{j,k}} \mu_k\,, \tag{2.19}$$

with

$$\Phi_{j,k} = \frac{1}{\sqrt{8}} \left(1 + \frac{W_k}{W_j}\right)^{-\frac{1}{2}} \left(1 + \left(\frac{\mu_k}{\mu_j}\right)^{\frac{1}{2}} \left(\frac{W_j}{W_k}\right)^{\frac{1}{4}}\right)^2\,. \tag{2.20}$$

The thermal conductivity is determined by [97]

$$\lambda = \frac{1}{2}\left(\sum_{k=1}^{N_{\text{sp}}} X_k \lambda_k + \frac{1}{\sum\limits_{k=1}^{N_{\text{sp}}} (X_k / \lambda_k)}\right)\,. \tag{2.21}$$

Pure species properties are obtained with the Chemkin interpreter [73] using a third-order fitting procedure ($N = 4$) based on the coefficients $a_{n,k}$,$b_{n,k}$ and $d_{n,j,k}$ provided in a transport file following the Chemkin format,

$$\ln \mu_k = \sum_{n=1}^{N} a_{n,k} (\ln T)^{n-1} , \tag{2.22}$$

$$\ln \lambda_k = \sum_{n=1}^{N} b_{n,k} (\ln T)^{n-1} , \tag{2.23}$$

and

$$\ln \mathcal{D}_{k,j} = \sum_{n=1}^{N} d_{n,k,j} (\ln T)^{n-1} . \tag{2.24}$$

2.2.2.3 Conservation of total sensible energy

The conservation equation for total sensible energy reads

$$\frac{\partial \rho E}{\partial t} + \frac{\partial}{\partial x_j} (\rho u_j E) = -\frac{\partial P u_i}{\partial x_i} + \frac{\partial \tau_{ij} u_j}{\partial x_i} + \frac{\partial}{\partial x_j} \left(\lambda \frac{\partial T}{\partial x_j} - \sum_{k=1}^{N_{\text{sp}}} \rho V_{k,j} h_k^{\text{s}} Y_k \right) - \sum_{k=1}^{N_{\text{sp}}} h_k^{\text{o}} \dot{\omega}_k , \tag{2.25}$$

where h_k^{s} is the specific sensible enthalpy and h_k^{o} is the specific enthalpy of formation of the k-th species [45]. Soret and Dufour effects are neglected. E denotes the specific total sensible energy, it accounts for the kinetic and the sensible energies but does not include the chemical energy,

$$E = \frac{1}{2} \mathbf{u} \cdot \mathbf{u} + \sum_{k=1}^{N_{\text{sp}}} Y_k \left(\int_{T^{\text{o}}}^{T} C_{v,k}(T^+) dT^+ - \frac{R}{W_k} T^{\text{o}} \right) . \tag{2.26}$$

with $C_{v,k}$ the specific heat capacity of species k at constant volume and T^{o} the reference temperature, typically 298.15 K. In the following, the term $\left(- \sum_{k=1}^{N_{\text{sp}}} h_k^{\text{o}} \dot{\omega}_k \right)$ will often be referred to as the energy source term or the heat release source term and noted $\dot{\omega}_{\rho E}$.

2.2.2.4 Species source term computation

The study of reactive flows requires to consider the combustion phenomenon. Kinetic mechanisms are employed in order to model the large amount of kinetic paths followed by the reactants to give the products of reaction. The present modelling uses these mechanisms to compute the species source terms $\dot{\omega}_k$ appearing in the N_{sp} species transport equations (2.18) and the energy conservation equation (2.25). The following describes how these source terms are computed.

A set of N_{sp} species reacts over N_{r} reversible reactions. For the N_{sp} species k of formula $\mathcal{M}_k$, the kinetic mechanism reads

$$\sum_{k=1}^{N_{\text{sp}}} \nu'_{k,j} \mathcal{M}_k \rightleftharpoons \sum_{k=1}^{N_{\text{sp}}} \nu''_{k,j} \mathcal{M}_k , \quad \text{with } j \in [1, N_{\text{r}}] , \tag{2.27}$$

with $\nu'_{k,j}$ and $\nu''_{k,j}$ the reactant and product stoichiometric coefficients of species k in reaction j. Please note from the double arrow that reactions are potentially reversible. The global source term $\dot{\omega}_k$ of species k is the sum of the contribution $\dot{\omega}_{k,j}$ from all reactions j of the mechanism,

$$\dot{\omega}_k = \sum_{j=1}^{N_\mathrm{r}} \dot{\omega}_{k,j} = W_k \sum_{j=1}^{N_\mathrm{r}} \nu_{k,j} \mathcal{Q}_j \,, \tag{2.28}$$

with $\nu_{k,j} = \nu''_{k,j} - \nu'_{k,j}$ the stoichiometric coefficient of species k in reaction j and $\mathcal{Q}_j$ the reaction rate of reaction j. This rate represents the speed at which reactants are converted into products, it accounts for forward and backward rates,

$$\mathcal{Q}_j = \mathcal{Q}_{\mathrm{f},j} - \mathcal{Q}_{\mathrm{b},j} \tag{2.29}$$

with

$$\mathcal{Q}_{\mathrm{f},j} = K_{\mathrm{f},j} \prod_{k=1}^{N_\mathrm{sp}} [X_k]^{\nu'_{k,j}} \quad \text{and} \quad \mathcal{Q}_{\mathrm{b},j} = K_{\mathrm{b},j} \prod_{k=1}^{N_\mathrm{sp}} [X_k]^{\nu''_{k,j}} \,, \tag{2.30}$$

where $K_{\mathrm{f},j}$ and $K_{\mathrm{b},j}$ are the forward and backward chemical constants of reaction j based on the Arrhenius law and $[X_k] = \rho Y_k / W_k$ is the molecular concentration of species k. The rate constant for the forward reaction j, which depends on the temperature, is given by the Arrhenius law

$$K_{\mathrm{f},j} = A_{\mathrm{f},j} T^{\beta_j} \exp\left(-\frac{E_{\mathrm{a},j}}{RT}\right) \,, \tag{2.31}$$

with $A_{\mathrm{f},j}$ the forward pre-exponential factor, β_j the temperature exponent and $E_{\mathrm{a},j}$ the molecular activation energy. The rate constant for backward reaction $K_{\mathrm{b},j}$ can either be computed similarly from a backward pre-exponential factor $A_{\mathrm{b},j}$ or deduced from the thermodynamic equilibrium constant,

$$K_{\mathrm{b},j} = \frac{K_{\mathrm{f},j}}{\exp\left(\frac{\Delta S^\mathrm{o}_j(T)}{R} - \frac{\Delta H^\mathrm{o}_j(T)}{RT}\right) \left(\frac{P^\mathrm{o}}{RT}\right)^{\sum_{k=1}^{N_\mathrm{sp}} \nu_{k,j}}} \,, \tag{2.32}$$

where the molecular entropy $\Delta S^\mathrm{o}_j(T)$ and enthalpy $\Delta H^\mathrm{o}_j(T)$ are the changes in reaction j, when passing from reactants to products at the temperature T and the standard pressure $P^\mathrm{o} = 1$ atm. These are computed from the NASA polynomials provided with the kinetic mechanism. The second method is presently selected to compute the backward chemical constant $K_{\mathrm{b},j}$. In the following, A corresponds to the forward pre-exponential factor.

2.2.3 Dimensionless numbers

To characterise the relative influence of various phenomena, dimensionless numbers are defined. Some usual numbers are now listed and evaluated for the configuration studied in this Ph. D. thesis work. The following representative data are employed: $\rho = 1.1$ kg.m^{-3}, $\mu = 1.8 \cdot 10^{-5}$ kg.m^{-1}.s^{-1}, $\ell_\mathrm{c} = 5$ mm the characteristic dimension being the channel height, $\mathcal{D}_{\mathrm{CH_4}} = 2.39 \cdot 10^{-5}$ m^2.s^{-1}, $u_\mathrm{c} = 0.45$ m.s^{-1} the characteristic bulk velocity, $C_p = 1077$ J.kg^{-1}.K^{-1} the specific heat capacity at constant pressure and $\lambda = 2.7 \cdot 10^{-2}$ W.m^{-1}.K^{-1}. Readers will

find these values in accordance with the coming observations. First the kinematic viscosity ν is introduced,

$$\nu = \frac{\mu}{\rho}\,, \tag{2.33}$$

and the thermal diffusion coefficient α,

$$\alpha = \frac{\lambda}{\rho C_p}\,. \tag{2.34}$$

- The Reynolds number (Re) compares the inertial to the viscous forces. It is used to predict the appearance of chaotic flows in fluid mechanics, especially the transition from laminar to turbulent flow,

$$\mathrm{Re} = \frac{\rho u_\mathrm{c} \ell_\mathrm{c}}{\mu} \simeq 130\,. \tag{2.35}$$

  In a canal, such a Reynolds number yields the conservation of a laminar flow.

- The Lewis number (Le) is the ratio of thermal diffusivity over mass diffusivity. In combustion this number is widely used as it gives an hint on flame stability with respect to curved flame fronts. Since depending on the species mass diffusion coefficient, a Lewis number can be associated to every species, but it usually refers the fuel,

$$\mathrm{Le} = \frac{\alpha}{\mathcal{D}_{\mathrm{CH_4}}} \simeq 0.95\,. \tag{2.36}$$

- The Prandtl number (Pr) is the ratio of the viscous diffusion to the thermal diffusion,

$$\mathrm{Pr} = \frac{\nu}{\alpha} \simeq 0.72\,. \tag{2.37}$$

- The Schmidt number (Sc), here again given for the fuel, is the ratio of the viscous diffusion to the mass diffusion,

$$\mathrm{Sc} = \frac{\nu}{\mathcal{D}_{\mathrm{CH_4}}} \simeq 0.68\,. \tag{2.38}$$

- The Péclet number (Pe), is the ratio of convective over conductive transfers,

$$\mathrm{Pe} = \mathrm{Re} \cdot \mathrm{Pr} \simeq 94\,. \tag{2.39}$$

- The Froude number (Fr), compares the kinetic energy of the flow to its potential gravitational energy,

$$\mathrm{Fr} = \frac{u_\mathrm{c}^2}{g\ell_\mathrm{c}} \simeq 3\,. \tag{2.40}$$

2.3 Solid/flow conjugate heat transfer: A solid solver

As evoked in the introduction, the behaviour of flames propagating in small-scale channels strongly depends on the surrounding thermal conditions. In order to provide a relevant analysis of the phenomenology occurring in such conditions, the thermal transfer between the flow, the

flame and the channel walls need to be accounted for. Accordingly, a heat transfer solver was developed during this Ph. D. thesis, and is now presented. The numerical methods used to solve the energy equation in the solid are first introduced. The imposition of the boundary conditions and the strategy selected to couple this solid solver to the flow solver SiTCom-B are then described. Finally, canonical computations are performed to assess the validity of the developments, first in 1D and 3D pure heat transfer problems, then in a coupled 1D solid/flow heat transfer canonical case. Although it will be employed in a 2D framework in the following of this manuscript, this development allows for complete three dimensional solid heat transfer computations.

2.3.1 Conservation of energy

In the solid, the conservation of energy equation is solved,

$$\rho_{\mathrm{s}} C_{p,\mathrm{s}}(T_{\mathrm{s}}) \frac{\partial T_{\mathrm{s}}}{\partial t} = \nabla \cdot (\lambda_{\mathrm{s}}(T_{\mathrm{s}}) \nabla T_{\mathrm{s}}) \,, \tag{2.41}$$

where T_{s} is the temperature, ρ_{s} is the density, $C_{p,\mathrm{s}}(T_{\mathrm{s}})$ is the heat capacity at constant pressure and $\lambda_{\mathrm{s}}(T_{\mathrm{s}})$ is the thermal conductivity of the solid. The thermal diffusion coefficient in the solid α_{s} is introduced,

$$\alpha_{\mathrm{s}} = \frac{\lambda_{\mathrm{s}}}{\rho_{\mathrm{s}} C_{p,\mathrm{s}}} \,. \tag{2.42}$$

In the following, variations of thermal conductivity and heat capacity will be accounted for, from the channel walls temperature varies significantly. Since λ_{s} is not assumed constant with the temperature, the heat equation

$$\frac{\partial T_{\mathrm{s}}}{\partial t} = \alpha_{\mathrm{s}} \Delta T_{\mathrm{s}} \,, \tag{2.43}$$

is not recovered. The complete formulation of the first law of thermodynamics accounts for the variations of the conductivity with the temperature. The decomposition of the divergence of the heat flux yields $\nabla \cdot (\lambda_{\mathrm{s}}(T_{\mathrm{s}}) \nabla T_{\mathrm{s}}) = \lambda_{\mathrm{s}}(T_{\mathrm{s}}) \Delta T_{\mathrm{s}} + \nabla \lambda_{\mathrm{s}}(T_{\mathrm{s}}) \cdot \nabla T_{\mathrm{s}}$. Equation (2.41) gives thus

$$\frac{\partial T_{\mathrm{s}}}{\partial t} = \alpha_{\mathrm{s}}(T_{\mathrm{s}}) \Delta T_{\mathrm{s}} + \frac{1}{\rho_{\mathrm{s}} C_{p,\mathrm{s}}(T_{\mathrm{s}})} \nabla \lambda_{\mathrm{s}}(T_{\mathrm{s}}) \cdot \nabla T_{\mathrm{s}} \,. \tag{2.44}$$

Please note that, in the rest of this section, the subscript relative to the solid $_{\mathrm{s}}$ and the dependency of the variables to the temperature (T_{s}) will not be written in order to lighten the notations and ease the comprehension.

A semi-implicit formulation is elected to model the equation (2.44). The Douglas-Gunn scheme is employed to solve implicitly the Laplacian of the temperature ΔT (in red) while the cross product term $\nabla \lambda(T) \cdot \nabla T$ (in black) is solved explicitly and added to the remaining part

of the Douglas-Gunn algorithm. On the Cartesian grid, this combination yields

$$\begin{cases} \dfrac{\partial T^{n+\frac{1}{3}}}{\partial t} &= \alpha\dfrac{1}{2}\dfrac{\partial^2 T^{n+\frac{1}{3}}}{\partial x^2} + \alpha\dfrac{\partial^2 T^{n}}{\partial y^2} + \alpha\dfrac{\partial^2 T^{n}}{\partial z^2} + \alpha\dfrac{1}{2}\dfrac{\partial^2 T^{n}}{\partial x^2} + \dfrac{1}{\rho C}\dfrac{\partial \lambda^n}{\partial x}\dfrac{\partial T^n}{\partial x}, \\ \dfrac{\partial T^{n+\frac{2}{3}}}{\partial t} &= \alpha\dfrac{1}{2}\dfrac{\partial^2 T^{n+\frac{2}{3}}}{\partial y^2} - \alpha\dfrac{1}{2}\dfrac{\partial^2 T^{n}}{\partial y^2} + \dfrac{1}{\rho C}\dfrac{\partial \lambda^n}{\partial y}\dfrac{\partial T^n}{\partial y}, \\ \dfrac{\partial T^{n+1}}{\partial t} &= \alpha\dfrac{1}{2}\dfrac{\partial^2 T^{n+1}}{\partial z^2} - \alpha\dfrac{1}{2}\dfrac{\partial^2 T^{n}}{\partial z^2} + \dfrac{1}{\rho C}\dfrac{\partial \lambda^n}{\partial z}\dfrac{\partial T^n}{\partial z}. \end{cases} \tag{2.45}$$

The Douglas-Gunn scheme belongs to the alternate direction implicit (ADI) schemes, it is unconditionally stable. This type of scheme can only be employed on Cartesian meshes, which is also the case of SiTCom-B. When compared to the Cranck-Nicholson scheme, which is often used on unstructured meshes, the advantage of the Douglas-Gunn scheme resides in the scaling. On one hand, the present formalism requires to invert $n_x \times n_y$ tridiagonal matrices of size n_z^2 and to perform analogous operations in the two other directions, n_x, n_y and n_z being the number of cells in each directions. On the other hand, the Crank-Nicholson scheme requires the use of more complex and costly methods to solve linear systems, such as the Gaussian Elimination or the Strassen algorithm for examples.

The present scheme resorting to a combination of explicit and implicit treatment, attention will be brought to the time step restrictions. For the configurations studied in this Ph.D. thesis, the cost relating to this solid solver is minor when compared to the flow solver.

2.3.2 Numerical resolution

To provide a clear view of the numerics employed, a complete description of the algorithm coded in the solid solver is now presented. The equation system 2.45 is temporally integrated over δt, to pass from iteration n to iteration $n+1$,

$$\begin{cases} T^{n+\frac{1}{3}} &= T^n + \dfrac{\alpha\delta t}{2}\dfrac{\partial^2 T^{n+\frac{1}{3}}}{\partial x^2} + \alpha\delta t\left(\dfrac{\partial^2 T^n}{\partial y^2} + \dfrac{\partial^2 T^n}{\partial z^2} + \dfrac{1}{2}\dfrac{\partial^2 T^n}{\partial x^2}\right) + \dfrac{\delta t}{\rho C}\dfrac{\partial \lambda^n}{\partial x}\dfrac{\partial T^n}{\partial x}, \\ T^{n+\frac{2}{3}} &= T^{n+\frac{1}{3}} + \dfrac{\alpha\delta t}{2}\dfrac{\partial^2 T^{n+\frac{2}{3}}}{\partial y^2} - \dfrac{\alpha\delta t}{2}\dfrac{\partial^2 T^n}{\partial y^2} + \dfrac{\delta t}{\rho C}\dfrac{\partial \lambda^n}{\partial y}\dfrac{\partial T^n}{\partial y}, \\ T^{n+1} &= T^{n+\frac{2}{3}} + \dfrac{\alpha\delta t}{2}\dfrac{\partial^2 T^{n+1}}{\partial z^2} - \dfrac{\alpha\delta t}{2}\dfrac{\partial^2 T^n}{\partial z^2} + \dfrac{\delta t}{\rho C}\dfrac{\partial \lambda^n}{\partial z}\dfrac{\partial T^n}{\partial z}. \end{cases} \tag{2.46}$$

The Laplacian is discretized to the second order, for example in the z direction at the position z_i,

$$\left.\frac{\partial^2 T^n}{\partial z^2}\right|_{z_i} = \frac{\frac{T^n_{z_{i+1}} - T^n_{z_i}}{z_{i+1} - z_i} - \frac{T^n_{z_i} - T^n_{z_{i-1}}}{z_i - z_{i-1}}}{\frac{z_{i+1} - z_{i-1}}{2}}. \tag{2.47}$$

To clarify the notation as well as the implementation, equation 2.47 is reformulated,

$$\left.\frac{\partial^2 T^n}{\partial z^2}\right|_{z_i} = a_z|_{z_i}\, T^n_{z_{i-1}} + b_z|_{z_i}\, T^n_{z_i} + c_z|_{z_i}\, T^n_{z_{i+1}}, \tag{2.48}$$

with

$$a_z|_{z_i} = \frac{2}{(z_i - z_{i-1})(z_{i+1} - z_{i-1})}\,, \tag{2.49}$$

$$b_z|_{z_i} = -\frac{2}{(z_{i+1} - z_i)(z_i - z_{i-1})}\,, \tag{2.50}$$

and

$$c_z|_{z_i} = \frac{2}{(z_{i+1} - z_i)(z_{i+1} - z_{i-1})}\,. \tag{2.51}$$

One can then write on the vectorial form,

$$\frac{\partial^2 \mathbf{T}^n}{\partial z^2} = \begin{pmatrix} b_z|_{l_z} & c_z|_{l_z} & 0 & \cdots & 0 \\ a_z|_{l_z+1} & b_z|_{l_z+1} & c_z|_{l_z+1} & & \vdots \\ 0 & \ddots & \ddots & \ddots & 0 \\ \vdots & & a_z|_{u_z-1} & b_z|_{u_z-1} & c_z|_{u_z-1} \\ 0 & \cdots & 0 & a_z|_{u_z} & b_z|_{u_z} \end{pmatrix} \begin{pmatrix} T^n|_{l_z} \\ \vdots \\ \\ \\ \\ \vdots \\ T^n|_{u_z} \end{pmatrix}, \tag{2.52}$$

with l_z and u_z the lower and upper indexes bounds in the z direction. The equation system 2.46 is now written as a combination of linear systems,

$$\begin{cases} \mathbf{T}^{n+\frac{1}{3}} &= \boldsymbol{X}^{-1}\mathbf{V}^{n+\frac{1}{3}}\,, \\ \mathbf{T}^{n+\frac{2}{3}} &= \boldsymbol{Y}^{-1}\mathbf{V}^{n+\frac{2}{3}}\,, \\ \mathbf{T}^{n+1} &= \boldsymbol{Z}^{-1}\mathbf{V}^{n+1}\,, \end{cases} \tag{2.53}$$

with for example in the z direction

$$\boldsymbol{Z} = \begin{pmatrix} 1 - \frac{\alpha\delta t}{2}\, b_z|_{l_z} & -\frac{\alpha\delta t}{2}\, c_z|_{l_z} & 0 & \cdots & 0 \\ -\frac{\alpha\delta t}{2} a_z|_{l_z+1} & 1 - \frac{\alpha\delta t}{2}\, b_z|_{l_z+1} & -\frac{\alpha\delta t}{2}\, c_z|_{l_z+1} & & \vdots \\ 0 & \ddots & \ddots & \ddots & 0 \\ \vdots & & -\frac{\alpha\delta t}{2} a_z|_{u_z-1} & 1 - \frac{\alpha\delta t}{2}\, b_z|_{u_z-1} & -\frac{\alpha\delta t}{2}\, c_z|_{u_z-1} \\ 0 & \cdots & 0 & -\frac{\alpha\delta t}{2}\, a_z|_{u_z} & 1 - \frac{\alpha\delta t}{2}\, b_z|_{u_z} \end{pmatrix}, \tag{2.54}$$

and the right hand side vectors

$$\begin{cases} \mathbf{V}^{n+\frac{1}{3}} &= \mathbf{T}^n + \alpha\delta t \left(\dfrac{\partial^2 \mathbf{T}^n}{\partial y^2} + \dfrac{\partial^2 \mathbf{T}^n}{\partial z^2} + \frac{1}{2} \dfrac{\partial^2 \mathbf{T}^n}{\partial z^2} \right) + \dfrac{\delta t}{\rho C} \dfrac{\partial \boldsymbol{\lambda}^n}{\partial z} \dfrac{\partial \mathbf{T}^n}{\partial z}\,, \\ \mathbf{V}^{n+\frac{2}{3}} &= \mathbf{T}^{n+\frac{1}{3}} - \dfrac{\alpha\delta t}{2} \dfrac{\partial^2 \mathbf{T}^n}{\partial y^2} + \dfrac{\delta t}{\rho C} \dfrac{\partial \boldsymbol{\lambda}^n}{\partial y} \dfrac{\partial \mathbf{T}^n}{\partial y}\,, \\ \mathbf{V}^{n+1} &= \mathbf{T}^{n+\frac{2}{3}} - \dfrac{\alpha\delta t}{2} \dfrac{\partial^2 \mathbf{T}^n}{\partial z^2} + \dfrac{\delta t}{\rho C} \dfrac{\partial \boldsymbol{\lambda}^n}{\partial z} \dfrac{\partial \mathbf{T}^n}{\partial z}\,. \end{cases} \tag{2.55}$$

One sees in relation 2.55 that the construction of the second and third right hand side vectors of relation 2.53 requires the resolution of the first and second linear systems of 2.53, respectively. This makes the Douglass-Gunn an alternate direction method. In practice, these systems are solved one after the other, via a tridiagonal linear solver based on a Thomas algorithm [145].

2.3.3 Imposition of the boundary conditions

The imposition of the boundary conditions is performed based on relation 2.53. In the simulations of flames propagating in a channel, fluxes are imposed in the solid part at the solid/flow interfaces as well as on the surfaces open to the ambient. Neumann type of boundary conditions are employed to prescribe this flux. For example, to impose a flux, Φ_{BC}, at the lower boundary l_z. $\boldsymbol{Z}$ and $\mathbf{V}^{n+1}$ are modified as follows,

$$\left\{\begin{array}{rcl} \boldsymbol{Z}(l_z,l_z) & = & -1\,, \\ \boldsymbol{Z}(l_z,l_z+1) & = & 1\,, \\ \mathbf{V}^{n+1}(l_z) & = & \frac{z_{l_z+1}-z_{l_z}}{\lambda_s}\Phi_{\text{BC}}\,, \end{array}\right. \tag{2.56}$$

with λ_s the conductivity in the solid. Please note that the thermal capacity does not act in the imposition of the flux, as it will be recalled later. The Dirichlet boundary conditions consist in prescribing a scalar, naturally the temperature in the present case. This boundary condition is used in some validation test cases. For example, to impose the temperature T_{BC} on the cell l_z. $\boldsymbol{Z}$ and $\mathbf{V}^{n+1}$ are modified accordingly to

$$\left\{\begin{array}{rcl} \boldsymbol{Z}(l_z,l_z) & = & 1\,, \\ \boldsymbol{Z}(l_z,l_z+1) & = & 0\,, \\ \mathbf{V}^{n+1}(l_z) & = & T_{\text{BC}}\,. \end{array}\right. \tag{2.57}$$

2.3.4 Coupling strategy

In this paragraph, subscripts are employed to specify either the variable belongs to the solid $_{\text{s}}$ or to the flow $_{\text{f}}$. Considering the coupling, two main strategies exist, the sequential and the parallel coupling. The present code relies on a parallel coupling as described in figure 2.1. Starting at the coupling iteration n, the temperatures at the interface T_{f} and T_{s} (taken at the neighbouring cells) are gathered and used to compute a new interface temperature T^n and the associated flux Φ^n. In the fluid solver, the prescribed boundary condition is the temperature T^n, prescribed at the interface, while the flux Φ^n is imposed in the solid solver. The solid and the fluid solvers advance in time simultaneously, with the prescribed boundary conditions, until the next coupling iteration. At this iteration $n+1$, the new boundary conditions Φ^{n+1} an T^{n+1} are once again computed from the temperatures on each side of the interface, T_{f} and T_{s}. Besides, in the present semi-implicit formalism, the Fourier criterion (Fo) in the solid

$$Fo = \frac{\alpha\delta t}{\delta z^2}\,, \tag{2.58}$$

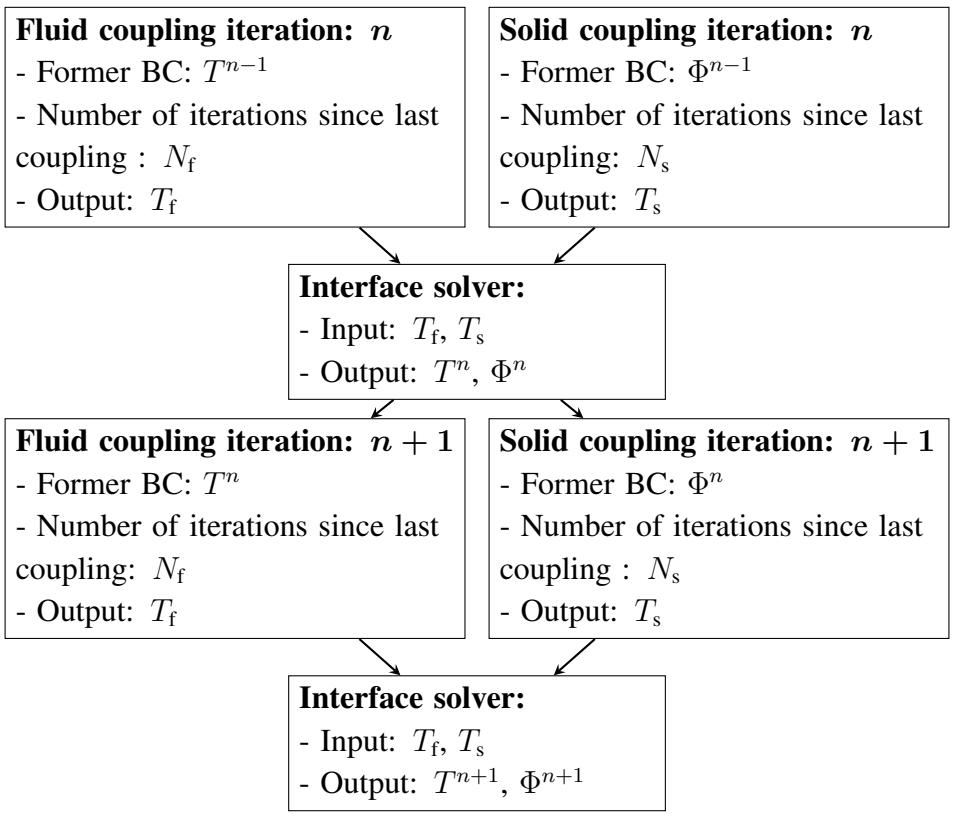

Figure 2.1: Parallel coupling principle.

is fixed to 0.8 to ensure stability and yields far bigger time steps than the Courant-Friedrich-Levy criterion (CFL) in the gas. Consequently, the relative numerical cost of the solid solver in front of the fluid solver is low. Accordingly, the coupling of the two solvers, as it does not impact the overall cost of the simulations, is performed after each solid solver iteration ($N_\mathrm{s} = 1$ in figure 2.1).

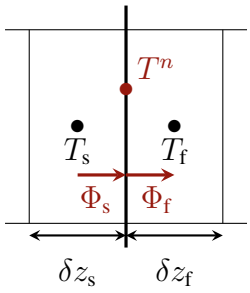

Figure 2.2: Interface solver scheme.

The interface solver principle is further depicted in figure 2.2. The thermal fluxes at the boundary of each solver are set equal, based on the flux continuity at the interface,

$$\Phi_\mathrm{s} = \Phi_\mathrm{f} \iff \lambda_\mathrm{s} \frac{T^n - T_\mathrm{s}}{\frac{\delta z_\mathrm{s}}{2}} = \lambda_\mathrm{f} \frac{T_\mathrm{f} - T^n}{\frac{\delta z_\mathrm{f}}{2}} \,. \tag{2.59}$$

The interface temperature T^n, used as a Dirichlet boundary condition in the flow solver, is then determined,

$$T^n = \frac{\frac{\lambda_\mathrm{f}}{\delta z_\mathrm{f}} T_\mathrm{f} + \frac{\lambda_\mathrm{s}}{\delta z_\mathrm{s}} T_\mathrm{s}}{\frac{\lambda_\mathrm{f}}{\delta z_\mathrm{f}} + \frac{\lambda_\mathrm{s}}{\delta z_\mathrm{s}}}\,, \tag{2.60}$$

along with the interface flux Φ^n, used as a Neumann boundary condition for the solid solver,

$$\Phi^n = \Phi_\mathrm{s} = \lambda_\mathrm{s} \frac{T^n - T_\mathrm{s}}{\frac{\delta z_\mathrm{s}}{2}}\,. \tag{2.61}$$

2.3.5 Validation

In this paragraph, the solid solver and the conjugate heat transfer with channel flow are validated in a general three-dimensional framework. One may note that in next chapters, the numerical simulations of the narrow channel will be performed in two dimensions (x and y directions).

2.3.5.1 Mono-dimensional semi-infinite flat plate

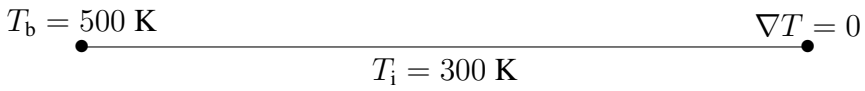

Figure 2.3: Semi-infinite plate test case.

The first test case, in this solver validation process, is the simulation of a semi-infinite flat plate submitted to a mono-dimensional temperature gradient (see fig 2.3).

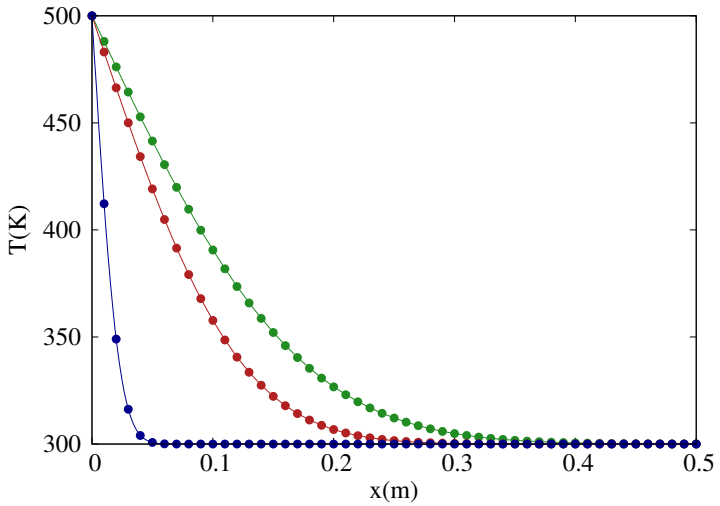

Figure 2.4: Temperature profiles at various times in a semi infinite flat plate with Dirichlet boundary conditions on one side. Dots: SiTCom-B solid solver. Lines: theoretical relation 2.62. Dark blue: $t = 1.7$ ms. Red: $t = 51$ ms. Green: $t = 102$ ms.

The domain is initially set at a temperature of $T(t=0) = T_\mathrm{i} = 300$ K. On the left side of the domain a Dirichlet boundary condition $T = T_\mathrm{b} = 500$ K is imposed. On the right side a Neumann boundary condition yielding a zero gradient is prescribed. The temporal evolution of the temperature profile in the semi-infinite flat plate follows the theoretical relation

$$T(x,t) = T_\mathrm{b} - (T_\mathrm{b} - T_\mathrm{i}) \cdot \mathrm{erf}\left(\frac{x}{2\sqrt{\alpha \cdot t}}\right) . \tag{2.62}$$

Imposing a Neumann boundary condition on the right side does not correspond strictly to a semi-infinite plate. The comparison with the analytical solution given by such an hypothesis is nevertheless possible until the temperature rise reaches the Neumann boundary condition. In the present simulation, the diffusion coefficient in the solid is set to $\alpha = 8,7.10^{-4}$ m^2.s^{-1}. Figure 2.4 shows the accordance between the theory and the simulation, validating the solid solver on this mono-dimensional test case.

2.3.5.2 Three-dimensional diffusion of a Dirac peak

It was evoked previously that the Douglas-Gunn scheme is an alternate direction method. Since the numerical treatment is not the same in all directions, it is relevant to verify that the scheme behaves correctly in an isotropic case. As a three-dimensional test case, the diffusion of a Dirac temperature peak is studied. The temperature profile passing through the peak center follows the theoretical relation,

$$T(\boldsymbol{x},t) = T_\mathrm{i} + \frac{k}{(4\pi \cdot \alpha \cdot t)^{\frac{3}{2}}} \cdot \exp\left(-\frac{\boldsymbol{x}\cdot\boldsymbol{x}}{4\alpha \cdot t}\right) . \tag{2.63}$$

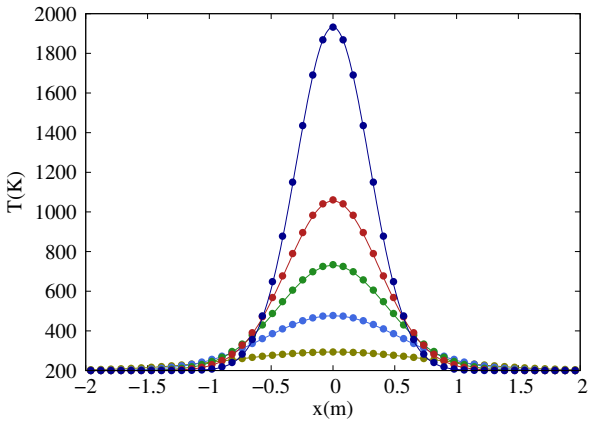

Figure 2.5: Temperature profiles at various times through a Dirac type temperature peak being diffused. Dots: SiTCom-B solid solver. Lines: theoretical relation 2.63. Dark blue: $t = 0.5$ s. Red: $t = 0.8$ s. Green: $t = 1.1$ s. Light blue: $t = 1.7$ s. Gold: $t = 3.5$ s.

The parameters of the problem are $T(\forall x, t = 0) = T_\mathrm{i} = 200$ K, $k = 700$ K.m^3 and $\alpha = 8,7.10^{-2}$ m^2.s^{-1}. Neumann boundary conditions of zero gradients are set on all six faces

of the cubic domain. As for the previous test case, the analogy between simulation and theory is valid until the temperature rise reaches the limits of the computational domain. For obvious numerical validity questions, the initial condition given to the code corresponds to a slightly diffused Dirac peak. Figure 2.5, which was repeated in the three dimensions, demonstrates that the results obtained with the solid solver fit theory. The two test cases presented so long validate the solid solver on pure heat transfer problems.

2.3.5.3 Infinitely Fast Flame test case

The aim of this last test case is to validate the coupling between the solid solver and the fluid solver SiTCom-B. To do so, the monodimensional test case of the Infinitely Fast Flame (IFF) is performed. This test was already used for such a purpose by Duchaine *et al.* [33]. Figure 2.6 depicts the initial state. A solid (modelled with the solid solver) and a fluid (modelled with SiTCom-B) exhibiting different temperatures, are put in contact. The two areas start thus exchanging energy.

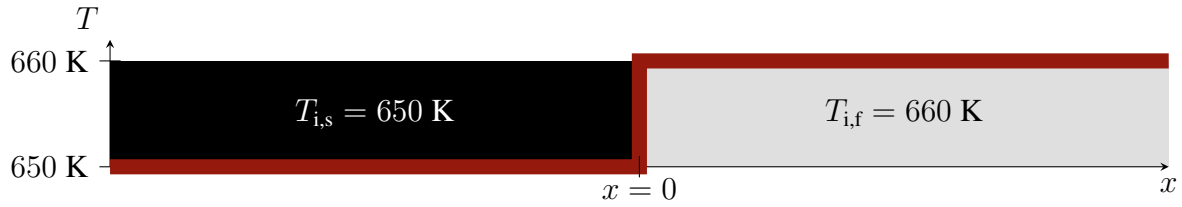

Figure 2.6: Initial state of the IFF coupling test case. Red line: temperature profile. Black rectangle: solid area. Gray rectangle: fluid area.

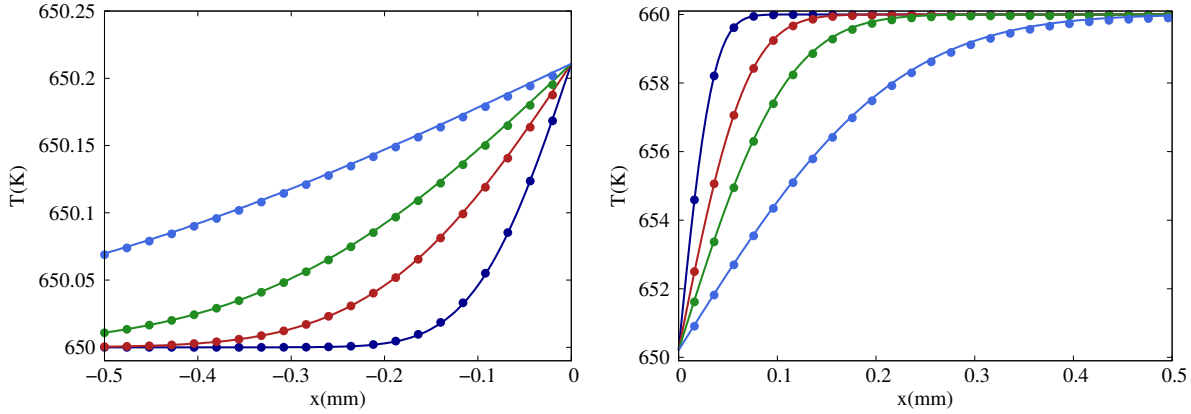

(a) Solid domain

(b) Fluid domain

Figure 2.7: Temperature profiles at various times in both domains. Zoom in the boundary area. Dots: SiTCom-B solid solver. Lines: theoretical relation 2.64. Dark blue: $t = 3.8$ µs. Red: $t = 15.1$ µs. Green: $t = 37.9$ µs. Light blue: $t = 1.5$ ms.

The temperature profiles in the solid and in the fluid are theoretically described by the relations,

$$\begin{aligned} T_{\mathrm{f}}(x,t) &= T_{\mathrm{i,s}} + b_{\mathrm{f}}\frac{T_{\mathrm{i,f}}-T_{\mathrm{i,s}}}{b_{\mathrm{f}}+b_{\mathrm{s}}}\cdot \mathrm{erfc}\left(-\frac{x}{2\sqrt{\alpha_{\mathrm{s}}t}}\right) \quad \text{for } x<0\,, \\ T_{\mathrm{s}}(x,t) &= T_{\mathrm{i,f}} - b_{\mathrm{s}}\frac{T_{\mathrm{i,f}}-T_{\mathrm{i,s}}}{b_{\mathrm{f}}+b_{\mathrm{s}}}\cdot \mathrm{erfc}\left(\frac{x}{2\sqrt{\alpha_{\mathrm{f}}t}}\right) \quad \text{for } x>0\,, \end{aligned} \tag{2.64}$$

with $b_{\mathrm{f}} = 10.21$ J.m^{-2}.K^{-1}.s$^{-\frac{1}{2}}$ the thermal effusivity and $\alpha_{\mathrm{f}} = 9.6.10^{-5}$ m^2.s^{-1} the thermal diffusion coefficient in the fluid. In the solid, $b_{\mathrm{s}} = \sqrt{\lambda_{\mathrm{s}}\rho_{\mathrm{s}}C_{p,\mathrm{s}}}$ and $\alpha_{\mathrm{s}} = \lambda_{\mathrm{s}}/\rho_{\mathrm{s}}C_{p,\mathrm{s}}$ are deduced from the parameters $\lambda_{\mathrm{s}} = 14.03$ W.m^{-1}.K^{-1}, $\rho_{\mathrm{s}} = 221$ kg.m^{-3} and $C_{p,\mathrm{s}} = 70.3$ J.kg^{-1}.K^{-1}.

Figures 2.7(a) and 2.7(b) display the agreement between the theory and the simulation. The temperatures at the interface tend to the same values in the solid and the fluid parts while the temporal evolutions of the profiles in both parts follow the theory. Based on the three test cases provided, the solid solver is considered validated.

2.4 Numerical solving with SiTCom-B

SiTCom-B is a numerical solver of the fully compressible form of the aerothermochemistry equations. This solver relies on the MPI (Message Passing Interface) libraries allowing for the paralleling of computations over several thousand processors. In subsection 2.4.1, the various numerical methods used along the present work are listed point by point. Subsection 2.4.2 gathers the parameters setted in the simulations presented along this work. Finally, an original method employed to stabilise flames in the channel is presented in subsection 2.4.3.

2.4.1 Numerical methods

The combination of numerical methods used in this work, in the explicit SiTCom-B flow solver, has been reported previously as a good compromise in terms of computational efficiency and accuracy for the Direct Numerical Simulation (DNS) of laminar and turbulent reactive flows [13, 31, 32, 91, 92, 98, 112, 141]. The conservation equations of mass 2.18, momentum 2.9 and total sensible energy 2.25 are solved in their fully compressible form over a structured mesh in a finite volume formulation resorting to the series of models listed bellow.

2.4.1.1 Space and time integration

The convective fluxes are computed from the fourth-order skew-symmetric-like formulation introduced by Ducros *et al.* [34]. Fourth-order centred schemes are employed for the viscous and diffusive fluxes. Time is advanced with the low-storage fourth-order Runge-Kutta scheme augmented by Shu *et al.* [135]. Further information on time step restrictions are given in 2.4.2.3.

2.4.1.2 Artificial viscosity

The skew-symmetric centred scheme is non-dissipative. To prevent from diverging, the fluxes are thus completed by an addition of the second and fourth-order artificial dissipation terms introduced by Jameson *et al.* [57, 142], which are set to their minimum contributions to avoid

perturbing the molecular diffusive transport of chemical species within the internal flame structure. This additional numerical flux is controlled by four parameters α_1, α_2, β_1 and β_2. The coefficients $\alpha_1 = 0.5$ and $\alpha_2 = 0.5$ are for the second-order terms, $\beta_1 = 0.06$ and $\beta_2 = 1$ for the fourth-order contribution [143]. For a case studied in this Ph.D. thesis, figure 2.8 gives the evolution of the various fluxes contributions to the momentum equation, at the flame crossing. In the momentum equation case, the contributions to the temporal variation of $\rho\mathbf{u}$ are the convective ($C_{\rho\mathbf{u}}$), diffusive ($D_{\rho\mathbf{u}}$) and artificial ($A_{\rho\mathbf{u}}$) ones, while these last result from the fluxes integration over the control volume. For example, the absolute contribution (in %) of the convective term displayed in figure 2.8, is defined as

$$\text{contrib}_C = \frac{\mid C_{\rho\mathbf{u}} \mid}{\mid C_{\rho\mathbf{u}} \mid + \mid D_{\rho\mathbf{u}} \mid + \mid A_{\rho\mathbf{u}} \mid} * 100\,. \tag{2.65}$$

In the present steady state, the diffusive and convective contributions balance each other, the norms of their contributions are thus close to 50%, while the artificial viscosity contribution is shown to be more than three orders bellow the others. The impact of the artificial viscosity on the results is thus negligible.

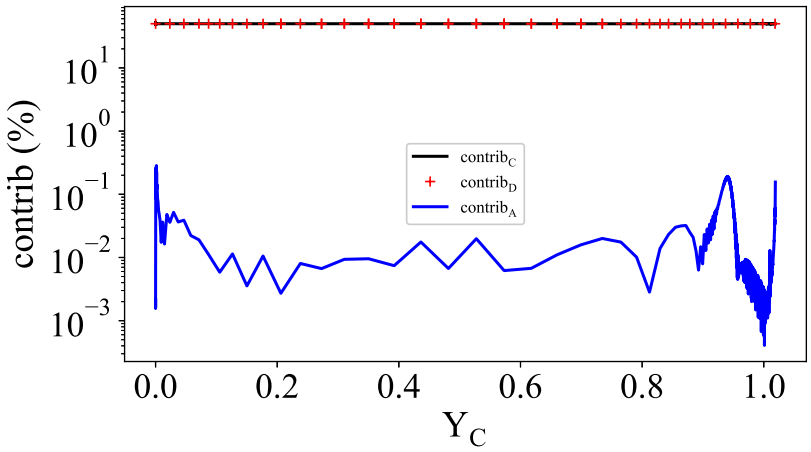

Figure 2.8: Evolution of the momentum equation absolute contributions across the flame studied in figure 3.7(b), superior half. C stands for convective (Black line), D for diffusive (Red cross) and A for artificial viscosity contributions (Blue line). Y_C is a progress variable used to probe the flame crossing.

In figure 2.8, the progress variable Y_C is employed to probe across the flame. Indeed, to track the flame crossing, this progress variable is defined based on the mass fractions of key species at the equilibrium of an adiabatic stoichiometric CH_4/air flame,

$$Y_C = \frac{Y_{CO} + Y_{CO_2} + Y_{H_2O}}{\left(Y^o_{CO} + Y^o_{CO_2} + Y^o_{H_2O}\right)_{eq}}\,, \tag{2.66}$$

with $Y^o_{CO,eq} = 0.0089$, $Y^o_{CO_2,eq} = 0.1370$ and $Y^o_{H_2O,eq} = 0.1202$. The progress variable is defined to present a monotonic behaviour across the flame. Figure 2.9, which is a close up of a

flame front, shows the position of some iso-Y_C lines and the construction of their normals and tangents.

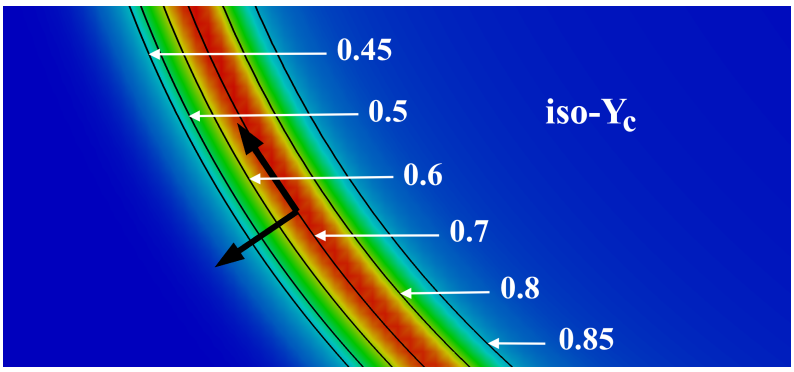

Figure 2.9: Progress variable Y_C iso-lines across the flame. The field is coloured with the energy release source term $\dot{\omega}_{\rho E}$.

2.4.1.3 Boundary conditions

One-dimensional Navier-Stokes Characteristic Boundary Conditions (NSCBC) are applied to the gas phase at the inlet and the outlet [118].

2.4.1.4 Kinetics and transport modelling

Fully transported chemistry is employed. In this method, each of the species present in the kinetic mechanism is transported in the set of mass equations (2.18). In addition, as presented in § 2.2.2.2, the mixture-averaged assumption is employed including the computation of transport properties from Curtiss and Hirschfelder [26]. This assumption is selected because it yields a good compromise in cost and accuracy compared to other available methods: on one hand, the multicomponent method is quite expensive as it resorts to the resolution of linear systems of dimension $N_{\text{sp}} \times N_{\text{sp}}$. One the other hand, the simplified model supposing that the species and energy diffusion are proportional to the viscosity μ, typically computed from the Sutherland law, may lack of precision.

2.4.1.5 Energy equation resolution in the solid

In the present work, the thermal coupling between the flow and the channel walls is accounted for. Based on the large difference in characteristic time scales in the solid and the flow, the de-synchronisation method by Koren [81] is applied to secure a fast convergence toward the steady state solutions. In this method, the heat capacity of the wall is numerically reduced to yield a higher diffusion coefficient and accelerate the transfers within the solid. As pointed out in § 2.3.3, heat capacity plays no role in the computation of boundary conditions, thus steady states solutions do not vary with this parameter, unlike transient states. Further details concerning the implementation and validation of the solid solver were given in section 2.3.

2.4.2 Simulations parameters

Most simulations performed in this Ph. D. thesis yield a flame propagating in a small-scale channel of internal height $\ell_i = 5$ mm. The parameters used in the setting of these simulations are now listed.

2.4.2.1 Domain dimensions

In most cases, the flame is stabilised in the channel via a method presented in subsection 2.4.3. Then, the origin $x = 0$ mm of the axial coordinate is taken at the flame position while the burnt gases far right coordinate is fixed to $x_{max} = 15$ mm. The inlet boundary at the left of the domain, x_{min} varies with the configuration: this coordinate is setted upstream enough from the flame position, to ensure a zero-velocity gradient in the stream-wise direction at the inlet while limiting the computational cost of the simulations. It depends thus strongly on the configuration:

- In the configurations where the **thermal coupling** between the wall and the fluid is fully accounted for, $x_{min} = -51$ mm is necessary to carefully capture the upstream heat diffusion through the wall and the preheating of the reactants (see chapters 4 and 6).
- In the study of the **upstream flame movement** after preheating (see chapter 5), $x_{min} = -101$ mm is needed to capture the flame translation while ensuring no inlet effects.
- In the case of a flame stabilised along **cold walls**, the inlet position could be limited to $x_{min} = -27$ mm.

In the transverse direction, the origin $y = 0$ mm corresponds to the channel central axis. The domain then spreads between $y = -2.5$ mm (wall) and $y = 0$ mm (axis), when the symmetry assumption is formulated. When the full channel is considered in the simulation, the domain spreads between $y = -2.5$ mm (inferior wall) and $y = 2.5$ mm (superior wall).

2.4.2.2 Mesh resolution

Two mesh resolutions have been used, $\delta x = 12.5$ µm for the detailed chemistry (GRI-1.2) and $\delta x = 25$ µm for the skeleton chemical schemes. A regular mesh composed of squares of side δx is used from the inlet (x_{min}) down to $x = 9$ mm, from where the mesh is progressively coarsened in the x direction down to the outlet (x_{max}), with a geometric coefficient of 1.0025. The span-wise mesh resolution is set to $\delta y = \delta x$, leading e.g. to a mesh composed of 456k cells in the case of a skeleton scheme employed on the longer domain ($x_{min} = -101$ mm).

2.4.2.3 Temporal advancement restriction

When solving the non-linear aerothermochemistry equations, various criteria must be considered in the limitation of the time steps in order to secure the convergence of simulations. For all the criteria, a time step is computed in each direction of each cell, and the minimum value is retained.

- Concerning the convective terms, the Courant-Friedrichs-Lewy (CFL) number requires that the information travels less than a cell size during a time step δt_{C},

$$(\mid u \mid + c)\,\frac{\delta t_{\text{C}}}{\delta x} < CFL\,, \tag{2.67}$$

  where c is the speed of sound. The CFL number is fixed to 0.6 in all simulations to ensure stability.

- For the diffusive terms, the Fourier (Fo) number indicates that the time step δt_{D} must respect,

$$\max_{i\in[1,N_{\text{var}}]}\left(D_i\frac{\delta t_{\text{D}}}{\delta x^2}\right) < Fo\,, \tag{2.68}$$

  with N_{var} the number of variables transported and D_i the diffusion coefficient of the i-th transported variable. This diffusion coefficient can either be, the mixture viscosity, the species diffusion coefficient or the thermal diffusion coefficient, depending on the equation considered. The Fo number is fixed to 0.2 in all simulations to ensure stability.

- A restriction is also associated to the integration of the source terms. The source terms, related to the kinetics, might generate non-realistic evolution of mass fraction when integrated over to large time steps. Typically, due to miscalculated source terms, radical species present in low concentrations could exhibit negative mass fraction at the flame front crossing. To prevent from these errors, one imposes the produced or consumed species mass to be inferior to a ratio $Chem = 0.1$ of the species mass transported in the control volume. The time step δt_{Ch} should then verify,

$$\max_{k\in[1,N_{\text{sp}}]}\left(\delta t_{\text{Ch}}\frac{\mid \dot{\omega}_k \mid}{\rho Y_k + \epsilon}\right) < Chem\,, \tag{2.69}$$

  with $\epsilon = 1.0 \cdot 10^{-12}$ kg.m^{-3} introduced to prevent the time step to go to zero when the mass fraction is null. Note that, when ρY_k tends to zero, $\mid \dot{\omega}_k \mid$ typically tends to zero as well. In this case the chemical time step will not limit the temporal advancement. From construction, the chemical time step can only exhibit low values where species take part in some reactions.

Finally, the time step employed in the time advancement is the minimum of all,

$$\delta t = \min\{\delta t_{\text{C}}; \delta t_{\text{D}}; \delta t_{\text{Ch}}\}\,. \tag{2.70}$$

Please note that in the context of this fully explicit solver of the compressible form of the aerothermochemistry equations, the CFL condition was always found more restrictive than the Fourier criterion or the criterion for chemistry integration. Finally, in the cases presented during this Ph. D. thesis, the spatial resolution combined with the CFL stability restriction lead to a time step limitation of the order of 35 ns for the skeletal mechanisms and 8.4 ns for the detailed chemistry.

2.4.2.4 Wall characteristics and coupling with the flow solver

The wall thermal properties are those of fused quartz, accounting for the variation with temperature of the thermal conductivity $\lambda_s(T)$ and calorific capacity $C_{p,s}(T)$ [102] (see figure 2.10), and with a fixed value of the density in the solid $\rho_s = 2200$ kg.m^{-3}.

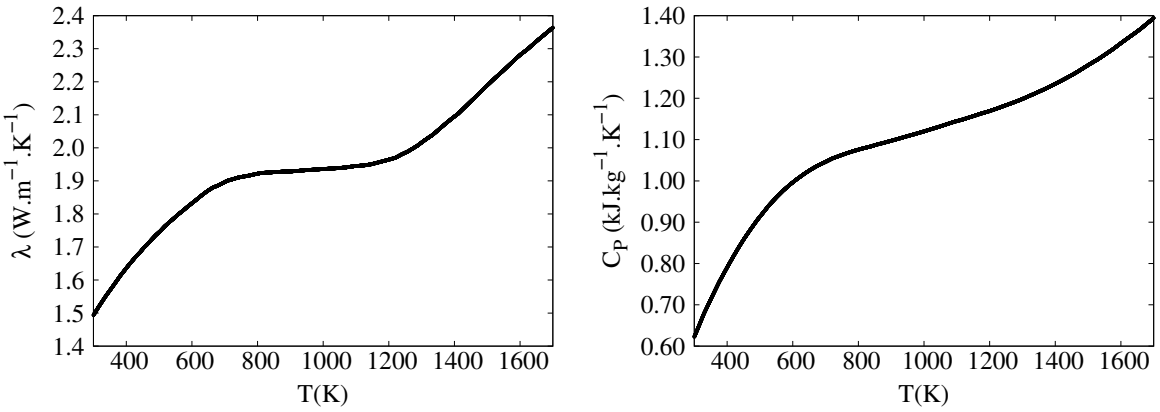

(a) Thermal conductivity (b) Heat capacity

Figure 2.10: Quartz thermal properties evolution with the temperature, from [102].

The exterior wall surface at the computed temperature T_{w_e} exchanges energy with the surrounding air at the fixed temperature $T_o = 300$ K with a global convective heat transfer coefficient $h_o = 30$ W.m^{-2}.K^{-1} (unless otherwise stated), which is at the upper limit for natural convection. The value of this coefficient and of the thermal conductivity in the wall are varied in some parts of the study (see chapter 4). Radiative heat loss of the solid external surface to the ambient air is accounted for through a gray body hypothesis, with an emission coefficient $\varepsilon(T)$ decaying linearly from 0.95 at 290 K to 0.75 at 1800 K. Therefore, over the wall outer surface in contact with ambient air, the boundary condition reads $\mathbf{n}_e \cdot (-\lambda_s \nabla T_s) = h_o(T_{w_e} - T_o) + \varepsilon\sigma(T_{w_e}^4 - T_o^4)$, with $\sigma = 5.670373 \cdot 10^{-8}$ W.m^{-2}.K^{-4} the Stefan-Boltzmann constant and $\mathbf{n}_e$ the normal vector to the outer wall. The boundary condition at the wall surface inside the channel expresses the continuity of the thermal flux, $\mathbf{n}_i \cdot (-\lambda \nabla T) = \mathbf{n}_i \cdot (-\lambda_s \nabla T_s)$, where $\mathbf{n}_i$ is the normal vector to the inner wall. The length of the channel is large enough so that approaching the extremities of the wall, the thermal fluxes in both directions become independent of the position. At the inlet, the temperature is 300 K and at the outlet, the temperature distribution over the wall is computed to match the uniform fluxes of heat inside the wall extremity, *i.e.* the temperature gradient at the extremity equals the one of the first neighbouring cell.

2.4.2.5 Inlet velocity profile

Depending on the dynamic boundary conditions at the solid/flow interface, slip or no-slip wall, a flat, U, or a Poiseuille, $U(1 - (2y/\ell_i)^2)$, velocity profile is imposed at the inlet.

2.4.3 Numerically stabilizing flames in channels

Stabilising a flame in a channel without thermal forcing is challenging, both in numerics and in experiments, as it requires to find the inlet mass flow rate that exactly matches the flame burning rate. The method developed to achieve such a result is now presented.

The mass transport equation for species k (equation 2.18) is first reformulated,

$$\frac{\partial \rho Y_k}{\partial t} + \boldsymbol{\nabla} \cdot (\rho(\mathbf{u} + \mathbf{V}_c) Y_k) = \boldsymbol{\nabla} \cdot \left(\rho \mathcal{D}_k \frac{W_k}{W} \boldsymbol{\nabla} X_k \right) + \dot{\omega}_k \,, \tag{2.71}$$

$$\rho \frac{\partial Y_k}{\partial t} + Y_k \underbrace{\left(\frac{\partial \rho}{\partial t} + \boldsymbol{\nabla} \cdot (\rho \mathbf{u}) \right)}_{=0 \text{ from continuity equation}} + \rho \mathbf{u} \cdot \boldsymbol{\nabla} Y_k + \boldsymbol{\nabla} \cdot (\rho \mathbf{V}_c Y_k) = \boldsymbol{\nabla} \cdot \left(\rho \mathcal{D}_k \frac{W_k}{W} \boldsymbol{\nabla} X_k \right) + \dot{\omega}_k \,, \tag{2.72}$$

$$\rho \frac{\partial Y_k}{\partial t} = -\rho \mathbf{u} \cdot \boldsymbol{\nabla} Y_k - \boldsymbol{\nabla} \cdot (\rho \mathbf{V}_c Y_k) + \boldsymbol{\nabla} \cdot \left(\rho \mathcal{D}_k \frac{W_k}{W} \boldsymbol{\nabla} X_k \right) + \dot{\omega}_k \,. \tag{2.73}$$

Let's note $\mathbf{u}_k^{\text{abs}}$ the absolute displacement velocity within the flame front of an iso-surface defined from the mass fraction Y_k. This absolute velocity measured in a fixed laboratory frame is decomposed into the fluid velocity $\mathbf{u}$ and $v_k \mathbf{n}$, the relative progression velocity of the surface in its normal direction $\mathbf{n} = -\boldsymbol{\nabla} Y_k / |\boldsymbol{\nabla} Y_k|$,

$$\rho \frac{\partial Y_k}{\partial t} = -\rho \mathbf{u}_k^{\text{abs}} \cdot \boldsymbol{\nabla} Y_k = -\rho \left(\mathbf{u} + v_k \mathbf{n} \right) \cdot \boldsymbol{\nabla} Y_k \,. \tag{2.74}$$

The combination of equations 2.73 and 2.74 yields,

$$v_k = \frac{-\boldsymbol{\nabla} \cdot (\rho \mathbf{V}_c Y_k) + \boldsymbol{\nabla} \cdot \left(\rho \mathcal{D}_k \frac{W_k}{W} \boldsymbol{\nabla} X_k \right) + \dot{\omega}_k}{\rho |\boldsymbol{\nabla} Y_k|} \,. \tag{2.75}$$

For $\mathbf{u}_k^{\text{abs}} = 0$ through the flame, the flow velocity verifies $\mathbf{u} = -v_k \mathbf{n}$. Then, the bulk velocity of the incoming flow exactly matches the burning velocity and the flame position is fixed in the reference frame of the laboratory. To reach this condition in the simulations of the narrow channel, the pseudo Galilean transformation discussed by Ruetsch *et al.* [125] to stabilise freely propagating triple-flames is applied. The component in the stream-wise direction of the absolute velocity of the CH_4 iso-surface is computed at $(x^\star, y^\star)$, the location of the peak burning rate of CH_4,

$$u_{\text{CH}_4}^{\text{abs}}(x^\star, y^\star) = \left(\mathbf{u}(x^\star, y^\star) + v_{\text{CH}_4}(x^\star, y^\star) \mathbf{n}(x^\star, y^\star) \right) \cdot \mathbf{e}_x \,, \tag{2.76}$$

where $\mathbf{e}_x$ is the stream-wise unit vector and v_{CH_4} is calculated with the relation (2.75). If $u_{\text{CH}_4}^{\text{abs}}(x^\star, y^\star) \neq 0$ the flame moves in the domain, because the relative progression velocity $v_{\text{CH}_4}(x^\star, y^\star) \mathbf{n}(x^\star, y^\star) \cdot \mathbf{e}_x$ is not balanced by the inflow velocity $\mathbf{u}(x^\star, y^\star) \cdot \mathbf{e}_x$. The stream-wise flow momentum may be rescaled in $\rho(x, y) u^{\text{new}}(x, y)$ over the computational domain, including boundary conditions, to secure a zero absolute velocity of the reactive front,

$$\rho(x, y) u^{\text{new}}(x, y) = \rho(x, y) u(x, y) - \left(\rho(x^\star, y^\star) u_{\text{CH}_4}^{\text{abs}}(x^\star, y^\star) \right) F(y) \,. \tag{2.77}$$

In this relation, $F(y) = (1 - (2y/\ell_i)^2)$ accounts for the boundary layer in the no-slip cases, while in the slip-wall case $F(y) = 1 \ \forall y$. The kinetic energy part of the transported total sensible

energy is rescaled accordingly. This transformation is applied only every 500 iterations until $u^{\text{abs}}_{\text{CH}_4}(x^\star, y^\star) < 10^{-6} S_\text{L}$, with S_L the burning velocity defined as the inlet bulk velocity. From this point, the simulation is pursued over 15 characteristic stoichiometric flame times ($\delta_\text{F}/S_\text{L}$), to fully secure convergence, with δ_F the flame thickness. As a check, this procedure was also applied to one-dimensional flames with an observed speed up of the convergence, to reach solutions perfectly matching those obtained using the dedicated flame solver Cantera [48].

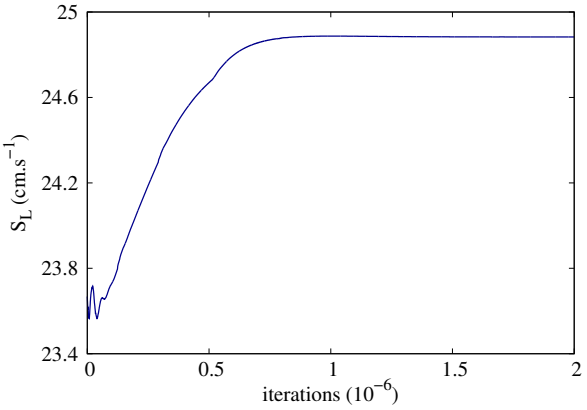

Figure 2.11: Evolution of the inlet bulk velocity prescribed at the channel inlet during the stabilisation process.

This procedure was employed on all the steady state simulations presented in this work, including more challenging cases of 2D flames propagating in small-scale channels. See for example the evolution of the flame bulk velocity prescribed at the inlet, subsequently to the corrections made from equation 2.75, displayed in figure 2.11. This case corresponds to the simulation in figure 6.7(a), treated later in chapter 6. Initially, the computed flame velocity undergoes some oscillations due to the imposition of new operating conditions. Then the bulk velocity evolves smoothly from the absolute flame speed is not zero yet. Finally, the flame burning rate matches the inlet mass flow rate yielding a motionless steady-state flame. Note that the transient states are not analysed in this work but are analogous to the process a experimentalist would follow, while aiming at stabilising the flame, through the setting of the inlet flow valve.

Chapter 3

Kinetic mechanism reduction strategy for small-scale combustion

Contents

3.1 Preamble 69
3.2 Introduction 70
3.3 Optimised and Reduced Chemistry: ORCh method 70
3.4 Reduction trajectories for small-scale combustion 71
3.5 Results on canonical problems 74
3.5.1 1D premixed flames with and without uniform heat loss 74
3.5.2 Auto-ignition delays 79
3.6 Results on the 2D case of a flame propagating in a small-scale channel . . 80
3.7 Computational performances 82

3.1 Preamble

In the introduction, the thermal coupling between the flame, the flow and the channel walls, was recalled to be a first order concern when modelling small-scale combustion. The previous chapter introduced the modelling strategy for the heat transfer coupling between the channel and the flow. Further, heat loss to the channel walls strongly affect the combustion modelling, as it rearranges the relative influence of reactions compared to an adiabatic case, and should be considered when electing or deriving a kinetic mechanism. This chapter is about deriving, cost-controlled, reduced mechanisms fitted to small-scale combustion.

3.2 Introduction

In the present work, methane/air flames are studied. Although CH_4 is among the most simple fuels, the detailed mechanisms modelling its combustion in air can reach 32 species and 177 elementary reactions for the GRI-1.2 mechanism [41], or 53 species and 325 reactions for the most complete GRI-3.0 mechanism [137]. Such complexity requires a tremendous computational effort, often unrealistic, discouraging the use of detailed mechanisms. Indeed, global and reduced mechanisms are widely preferred by the CFD community, as they lower the cost and duration of simulations. The savings due to the reduction of detailed schemes allow for studying a wider variety of configurations, but the reduction process narrows simultaneously the validity range of the resulting schemes.

As evoked in the literature review, because of the numerous couplings between chemistry, heat transfer and flame propagation in flame/wall interactions, the fidelity of chemistry modelling is essential in small-scale combustion. In the following, small discrepancies, of a reduced to the detailed mechanism on 1D flames, are shown to result in non-negligible differences when confronted to 2D flame/wall interaction configurations. The derivation of reduced kinetic mechanisms tailored for such a purpose would thus be valuable. In this chapter, a reduction method developed in the CORIA lab by Jaouen *et al.* [58] is employed to derive reliable skeleton mechanisms specific to small-scale combustion study.

Section 3.3 presents the reduction method employed to produce the skeleton mechanisms. The development of a reduction strategy fitted to small-scale combustion problems is then addressed in section 3.4. The validity of the derived mechanisms is assessed against the initial detailed mechanism on canonical (section 3.5) and 2D realistic (section 3.6) cases. Finally, section 3.7 comments the computational savings made from the use of the reduced mechanisms.

3.3 Optimised and Reduced Chemistry: ORCh method

Among the vast literature on chemistry reduction for hydrocarbon combustion [111, 148], automated methods have been recently developed and applied with success to generate skeleton mechanisms valid under given operating conditions. See the work of Lu *et al.* [94], Pepiot *et al.* [110], Lovas [93], Koniavitis *et al.* [80] and Jaouen *et al.* [58]. In these methods, a detailed chemical scheme is first selected and canonical problems are simulated to generate reference chemical responses for the mixture evolving from fresh to fully burnt products. Then, a procedure is applied along these chemical evolutions to rank the chemical species and the elementary reactions according to their relative influence on targeted species, whose responses should stay close to the detailed chemistry ones. Once the less influential species and reactions removed, the parameters (pre-exponential factors, temperature exponents and activation energies) of the remaining skeleton mechanism are sometimes further optimised to better match the reference detailed chemistry.

In this work, the ORCh (Optimised and Reduced Chemistry) method previously reported in detail by Jaouen *et al.* [58] is employed. It relies on the Cantera package [49] for the simulation

of canonical combustion problems. To reduce the computational cost of the kinetic mechanism, ORCh applies the following steps:

- A selection of the species and reactions that can be removed from the detailed kinetic mechanism, without notably modifying the solution, is obtained based on the Directed Relation Graph with Error Propagation (DRGEP) procedure [94, 110].
- If the Quasi-Steady State [18, 95] (QSS) hypothesis applies to species, these are expressed analytically as a function of the transported species. This step is not used in the present work.
- After reducing the number of species and reactions of the complex mechanism down to a tractable set, the reactions Arrhenius constants are optimised, based on a Genetic Algorithm [119], so that the new scheme fits the best possible the initial detailed mechanism on the reference configurations.

Please refer to Jaouen *et al.* [58] for a complete and comprehensive description of this automated reduction procedure.

3.4 Reduction trajectories for small-scale combustion

There exist many reference detailed methane/air chemistries in the literature, targeting different objectives. Because of the physical complexity at play in the edge-flame quenching close to the wall in the narrow channel, none of these schemes can be considered as a definitive reference for simulating the flame/wall interactions. Accordingly, the objective here is more to quantify the impact of the choice of the canonical problems for chemistry reduction, than to provide absolute values on flame speeds and species distributions. However, the detailed mechanism used as a starting point (GRI-1.2 [41]) has been widely employed as a reference for modelling chemistry in the study of turbulent lean premixed combustion [132], Bunsen flames [133] and mild combustion [46] via direct numerical simulation (DNS). Tabulation [53] and other reduction [80] methods were also validated using this scheme. It has again been used to predict methane flames lift-off height [124], with success. In the present case, this detailed mechanism is of interest because of its modest size (32 species), which allows for performing a reference two-dimensional channel flame simulation. Only major species are targeted in the reduction: CH_4, O_2, H_2O, CO_2 and CO. These species are qualified as major from they are typically representative of the fresh or the burnt gases equilibrium. The fitness function defined for optimisation [58] involves the evolution of these species (versus space or time), temperature and the flame speed in the case of one-dimensional propagating premixed flames.

Since the present physical configuration exhibits a perfectly premixed inlet, a different skeleton mechanism is derived for each of the studied equivalence ratios ($\phi = 0.7$, $\phi = 0.8$ and $\phi = 1.0$), allowing to further reduce the schemes dimensions. Indeed, the thickening of the equivalence range targeted, typically requires more complex reduced mechanisms. In the following, only the stoichiometric case is depicted. Appendix A gathers the results for $\phi = 0.7$ and $\phi = 0.8$.

Among other configurations, the method ORCh permits to perform the complete reduction based on multiple 1D flames at a time. This possibility allows a better representation of most multi-dimensional cases, where various kinetic paths are experienced by the reactants. In the channel, the flame is subjected to quenching at the wall because of heat loss and may potentially undergo self ignition for an excess of enthalpy transferred to the fresh gases. Three canonical problems are thus considered during chemistry reduction and optimisation, in which the fresh gases at atmospheric pressure are those of the stoichiometric CH_4/air condition:

- A zero-dimensional homogeneous reactor, whose initial temperature is varied between 1000 K and 1600 K.
- A freely propagating adiabatic one-dimensional premixed flame.
- A set of freely propagating one-dimensional premixed flames subjected to an amount of heat loss modelled by a linear sink term $\alpha_{\text{loss}}(T - T_{\text{o}})$, added in the energy equation for values of α_{loss} increasing up to flame quenching. In this case, the Cantera budget equations for the multicomponent flow are solved in their one-dimensional form, with an energy equation cast as,

$$\rho u C_p \frac{\partial T}{\partial x} = \frac{\partial}{\partial x}\left(\lambda \frac{\partial T}{\partial x}\right) - \sum_{k=1}^{N_{\text{sp}}} j_k C_{p,k} \frac{\partial T}{\partial x} - \sum_{k=1}^{N_{\text{sp}}} h_k W_k \dot{\omega}_k^m - \alpha_{\text{loss}}(T - T_{\text{o}}) \,, \qquad (3.1)$$

  where for species k, $\dot{\omega}_k^m$ is the molar production rate, h_k is the specific enthalpy and j_k is the diffusive mass flux, which is approximated as in the two-dimensional simulations from the mixture-averaged model [26]. Other notations were introduced before. The temperature driving the heat loss from the gas is set to $T_{\text{o}} = 300$ K.

Reduction and optimisation configurations	1D adiabatic premixed flame	1D premixed flames with heat loss down to quenching	Auto-ignition delays
15S-26R (see table 3.3)	X		
17S-53R-1.0 (see table 3.2)	X	X	X

Table 3.1: Reduction and optimisation trajectories of the two skeleton mechanisms. Both are reduced from the GRI-1.2 mechanism, at stoichiometric conditions.

A first reduced mechanism, called thereafter '15S-26R' (15 species, H_2, H, O, O_2, OH, H_2O, HO_2, CH_3, CH_4, CO, CO_2, HCO, CH_2O, CH_3O, N_2, and 26 reactions, Table 3.3) is calibrated to reproduce only the freely propagating flame without heat loss. A second skeleton mechanism, '17S-53R-1.0' (17 species, adding H_2O_2 and C_2H_6 to 15S-26R and 53 reactions at $\phi = 1.0$, Table 3.2), is generated targeting both the freely propagating premixed flames for levels of heat loss from adiabatic up to quenching and auto-ignition in homogeneous reactors at various initial temperatures. Table 3.1 sums up the canonical problems accounted for during the

	Reaction	A	β	E_a
1	$O+H_2 \leftrightharpoons H+OH$	5.010E+04	2.601	6271
2	$O+HO_2 \leftrightharpoons OH+O_2$	1.630E+13	0	0
3	$O+H_2O_2 \leftrightharpoons OH+HO_2$	7.470E+06	1.979	3969
4	$O+CH_3 \leftrightharpoons H+CH_2O$	4.610E+14	0	0
5	$O+CH_4 \leftrightharpoons OH+CH_3$	1.200E+09	1.481	8726
6	$O+HCO \leftrightharpoons OH+CO$	4.450E+13	0	0
7	$O+HCO \leftrightharpoons H+CO_2$	4.840E+13	0	0
8	$O+CH_2O \leftrightharpoons OH+HCO$	6.440E+13	0	3473
9	$O+CH_3O \leftrightharpoons OH+CH_2O$	1.780E+13	0	0
10	$O_2+CH_2O \leftrightharpoons HO_2+HCO$	1.360E+14	0	38456
11	$H+O_2+M \leftrightharpoons HO_2+M$	5.700E+18	-0.740	0
12	$H+2O_2 \leftrightharpoons HO_2+O_2$	4.350E+20	-1.660	0
13	$H+O_2+H_2O \leftrightharpoons HO_2+H_2O$	6.740E+18	-0.670	0
14	$H+O_2+N_2 \leftrightharpoons HO_2+N_2$	1.820E+20	-1.660	0
15	$H+O_2 \leftrightharpoons O+OH$	7.050E+13	0	14056
16	$H+HO_2 \leftrightharpoons O+H_2O$	2.080E+12	0	688
17	$H+HO_2 \leftrightharpoons O_2+H_2$	5.070E+13	0	1057
18	$H+HO_2 \leftrightharpoons 2OH$	5.680E+13	0	653
19	$H+H_2O_2 \leftrightharpoons HO_2+H_2$	1.070E+07	2.092	5369
20	$H+CH_3+M \leftrightharpoons CH_4+M$	3.870E+16	-0.480	382
21	$H+CH_4 \leftrightharpoons CH_3+H_2$	7.880E+08	1.589	10843
22	$H+HCO+M \leftrightharpoons CH_2O+M$	5.550E+11	0.480	0
23	$H+HCO \leftrightharpoons H_2+CO$	7.310E+13	0	0
24	$H+CH_2O+M \leftrightharpoons CH_3O+M$	1.010E+12	0.450	2681
25	$H+CH_2O \leftrightharpoons HCO+H_2$	2.570E+10	1.030	3335
26	$H+CH_3O \leftrightharpoons H2+CH_2O$	1.790E+13	0	0
27	$H+CH_3O \leftrightharpoons OH+CH_3$	5.160E+13	0	0
28	$OH+H_2 \leftrightharpoons H+H_2O$	3.880E+08	1.560	3568
29	$2OH+M \leftrightharpoons H_2O_2+M$	5.980E+13	-0.250	0
30	$2OH \leftrightharpoons O+H_2O$	4.260E+04	2.491	0
31	$OH+HO_2 \leftrightharpoons O_2+H_2O$	1.480E+14	0	0
32	$OH+H_2O_2 \leftrightharpoons HO_2+H_2O$	7.890E+14	0	9135
33	$OH+CH_4 \leftrightharpoons CH_3+H_2O$	7.240E+07	1.590	3147
34	$OH+CO \leftrightharpoons H+CO_2$	3.950E+07	1.271	70
35	$OH+HCO \leftrightharpoons H_2O+CO$	5.620E+13	0	0
36	$OH+CH_2O \leftrightharpoons HCO+H_2O$	4.330E+09	1.231	0
37	$OH+CH_3O \leftrightharpoons H_2O+CH_2O$	2.160E+13	0	0
38	$2HO_2 \leftrightharpoons O_2+H_2O_2$	1.780E+11	0	0
39	$2HO_2 \leftrightharpoons O_2+H_2O_2$	5.800E+14	0	12239
40	$HO_2+CH_3 \leftrightharpoons O_2+CH_4$	1.390E+12	0	0
41	$HO_2+CH_3 \leftrightharpoons OH+CH_3O$	3.050E+13	0	0
42	$HO_2+CO \leftrightharpoons OH+CO_2$	2.450E+14	0	23452
43	$HO_2+CH_2O \leftrightharpoons HCO+H_2O_2$	1.270E+12	0	7709
44	$CH_3+O_2 \leftrightharpoons O+CH_3O$	2.780E+13	0	28747
45	$CH_3+O_2 \leftrightharpoons OH+CH_2O$	2.070E+10	0	9098
46	$CH_3+H_2O_2 \leftrightharpoons HO_2+CH_4$	2.790E+04	2.631	4921
47	$2CH_3+M \leftrightharpoons C_2H_6+M$	1.190E+16	-0.820	605
48	$CH_3+HCO \leftrightharpoons CH_4+CO$	3.430E+13	0	0
49	$CH_3+CH_2O \leftrightharpoons HCO+CH_4$	3.570E+03	2.721	6054
50	$HCO+H_2O \leftrightharpoons H+CO+H_2O$	1.040E+18	-0.890	17099
51	$HCO+M \leftrightharpoons H+CO+M$	1.370E+17	-0.870	16643
52	$HCO+O_2 \leftrightharpoons HO_2+CO$	4.880E+12	0	398
53	$CH_3O+O_2 \leftrightharpoons HO_2+CH_2O$	4.280E-13	7.943	0

Table 3.2: 17S-53R-1.0 kinetic mechanism. Units are mol, s, cm^3, cal and K. Reduced CH_4/Air scheme for the modelling of small-scale combustion at stoichiometric condition. The Chaperon efficiencies of the GRI-1.2 mechanism are preserved for both three-body and fall-off reactions.

	Reaction	A	β	E_a
1	$O+CH_3 \leftrightharpoons H+CH_2O$	1.710E+14	0	0
2	$O+CH_4 \leftrightharpoons OH+CH_3$	8.680E+08	1.48	8691
3	$H+O_2(+M) \leftrightharpoons HO_2(+M)$	2.270E+18	-0.81	0
4	$H+2O_2 \leftrightharpoons HO_2+O_2$	8.870E+19	-1.65	0
5	$H+O_2+H_2O \leftrightharpoons HO_2+H_2O$	1.600E+19	-0.69	0
6	$H+O_2+N_2 \leftrightharpoons HO_2+N_2$	2.020E+20	-1.7	0
7	$H+O_2 \leftrightharpoons O+OH$	8.840E+13	0	14475
8	$H+HO_2 \leftrightharpoons 2OH$	1.720E+14	0	640
9	$H+CH_3(+M) \leftrightharpoons CH_4(+M)$	5.200E+16	-0.6	387
10	$H+CH_4 \leftrightharpoons CH_3+H_2$	7.000E+08	1.6	11035
11	$H+CH_2O(+M) \leftrightharpoons CH_3O(+M)$	9.590E+11	0.45	2604
12	$H+CH_2O \leftrightharpoons HCO+H_2$	3.900E+10	1.06	3249
13	$H+CH_3O \leftrightharpoons OH+CH_3$	3.320E+13	0	0
14	$OH+H_2 \leftrightharpoons H+H_2O$	2.060E+08	1.53	3441
15	$2OH \leftrightharpoons O+H_2O$	3.690E+04	2.4	-2057
16	$OH+HO_2 \leftrightharpoons O_2+H_2O$	5.210E+13	0	-503
17	$OH+CH_4 \leftrightharpoons CH_3+H_2O$	9.330E+07	1.57	3235
18	$OH+CO \leftrightharpoons H+CO_2$	4.300E+07	1.21	70
19	$OH+CH_2O \leftrightharpoons HCO+H_2O$	4.310E+09	1.17	-448
20	$HO_2+CH_3 \leftrightharpoons OH+CH_3O$	1.300E+13	0	0
21	$CH_3+O_2 \leftrightharpoons O+CH_3O$	2.450E+13	0	29409
22	$CH_3+O_2 \leftrightharpoons OH+CH_2O$	5.140E+10	0	8593
23	$HCO+H_2O \leftrightharpoons H+CO+H_2O$	2.750E+18	-0.98	17220
24	$HCO+M \leftrightharpoons H+CO+M$	5.930E+17	-0.95	17320
25	$HCO+O_2 \leftrightharpoons HO_2+CO$	6.950E+12	0	402
26	$CH_3O+O_2 \leftrightharpoons HO_2+CH_2O$	4.280E-13	7.67	-3643

Table 3.3: 15S-26R kinetic mechanism. Units are mol, s, cm^3, cal and K. Reduced CH_4/Air scheme for the stoichiometric adiabatic condition. The Chaperon efficiencies of the GRI-1.2 mechanism are preserved for both three-body and fall-off reactions.

reduction and optimisation of the two skeleton mechanisms. The 15S-26R scheme is derived only for the stoichiometric case while different 17S-53R schemes are obtained for the three targeted equivalence ratios. Please refer to appendix A for 17S-53R-0.8 at $\phi = 0.8$ and for 17S-53R-0.7 at $\phi = 0.7$. In the three 17S schemes, the species and reactions are conserved, while the equivalence ratio varies, making their discrepancies result from the reaction rates optimisation only.

3.5 Results on canonical problems

3.5.1 1D premixed flames with and without uniform heat loss

Figure 3.1 shows the flame speeds obtained with the two skeletal mechanisms and the detailed chemistry. The parameter α_{loss} is varied from the adiabatic condition ($\alpha_{\text{loss}} = 0$) up to flame quenching, *i.e.* a solution is converged for every value of α_{loss}. Quenching is observed for $\alpha_{\text{loss}} = 85.4$ kW.m^{-3}.K^{-1}, with the reference detailed mechanism. As expected, the departure found including only the adiabatic condition during reduction and optimisation of the chemistry, almost vanishes adding the flames with heat losses and auto-ignition. The heat loss coefficients leading to complete flame quenching are $\alpha_{\text{loss}} = 68.5$ kW.m^{-3}.K^{-1} for 15S-26R and

83.3 kW.m^{-3}.K^{-1} for 17S-53R-1.0, respectively. The 20% error made on the parameter calibrating the amount of heat loss needed to quench the flame with 15S-26R is therefore reduced down to 2.5% with 17S-53R-1.0.

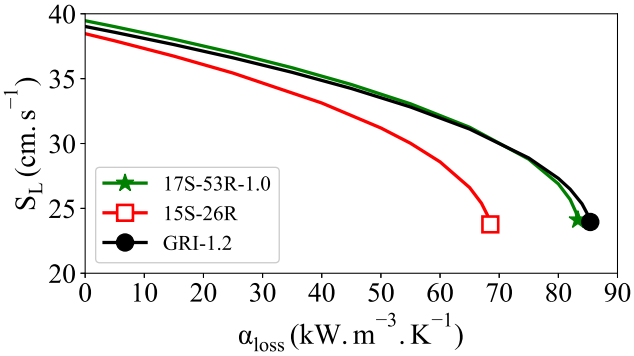

Figure 3.1: Flame velocity *vs* heat loss coefficient. Black circle: detailed chemistry [41]. Red square: 15S-26R (Table 3.3). Green star: 17S-53R-1.0 (Table 3.2). Symbols mark the flame quenching.

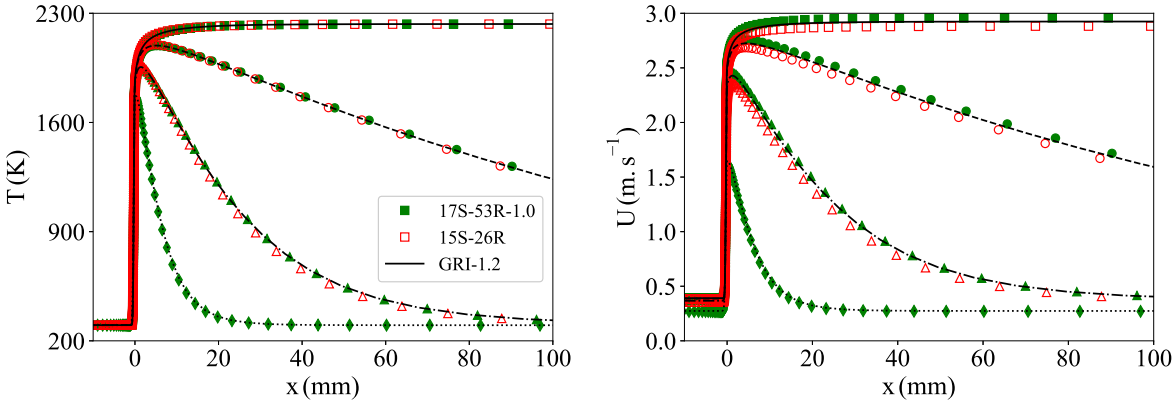

(a) T (b) U

Figure 3.2: Premixed flame with heat loss. Temperature and velocity. Detailed chemistry (GRI-1.2 [41]): black lines. 15S-26R (Table 3.3): hollow markers (red). 17S-53R-1.0 (Table 3.2): full markers (green). $\alpha_{loss} = 0$ kW.m^{-3}.K^{-1}: solid line and squares. $\alpha_{loss} = 5$ kW.m^{-3}.K^{-1}: dashed line and circles. $\alpha_{loss} = 25$ kW.m^{-3}.K^{-1}: dash-dotted line and triangles. $\alpha_{loss} = 80$ kW.m^{-3}.K^{-1}: dotted line and diamonds.

The distributions of temperature, velocity, major and minor species mass fractions obtained with the 15S-26R (red in figures) and 17S-53R-1.0 (green) chemical kinetics are compared in figures 3.2-3.4 to the detailed reference mechanism (black). Note that for the 15S-26R mechanism, the case with $\alpha_{loss} = 80$ kW.m^{-3}.K^{-1} is already quenched. For the lower levels of heat loss, figure 3.2(a) suggests that the performances of the 15S-26R chemistry are satisfying on the temperature profiles.

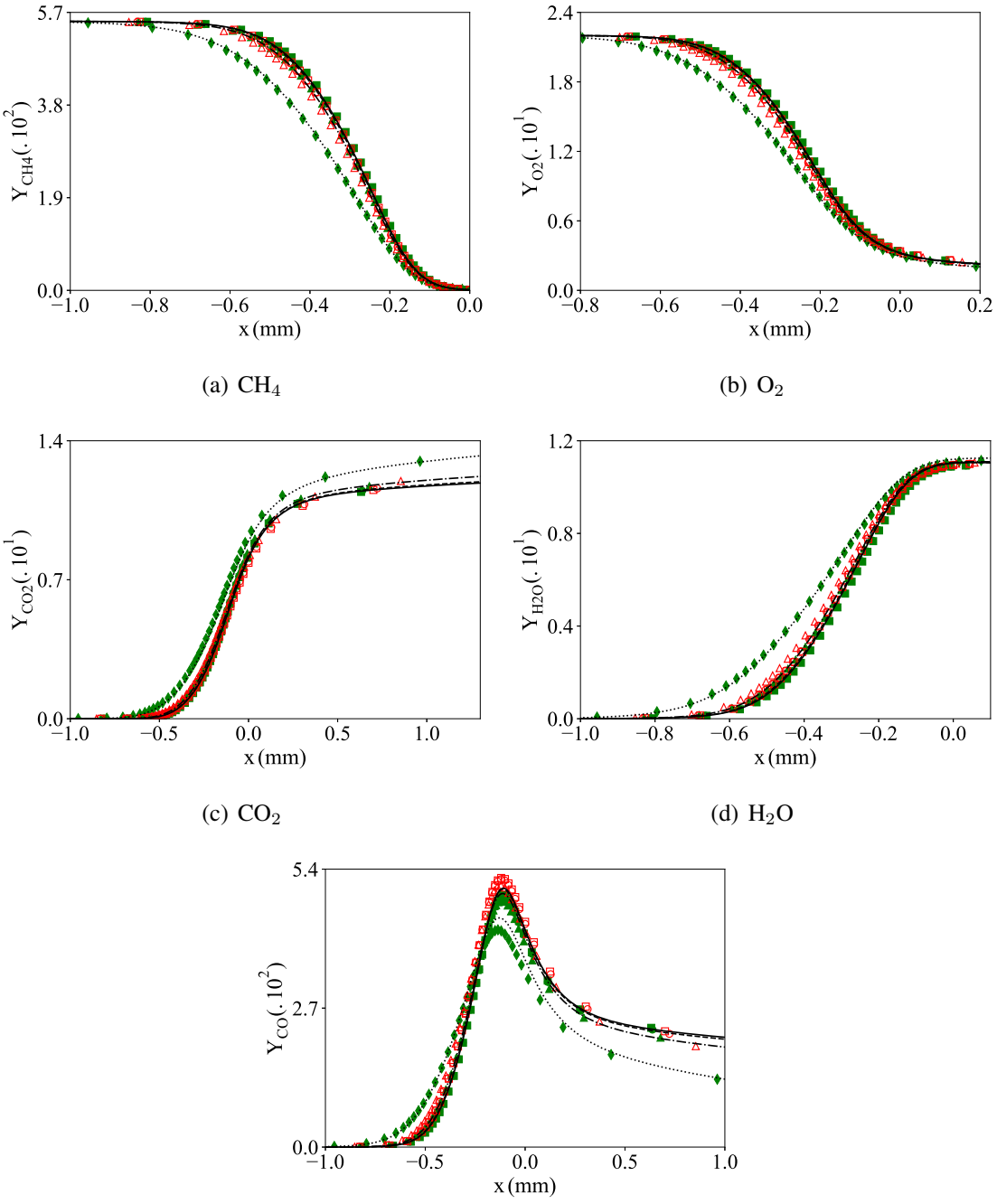

(a) CH_4 (b) O_2

(c) CO_2 (d) H_2O

(e) CO

Figure 3.3: Premixed flame with heat loss. Target species. Detailed chemistry (GRI-1.2 [41]): black lines. 15S-26R (Table 3.3): hollow markers (red). 17S-53R-1.0 (Table 3.2): full markers (green). $\alpha_{\text{loss}} = 0$ kW.m^{-3}.K^{-1}: solid line and squares. $\alpha_{\text{loss}} = 5$ kW.m^{-3}.K^{-1}: dashed line and circles. $\alpha_{\text{loss}} = 25$ kW.m^{-3}.K^{-1}: dash-dotted line and triangles. $\alpha_{\text{loss}} = 80$ kW.m^{-3}.K^{-1}: dotted line and diamonds.

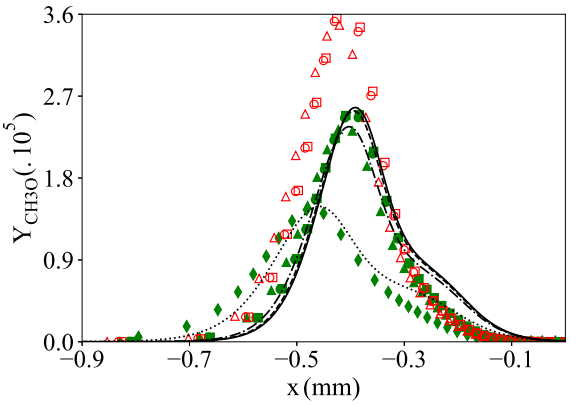

(a) CH_3O

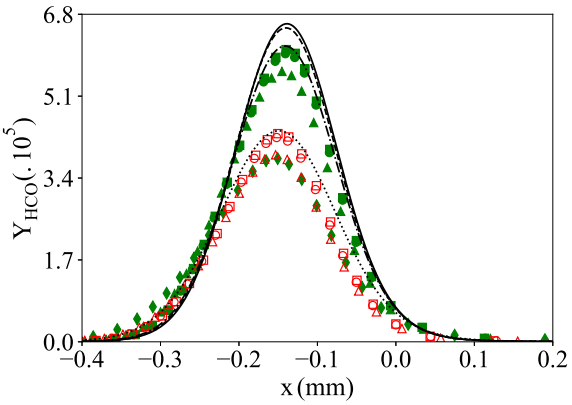

(b) HCO

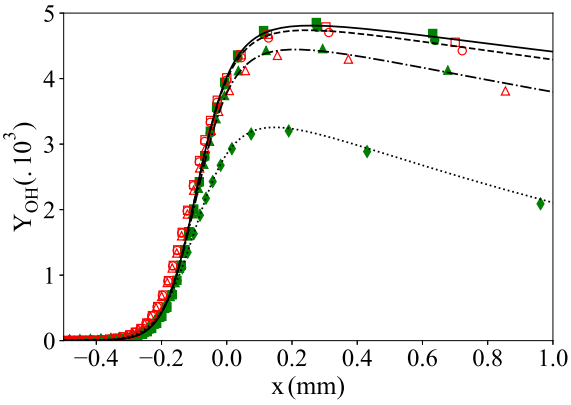

(c) OH

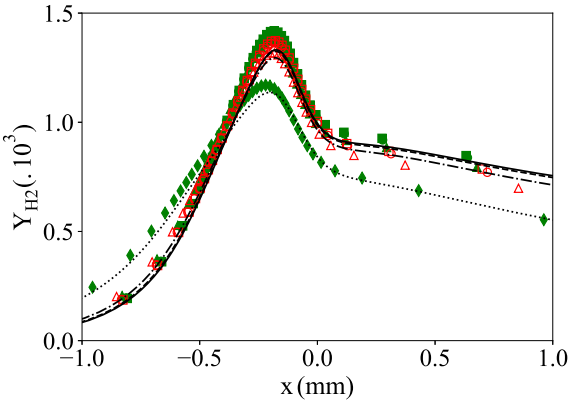

(d) H_2

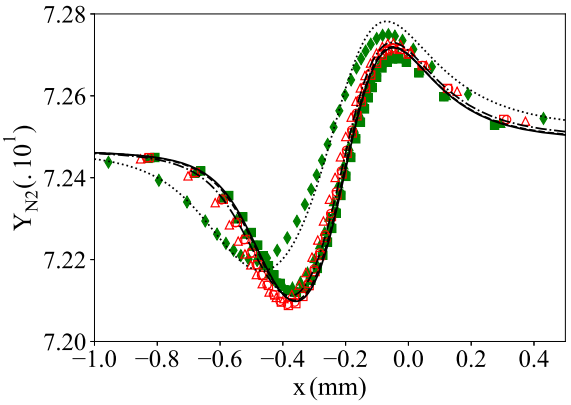

(e) N_2

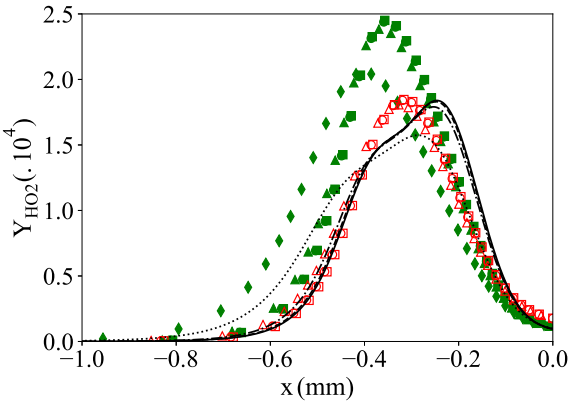

(f) HO_2

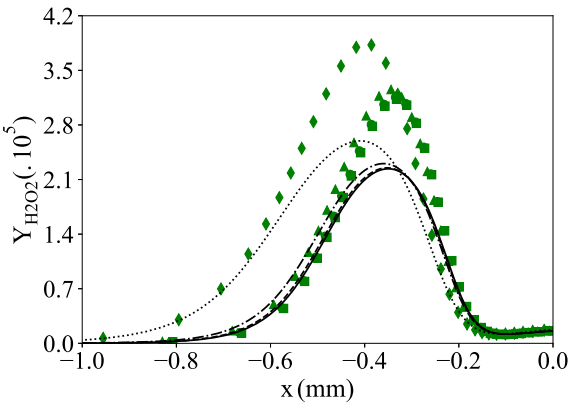

(g) H_2O_2

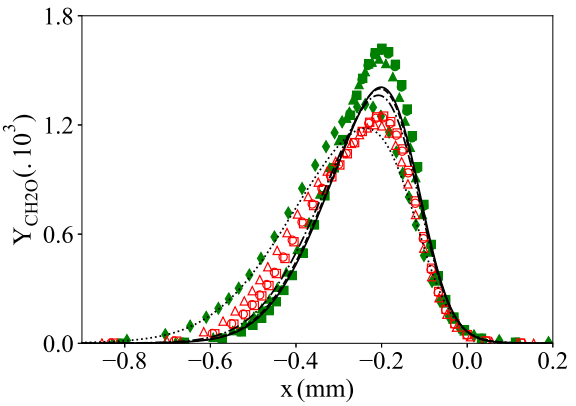

(h) CH_2O

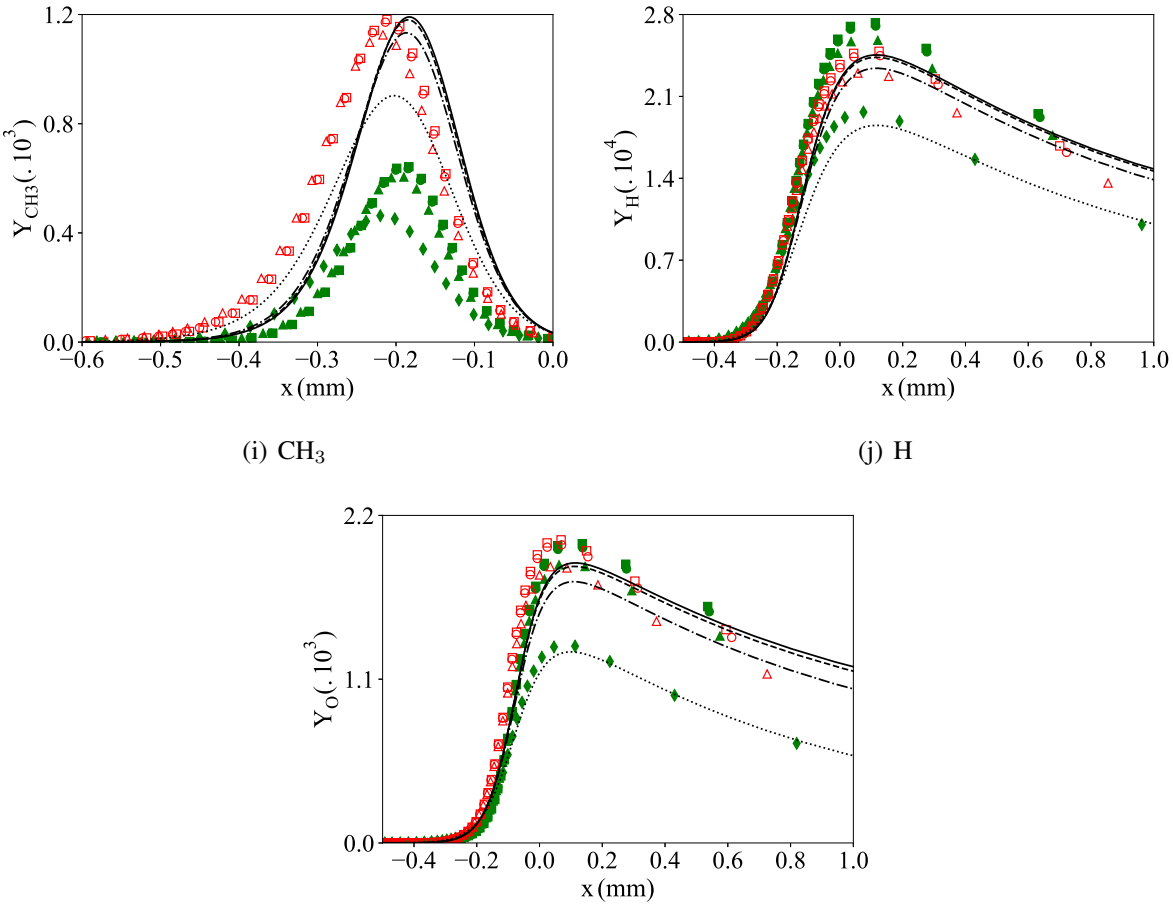

(i) CH_3 (j) H

(k) O

Figure 3.4: Premixed flame with heat loss. Representative minor species. Detailed chemistry (GRI-1.2 [41]): lines. 15S-26R (Table 3.3): hollow markers (red). 17S-53R-1.0 (Table 3.2): full markers (green). $\alpha_{\text{loss}} = 0$ kW.m^{-3}.K^{-1}: full line and squares. $\alpha_{\text{loss}} = 5$ kW.m^{-3}.K^{-1}: dashed line and circles. $\alpha_{\text{loss}} = 25$ kW.m^{-3}.K^{-1}: dash-dotted line and triangles. $\alpha_{\text{loss}} = 80$ kW.m^{-3}.K^{-1}: dotted line and diamonds.

In fact, for 15S-26R a small discrepancy (1.4%) on the adiabatic flame speed exists (figure 3.1), without much consequence on the adiabatic flame temperature profile (figure 3.2(a)). Considering heat loss, the scenario is quite different. The underestimation of the flame velocity (figure 3.1), increasing the residence time of particles, results in an overestimation of the heat loss in the burnt gases. Thereby, the temperature profiles fit less and less the reference in the presence of increasing levels of heat losses (see figure 3.2(a)), ending up with the anticipation of quenching reported above. Figure 3.2(b) also permits to observe the increase of the velocity gap, between the 15S-26R and the GRI-1.2 mechanisms, when approaching quenching. The 17S-53R-1.0 mechanism allows for overcoming these deficiencies.

Target species are first analysed in figure 3.3, such as CH_4 (figures 3.3(a)) and O_2 (figure 3.3(b)). Although results given with 15S-26R are satisfying under the adiabatic condition, they depart from the reference for intermediate values of heat loss coefficient, as $\alpha_{\text{loss}} = 25$ kW.m^{-3}.K^{-1}. This departure is reduced with the 17S-53R-1.0 mechanism, as it is also the case for CO (figure 3.3(e)). Considering the minor species mass fraction profiles in figure 3.4, some species predictions are also improved with the 17S-53R-1.0 compared to the 15S-26R scheme. It is the case for HCO (figure 3.4(b)) and CH_3O (figures 3.4(a)). Some other minor species find their prediction deviated from the detailed mechanism, see HO_2 (figure 3.4(f)) or CH_3 (figure 3.4(i)), as one shall recall that the fitness function permits to optimise the kinetic mechanism for targets while considering other parameters as degrees of freedom.

3.5.2 Auto-ignition delays

It is well-known from the literature that reduced mechanisms can hardly match both, premixed propagating flame properties undergoing heat loss, and auto-ignition delay. Figure 3.5 shows that the 17S-53R-1.0 scheme derived from an automated method allowing for targeting multiple canonical problems, also perfectly matches the auto-ignition delay for $T_o \in \{1000\text{ K}: 1600\text{ K}\}$. As expected, the 15S-26R skeletal mechanism, whose reduction and optimisation procedure lack the auto-ignition problem, fails to pass this last test (figure 3.5).

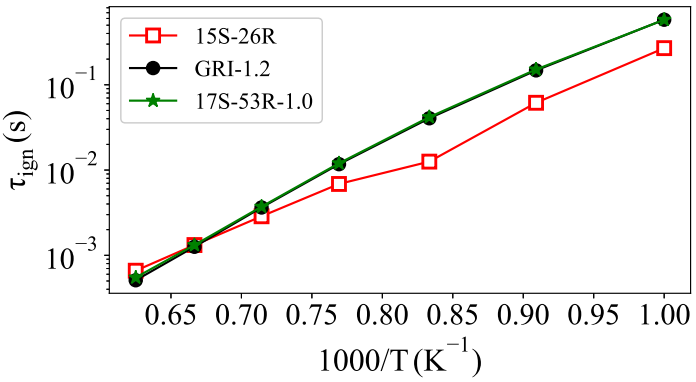

Figure 3.5: Auto-ignition delays. Black circles: detailed chemistry [41]. Red squares: 15S-26R (Table 3.3). Green stars: 17S-53R-1.0 (Table 3.2).

3.6 Results on the 2D case of a flame propagating in a small-scale channel

In this paragraph, the skeletal kinetic flames stabilised in the 2D narrow channel are compared to the channel flame computed with the detailed GRI-1.2 mechanism (figure 3.7). Because of the channel dimensions, the close to unity Lewis number of the mixture and the absence of gravity, the problem may be assumed symmetrical with respect to the longitudinal mid-plane ($y = 0$) [43, 85]. The validity of this hypothesis is confirmed in figure 3.6, comparing flame shapes obtained with and without formulating the symmetry assumption (computation with the 17S-53R-1.0 scheme).

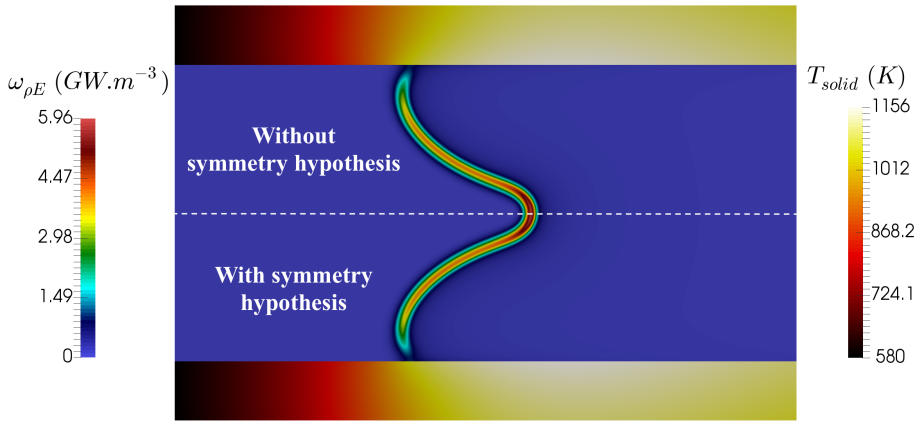

Figure 3.6: Heat release source term distributions. Top: view of top-half channel with full domain simulation. Bottom: simulation with symmetry hypothesis.

The so-called tulip flame topology is obtained in all cases. This shape yields a concave flame front relative to the fresh gases, on the axis of symmetry, with inflexion points near the walls. As shown in appendix C, the flame shape depends on the equivalence ratio and in the present stoichiometric case, the topology of the reactive front is explained by the heat retrocession by the wall [89]. Part of the heat transferred to the wall by the flame and the burnt gases, is conducted within the wall up to the fresh gases, therefore upstream of the flame position. This recirculation of energy leads to the development of a thermal boundary layer, preheating the fresh gases and enhancing combustion close to the wall. The edge flame near the wall is thus positioned upstream of the centreline (axis of symmetry) reaction zone (figure 3.7), a behaviour also supported by the lower velocity close to the wall. Finally, at the very edge of the reaction zone submitted to intense heat transfer to the wall, the reaction rate decreases dramatically along with the local propagation velocity of the reactive front, which leads to the formation of an inflection point. There the flame points downstream toward the wall, to finally be quenched. Further analysis on the various parameters controlling the flame topology and velocity are provided in chapter 4.

Coming back to the evaluation of the skeleton schemes. The flame length is shorten with the 15S-26R chemistry (figure 3.7(a)), resulting in an error of 13.2% on the bulk flame velocity with respect to the detailed mechanism. A departure which is reduced to 1.6% when using the

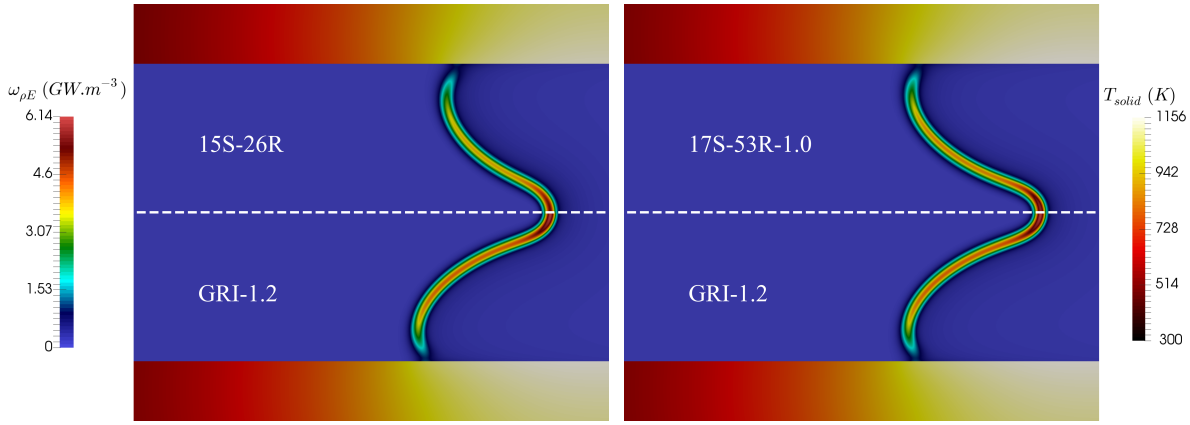

(a) 15S-26R (Table 3.3) against GRI-1.2 [41] (b) 17S-53R-1.0 (Table 3.2) against GRI-1.2 [41]

Figure 3.7: Heat release rate distribution. Comparison between the reduced schemes and the reference detailed mechanism.

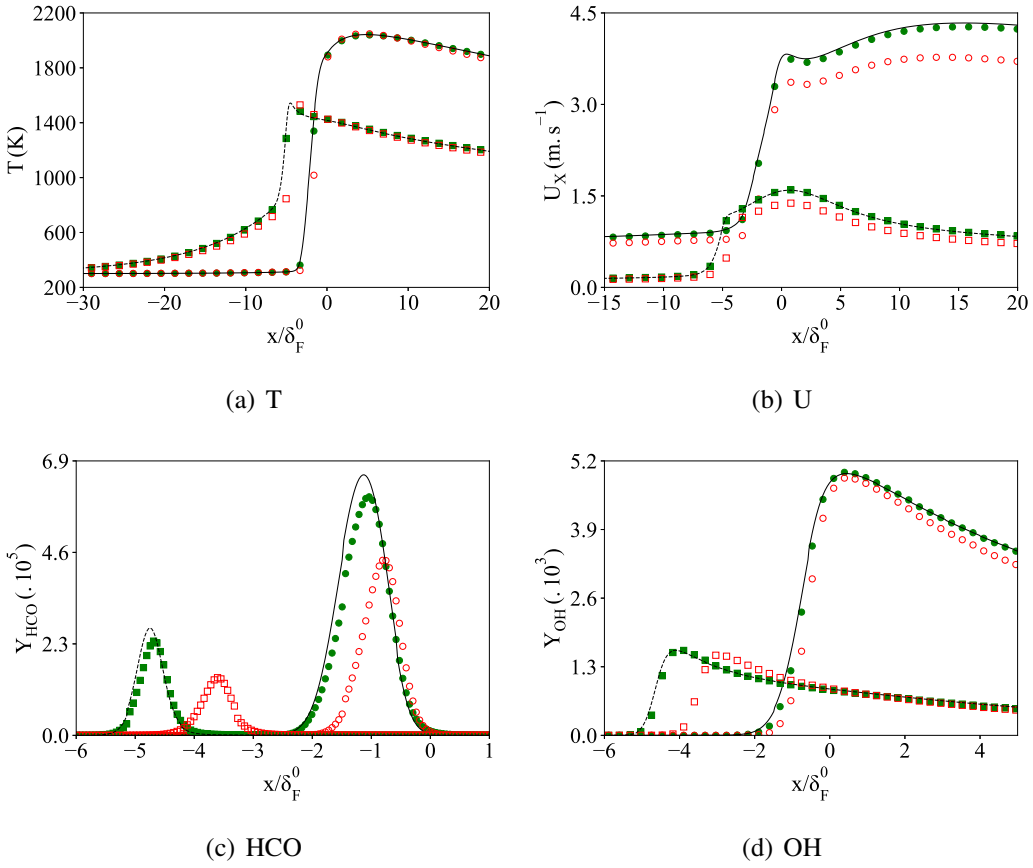

(a) T (b) U

(c) HCO (d) OH

Figure 3.8: Comparison of longitudinal profiles in the 2D case. Temperature, velocity and minor species. Detailed chemistry (GRI-1.2 [41]): lines. 15S-26R (Table 3.3): hollow markers (red). 17S-53R-1.0 (Table 3.2): full markers (green). $y = -0.5$ mm: full line and circles. $y = -2.3$ mm: dashed line and squares.

17S-53R-1.0 skeletal mechanism, interestingly with only the supplemental cost of solving for two additional species, C_2H_6 and H_2O_2, the latter being reported in the literature as a marker of auto-ignition [50, 105]. Figure 3.7(b) shows that the overall flame topology is also better reproduced. Further comparison of the three kinetic mechanisms is provided in figure 3.8. It points out the excellent accordance in velocity, temperature and species profiles of the 17S-53R-1.0 scheme with the reference GRI-1.2 mechanism on this complex physical set up, both close to the wall ($y = -2.3$ mm) and to the axis ($y = -0.5$ mm).

Table 3.4 gathers various characteristic results for the three chemical mechanisms, pointing out the overall benefit of reducing and optimising the scheme against canonical problems representative of the multi-physics character of the study (flame propagation, heat loss at the wall and auto-ignition).

	GRI-1.2	17S-53R-1.0	15S-26R	Units
S_L	53.65	52.79	46.55	cm·s^{-1}
ΔS_L	–	1.6	13.2	%
max($\omega_{\rho E}$)	6.14	5.96	5.30	GW·m^{-3}
max(T_{solid})	1156	1156	1142	K

Table 3.4: Comparison of the three kinetic mechanisms on the 2D case. S_L: flame speed. ΔS_L: error to the reference GRI-1.2 flame speed. max($\omega_{\rho E}$): maximum heat release rate in the flame. max(T_{solid}): maximum temperature in the solid wall.

3.7 Computational performances

The objective of reducing kinetic mechanisms being to limit the computational efforts and allow for addressing multiple cases, the performances related to each of the mechanisms employed are now evaluated. Different mesh resolutions are required, depending on the scheme running. For each mechanism, appendix B gathers the test of several mesh resolutions on adiabatic flames. Errors made from the discretisation in SiTCom-B are then evaluated and a mesh refinement is selected in the light of the expected time of return and precision. In the case of the detailed GRI-1.2 mechanism, the mesh resolution selected to capture the flame front is $\delta x = 12.5$ µm. The skeleton mechanisms permit for increasing the mesh size up to $\delta x = 25$ µm due to the removal of some radical and intermediate species.

	GRI-1.2	17S-53R-1.0	15S-26R	Units
δt	8.4	16.8	16.8	ns
t_{CPU} (1 ms)	38309	4310	4090	s

Table 3.5: Computational performances associated with each of the kinetic schemes applied to the case in figure 3.7.

For the three mechanisms employed at stoichiometric conditions, table 3.5 gathers the controlling time step and the CPU time required to simulate 1 ms of physical time. CPU time is defined as the number of processors multiplied by the duration of the computation. In all cases, the time step restriction is dictated by the CFL condition, with a coefficient fixed at 0.6 to ensure stability. These data were collected on simulations of the stoichiometric flame thermally coupled with the channel walls (see previous section, figure 3.7). The mesh resolution in the flame front was indeed twice thinner in the detailed chemistry case than for the reduced chemistries. The 1.6 % error achieved by the 17S-53R-1.0, on the flame velocity of the thermally coupled flame/wall case, accounts thus for the coarsening of the mesh.

In table 3.5, when comparing the detailed to the reduced mechanisms, one remarks that the resolution of a lower amount of species transport equations 2.12, combined with the possible coarsening of the mesh is followed by a decrease of the CPU time of one order. When comparing the two reduced mechanisms, the time steps are logically the same. Indeed it depends on the mesh resolution, unchanged, and the convective velocity plus the sound speed, the first being negligible in front of the second (see equation 2.67). Finally, compared to the 15S-26R, the 5 % increase in CPU time of the 17S-53R-1.0 scheme comes from the additional 2 transport equations solved. Finally, the use of the 17 species mechanism yields 21 transport equations (3 for momentum, 1 for energy and 17 for species), against 19 for the 15 species mechanism.

Due to the low velocity of the flow entering the channel and the consideration of the thermal coupling with the channel walls, it is quite long for computations to reach the steady state. The cost of the reference GRI-1.2 mechanism simulation attains 1200k CPU hours. This corresponds to 49 runs of two days over 512 processors.

In conclusion, the use of reduced mechanisms decreases drastically the duration of computations, allowing for the coming studies. Furthermore, when compared to classical adiabatic trajectories, the increase of the reduced mechanism size due to the consideration of reduction trajectories adapted to small-scale combustion is shown not to impact significantly the cost of simulations.

Chapter 4

Premixed flame/wall interaction in a narrow channel under microgravity: Impact of wall thermal conductivity and heat losses

Contents

4.1 Introduction 86

4.2 Configuration 86

4.3 Analysis of the burning velocity 90

4.3.1 Observations 90

4.3.2 Scaling law 91

4.4 Effect of the sheared flow 93

4.4.1 Quenching 93

4.4.2 Flow deviation 93

4.4.3 Kinetics 95

4.5 Thermal coupling influence 97

4.5.1 Heat transfer at the wall 97

4.5.2 Flow deviation 98

4.5.3 Energy budget on the thermally coupled flame 99

4.5.4 Kinetics 101

4.6 Flame response to wall heat transfer properties in a regime diagram . . . 103

4.6.1 Asymptotic behaviours 103

4.6.2 Competition of the influence of conductivity and convection on the flame characteristics 105

4.1 Introduction

In this chapter, the flow physics controlling the stabilisation of a stoichiometric laminar premixed flame in a narrow channel ($\ell_\mathrm{i} = 5$ mm) is revisited from numerical simulations. Combustion is described with complex chemistry and transport properties, along with a coupled simulation of heat transfer at and within the wall. To conduct a thorough analysis of the flame-wall interaction, the steady flame is obtained after applying the procedure to find the inlet mass flow rate that exactly matches the flame mass burning rate (see § 2.4.3). Objectives of this chapter are:

- To analyse the response of the premixed flame shape to various operating conditions in terms of flame propagation velocity and flow topology in the vicinity of the reactive front.
- To clarify the interrelations between the flame speed, the configuration taken by the flame surface, the flow deviation induced by the heat released and the fluxes at the wall.
- To provide scaling laws for the flame speed under the various configurations.
- To produce a regime diagram delineating between flame shapes in order to build a classification versus heat transfer properties.

First, section 4.2 depicts the configurations under study and advances a strategy to isolate boundary layer effects from wall thermal coupling. In section 4.3, a preliminary analysis of a scaling law for the burning velocities observed is conducted, versus the reference stoichiometric planar flame speed, the flame surface and the amount of heat losses at the wall. The influences, over the flame behaviour, of the dynamic boundary layer and of the thermal coupling with a quartz wall are then analysed in sections 4.4 and 4.5, respectively. Finally, the flame response to variations of the wall thermal conductivity and the external convective coefficient is analysed. In section 4.6, a regime diagram for flame velocity and topology is built against heat-transfer properties. The major part of this chapter is the object of a publication in the international *Journal of Fluid Mechanics* in 2018 [10].

4.2 Configuration

As exposed in § 1.3.3.6, because of the close to unity Lewis number of the methane/air mixture, the absence of gravity and the dimensions of the channel, the problem is supposed symmetrical with respect to the longitudinal mid-plane $y = 0$ mm (figure 4.1). In chapter 3, figure 3.6 shows that this hypothesis is valid under the present conditions, while further analysis on this point is provided in chapter 6. Presently, a stoichiometric mixture of methane/air at the ambient air temperature $T_\mathrm{o} = 300$ K and atmospheric pressure, flows in a laminar regime from the left into the channel at the mass flow rate $\dot{Q}_\mathrm{m}$, with the bulk velocity $S_\mathrm{L} = \dot{Q}_\mathrm{m}/(\rho_\mathrm{o} A)$, where ρ_o is the density of the fresh gases and $A = (\ell_\mathrm{i}/2) \times 1$ is the channel half section. ('$\times 1$' denotes the third direction, in which the problem is assumed uniform.) Because this part of the study was

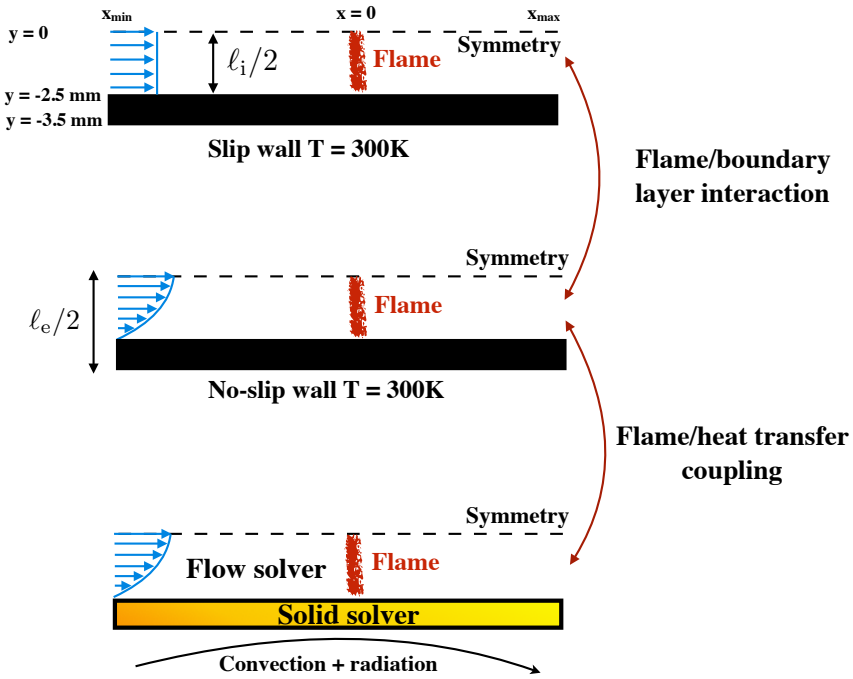

Figure 4.1: Cases simulated. Internal channel height: $\ell_i = 5$ mm. External channel height: $\ell_e = 7$ mm.

chronologically performed before the reduction of the skeleton mechanism 17S-53R, the 15S-26R scheme is presently used. In chapter 3, the 15S-26R mechanism was demonstrated to give the same global flame topology as the detailed GRI-1.2 mechanism in the complex flame/wall coupled configuration, justifying for the coming study. To answer to the objectives of the present chapter, flames stabilized in the channel by an incoming flow have been obtained for various wall boundary conditions (figure 4.1). To isolate the various effects at play, three simulations are examined (figure 4.2): a flame propagating in a channel with a slip wall at 300 K; a no-slip wall at 300 K and finally a quartz wall with solid heat-transfer coupled to the flow:

- The comparison of the two isothermal cold wall simulations allows for isolating the flame/boundary layer interaction from the influence of thermal coupling with the wall.
- Comparing the no-slip wall simulations, with and without thermal coupling with the wall, the influence of heat-transfer can be discussed.
- In last section the impact of the wall heat-transfer properties is then further examined and the results collected in a diagram that delineates between the flame regimes observed in the simulations. Parameters are thus varied based on the initial quartz wall configuration.

The freely propagating adiabatic flame speed taken as reference for normalisation of the results is $S_L^o = 0.3803$ m.s^{-1}, the corresponding adiabatic flame temperature is $T_F^o = 2231$ K, the thermal flame thickness based on the temperature gradient is $\delta_F^o = 451$ µm and the peak of heat release rate is $\dot{\omega}_{\rho E}^o = 4.10$ GW.m^{-3}. This reference corresponds to the adiabatic flame

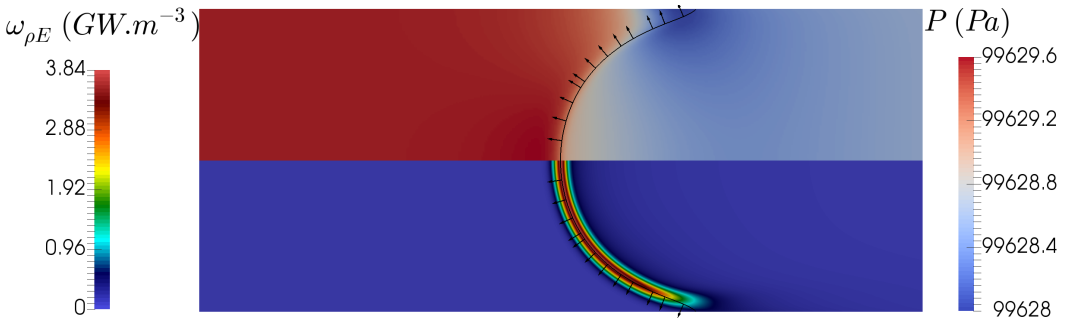

(a) Slip and isothermal wall at 300 K

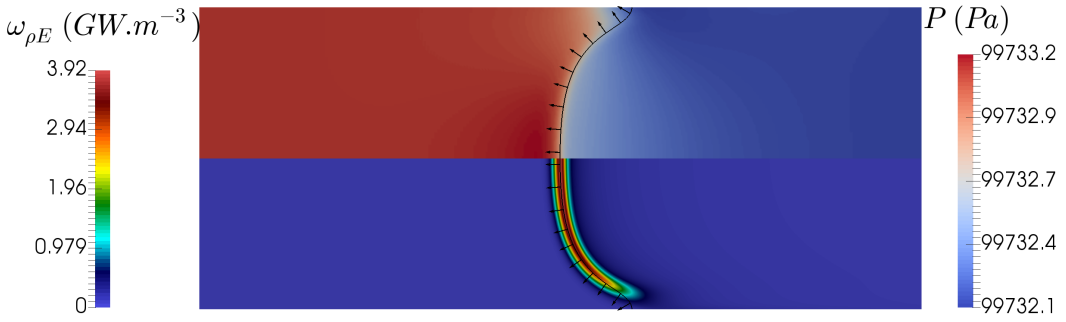

(b) No-slip and isothermal wall at 300 K

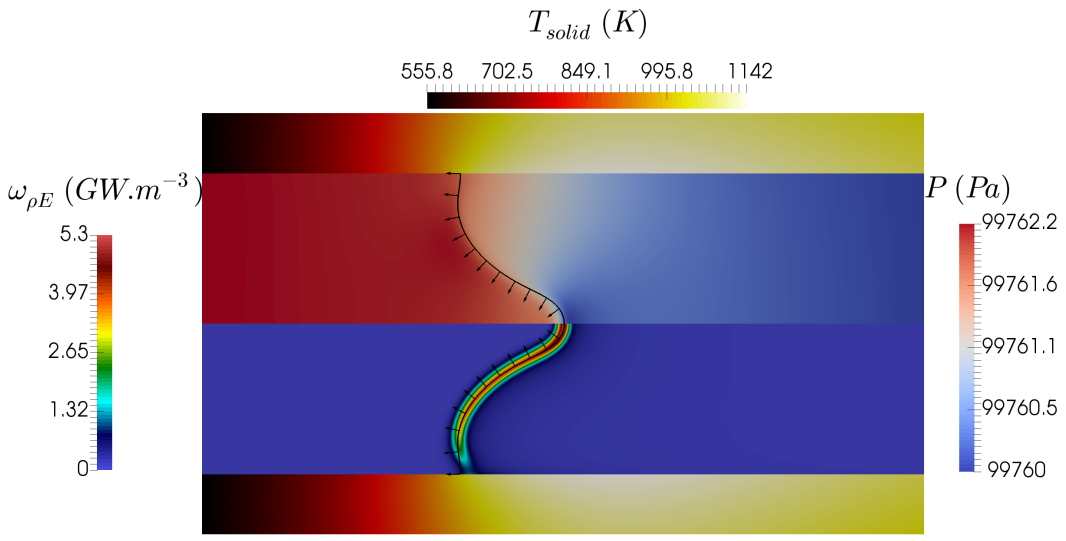

(c) No-slip quartz wall with heat transfer

Figure 4.2: Above symmetry-axis: Pressure. Below symmetry-axis: heat release source term. Black line: iso-$Y_C = 0.7$. Vector: flame front normal toward fresh gases. Flow from left to right. Zoom in the flame zone. 15S-26R scheme.

computed with the 15S-26R mechanism over a 25 µm mesh resolution (see appendix B). Approaching the cold wall, the flame surface will be considered quenched when the local heat release rate is an order of magnitude below $\dot{\omega}^{o}_{\rho E}$, value at which the relative displacement speed of the front vanishes.

The flame stabilized in the narrow channel is obtained starting from a preliminary simulation of a one-dimensional freely propagating and adiabatic stoichiometric premixed flame. This flame solution is applied to the two-dimensional domain, first imposing the flame temperature profile in the wall. Then, the temperature in the wall is relaxed progressively to $T_{\mathrm{o}} = 300$ K, to reach the first case of a slip isothermal wall (figures 4.1 and 4.2(a)). From this converged solution, the no-slip isothermal wall case is addressed by modifying both the inlet profile and the wall boundary condition (figure 4.2(b)). Finally, the last case is obtained coupling the flow solver with the solution of heat transfer at and within the wall (figure 4.2(c)). As exposed by Weinberg *et al.* [156] and Vican *et al.* [152], most small-scale burners rely on anchored flames rather than moving ones and having stable flames exchanging heat with the wall is more likely in practice. The objective is thus to exactly match the flow rate with the flame burning rate in order to control the flame location. Also, for each of these converged solutions, the flame is freely stabilized in the channel by the incoming flow, after applying the specific transient procedure based on a pseudo-galilean transformation presented in subsection 2.4.3. Notice that, due to the large heat capacities of solids, the heat wave in the solid propagates upstream at a much slower speed than the flame. In case the mass flow rate would be significantly below the overall flame burning rate, the reaction zone would therefore propagate upstream over a wall at 300 K. Thus, an upstream flame movement actually corresponds to a flame propagating over an isothermal wall (figure 4.2(b)). The flame moving downstream in the channel is not considered here because, in a real small-scale combustion devices, it would correspond to flame blow-off due to lack of proper system calibration, an issue which is out of the scope of this study.

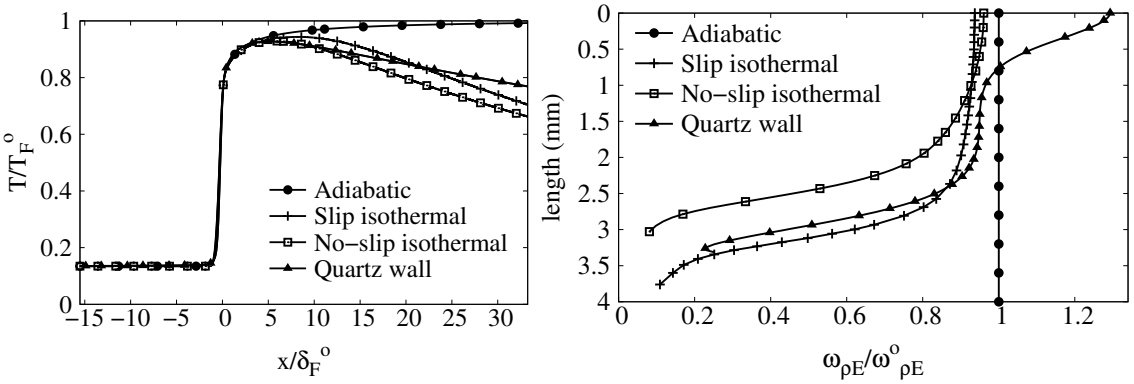

(a) Centreline temperature

(b) Normalized heat release source term

Figure 4.3: Flame properties. Quartz wall: Heat conductive-wall.

Wall	Slip Adiabatic	Slip 300 K	No-slip 300 K	No-slip heat transfer	Units
T_F	2231	2104	2070	2067	K
δ_F	451	444	423	338	µm
Σ_F	2.5	3.76	3.01	3.31	mm
k_w	–	112	87	59	$W.m^{-2}.K^{-1}$
S_L/S_L^o	1	1.23	0.96	1.22	–
S_L	0.3803	0.4670	0.3640	0.4655	$m.s^{-1}$
S_L Eq. (4.1)	–	0.4562	0.3655	0.4496	$m.s^{-1}$
ΔS_L	–	2.3	0.4	3.4	%

Table 4.1: Flame parameters. T_F: maximum temperature in the burnt gases. δ_F: thermal flame thickness on the axis. Σ_F: flame length. k_w: wall heat transfer coefficient inside the channel. S_L: flame speed. S_L^o: adiabatic flame speed. ΔS_L: Departure between S_L by Eq. (4.1) and by simulation.

4.3 Analysis of the burning velocity

4.3.1 Observations

First focusing on the gas temperature evolution in figure 4.3(a). Quite naturally, from the enhanced heat transfers at the wall, the centreline gas temperature decrease follows a steeper slope in the isothermal cold wall cases than in the thermally coupled case. As one might expect, all temperatures stay bellow the adiabatic flame temperature.

Besides, the flame burning velocity S_L is defined as the bulk velocity computed from the mass flow rate in the channel (table 4.1). As referred above, the adiabatic methane/air flame propagates at $S_L^o = 0.3803\ m.s^{-1}$ with the 15S-26R reduced chemical mechanism. The slip-wall at 300 K leads to $S_L = 0.4670\ m.s^{-1} > S_L^o$, the no-slip wall at 300 K to $S_L = 0.3640\ m.s^{-1} < S_L^o$ and the no-slip wall with heat transfer $S_L = 0.4655\ m.s^{-1} > S_L^o$ (figure 4.2). Therefore, the flame speed increases with edge-flame quenching at an isothermal cold and slip-wall, decreases with the introduction of the boundary layer, to increase again with heat transfer coupling within the wall.

In all cases, heat loss at the wall quenches the flame. Moving along the flame surface from its peak value on the centreline to the quenched zone, with isothermal walls the heat release source term decreases first exponentially to then follow an almost linear decay, before a drop toward quenching (figure 4.3(b)). The maximum heat release rate located at the axis of symmetry differs from the reference adiabatic one, it reaches 94% of $\dot{\omega}^o_{\rho E}$ in the case of an isothermal slip wall, 96% with an isothermal no-slip wall and 129% for a wall with heat transfer. In the latter, the heat release first decays linearly from the axis, before a rapid decrease follows with a response similar to the isothermal wall cases.

As previously discussed in the literature by Gonzalez *et al.* [47] and Michaelis *et al.* [99],

the shape taken by the flame strongly depends on the wall boundary conditions (figure 4.2). On one hand, the slip isothermal wall promotes a shape convex toward the fresh gases (a mushroom shape) and the boundary layer flattens the flame along the axis, as observed by Kim *et al.* [78]. On the other hand, the heat transferred in the wall fastens the reaction zone at the wall so that the flame front recedes on the axis of symmetry. The flame becomes then concave toward the fresh gases close to the axis (a tulip shape). This topological change was already observed by Clanet *et al.* [22] in the case of flames propagating in half open channels, and discussed by Norton *et al.* [106] and Li *et al.* [89] in the case of a flame anchored near the inlet of a small-scale combustion device.

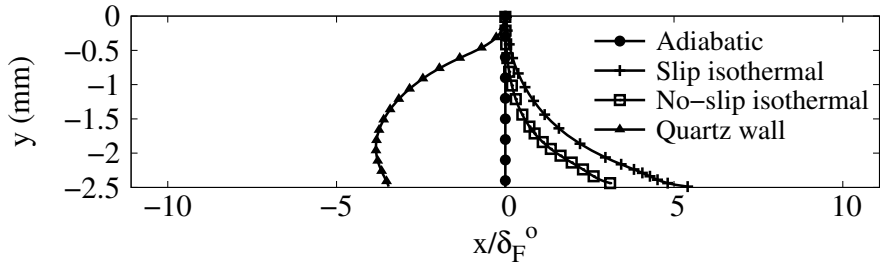

Figure 4.4: Flame shape defined from the maximum heat release rate (symmetry axis: $y = 0$, wall: $y = -2.5$ mm).

The flame length is measured following the peak heat release rate along the curve front and is denoted Σ_F (see figure 4.4). Flame lengths are listed in table 4.1, for all configurations. In the case of an adiabatic wall, the one-dimensional flame is actually recovered with $\Sigma_F^o = \ell_i/2 = 2.5$ mm, the distance between the axis and the channel walls. With a slip wall at 300 K, the lengthening of the flame gives $\Sigma_F/\Sigma_F^o = 1.50$. The increase in burning velocity is $S_L/S_L^o = 1.23$, hence smaller than Σ_F/Σ_F^o because of the decay of the burning rate when approaching flame quenching at the wall (figure 4.3(b)). The no-slip condition at 300 K gives $\Sigma_F/\Sigma_F^o = 1.20$ for $S_L/S_L^o = 0.96$. The addition of heat transfer in the wall leads to $S_L/S_L^o = 1.22$ with $\Sigma_F/\Sigma_F^o = 1.32$.

4.3.2 Scaling law

One might guess that the flame acceleration is directly proportional to the length of the surface of the reactive front. Still, comparing the flame lengthening and corresponding acceleration ratios displayed above, the decrease in heat release source term related to the heat loss visibly impacts the flame velocity, leading to a limitation of the acceleration. Thus, in order to build a scaling law for the flame speed, the heat losses to the wall and the flame lengthening are accounted for. The flame lengthening effect may be added to the planar flame analysis of

Kazakov [72], expressing the effect of heat loss, at first order, with a linear damping factor:

$$\frac{S_{\mathrm{L}}}{S_{\mathrm{L}}^{\mathrm{o}}} = \overbrace{\frac{\Sigma_{\mathrm{F}}}{\Sigma_{\mathrm{F}}^{\mathrm{o}}}}^{\text{Flame lengthening}} \underbrace{\left(1 - \frac{k_{\mathrm{w}}}{(\dot{Q}_{\mathrm{m}}/A)C_{p,\mathrm{o}}}\right)}_{\text{Heat loss}}, \tag{4.1}$$

where $k_{\mathrm{w}} = \dot{q}_{\mathrm{w}}/\Delta\overline{T}$ [W.m^{-2}.K^{-1}] is a heat transfer coefficient, with $\dot{q}_{\mathrm{w}}$ [W.m^{-2}] defined as a positive heat flux at the wall downstream of the flame, for a gain in fluid internal energy between the two channel sections located at the stream-wise positions x_1 and $x_{\max}$,

$$\dot{q}_{\mathrm{w}} = -\frac{1}{x_{\max} - x_1} \int_{x_1}^{x_{\max}} \left(\lambda_{\mathrm{f}} \frac{\partial T}{\partial y}\right)_{y=-\ell_{\mathrm{i}}/2} dx\,, \tag{4.2}$$

λ_{f} is the thermal conductivity of the fluid and $\Delta\overline{T}$ is computed from temperatures averaged between the two channel sections in the gas and in the solid

$$\Delta\overline{T} = \frac{1}{(x_{\max} - x_1)} \int_{x_1}^{x_{\max}} \left(\underbrace{\frac{1}{(\ell_{\mathrm{e}} - \ell_{\mathrm{i}})/2} \int_{-\ell_{\mathrm{e}}/2}^{-\ell_{\mathrm{i}}/2} T(x,y)dy}_{\text{solid}} - \overbrace{\frac{1}{\ell_{\mathrm{i}}/2} \int_{-\ell_{\mathrm{i}}/2}^{0} T(x,y)dy}^{\text{gas}} \right) dx\,. \tag{4.3}$$

The integration domain is defined starting at x_1, in the burnt gases at the most downstream position reached by the curved flame surface, to expend in the stream-wise direction up to $x_{\max}$, the end of the computational domain. The transfer coefficient $k_{\mathrm{w}} = \dot{q}_{\mathrm{w}}/\Delta\overline{T}$ varies significantly with the type of boundary condition at the wall. The highest level, $k_{\mathrm{w}} = 112$ W.m^{-2}.K^{-1} ($\dot{q}_{\mathrm{w}} = 145$ kW.m^{-2}, $\Delta\overline{T} = 1300$ K), is for the isothermal slip-wall. k_{w} decreases to 87 W.m^{-2}.K^{-1} ($\dot{q}_{\mathrm{w}} = 102$ kW.m^{-2}, $\Delta\overline{T} = 1170$ K) with the development of the boundary layer along the isothermal wall and further down to 59 W.m^{-2}.K^{-1} ($\dot{q}_{\mathrm{w}} = 38$ kW.m^{-2}, $\Delta\overline{T} = 644$ K) with the heat conductive wall.

For the two isothermal cases, the departure between S_{L} measured in the simulation and the relation (4.1) stays below 2.5% (table 4.1). The departure attains 3.4% for the quartz wall case, exhibiting a lower theoretical flame speed than the flame speed observed in the simulation. This departure is due to the preheating of the reactants, not considered by the scaling low, and which increases the flame velocity. This applicability to the simulation of the combination of a global budget with a scaling law for the flame speed, comforts our confidence in the relevance of the numerical framework, which will be assessed further in the following through additional budgets. These budgets will be the occasion to emphasize on the influence of preheating on the observed velocities.

4.4 Effect of the sheared flow

4.4.1 Quenching

The isothermal slip and no-slip configurations are first examined to revisit the interaction between the boundary layer and the flame in the narrow channel. The first observation concerns the temperature field, the adiabatic flame temperature is never reached because of the thermal influence of the cold wall up to the center of the channel. The departure to the adiabatic flame temperature is more pronounced in the no-slip wall case (figure 4.3(a)).

The local flame displacement speed decreases when approaching the isothermal wall, following the lowering of the burning rate due to heat loss (figure 4.3(b)). The velocity difference between the flow and the flame is reduced by the boundary layer and the flame is flattened in the no-slip wall case compared to the slip-wall case, as observed in figures 4.2 and 4.4. The development of the thermal boundary layer also benefits from the rising of the fluid particle residence time in the no-slip wall case, favouring in return the rate of heat losses at the edge-flame close to the wall. In consequence, the maximum temperature is lowered (figure 4.3(a)) and the flame quenches 69 µm away from the no-slip wall, while it almost touches the slip-wall (figure 4.4).

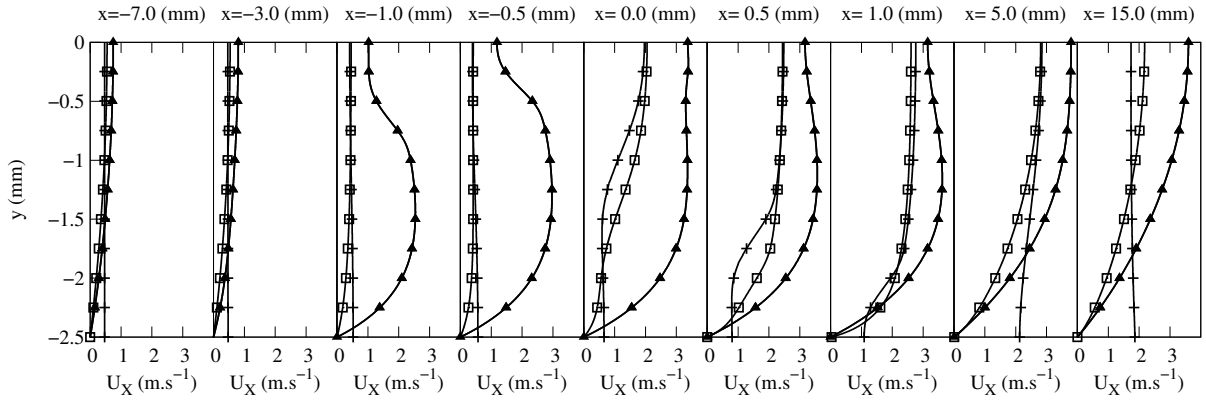

Figure 4.5: Spanwise (y) distributions of streamwise velocity component at various x locations. Line with plus: isothermal slip wall. Line with square: isothermal no-slip wall. Line with triangle: quartz heat conductive wall.

4.4.2 Flow deviation

The velocity profiles progressively evolve from the fresh to the burnt gas sides of the channel according to the flame shape (figure 4.5). In the slip-wall case, the velocity increases at the axis when crossing the flame, to recover an almost flat profile in the burnt gases (line with plus in figure 4.5). In the no-slip case, the transfer of momentum in the wall normal direction is visible up to the axis, with a reduction of the velocity peaks (figure 4.6). In both cases, the flow acceleration on the axis at the flame location is larger than in the adiabatic case (figure 4.6).

The confinement without the boundary layer (slip-wall) leads for $x > 25\delta_F$ in figure 4.6(a) to a flow that is even faster close to the wall, whereas the viscous layer preserves the expected hierarchy in the velocity distribution, with a continuous acceleration when proceeding toward the axis (figure 4.6(b)). In the case of a heat conductive wall, the picture is different and it will be discussed in a separated section thereafter (line with triangle in figure 4.5).

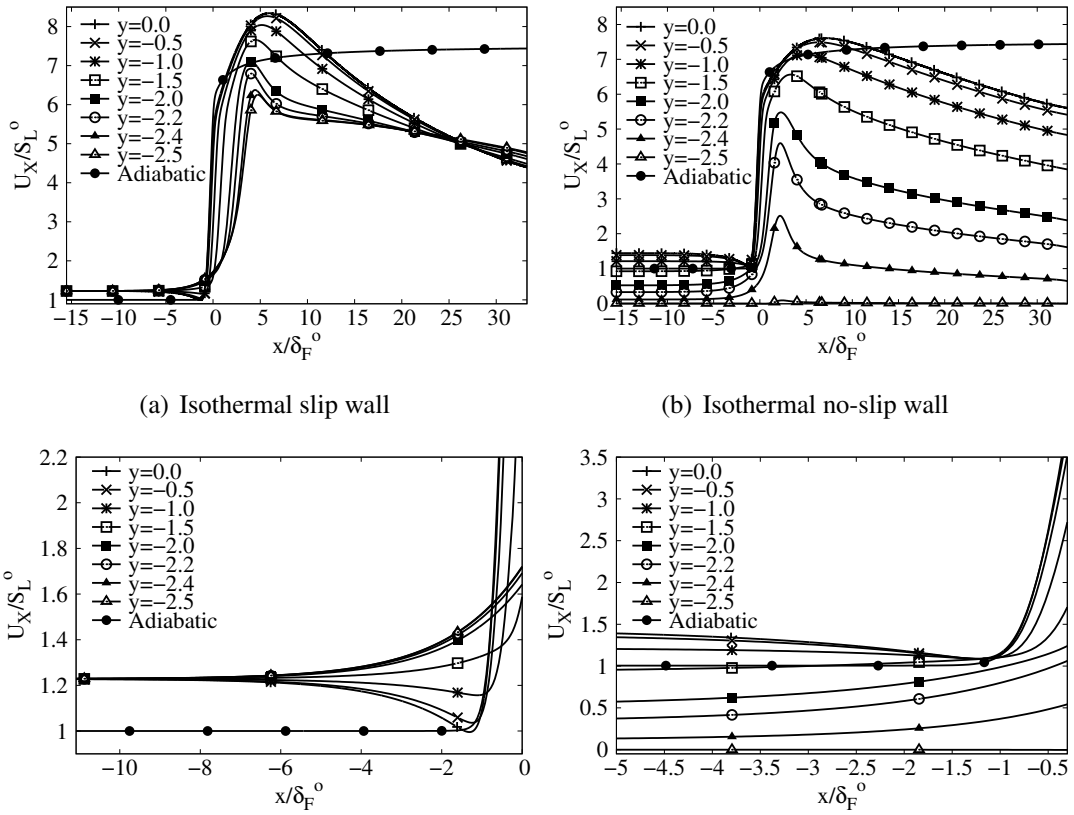

(a) Isothermal slip wall

(b) Isothermal no-slip wall

(c) Isothermal slip wall. Close to flame

(d) Isothermal no-slip wall. Close to flame

Figure 4.6: Streamwise velocity component *vs* x position at various y locations.

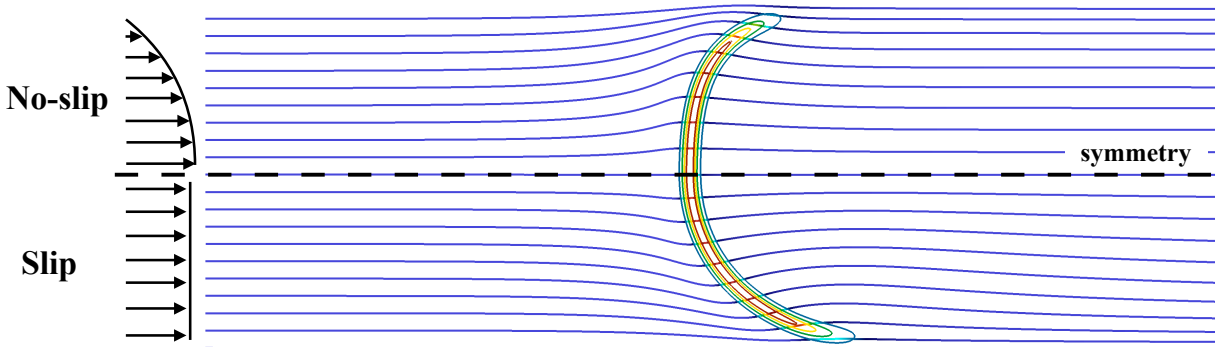

Figure 4.7: Isothermal slip and no-slip configurations are compared taking advantage of the symmetry. Streamlines and flame with contours of 20, 40, 60 and 80% of $\max(\dot{\omega}_{\rho E})$.

Figures 4.6(c) and 4.6(d) are streamwise velocity profiles close to the flame front. On the axis, the longitudinal velocity component drops before the flame to a minimum value equal to $0.99S_L^o$ and $1.07S_L^o$, in the slip and no-slip case, respectively. Moving away from the axis, as pointed out by Clavin *et al.* [23, 25] about curved reaction zones, the component of the velocity in the direction normal to the front benefits from gas expansion, while the tangential velocity component is left unchanged. The gas expansion produced by the heat release thus deviates the streamlines in the flame normal direction, causing their convergence toward the axis right after the reaction zone (figure 4.7). Mass conservation in these low-Mach number flow implies a corresponding divergence of the streamlines upstream of the flame. This response of the incoming streamlines is also visible in figure 4.8, showing the near-wall acceleration due to the streamlines concentration and corresponding deceleration approaching the axis. This flow topology may be put in line with the overall increase of the flame surface promoting the flame acceleration discussed in the relation (4.1).

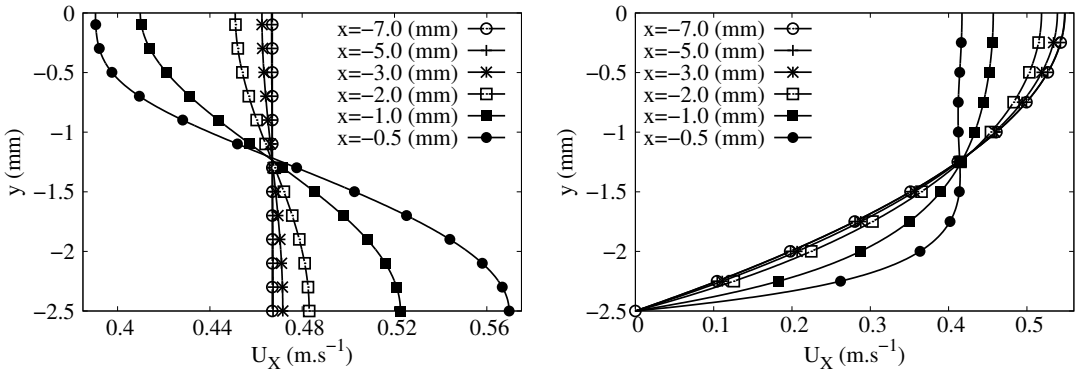

(a) Isothermal slip wall

(b) Isothermal no-slip wall

Figure 4.8: Spanwise distributions of streamwise velocity component at various x locations upstream of the flame (symmetry axis: $y = 0$, wall: $y = -2.5$ mm).

4.4.3 Kinetics

The influence of the wall sheared flow is also visible through intermediate chemical species. An intensified recombination of the H and HO_2 radical is observed with the no-slip wall, as seen comparing for the radical H the lines with hollow circles ($y = -2.2$ mm) in figures 4.9(a) and 4.9(b), and for HO_2 the lines with hollow triangles ($y = -2.5$ mm) in figures 4.9(c) and 4.9(d). The mass fraction of hydrogen is reduced by a factor two with the viscous wall, following the lower temperature levels observed in presence of the boundary layer (figure 4.10). The reduction of the overall spreading of the reaction zones in the streamwise direction from slip to no-slip wall is also visible in these figures, through the narrowing of the profiles of H and HO_2, in direct relation with the change in flame shape (figure 4.7).

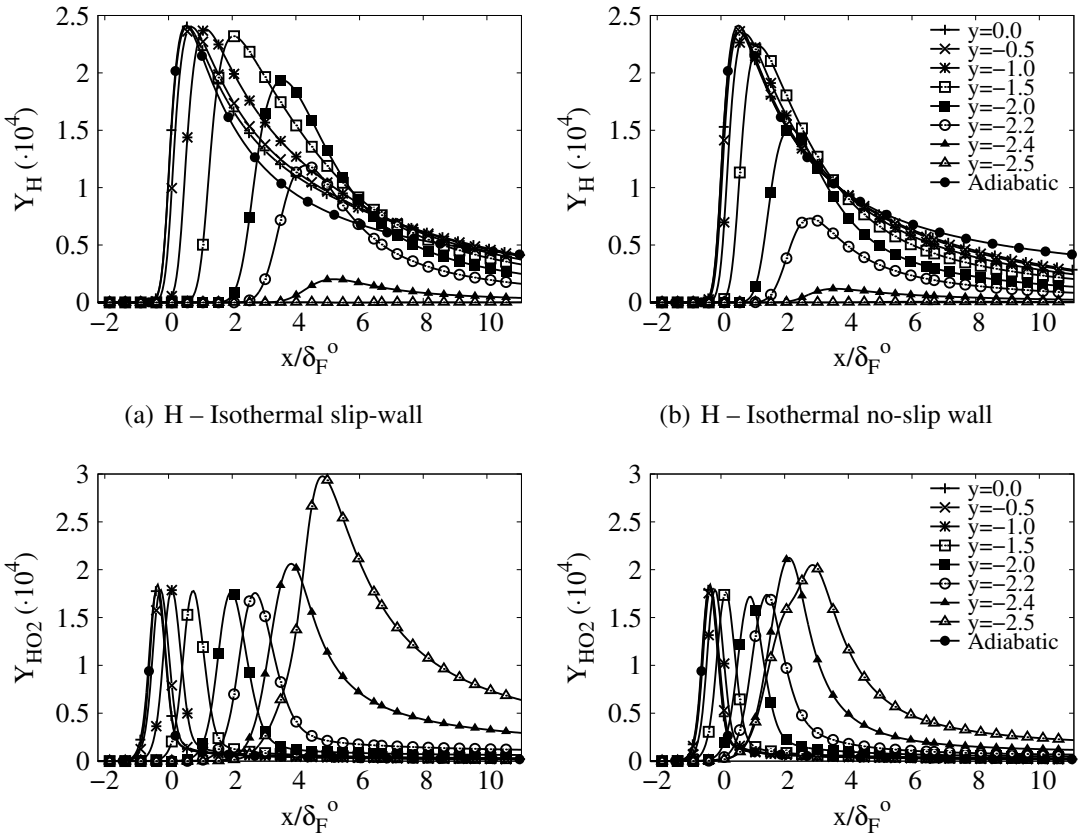

(a) H – Isothermal slip-wall

(b) H – Isothermal no-slip wall

(c) HO_2 – Isothermal slip-wall

(d) HO_2 – Isothermal no-slip wall

Figure 4.9: Streamwise distribution of species mass fractions at various spanwise y locations.

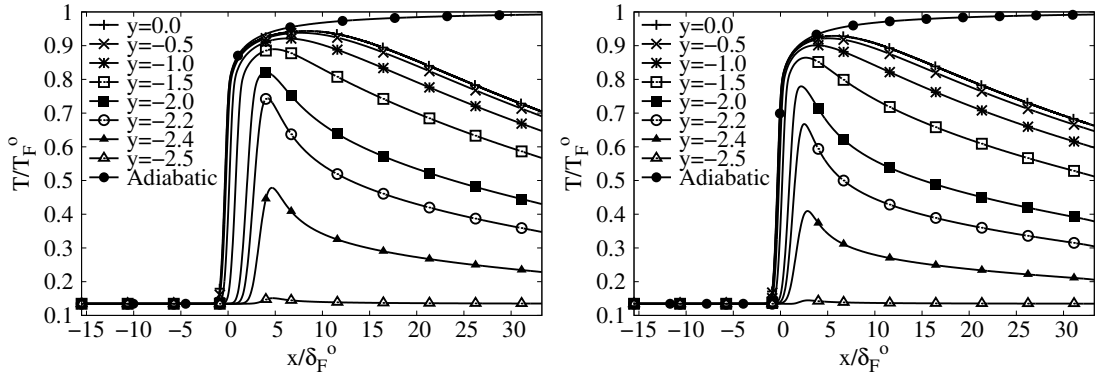

(a) Isothermal slip-wall

(b) Isothermal no-slip wall

Figure 4.10: Temperature distribution at various spanwise y locations.

4.5 Thermal coupling influence

4.5.1 Heat transfer at the wall

Temperatures much higher than 300 K are observed in the wall heated by the flame (figure 4.11). In the burnt gases, the temperature gradient in the wall normal direction drops significantly (figure 4.12(a)). Consequently, the heat flux at the wall decreases by a factor 1.5 compared to the isothermal no-slip case (table 4.1), making the edge of the flame close to the wall more robust. Besides, the temperature distribution inside the wall is non-uniform in the transverse direction (figure 4.11). Thus a fully multi-dimensional temperature field is obtained for a quartz channel under the present dimensions. Considering the strong influence of the wall temperature on the flame behaviour, the variation of more that 50 K, which is observed in figure 4.11, can hardly be neglected, as it would in the hypothesis of a one-dimensional wall featuring heat transfer in the longitudinal direction only. In this direction, the heat diffuses inside the quartz wall well upstream of the flame location, over a length of the order of 20 mm $\approx 45\delta_F^o$ (figure 4.11(b)). This promotes the development of a thermal boundary layer upstream of the flame, which spreads over more than half of the computational domain in the direction normal to the wall (figure 4.12(b)). The fresh gases flowing close to the wall are therefore now preheated before entering the reaction zone (figure 4.12(a)). This preheating effect does not significantly impacts the centreline of the channel, before the flame.

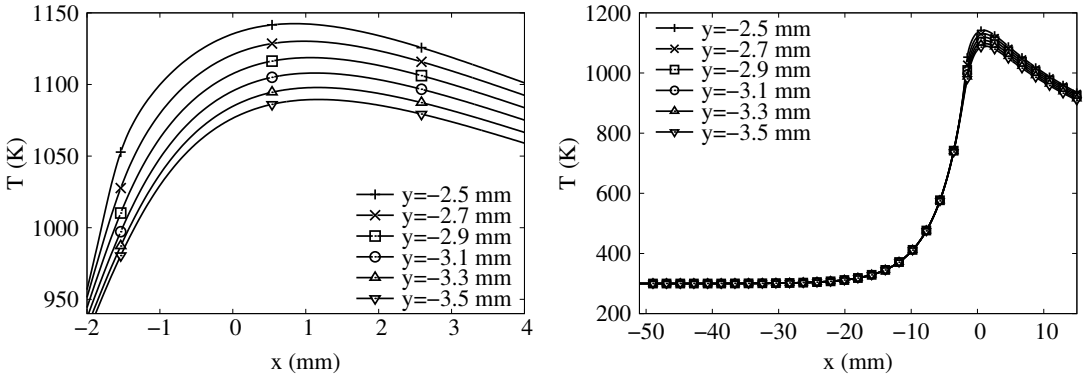

(a) Close to maximum temperature

(b) Full domain

Figure 4.11: Temperature distribution in the quartz wall *vs* x position for various y locations.

Further, because of the reduction of the heat flux at the wall, the decay of the temperature in the burnt gases along the centreline is reduced compared to the isothermal wall condition (see figure 4.3(a) for $x > 20\delta_F^o$). These heat transfers provoke a drastic change in the shape of the flame (shapes comparisons in figure 4.4). The edge-flame propagates faster close to the wall and the flame surface features an inflection point. A flame shape which is inverted compared to the isothermal case, with its trailing part now on the axis of symmetry (figure 4.13). The flame which was convex toward the fresh gases on the centreline (so-called mushroom flame) with the isothermal wall condition, becomes concave (tulip flame). As exposed by Choi *et al.* [21] about

concave flame fronts, the burning rate is enhanced in the curved flame close to the centreline (figure 4.3(b)). In addition, because of the reduction in heat flux at the wall, the burning rate stays above the one of the two isothermal cases up to the length of 2.6 mm over the flame surface, and always above the burning rate of the no-slip isothermal case (figure 4.3(b)).

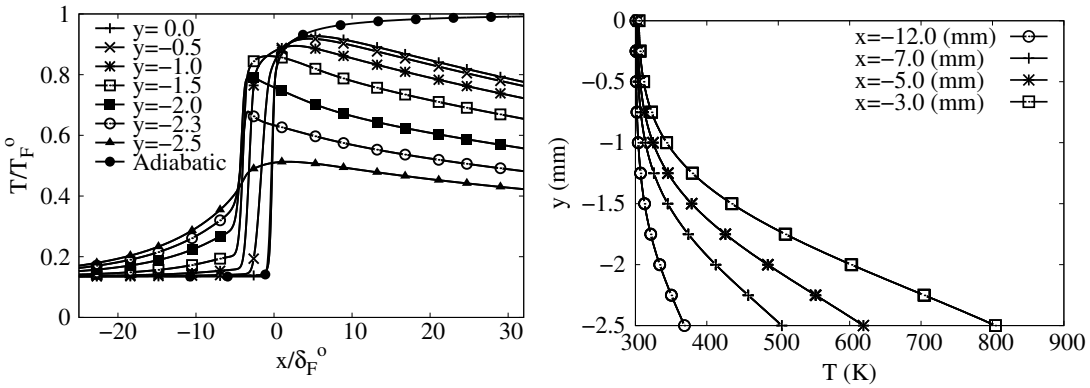

(a) Streamwise (flame at $x = 0$)

(b) Spanwise (wall at $y = -2.5$ mm)

Figure 4.12: Temperature distributions in the gas at various x and y positions. Heat conductive wall case.

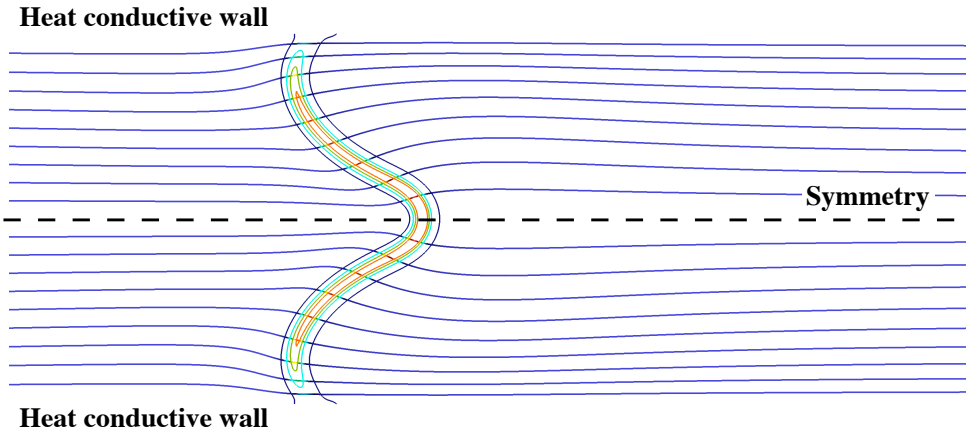

Figure 4.13: Quartz heat conductive wall (symmetric view). Streamlines and flame with contours of 10, 30, 50 and 70% of $\max(\dot{\omega}_{\rho E})$.

4.5.2 Flow deviation

Near the axis of symmetry upstream of the reaction zone, the flame shape implies the deviation of the streamlines toward the centre of the channel (figure 4.13). As discussed above, the fluid is mainly accelerated in the normal direction to the local flame surface, which is now not aligned with the centreline, leading to an increase of the transverse velocity component toward the wall (figure 4.14). This induces a decay of the streamwise velocity right after its first peak (figure 4.15). Upstream of the flame, at $x_{\text{fg}} = -15\delta_{\text{F}}^{\text{o}}$, this centreline velocity is $1.98 S_{\text{L}}^{\text{o}}$,

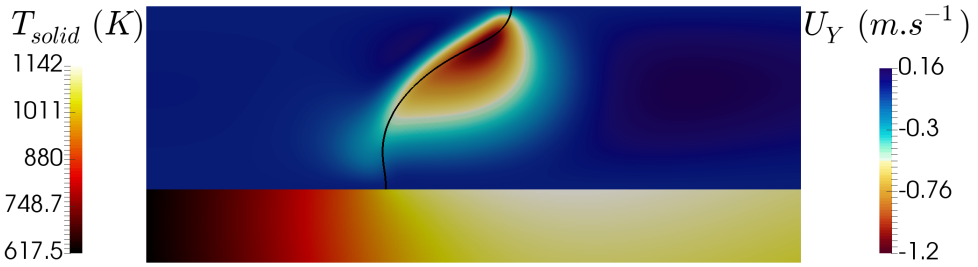

Figure 4.14: Top: transverse (spanwise) fluid velocity component (black line: iso-c = 0.7). Bottom: temperature distribution in the quartz wall.

while the inlet bulk flame velocity with the heat conductive wall is $1.22S_{\mathrm{L}}^{\mathrm{o}}$ (table 4.1), thus with a centreline velocity of $1.22\times(3/2)S_{\mathrm{L}}^{\mathrm{o}}$ = $1.83S_{\mathrm{L}}^{\mathrm{o}}$ in the inlet Poiseuille flow. This slight acceleration well before the flame, from $1.83S_{\mathrm{L}}^{\mathrm{o}}$ to $1.98S_{\mathrm{L}}^{\mathrm{o}}$, results from the flow dilatation within the thermal boundary layer. An acceleration which is in fact visible in figure 4.15 for $x/\delta_{\mathrm{F}}^{\mathrm{o}} \in [-15, -7]$ (see also line with triangle in figure 4.5), through the positive slope in the axial velocity before the strong velocity jump across the reaction zone. Hence, the coupling with wall heat transfer modifies dramatically the landscape, through a profound re-organisation of the variable density flow and the propagating flame. This combination of the heat loss reduction at the edge-flame close to the wall and in the burnt gases, with the preheating of the fresh gases by heat conduction in the wall, results in a burning velocity 28% larger than in the no-slip isothermal case (table 4.1).

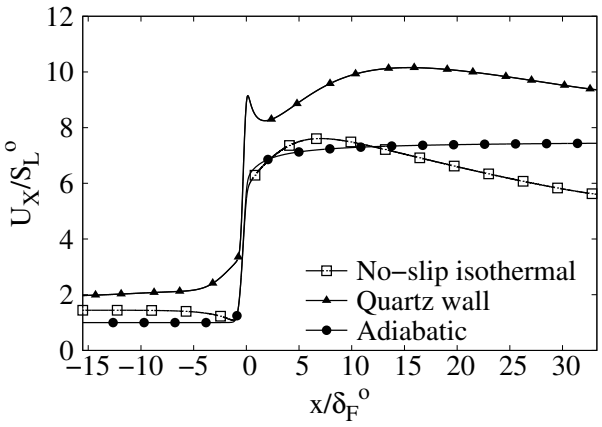

Figure 4.15: Streamwise velocity component along the axis of symmetry.

4.5.3 Energy budget on the thermally coupled flame

The present objective is to further examine the acceleration upstream of the flame, finally to capture how this process impacts the flow dynamics. To do so, in the numerical simulation, the enthalpy budget between the channel inlet at $x = x_{\mathrm{min}}$ (ρ_{o}, T_{o}, $C_{p,\mathrm{o}}$ and $S_{\mathrm{L}} = \dot{Q}_{\mathrm{m}}/(\rho_o A)$) and

the position $x_{\rm fg} = -15\delta^{\rm o}_{\rm F}$ upstream of the flame as previously defined, may be written

$$\rho_{\rm o} S_{\rm L} \Sigma^{\rm o}_{\rm F} C_{p,{\rm o}} T_{\rm o} - \int_{-\ell_{\rm i}/2}^{0} \left[\rho u C_p T\right](x_{\rm fg}, y) dy + \dot{\phi}(x_{\rm fg}) + \dot{q}^{\rm o}_{\rm w} = 0\,, \tag{4.4}$$

where $\Sigma^{\rm o}_{\rm F} = \ell_{\rm i}/2$ is the adiabatic flame length as above and $\dot{q}^{\rm o}_{\rm w}$ and $\dot{\phi}(x_{\rm fg})$ are, respectively, the diffusive heat flux at the wall, and, across a channel section just before the flame (see figure 4.16).

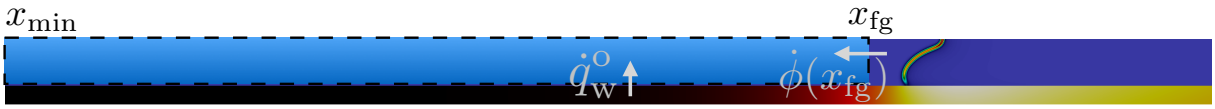

Figure 4.16: Domain for the enthalpy budget in equation 4.4.

These additional diffusive fluxes can be written,

$$\dot{q}^{\rm o}_{\rm w} = -\int_{x_{\rm min}}^{x_{\rm fg}} \left[\lambda_{\rm f} \frac{\partial T(x, -\ell_{\rm i}/2)}{\partial y}\right] dx\,, \tag{4.5}$$

$$\dot{\phi}(x_{\rm fg}) = \int_{-\ell_{\rm i}/2}^{0} \left[\lambda_{\rm f} \frac{\partial T(x_{\rm fg}, y)}{\partial x}\right] dy\,. \tag{4.6}$$

The relation (4.4) may be re-organised in

$$\dot{q}^{\rm o}_{\rm w} = u^+(x_{\rm fg}) \int_{-\ell_{\rm i}/2}^{0} \left[\rho C_p T\right](x_{\rm fg}, y) dy - \rho_{\rm o} S_{\rm L} \Sigma^{\rm o}_{\rm F} C_{p,{\rm o}} T_{\rm o} - \dot{\phi}(x_{\rm fg})\,, \tag{4.7}$$

or

$$\dot{q}^{\rm o}_{\rm w} = T^+(x_{\rm fg}) \int_{-\ell_{\rm i}/2}^{0} \left[\rho u C_p\right](x_{\rm fg}, y) dy - \rho_{\rm o} S_{\rm L} \Sigma^{\rm o}_{\rm F} C_{p,{\rm o}} T_{\rm o} - \dot{\phi}(x_{\rm fg})\,, \tag{4.8}$$

with $u^+(x)$ and $T^+(x)$ defined as spanwise weighted averages of velocity and temperature,

$$\int_{-\ell_{\rm i}/2}^{0} \left[\rho u C_p T\right](x, y) dy = u^+(x) \int_{-\ell_{\rm i}/2}^{0} \left[\rho C_p T\right](x, y) dy = T^+(x) \int_{-\ell_{\rm i}/2}^{0} \left[\rho u C_p\right](x, y) dy\,. \tag{4.9}$$

In the simulation, the relation $(3/2)u^+(x_{\rm fg}) = 1.98 S^{\rm o}_{\rm L}$ is verified as in a Poiseuille flow. Where $1.98 S^{\rm o}_{\rm L}$ is the accelerated centreline velocity discussed above, suggesting that u^+ behaves as an equivalent Poiseuille channel flow bulk velocity. Further assuming a low Mach number flow

with a constant background pressure in the fresh gases, $\rho_o T_o = \rho T$, and a constant heat capacity, $C_p = C_{p,o}$, the relations (4.7 and 4.8) become

$$\frac{u^+(x_{fg}) - S_L}{S_L} = \frac{T^+ - T_o}{T_o} = \frac{\dot{q}_w^o + \dot{\phi}(x_{fg})}{\rho_o S_L \Sigma_F^o C_{p,o} T_o} \,. \tag{4.10}$$

The equations (4.10) and (4.1) may be combined to express the coupling between heat transfer and the flow velocity upstream of the flame

$$u^+(x_{fg}) = S_L^o \left(\frac{\Sigma_F}{\Sigma_F^o} \overbrace{\left(1 - \frac{k_w}{(\dot{Q}_m/A) C_{p,o}} \right)}^{(i)} + \underbrace{\frac{\dot{q}_w^o + \dot{\phi}(x_{fg})}{\rho_o S_L^o \Sigma_F^o C_{p,o} T_o}}_{(ii)} \right) . \tag{4.11}$$

The term (i) represents the heat extracted to the flame by the wall in the zone of the burnt gases, while the term (ii) informs on the heat that is transferred to the fresh gases by the wall ($\dot{q}_w^o$) and by the flame ($\dot{\phi}(x_{fg})$). The conductive flux in the wall connects these heat transfers, leading to the observed fluid acceleration upstream of the reactive front. The relative variations of the normalised velocity and temperature of the relation (4.10) differ by only 0.95% in the simulation, with u^+ and T^+ computed from the relation (4.9). This confirms the almost isobaric behaviour of the heated flow of fresh gases upstream of the flame and the convergence of the coupled fluid/solid simulation. Most of this departure actually comes from the variation of C_p, whose average over the channel sections evolves by 1.5% between the inlet and x_{fg}.

4.5.4 Kinetics

In chapter 3, is was pointed out that the response of the low temperature chemistry observed in the simulations close to wall can easily be questioned in terms of accuracy of the chemical kinetics prediction. Still, some global behaviour may be underlined. Intermediate hydrocarbon radicals, such as CH_3O, which accumulates close to a cold wall, completely vanish in the presence of a hot conductive wall (figure 4.17(a)). Similarly, the increased temperature close to the wall promotes OH concentrations higher than in the isothermal case (compare figures 4.17(b) and 4.17(c)). This observation relates to temperature levels which, in the heat conductive wall case, are large enough for triggering some of the reactions with high activation energies typically controlling the OH radical production. The following reactions stand for OH production (see 15S-26R scheme in table 3.3),

	Reaction	E_a
2	$O+CH_4 \leftrightharpoons OH+CH_3$	8691
7	$H+O_2 \leftrightharpoons O+OH$	14475
8	$H+HO_2 \leftrightharpoons 2OH$	640
13	$H+CH_3O \leftrightharpoons OH+CH_3$	0
20	$HO_2+CH_3 \leftrightharpoons OH+CH_3O$	0
22	$CH_3+O_2 \leftrightharpoons OH+CH_2O$	8593

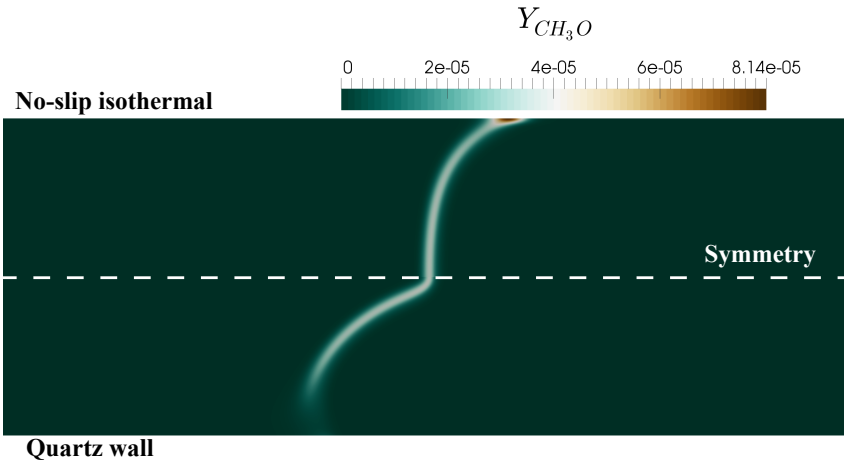

(a) CH_3O mass fraction.

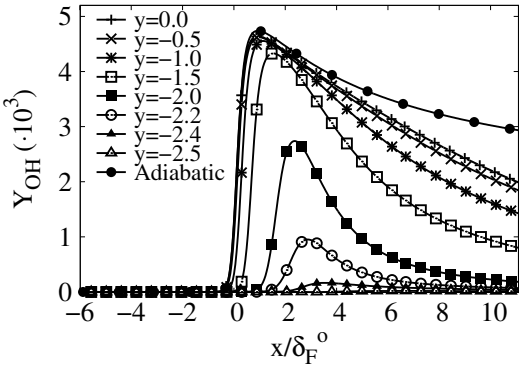

(b) OH isothermal no-slip wall

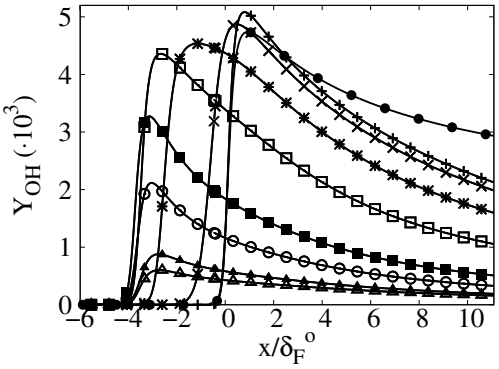

(c) OH heat conductive wall

Figure 4.17: Distributions of CH_3O in the flame zone and streamwise OH profiles at various distances from the axis.

The cold walls prevent from enhancing some of the above reactions (reactions 2, 7 and 22) while the reactions consuming OH are activated in all cases because they depend globally on much lower activation energies (see bellow). Furthermore, some of the OH consumption reactions exhibit negative activation energies, indicating that their direct conversion rate diminishes with the rise in temperature. At the high wall temperatures observed, these reactions are thus further limited.

	Reaction	E_a
14	$OH+H_2 \leftrightharpoons H+H_2O$	3441
15	$2OH \leftrightharpoons O+H_2O$	-2057
16	$OH+HO_2 \leftrightharpoons O_2+H_2O$	-503
17	$OH+CH_4 \leftrightharpoons CH_3+H_2O$	3235
18	$OH+CO \leftrightharpoons H+CO_2$	70
19	$OH+CH_2O \leftrightharpoons HCO+H_2O$	-448

4.6 Flame response to wall heat transfer properties in a regime diagram

The results discussed above have been obtained with either an isothermal wall or a heat conductive wall made of quartz. The channel is also submitted to an outside convective flux representative of natural convection. Important differences have been observed between these wall thermal conditions, both in terms of flame shape and burning velocity. To further investigate the effect of heat transfers, the conductivity of heat in the wall λ and h_o, the convective heat transfer coefficient with the surrounding air, are now varied. Fifteen simulations have been performed varying the ratio λ/λ_{quartz} between 0.2 and 50. This ratio is applied to the conductivity of quartz [102], in order to mimic the change in material, however keeping the same normalized response of λ versus temperature (figure 2.10(a)). The convective heat transfer coefficient h_o ranges between 30 W.m^{-2}.K^{-1} and 225 W.m^{-2}.K^{-1}, plus two extreme cases at 300 W.m^{-2}.K^{-1} and 1500 W.m^{-2}.K^{-1}, which have been added to approach the asymptotic limit of very intense heat convection on the outside surface of the channel (figure 4.18). Even though unrealistic in practice, these additional cases are useful to better understand the limit regimes of the problem. Please note that in the cases exhibiting a high thermal conductivity λ, a zero temperature gradient in the solid at the inlet could not be obtained, due to the very long thermal penetration length related. In these cases, the preheating of the reactants depends thus on the upstream channel length, which would also be the case in reality. One may note that the upstream length is 5.1 cm in the present case.

4.6.1 Asymptotic behaviours

In a plane defined by (λ, h_o), four asymptotic behaviours can be anticipated, which are recovered in the simulations:

- (i) In the case of $\lambda \to 0$, the flux of heat in the wall vanishes and an adiabatic flame develops whatever the value of h_o. Therefore for small value of λ, almost flat flames are expected. This is what is observed in figure 4.18(a) and (h) when decreasing λ by a factor 5 ($\lambda/\lambda_{quartz} = 0.2$). For h_o set at 150 W.m^{-2}.K^{-1}, a small deviation from the adiabatic case is observed with a convex flame. For a smaller h_o level, a larger temperature gradient develops in the solid, and a slightly concave-shaped flame appears (figure 4.18(a)).

- (ii) For very weak levels of the convective flux, $h_o \to 0$, the outside surface of the wall is insulated and all of the heat transferred to the wall propagates in the solid in the longitudinal direction, downstream and upstream of the flame. The fresh gases collect heat, increase their temperature leading to a rise of the flame speed compared to the adiabatic case. This acceleration proceeds up to the point where a new balance is found between the upstream conduction of the heat extracted from the burnt gases, the preheating of the fresh gases and the amount of heat released by the flame. The flame shape should therefore be very similar to the one reported above for a quartz wall with heat transfer, with a flame speed measured above the adiabatic value S_L^o. Starting from λ_{quartz} (figure 4.18(b)),

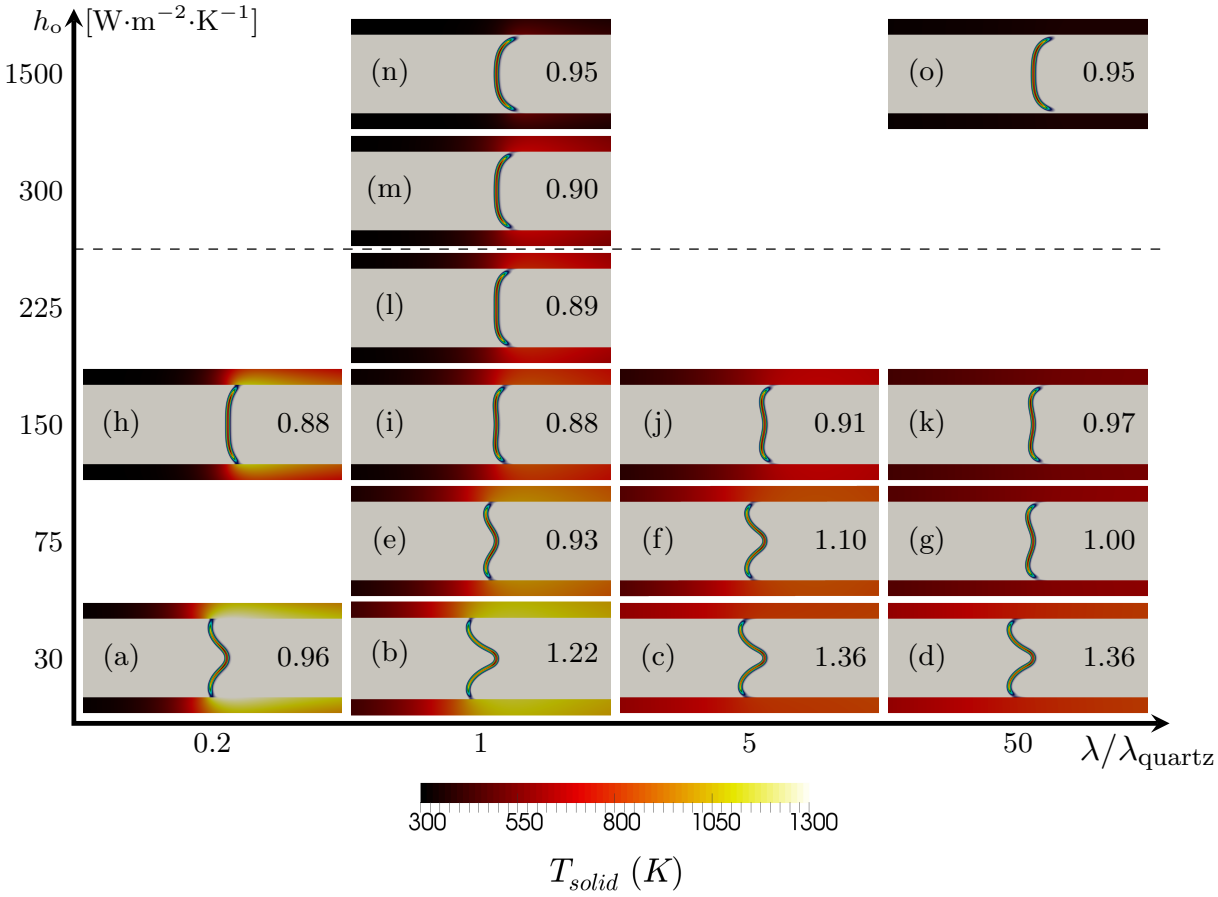

Figure 4.18: Flame response to heat transfer properties. h_o: heat transfer coefficient with surrounding air. λ: thermal conductivity of channel wall. S_L/S_L^o indicated in the graphs. Conditions above dashed line are unrealistic in practice.

two of such cases are in figures 4.18(c) and 4.18(d) for $h_o = 30$ W.m^{-2}.K^{-1} with λ increased by the factors 5 and 50. The flame shape is unchanged and the flame speed indeed increases with the rate of heat transfer in the wall. However, a smaller value of λ limits the diffusion of heat in the wall and the flame speed decreases, even below S_L^o for $\lambda/\lambda_{quartz} = 0.2$ (figure 4.18(a)).

- (iii) A wall with a very large level of conductivity, $\lambda \to \infty$, will behave as isothermal, with an almost uniform temperature in the solid. A temperature whose level varies according to the convective heat transfer coefficient. For small values of h_o, the wall will be isothermal and hot. For larger values of h_o, an isothermal cold wall type flame with a convex shape is expected. The flame speed should also decrease with the increase of the level of heat extracted over the outside surface of the wall. This is confirmed in figure 4.18(d), 4.18(g), 4.18(k) and 4.18(o), when h_o varies from 30 W.m^{-2}.K^{-1} to 1500 W.m^{-2}.K^{-1}, for $\lambda/\lambda_{quartz} = 50$. The flame speed diminishes from $1.36S_L^o$ (case d) to $0.95S_L^o$ (case o), with the amplification of the outside convective heat transfer h_o. The flame shape is convex, as in the cold wall case, for the largest value of h_o. Decreasing h_o, the edge-flame close to

the wall is submitted to a smaller heat flux and it progressively moves upstream, up to the apparition of the flame shape with an inflexion point (figure 4.18(d)), typical of a flame propagating in a boundary layer with both convective and conductive heat transfer in the wall.

- (iv) For very large values of h_o whatever λ, the heat is directly transferred to the ambient, the wall gets cold, and the flame is of convex shape. Finally, the flame speed falls to $0.95S_L^o$, as seen in figure 4.18(n) and 4.18(o) for $h_o = 1500$W.m^{-2}.K^{-1}, λ_{quartz} and 50 λ_{quartz}. Note that these extreme cases coherently almost permit the recover the isothermal cold no-slip wall simulation results of figure 4.2(b), which exhibited a $0.96S_L^o$ flame velocity and similar flame topology.

4.6.2 Competition of the influence of conductivity and convection on the flame characteristics

Overall, the burning velocity S_L increases with λ, the conductivity in the wall, and S_L decreases with an increase of h_o, the convective heat transfer coefficient (figure 4.18). Still, these general trends may not be verified for the extreme values of h_o (see for instance figure 4.18(m) and 4.18(n)). For these high levels of h_o, the flame propagates in the vicinity of an almost cold wall, with a pronounced lengthening of the edge-flame because of quenching. A lengthening of the flame surface that is followed by an increase of the burning velocity. Similarly, for $h_o = 75$ W.m^{-2}.K^{-1}, when moving from $5\lambda_{quartz}$ (figure 4.18(f)) to $50\lambda_{quartz}$ (figure 4.18(g)), the burning velocity decreases even though heat conductivity in the wall has been enhanced. Here, the wall becomes close to isothermal and is thus efficiently cooled by the ambient. The resulting disappearance of the inflexion point in the flame shape leads to an almost planar flame, with a reduced burning velocity. Nevertheless, still looking at this case (figure 4.18(g)), but against others at the same value of λ, the expected decay of the burning velocity when h_o increases is found. Once again, these alterations of the global trends point out the intricate coupling existing between the flame dynamics and its topology. It is consequently hopeless to expect monotonic response of flame velocity with thermal characteristics. Multi-dimensional simulations, able to capture the flame topology, are thus required to seize the complete picture.

A diagram of axis (λ, h_o) may be drawn to delineate between the flame regimes observed in the simulations and to provide the global picture summarising this work (figure 4.19). In the limit of an adiabatic wall, the flames are planar and feature the properties of a one-dimensional reactive front. For small levels of convective heat transfer over the external surface of the channel, the increase of the heat conductivity in the solid wall accelerates the edge-flame at the wall leaving the centreline reaction zone behind. The flame front then becomes concave toward fresh gases on the axis of symmetry and globally propagates faster than the stoichiometric laminar burning velocity. Progressively increasing the heat loss at the wall through convection with ambient air, the propagation speed of the reactive front decreases close to the wall and at some point, the flame propagates faster along the centreline than close to the wall and the flame shape becomes convex, with a flame speed smaller than the stoichiometric burning velocity. It

is important to note that figure 4.19 was drawn for the operating conditions studied. The exact location in this diagram where the transition in the flame shape is observed cannot be fully generic, only the asymptotic limits (boundaries of the diagram) should not depend too much on the flow parameters.

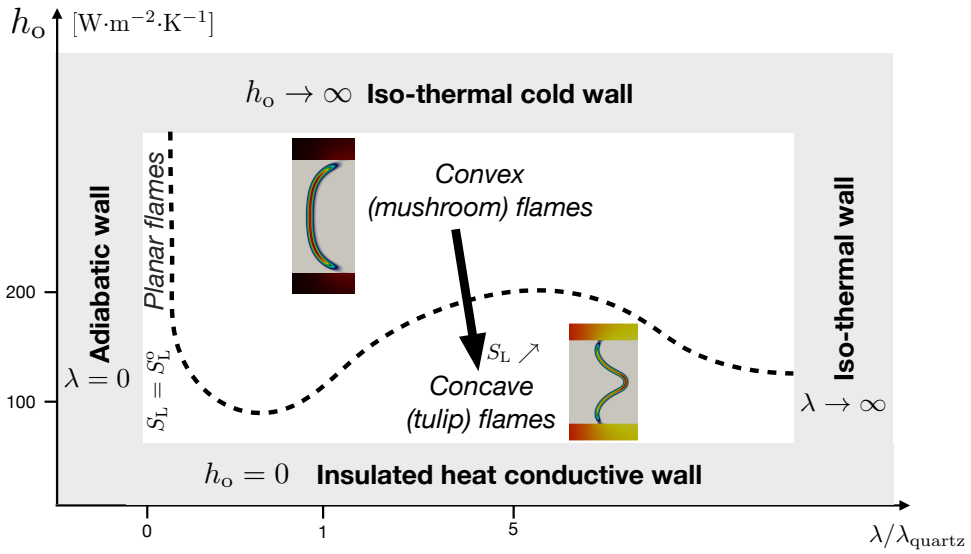

Figure 4.19: Diagram summarising the flame shape behaviour versus wall heat transfer parameters. λ: wall conductivity. h_o: coefficient of convective heat transfer with outside environment. Internal channel height: 5 mm. Wall thickness: 1 mm. Stoichiometric CH_4/air flame.

These results consolidate previously published findings on flame propagation in narrow channels, based on both experimental and numerical works, and the knowledge of these regimes may be of precious help in the design of small-scale combustion devices.

Chapter 5

Simulating upstream flame propagation in a narrow channel after wall preheating under microgravity

Contents

5.1 Introduction 108

5.2 Configuration 109

5.2.1 Numerics 109

5.2.2 Heating scenario 110

5.3 Downstream movement by fresh gases dilatation 113

5.4 Flame acceleration from convective heat transfer 114

5.5 Flame translation and final position 116

5.1 Introduction

In this chapter, the response of a stoichiometric premixed laminar flame, stabilised in a narrow channel ($\ell_i = 5$ mm), is investigated for an amount of heat supplied upstream through the wall. The stoichiometric methane/air flame numerical simulations performed include complex molecular transport and the fully coupled solving of heat transfer at and within the wall. Initially, the flame is stabilised by an inlet mass flow rate matching the flame burning velocity. This numerical study is inspired by the experiments conducted by A. Pieyre and F. Richecoeur (EM2C lab, UPR 288 CNRS), who observed the response of a flame to an upstream heating. In these experiments (figure 5.1), the flame is initially ignited and stabilised at the channel outlet. The tube is heated with a lighter upstream of the flame position until the flame undergoes a translation to finally stabilise in the heated area. In response to these observations, the objectives of this chapter are to:

- Consider various heating intensities over a given heating time and to observe their effect on flame translation.
- Pay a specific attention on the relative contributions, of heat convection in the flow and heat conduction in the solid, on the translation.
- Depict and analyse the various stages followed by the flame during its translation.
- Track the shape, the flash back speed and the final position of the flame with respect to the amplitude of the heat flux brought to the external surface of the wall.

First, section 5.2 presents in details the configuration under study along with the specific numerics associated. Section 5.3 depicts the first step of the flame translation, a downstream movement due to the fresh gases dilatation responding to the preheating. The role of heat convection, on flame translation, in then revealed in section 5.4. Finally, section 5.5 gathers the flame evolution in the case leading to a complete translation up to the heated area. Along with the kinetic reduction strategy for small-scale combustion presented in chapter 3, the major part of this chapter was published in the *Combustion and Flame* journal in 2019 [9].

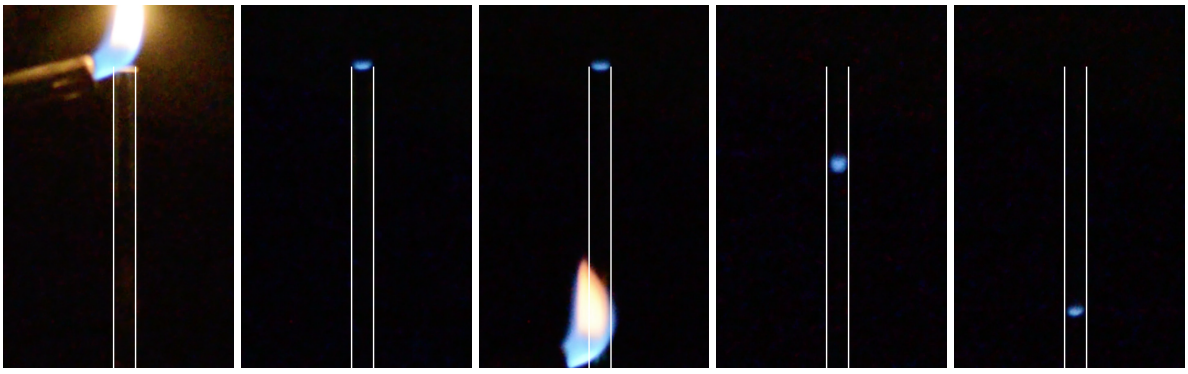

(a) Ignition (b) Initial (c) Heating (d) Translation (e) Final

Figure 5.1: Main stages of flame translation, after wall preheating, in an experimental demonstration of A. Pieyre and F. Richecoeur.

5.2 Configuration

5.2.1 Numerics

In this chapter, a focus is made on the transient states observed when an excess of energy is supplied through the walls of a channel to the fresh gases, upstream of the position of a stabilised premixed flame. The application of this punctual thermal forcing allows for stabilising the flame at a desired position, typically optimised for receiving the excess of enthalpy. Numerical

solutions of a methane/air stoichiometric premixed flame stabilised in a narrow channel are performed for complex transport properties and chemistry. The multi-component flow simulation is coupled with the solving of heat transfer at and within the solid wall.

Concerning the solid modelling, a de-synchronisation method is employed, traduced by the reduction of the heat capacity within the wall. As pointed out in § 2.4.1.5, the modification of the heat capacity does not impact steady state solutions. While employing such an artifice, the normalised heat capacity in the solid $C_s(T)/C_s(T_o)$ also varies with temperature following the typical response of quartz. Presently, as in the study by Gauthier *et al.* [43], $C_s(T_o)$ in the solid is of the order of 0.01 kJ.kg^{-1}.K^{-1}, a value which is smaller than for quartz in order to limit the CPU cost by reducing the gap between the characteristic times of heat transfer in the solid and in the gas. In the present unsteady study this sensitive point will be analysed below, to conclude that it does not impair the physical observations. Indeed, the upstream flame movement is found to be triggered by heat convection in the flow and not by the unsteady wall heating close to the flame zone, even under such large values of the wall heat diffusivity ($\lambda_s/\rho_s C_s$).

Flash-back simulations are now conducted with the 17S-53R-1.0 mechanism, validated in chapter 3. Because of the channel dimensions, the close to unity Lewis number of the mixture and the absence of gravity, the problem may be assumed symmetrical with respect to the longitudinal mid-plane ($y = 0$) [43, 85]. The bulk velocity of the incoming Poiseuille velocity profile which stabilises the initial flame is $S_L = 52.79$ cm.s^{-1} (see figure 3.6). To obtain this initial stabilised channel flame, a series of simulations were performed where the flow is initialised with an adiabatic flame, to then progressively relax toward the fully coupled flame/wall solution. During this process, the inlet mass flow rate is adjusted following the procedure in paragraph 2.4.3. As evoked in the previous chapter, the initial curved flame features a burning flame surface larger than the channel section and propagates faster than an adiabatic flame (adiabatic flame speed of the order of 38 cm.s^{-1}).

5.2.2 Heating scenario

Starting from the stable flame (figure 3.6), a source of energy is applied over the external surface of the wall, upstream of the reaction zone. The heating power is calibrated to be representative of an energy deposition from an embedded low power source, with the maximum energy deposition ranging from 10% to 40% of the energy released by the flame. The evolution of the incoming heat flux is given in figure 5.2 showing the ratio (in %) between Q_{heating}, the integral over the external wall surface of the added heat flux, and Q_{flame}, the integral over the computational domain of the heat release rate per unit volume. In practice, this is done imposing a variation of $T_{\text{ext}}(x,t)$, the ambient air temperature in the convective and radiative fluxes varying with the stream-wise position, between $T_o = 300$ K and $T_h(t)$, with $T_h(t)$ progressively increasing and decreasing over time (at $t = 0$ the flame is in its initial steady state). For $x < x_1$ and $x > x_2$:

$$T_{\text{ext}}(x,t) = T_o + (T_h(t) - T_o) \times \exp\left(-(x - x_o)^2/(2\sigma_x^2)\right) , \tag{5.1}$$

with $x_o = x_1$ if $x < x_1$ and $x_o = x_2$ if $x > x_2$.

For $x_1 < x < x_2$:

$$T_{\text{ext}}(x,t) = T_{\text{h}}(t)\ , \tag{5.2}$$

with $x_1 = -4$ cm, $x_2 = -3$ cm and $\sigma_x = 0.55$ cm. $T_{\text{h}}(t)$ mimics a gradual imposition of an external energy source. For $t < t_1$ and $t > t_2$:

$$T_{\text{h}}(t) = T_{\text{o}} + (T^\star - T_{\text{o}}) \times \exp\left(-(t-t_{\text{o}})^2/(2\sigma_t^2)\right)\ , \tag{5.3}$$

with $t_{\text{o}} = t_1$ if $t < t_1$ and $t_{\text{o}} = t_2$ if $t > t_2$. For $t_1 < t < t_2$:

$$T_{\text{h}}(t) = T^\star\ , \tag{5.4}$$

with $t_1 = 0.025$ s, $t_2 = 0.375$ s, $\sigma_t = 0.008$ s and $T^\star = 900$ K, 1100 K or 1300 K.

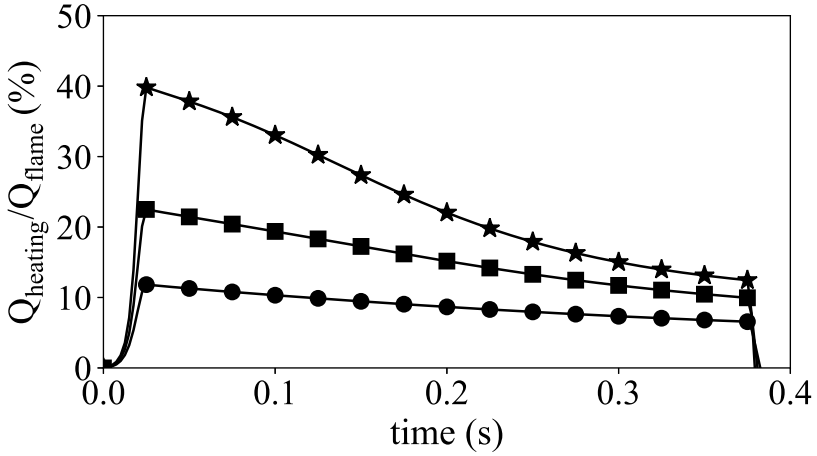

Figure 5.2: Ratio between rate of enthalpy excess introduced and total channel flame power. Star: $T^\star = 1300$ K. Square: $T^\star = 1100$ K. Circle: $T^\star = 900$ K.

The temporal evolution of the flame initially stable in the channel subjected to an external heat source ($T^\star = 1300$ K) is shown in figure 5.3. By gradually transferring heat to the external surface of the wall, the energy diffuses inside the solid and also in the fresh mixture. As shown thereafter, a thermal boundary layer develops up to the channel center, well upstream of the flame. After a transient, the flame moves upstream to become stable again. The overall process may be decomposed in two stages, the flame first moves downstream (figure 5.3, $t = t_{\text{d}} = 65$ ms), to then accelerate and proceed upstream (figure 5.3, $t > t_{\text{d}}$). This flame movement is thus controlled by an intricate coupling between the transfer of heat in the wall by conduction, the subsequent convection of heat in the gas, and finally its impact on the flow and flame dynamics.

During the heating phase, the wall temperature increases in the zone centred at $x = -3.5$ mm up to $t = 375$ ms (figure 5.4). Heating stops at $t = 375$ ms and the maximum wall temperature decreases while the flame reaches the heating location to transfer further heat to the wall, as seen in the line with circle at $x = -1.5$ mm in figure 5.4. The wall temperature goes up again, to recover a distribution similar to the initial one, but shifted upstream (squares and triangles in figure 5.4).

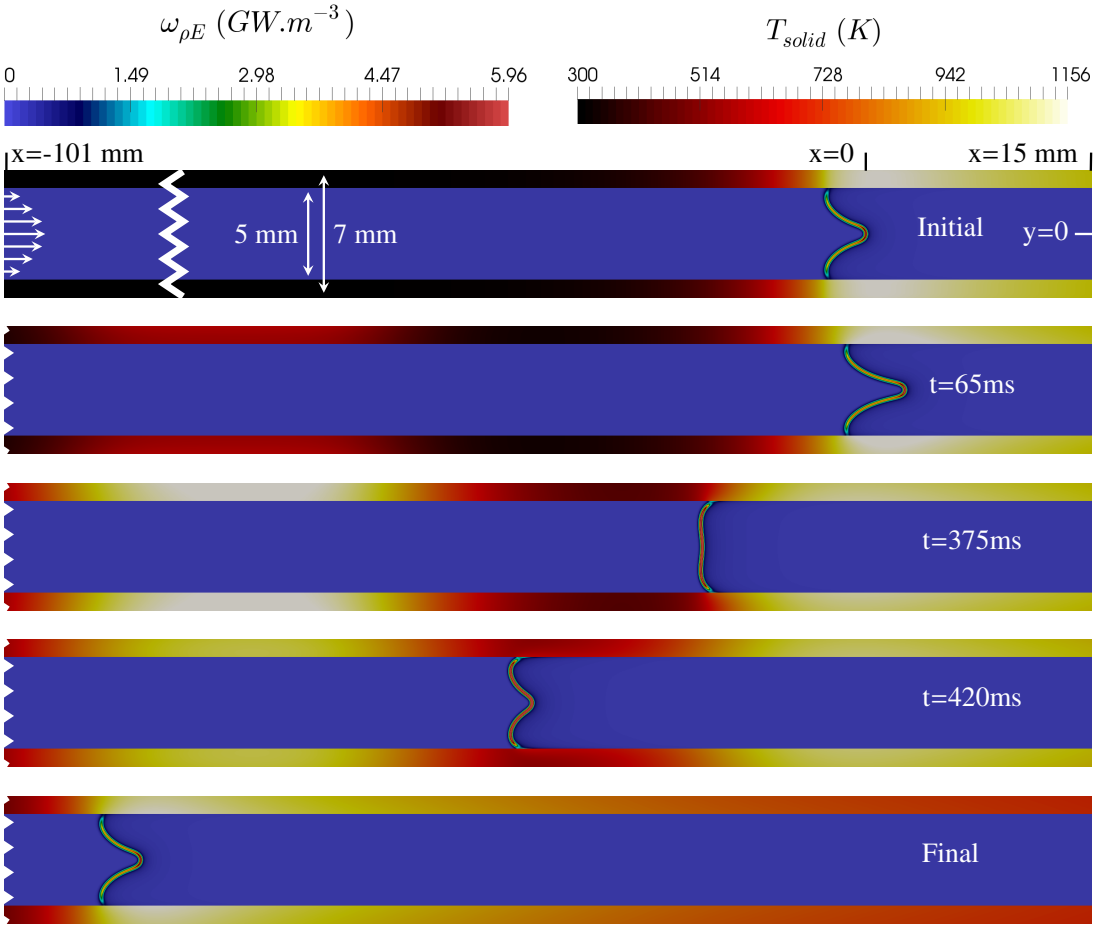

Figure 5.3: Reacting flow configuration. Zoom in relevant flow and wall zones at various stages of the upstream flame propagation. Heat release rate and wall temperature. Case with $T^\star = 1300$ K (equation (5.3)) and 17S-53R-1.0 chemistry (table 3.2).

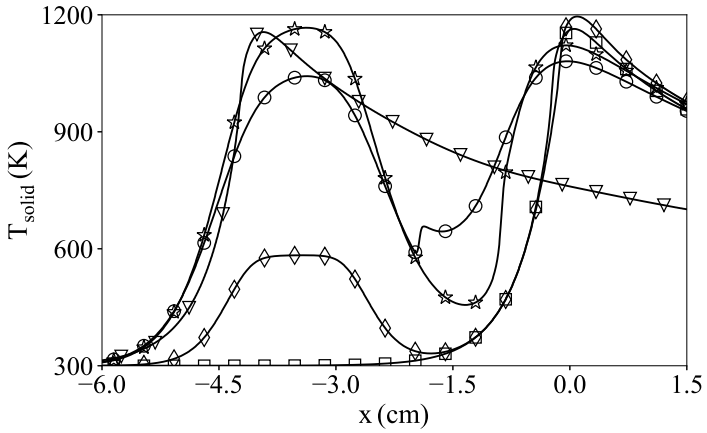

Figure 5.4: Wall temperature profiles at the solid/flow interface, for the various stages depicted in figure 5.3, case with $T^\star = 1300$ K (Eq. (5.3)). Squares: initial stage. Diamonds: $t = t_\mathrm{d} = 65$ ms. Stars: $t = 375$ ms. Circles: $t = 420$ ms. Triangles: final stage.

5.3 Downstream movement by fresh gases dilatation

During the transient, before proceeding upstream, the flame front is pushed downstream (figures 5.3 for $t = 65$ ms and 5.5). The larger the intensity of the heating, the further away and the faster the flame moves downstream of its initial condition, $x = 0.89$ mm at $t_d = 72.5$ ms for $T^\star = 900$ K, $x = 1.44$ mm at $t_d = 70$ ms for $T^\star = 1100$ K and $x = 2.15$ mm at $t_d = 65$ ms for $T^\star = 1300$ K (figure 5.6, stage 2). The change in shape of the flame during the upstream movement also depends on the amount of heat introduced.

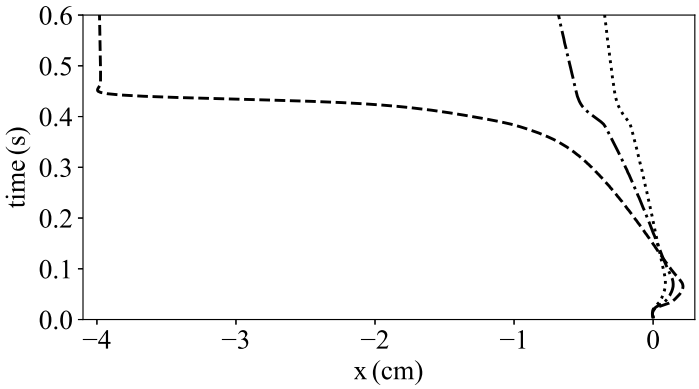

Figure 5.5: Trajectory of the flame position (maximum heat release rate) at the axis of symmetry *vs* time. Dotted line: $T^\star = 900$ K. Dash-dot line: $T^\star = 1100$ K. Dashed line: $T^\star = 1300$ K.

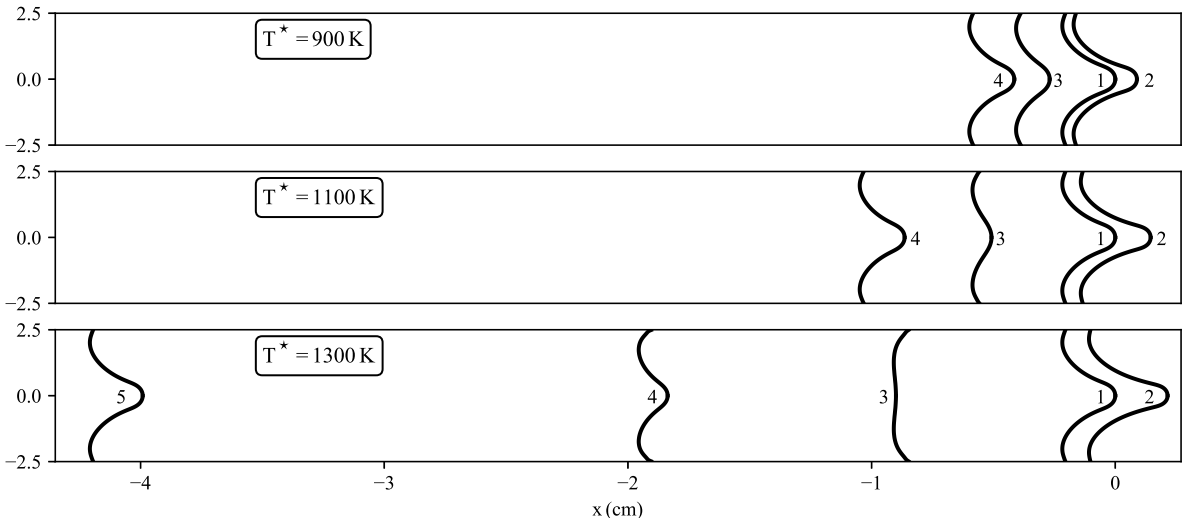

Figure 5.6: Flame shape defined from the maximum heat release rate at key stages of the simulation. $T^\star = 900$ K: (1) initial, (2) $t = t_d = 72.5$ ms, (3) $t = 437.5$ ms, (4) final. $T^\star = 1100$ K: (1) initial, (2) $t = t_d = 70$ ms, (3) $t = 420$ ms, (4) final. $T^\star = 1300$ K: (1) initial, (2) $t = t_d = 65$ ms, (3) $t = 375$ ms, (4) $t = 420$ ms, (5) final.

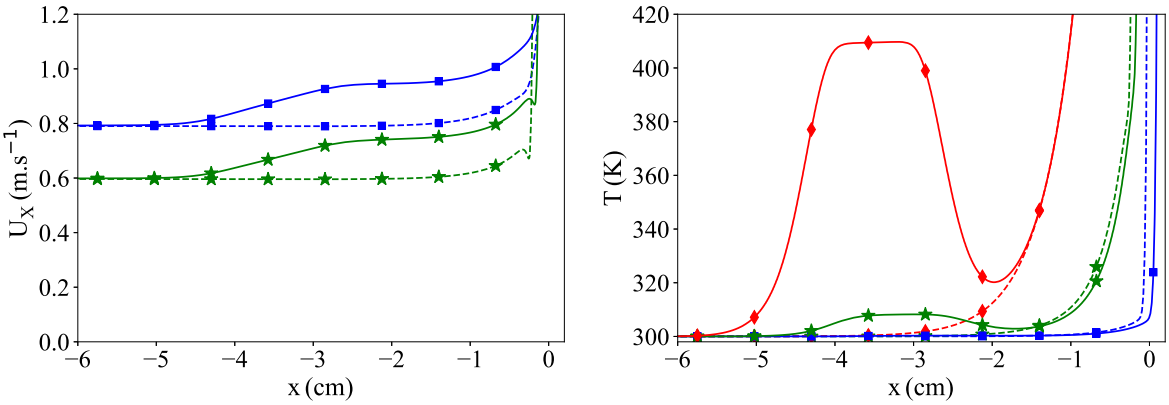

(a) Streamwise velocity

(b) Temperature profiles

Figure 5.7: Streamwise velocity and temperature profiles *vs* x-position. $T^\star = 1300$ K. Dashed line: $t = 0$ ms. Solid line: $t = 35$ ms. Square (blue): $y = 0$ (axis). Star (green): $y = -1.25$ mm. Diamond (red): $y = -2.5$ mm (wall).

In the quasi-isobar thermal boundary layer above the heated wall, the flow density ρ decreases and a dilatation of the fresh gases is generated according to

$$(1/T)DT/Dt = -(1/\rho)D\rho/Dt = \nabla \cdot \mathbf{u}\,, \tag{5.5}$$

where usual notations are used. The acceleration of the flow is in fact visible all over the thermal boundary layer. This is seen in figure 5.7(a), where the stream-wise velocity on the axis of symmetry (blue lines with square) is significantly enhanced well before the flame position after heating the wall (compare the dashed lines, corresponding to $t = 0$ ms, with the solid lines at $t = 35$ ms).

The temperature profiles in figure 5.7(b) confirm that the boost in velocity reaches the flame well before the heat wave. The temperature profiles at $x = -1.5$ cm are not modified while the velocity has already been increased down to the flame location. At the same instant in time, the heat wave is only visible between $x = -5.5$ cm and $x = -1.5$ cm at the wall ($y = -2.5$ mm) and between $x = -4.5$ cm and $x = -1.5$ cm in the plane $y = -1.25$ mm. This flow acceleration due to thermal expansion promotes the first downstream movement of the flame, *i.e.* the downstream shift also observed between the dashed and solid blue lines in figure 5.7(b).

5.4 Flame acceleration from convective heat transfer

After being pushed downstream by the flow dilatation, the flame proceeds upstream. Potentially two scenarios compete. (i) The preheating of the gases reaches the flame, which diminishes the ignition delay, the progression velocity of the reaction zone relative to the fluid increases and the flame propagates upstream. (ii) The diffusion of heat in the solid reaches the flame zone and the edge flame flashes back in the vicinity of the wall.

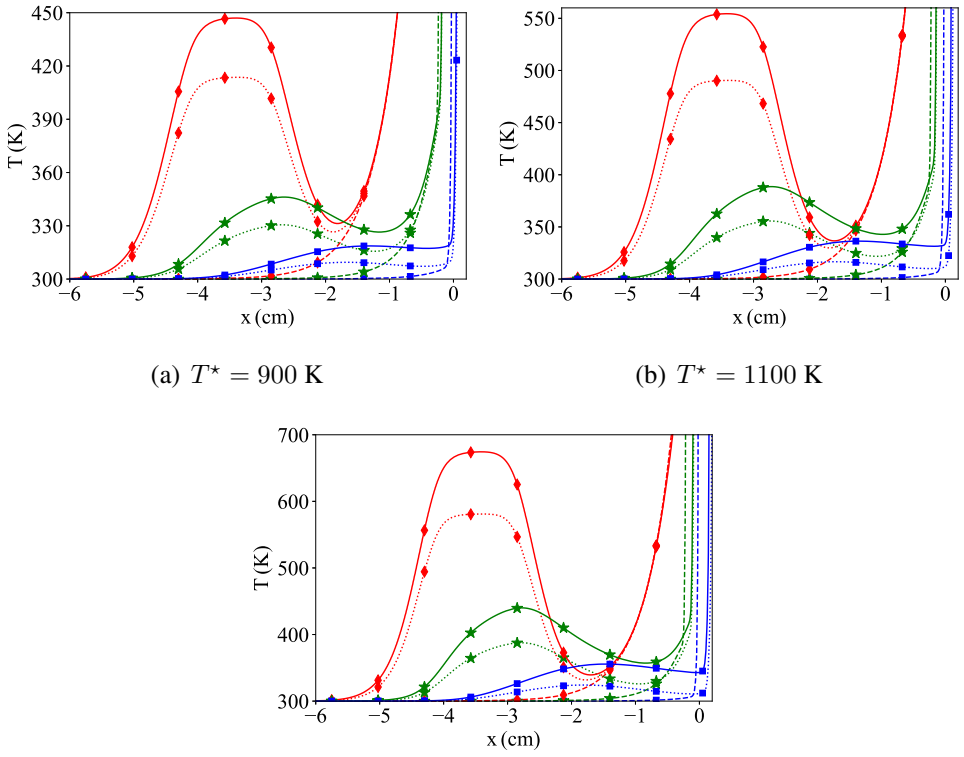

(a) $T^\star = 900$ K

(b) $T^\star = 1100$ K

(c) $T^\star = 1300$ K

Figure 5.8: Streamwise temperature profiles *vs* x-position. Dashed line: $t = 0$ ms. Dotted line: $t = t_\mathrm{d}$. Solid line: $t = t_\mathrm{d} + 20$ ms. t_d: time of the most downstream flame position (differs from case to case). Square (blue): $y = 0$ (axis). Star (green): $y = -1.25$ mm. Diamond (red): $y = -2.5$ mm (wall).

Figure 5.8 shows the temperature distributions at three consecutive instants, the initial time $t = 0$ (dashed line), at the time t_d at which the flame reaches its most downstream position (dotted line), and 20 ms after (solid line). Let us focus first on the temperature at the wall (red line). At these three instants, the edge-flame is located after $x = -1$ cm. Up to $x = -1.5$ cm, thus well upstream of the reaction zone, the three temperature profiles perfectly match, while the temperature increases because of conduction in the wall, but only further upstream ($x < -2$ cm). This is not the case within the channel (blue and green lines), where the temperature increases with time down to the flame front.

Therefore, it is the heat transferred to the flame by convection in the gas that triggers its upstream movement. So, even with a thermal diffusivity of the solid which has been artificially increased as in [43] (keeping the conductivity of quartz) to reduce the CPU time, conduction in the streamwise direction does not prevail over the convection of heat in the fluid in the control of the flash back. Actually, it can reasonably be expected that decreasing the thermal diffusivity of the solid in the simulations would favour even more the role of heat convection.

5.5 Flame translation and final position

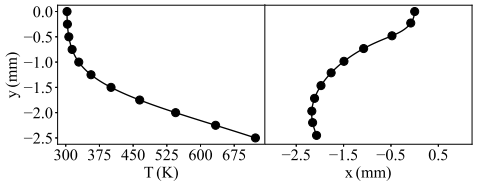

(a) $x = -4.17$ mm, $t = 0$ ms

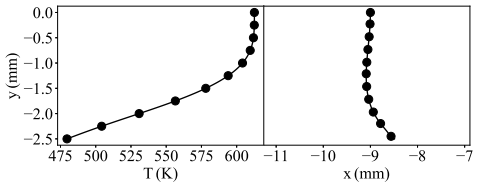

(b) $x = -11.09$ mm, $t = 375$ ms

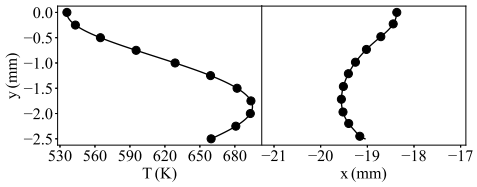

(c) $x = -21.55$ mm, $t = 420$ ms

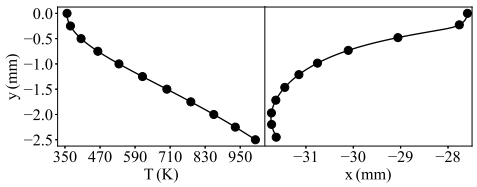

(d) $x = -33.74$ mm, $t = 432.5$ ms

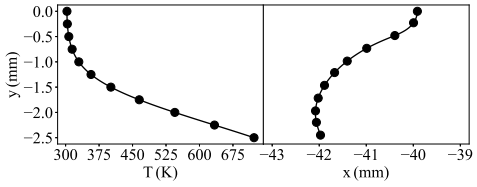

(e) $x = -44.08$ mm, Final

Figure 5.9: Temperature profiles (left) in the fresh gases 5 flame thickness upstream of the flame position (max heat release rate) and corresponding flame shape (right). $T^\star = 1300$ K (equations (5.3) and (5.4)).

For the heating characteristic times given in paragraph 5.2.2, only $T^\star = 1300$ K secures the full flash back of the flame up to the heating zone. Therefore the upstream translation of the flame occurs for Q_{heating} peaking at $0.4Q_{\text{flame}}$ (figures 5.2 and 5.5). Both other cases result in an

upstream movement of the flame, which then stabilises around $x = -4$ mm for $T^\star = 900$ K and $x = -9$ mm for $T^\star = 1100$ K (figures 5.5 and 5.6).

Interestingly, the flame shape strongly evolves during its upstream movement. Figure 5.9 shows both temperature profiles taken in the fresh gases at a stream-wise position located 5 thermal flame thickness before the most upstream position along the flame shape, and the flame shape probed from the maximum heat release rate for every span-wise locations. Starting from the initial stable flame condition (figure 5.9(a)), the temperature first increases mostly in the centreline due to heat convection (figure 5.9(b)). The flame thus evolves toward a mushroom shape with its most upstream point on the axis of symmetry (figure 5.9(b)). This shape is kept by the reaction zone during the flash back, till it approaches the zone of the wall which is heated. There, the temperature gets higher close to the wall, the burning rate and the local flame speed increase promoting the development of the inflexion point already seen in the initially stable flame (figure 5.9(c)). Later in time, the flame tends toward its initial shape with the temperature distribution in the direction normal to the wall featuring those typical of a thermal boundary layer (figure 5.9(d)). Finally, the flame stabilises at a new location and relaxes toward its initial shape (figure 5.9(e)). In the cases where the reaction zone does not reach the upstream position of the heating ($T^\star = 900$ K and 1100 K), the flame is flattened when moving upstream, still without passing by a fully convex topology (figure 5.6).

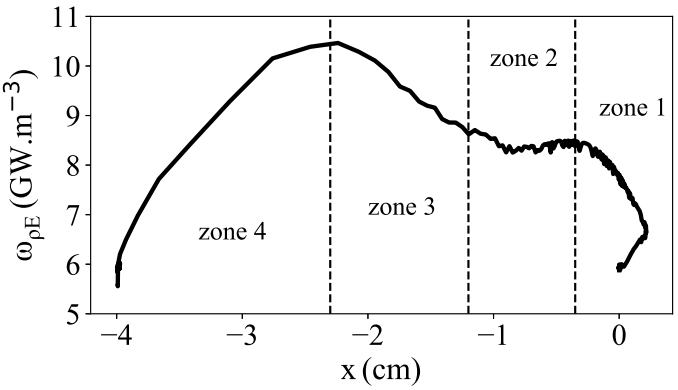

Figure 5.10: Heat release rate at the axis during the flame upstream movement. $T^\star = 1300$ K.

The maximum flash back burning velocity of the flame fronts are $1.060 S_\mathrm{L}$ for $T^\star = 900$ K, $1.095 S_\mathrm{L}$ for $T^\star = 1100$ K and $3.594 S_\mathrm{L}$ for $T^\star = 1300$ K, where as above, S_L denotes the bulk velocity of the stabilized 2D channel flame. The variations of the heat release rate at the axis during the simulation with $T^\star = 1300$ K (figure 5.10), are closely related to the flame shape evolution. First, during the initial downstream blow and the early moments of the upstream movement, until the flame reaches the position $x = -0.35$ cm (zone 1), the heat release source term rises sharply. The flame takes a stronger concave tulip shape while its initial downstream movement. As expected from Choi *et al.* [21], the increasingly concave flame front (figure 5.6) enhances the heat release at the axis of symmetry. The impact of the thermal boundary layer at the axis participates in the rise of the heat release rate during the early moments of the upstream movement. Subsequently, from $x = -0.35$ cm to $x = -1.2$ cm (zone 2 in figure 5.10), the heat

release stays globally stable although the flame propagates into a hotter flow (figure 5.8(c)). This is due to the change in flame topology. Indeed, the acquired convex flame shape limits the increase of the source term in comparison to the precedent concave flame front. Starting from $x = -1.2$ cm, the progressive recovery of a tulip flame shape causes the peak in heat release observed at $x = -2.3$ cm (zone 3), even though the flow temperature at the axis in this zone already diminishes (figure 5.8(c)). The heat release source term diminishes then due to the low flow temperature seen by the flame at the axis (zone 4). Finally, the flame stabilises close to $x = -4$ cm and relaxes to a stable state similar to the initial one.

The present analyses contributes to the understanding of upstream flame propagation in response to preheating. In micro-combustion, it may help in the building of a strategy to position flames at optimised locations for excess enthalpy.

Chapter 6

The role of gravity and external heating in the asymmetry of flames stabilized in a narrow combustion chamber

6.1 Introduction

Up to this point, the operating conditions simulated yield only symmetrical flame shapes. However, recent numerical [60, 83, 114, 146] and experimental [65, 161] studies reveal the apparition of non-symmetric flame shapes for various conditions. Depending on the configuration, the physical phenomena susceptible to break the symmetry are numerous and the objective of the present chapter is to focus on the role of gravity. Also, the influence of external heating on the stability of symmetric flame shapes is discussed.

In the previous experiments, the slanted flames observation was explained by a stabilisation mechanism influenced by the free convection in the air surrounding the tube. A decrease of the Nusselt number toward the top of the cylinder, as the outside boundary layer thickens, has been reported in thermal and flow plume developing around heated tubes [1, 129, 154]. The plume insulates the cylinder from the surrounding air and the reaction zone in the upper part of the tube is then submitted to a lower heat transfer coefficient. Then gravity is driving the flame shape indirectly by affecting the flow surrounding the tube. Besides, a direct influence of gravity inside wider channels was also discussed in the literature using a model equation for flame propagation [72]. In this work, the role of buoyant-induced baroclinic torque was supposed to affect the flame shape inside a wide channel. Finally, the precise role of gravity in the observation of slanted flames, propagating in narrow channels, remains unclear.

Accordingly, the symmetry breaking of a lean ($\phi = 0.8$) premixed laminar methane/air flame, propagating in an horizontal narrow channel or tube of internal width or diameter $\ell_i = 5$ mm, is investigated. Numerical and experimental analyses are provided in a joint work with the experimental team composed of A. Pieyre and F. Richecoeur (EM2C lab, UPR 288 CNRS).

The objective of this chapter is to progress on the understanding of the 'internal' gravity effects by combining experiments and numerical simulations. The chapter is organised as fol-

lows: the experimental and numerical set-up are first described in section 6.2. Then, the overall flame properties are reported in section 6.3, flame which is asymmetrical in all the conducted experiments. Two cases are studied, a flame freely propagating above an isothermal cold wall and a stabilised one, the latter subjected to strong coupling with wall heat transfer. The experimentally observed flame shape is reproduced by the simulation only in the presence of gravity and the breaking of symmetry is explained by the change of behaviour of the baroclinic effects across the flame front after introducing gravity. To finish, section 6.4 gathers an additional insight on the effect of external heating on the flame symmetry breaking. Numerically, external heating, combined with the diminution of the channel internal height, is found to allow stable tulip-shaped flames while submitted to gravity effects, result which is consistent with former experimental observations [29]. In this case, auto-ignition is shown to condition the flame topology.

The part of this chapter concerning gravitational effects on the flame was published in the *Combustion and Flame* journal in 2019 [8].

6.2 Experimental and numerical set-up

6.2.1 Experimental configuration

The experimental set-up shown in figure 6.1 consists in a $\ell_i = 5$ mm inner diameter and $e_w = 1$ mm thick quartz tube placed in horizontal position. The methane/air fresh mixture at a temperature $T_o = 300$ K flows from the left to the right at an equivalence ratio of 0.8, with a Reynolds number of about 50. The length of the tube is 200 mm. The mixture is first ignited at the free end of the tube $x_e = 150$ mm, then the mass flow rate is decreased for the flame to enter the tube and it may be stabilised at a given position for a bulk velocity of the incoming flow balancing the flame burning velocity.

The quartz was chosen for its thermal and optical properties, allowing for a direct visualization of the flame and its propagation.

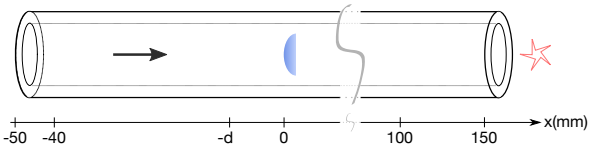

Figure 6.1: Schematic view of the experimental set-up composed of a quartz tube of $\ell_i = 5$ mm inner diameter and $e_w = 1$ mm thickness, inside which a lean methane/air mixture is injected. The inlet ($x_i = -50$ mm) is connected to the mass flow controllers while the outlet ($x_e = 150$ mm) is in open-air, where the flame is first ignited to then propagate inside the tube.

Two mass flow controllers (EL-FLOW Bronkhorst) with 0-700 Nml/min range for air and 0-70 Nml/min for methane are enslaved to command the velocity and equivalence ratio of the flow. A mixture chamber prior to the quartz tube entrance (not shown in figure 6.1) secures the

premixing of the gas. With a precision of 0.35 mL/min, the mass flow controllers allow to adjust the bulk velocity to stabilize the propagating flame. The position and the motion of the flame in the tube is tracked by a camera (Nikon 7000D - Lens micro Nikkor 60 mm f/2.8G) recording videos, which are then decomposed in series of individual pictures. To observe accurately the flame front, and especially the CH^* chemiluminescence, a band-pass interference filter centered at 430.0 nm with a fwhm of 10 nm (± 2 nm) and 40% minimum peak transmission is used.

Case	Wall seen by the flame	V_{bulk} (cm·s^{-1})	V_p (cm·s^{-1})	t_{cd}/t_{res}	S_L (cm·s^{-1})
(i)	Heat-conductive	23.10	≈ 0	≈ 0	23.10
(ii)	isothermal	20.70	0.46	53	21.16

Table 6.1: Experimental conditions. Lean premixed methane/air flame ($\phi = 0.8$). $V_{bulk}\mathbf{x}$ is the bulk flow velocity. $-V_p\mathbf{x}$ is the flame front velocity in the laboratory frame (see figure 6.1 for axis). t_{cd} is the heat conduction time in the solid. t_{res} is the flame residence time. S_L is the burning velocity.

The flame is examined, (i) stabilised by an adjusted incoming flow and (ii) during an upstream propagation after decreasing the mass flow rate. Because the heat diffusivity is much larger in the gas than in the solid, in case (ii) the flame propagates along an almost isothermal wall. In case (i), the stabilisation mechanism of the steady flame depends also on complex heat exchanges with and within the wall, including heat transfer between the gas and the wall, conduction of heat in the solid wall and convective heat transfer between the outside wall and the environment [10, 60]. The slowest thermal exchanges occurring in this configuration is heat conduction through the quartz wall, featuring a characteristic time $t_{cd} = e_w^2/\alpha_s$, where α_s is the quartz thermal diffusivity [102]. A flame residence time $t_{res} = \delta_F/V_p$ is defined from $\delta_F = \alpha_g/S_L^o = 94.2$ µm, a characteristic flame thickness and $-V_p\mathbf{x}$, the absolute velocity of the flame front in the laboratory frame, where α_g denotes the fresh gases diffusivity. For $t_{cd}/t_{res} < 1$, the budget of heat fluxes reaches a steady state with a non-isothermal wall. In practice this is observed experimentally when $V_p \to 0$, representative of a stabilised flame (case (i)). For the ratio $t_{cd}/t_{res} >> 1$, the wall temperature at the flame position stays of the order of 300 K and the flame propagates over an isothermal wall (case (ii)). These two operating points are summarised in Table 6.1. The burning velocity, $S_L = V_{bulk} + V_p$, where V_{bulk} is the bulk velocity of the incoming fresh gases, increases by 9.17% between the flame moving upstream and the stabilised one. This enhancement of the burning velocity results from heat retrocession by the wall to the flow slightly upstream of the stabilised flame front, a mechanism which was discussed in chapter 4 and can be found in [10]. Please note that the increase in amplitude of the flame speed depends on the amount of heat release and therefore on the equivalence ratio of the mixture.

6.2.2 Numerical set-up

To verify that the studied gravity mechanisms do not depend significantly on the very detail of the flow configuration, and also because experiments in the flame tube show no sign

of azimuthal effects, the most simple case of a planar channel is numerically studied in two-dimension, with a channel height $\ell_i = 5$ mm and quartz walls of thickness $e_w = 1$ mm thick, thereby with characteristic lengths similar to the experimental ones. This numerical configuration is the same as the one studied in the precedent chapters.

The reduced chemical mechanism composed of 17 species and 53 reactions employed in this chapter (17S-53R-0.8, table A.1 in appendix A) has been specifically developed based on the GRI-1.2 mechanism [41] following the strategy presented in chapter 3. The reference adiabatic flame speed with the detailed scheme for the equivalence ratio $\phi = 0.8$ is S_L^o = 28.40 cm·s^{-1} and the reduced scheme leads to S_L^o = 28.56 cm·s^{-1}. Representative species and temperature profiles compared in the one-dimensional flames at equivalence ratio $\phi = 0.8$, between the detailed and reduced schemes are given in the appendix A.

Wall boundary conditions similar to the two experimental cases of Table 6.1 are considered, *i.e.* (i) heat-conductive with all heat transfers active and (ii) isothermal (T = 300 K). In the two-dimensional isothermal channel with gravity, the flame burning velocity is $S_L = 24.95$ cm·s^{-1}, to become 27.09 cm·s^{-1} with wall heat-transfer. As it should, the absolute values of these flame burning velocities differ between the axi-symmetric tube in the experiment (Table 6.1) and the two-dimensional channel in the simulation. However, the relative increase in burning velocity between isothermal and non-isothermal wall cases are quite close, 9.17% in the experiment and 8.57 % in the simulation, which brings some confidence in the retained strategy.

6.3 Analysis of gravity effects

6.3.1 Case (i): Flame stabilised with heat-conductive wall

The flame stabilised by an incoming flow exactly balancing its burning rate is considered at first (case (i) of Table 6.1). The CH* chemiluminescence is collected in the experiment over an exposure time of 2 s and the mean flame emission is represented in figure 6.3 left. The reaction zone makes an angle with the vertical of $\beta = 24°$ (see figure 6.2), whereas the numerical simulation without gravity reports a fully symmetrical flame shape (figure 6.3 top-right). Adding the gravity force in the Navier-Stokes equation solved, the flame takes a inclination as in the experiment (figure 6.3 bottom-right), even though the simulation is planar and the experiments axi-symmetrical. The angle of the reaction zone with the vertical is 30° in the simulation.

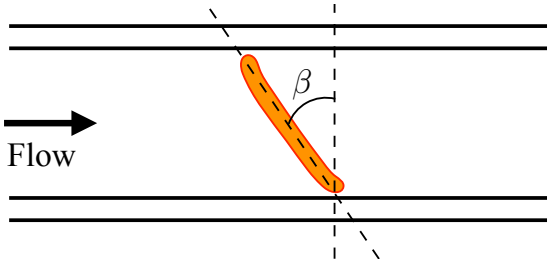

Figure 6.2: Representation of the inclination angle β of a slanted flame.

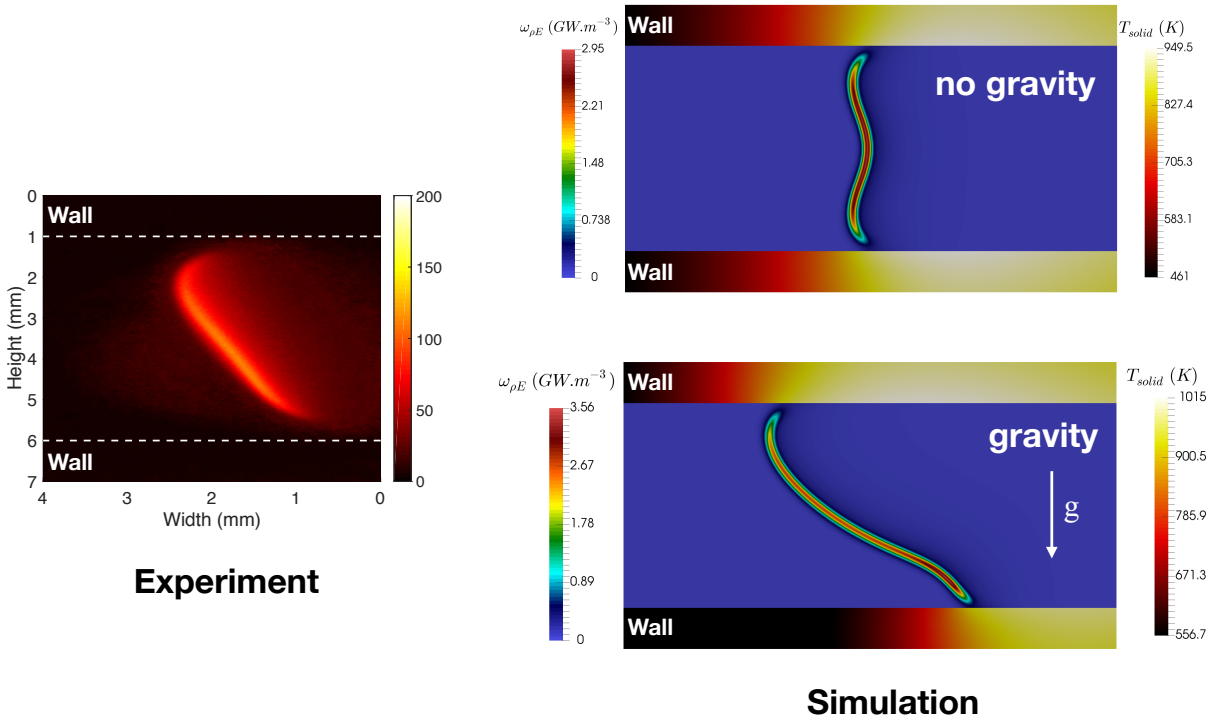

Figure 6.3: Case (ii) of Table 6.1. Experiment: Mean chemiluminescence CH^*. Simulation: Wall temperature and heat release rate.

In the case with gravity, the top and bottom close-to-wall edge-flame shapes differ (figure 6.3). The topology and the relative progression velocity of these edge-flames benefit from the preheating of the gases upstream of the flame after diffusion of heat inside the wall [10]. Streamwise profiles of velocity and temperature taken at a distance of 0.7 mm from the top and bottom channel walls are now analysed. The streamwise component of the velocity is larger at the bottom due to the confinement of the flow by the concave flame shape (figure 6.4(a)). This higher velocity goes with smaller residence times and thus a less efficient preheating by the wall thermal boundary layer, leading to lower temperature levels ahead of the bottom edge-flame (figure 6.4(b)). At the top, the effect of the preheating by the channel wall on the streamwise velocity ahead for the flame, is compensated by the spreading of the streamlines associated to the flame topology (see chapter 4). As a result, the flow acceleration ahead of the flame is quite low at the top wall (figure 6.4(a)) and the fresh gases benefit from an efficient preheating (figure 6.4(b)). In both experiments and simulations, the heat release rate is found larger at the bottom than at the top wall edge-flame (figure 6.3). As pointed out in [21], the burning rate is intensified by the curvature of concave flame fronts. This enhancement also explains the reduced quenching distance to the wall at the bottom edge-flame.

Because an eventual modification by gravity of the free convection surrounding the channel is not included in the simulation, another mechanism driven by gravity is at play inside the channel. To isolate this mechanism from heat transfer inside and outside the wall, the flame propagating over an isothermal wall is further examined (case (ii) of Table 6.1).

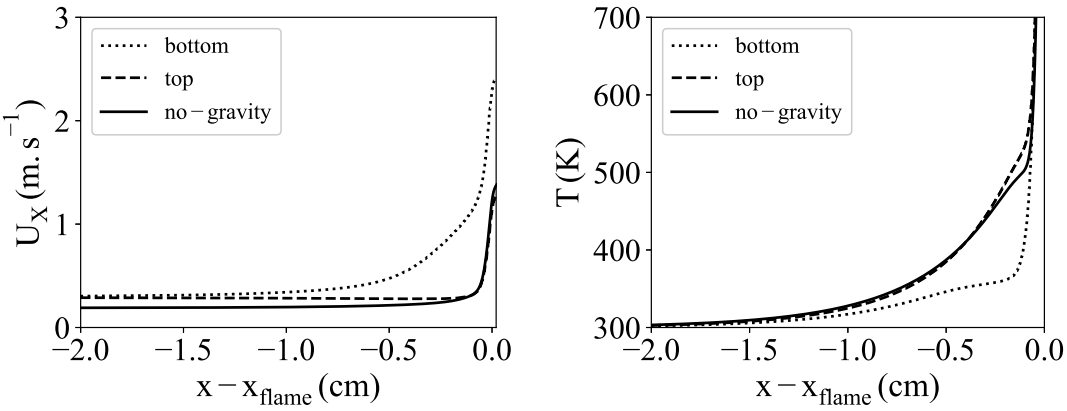

(a) Streamwise velocity

(b) Temperature

Figure 6.4: Velocity and temperature distribution at a distance of 0.7 mm from the top and bottom wall. x_{flame}: maximum of heat release on the probed line (top or bottom). No-gravity case is symmetrical.

6.3.2 Case (ii): Flame propagating over a quasi-isothermal wall

In the experiment, starting from a stabilised flame (case (i)), the mass flow rate is lowered to reach the operating point of case (ii), in which the flame proceeds inside the tube over quasi-isothermal walls. The diagnostics reported above are applied, the recording starts ten seconds before the mass flow rate modification and is pursued up to a steadily propagating flame. Figure 6.5 shows flame images taken initially and then subsequently at 10 and 15 seconds. The flame inclination is significantly reduced.

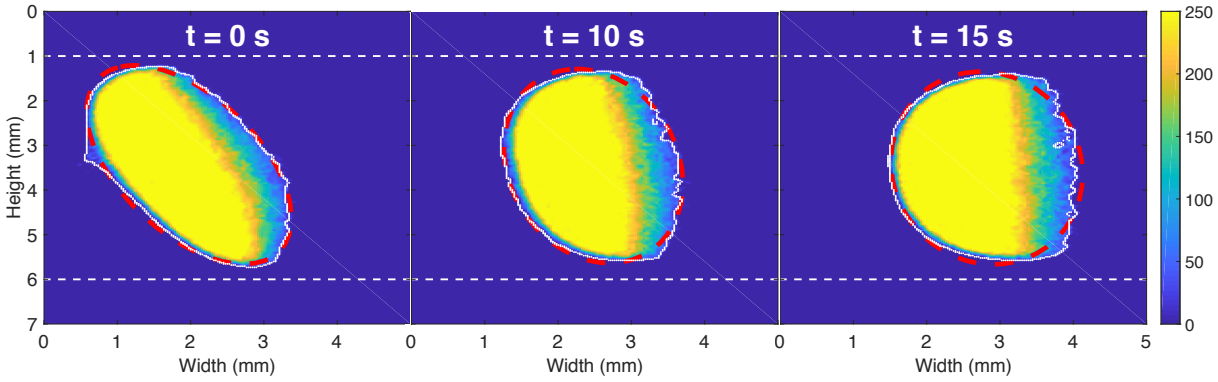

Figure 6.5: Experimental snapshots at $t = 0$ s, $t = 10$ s and $t = 15$ s. White dotted line: flame detected contour. Red dashed line: fitted ellipse.

The time evolution of the flame angle with the vertical determined from the fitted ellipse is given in figure 6.6. Starting at a steady state with an angle of 24°, the propagation state is reached at which the angle is 3°, yielding a relative decrease in inclination of 87.5%. This decrease of angle to the vertical (reduction of inclination) is also observed in the simulation.

Snapshots of the isothermal wall simulations with and without gravity are shown in figure 6.7. The angle taken by the flame with gravity and isothermal wall is 6°, also much less pronounced than in case (i) (30°). The relative decrease in inclination of flame simulated is of 80%. The breaking of the symmetry is thus reported in both experiments and simulations with isothermal and cold (T =300 K) wall.

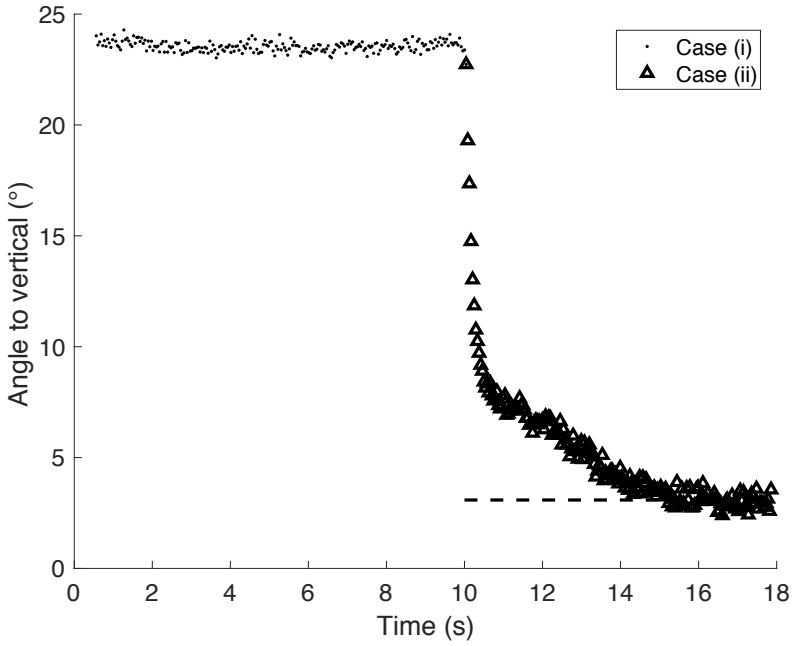

Figure 6.6: Time evolution of the flame angle to the vertical in the experiment. $t = 0$ denotes the decrease in mass flow rate. Dotted: Stabilised flame with heat-conductive wall (case (i)). Triangle: Propagating flame with isothermal wall (case (ii)).

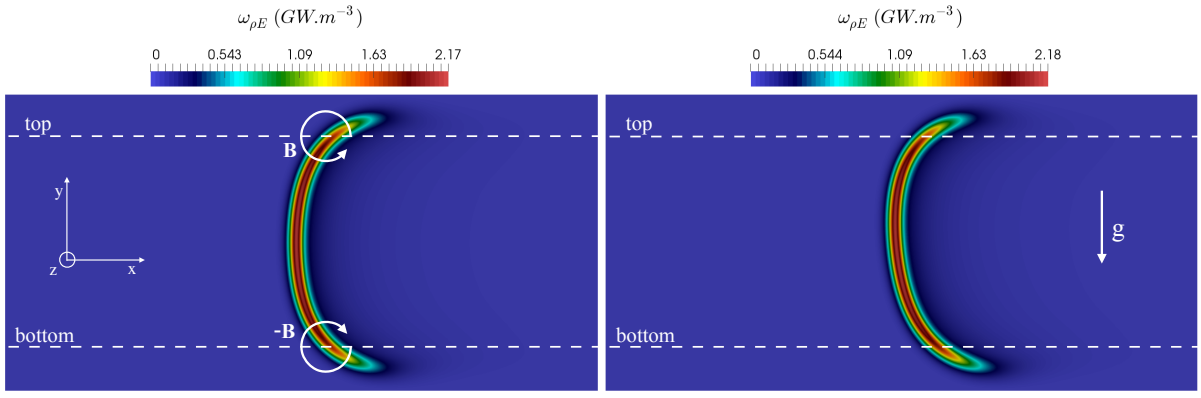

(a) Without gravity (b) With gravity

Figure 6.7: Simulation of isothermal wall (case (ii)) of Table 6.1), with and without gravity. Dashed-line: lines used for probing the vorticity budget.

6.3.3 Analysis of baroclinic-torque response to gravity

Kazakov [72] pointed out, in a theoretical analysis, that the effect of gravity on confined flames should be expressed via baroclinic effect. Body forces generate pressure and density gradients and among the numerous coupling between density and pressure gradient present in flames, the baroclinic torque is a well-established source of vorticity in curved reaction zones [25]

$$\mathbf{B} = \frac{1}{\rho^2}\nabla\rho \times \nabla P = \frac{1}{\rho^2}\left(\frac{\partial\rho}{\partial x}\frac{\partial P}{\partial y} - \frac{\partial\rho}{\partial y}\frac{\partial P}{dx}\right)\mathbf{z}\,, \tag{6.1}$$

where ρ is the density and P is the pressure. $\mathbf{x}$ is the streamwise coordinate (flow direction), $\mathbf{y}$ is the transverse coordinate (gravity acceleration is $-g\mathbf{y}$) and $\mathbf{z}$ the coordinate normal to the channel plane. To seize the complete picture on vorticity effects over the flame, the balance equation of the vorticity, $\boldsymbol{\omega} = \boldsymbol{\nabla} \times \mathbf{u}$, is derived. To obtain this equation, the Navier-Stokes momentum equation is manipulated to isolate the density in the left hand side,

$$\frac{\partial\rho\mathbf{u}}{\partial t} + \boldsymbol{\nabla}\cdot(\rho\mathbf{u}\mathbf{u}) = -\boldsymbol{\nabla}P + \boldsymbol{\nabla}\cdot\boldsymbol{\tau} + \rho\mathbf{g}\,, \tag{6.2}$$

$$\rho\left(\frac{\partial\mathbf{u}}{\partial t} + (\mathbf{u}\cdot\boldsymbol{\nabla})\mathbf{u}\right) + \mathbf{u}\underbrace{\left(\frac{\partial\rho}{\partial t} + \overbrace{(\mathbf{u}\cdot\boldsymbol{\nabla}\rho) + \rho(\boldsymbol{\nabla}\cdot\mathbf{u})}^{\boldsymbol{\nabla}\cdot(\rho\mathbf{u})}\right)}_{=0 \text{ from continuity equation}} = -\boldsymbol{\nabla}P + \boldsymbol{\nabla}\cdot\boldsymbol{\tau} + \rho\mathbf{g}\,, \tag{6.3}$$

with the velocity vector $\mathbf{u} = (u, v, w)^{\mathrm{T}}$, the viscous tensor $\boldsymbol{\tau}$ and usual notations for the other variables. This equation is divided by the density and the curl operator is applied to derive the vorticity equation,

$$\frac{\partial\boldsymbol{\nabla}\times\mathbf{u}}{\partial t} + [\boldsymbol{\nabla}\times(\mathbf{u}\cdot\boldsymbol{\nabla})]\,\mathbf{u} + (\mathbf{u}\cdot\boldsymbol{\nabla})\boldsymbol{\nabla}\times\mathbf{u} = \boldsymbol{\nabla}\times\left(-\frac{\boldsymbol{\nabla}P}{\rho}\right) + \boldsymbol{\nabla}\times\left(\frac{\boldsymbol{\nabla}\cdot\boldsymbol{\tau}}{\rho}\right) + \boldsymbol{\nabla}\times\mathbf{g}\,, \tag{6.4}$$

$$\frac{\partial\boldsymbol{\omega}}{\partial t} = \underbrace{-(\mathbf{u}\cdot\boldsymbol{\nabla})\boldsymbol{\omega}}_{\text{i}}\underbrace{+(\boldsymbol{\omega}\cdot\boldsymbol{\nabla})\mathbf{u}}_{\text{ii}}\underbrace{-\boldsymbol{\omega}(\boldsymbol{\nabla}\cdot\mathbf{u})}_{\text{iii}}\underbrace{+\mathbf{B}}_{\text{iv}}\underbrace{+\boldsymbol{\nabla}\times\left(\frac{\boldsymbol{\nabla}\cdot\boldsymbol{\tau}}{\rho}\right)}_{\text{v}}\underbrace{+\boldsymbol{\nabla}\times\mathbf{g}}_{\text{vi}}\,. \tag{6.5}$$

The various terms of the vorticity equation are now listed and simplified when possible. One notes that $\boldsymbol{\nabla}\times\boldsymbol{\nabla}P = \mathbf{0}$ and in the present two-dimensional case, $w = 0$ and $\partial/\partial z = 0$.
(i) is the transport of vorticity by convection.
(ii) is the vorticity due to vortex stretching and yields 0 in the present case,

$$(\boldsymbol{\omega}\cdot\boldsymbol{\nabla})\mathbf{u} = \left[\begin{pmatrix} 0 \\ 0 \\ \frac{\partial v}{\partial x} - \frac{\partial u}{\partial y} \end{pmatrix}\cdot\begin{pmatrix} \frac{\partial}{\partial x} \\ \frac{\partial}{\partial y} \\ \frac{\partial}{\partial z} \end{pmatrix}\right]\mathbf{u} = \mathbf{0}\,. \tag{6.6}$$

(iii) is the vorticity stretching by density change.
(iv) is the baroclinic contribution to vorticity, called the baroclinic torque (equation (6.1)).
(v) is the transport of vorticity by viscous effects.

(vi) is the body force term, presently reduced to zero,

$$\boldsymbol{\nabla} \times \mathbf{g} = \left(\frac{\partial g_y}{\partial x} - \frac{\partial g_x}{\partial y} \right) \mathbf{z} = \mathbf{0} \,. \tag{6.7}$$

Finally, the budget equation yields,

$$\frac{\partial \boldsymbol{\omega}}{\partial t} = \underbrace{-(\mathbf{u} \cdot \boldsymbol{\nabla})\boldsymbol{\omega}}_{\text{i}} \underbrace{-\boldsymbol{\omega}(\boldsymbol{\nabla} \cdot \mathbf{u})}_{\text{iii}} \underbrace{+\mathbf{B}}_{\text{iv}} \underbrace{+\boldsymbol{\nabla} \times \left(\frac{\boldsymbol{\nabla} \cdot \boldsymbol{\tau}}{\rho} \right)}_{\text{v}} \,. \tag{6.8}$$

In the isothermal case without gravity, approaching the edge-flame close to the wall, the pressure and density gradients in the y-direction feature opposite sign on both sides of the channel centreline, whereas the density and pressure gradient in the x-direction stay the same. The baroclinic torque given by relation (6.1) therefore changes its sign on both sides of the channel centreline,

$$\begin{aligned} \mathrm{B} &= \mathrm{B}_{\text{top}} = \frac{1}{\rho^2} \boldsymbol{\nabla}\rho \times \boldsymbol{\nabla} P \Big|_{\text{top}} = \frac{1}{\rho^2} \left(\frac{d\rho}{dx} \frac{dP}{dy} \Big|_{\text{top}} - \frac{d\rho}{dy} \Big|_{\text{top}} \frac{dP}{dx} \right) \mathbf{z} \\ &= -\frac{1}{\rho^2} \left(\frac{d\rho}{dx} \frac{dP}{dy} \Big|_{\text{bottom}} - \frac{d\rho}{dy} \Big|_{\text{bottom}} \frac{dP}{dx} \right) \mathbf{z} = -\frac{1}{\rho^2} \boldsymbol{\nabla}\rho \times \boldsymbol{\nabla} P \Big|_{\text{bottom}} = -\mathrm{B}_{\text{bottom}} \,. \end{aligned} \tag{6.9}$$

This is verified in figure 6.8 displaying the amplitude of the baroclinic torque along the dashed-lines seen in figure 6.7(a). These plots are versus a reaction progress variable defined from the CO_2 mass fraction normalised by its value in the fully burnt gases ($Y^{\text{b}}_{\text{CO}_2} = 0.122576$), also collected along the dashed lines of figure 6.7. The baroclinic torque is thus positive on upper part of the channel and negative on the bottom part, confirming the symmetric effects pictured by the white arrows in figure 6.7(a).

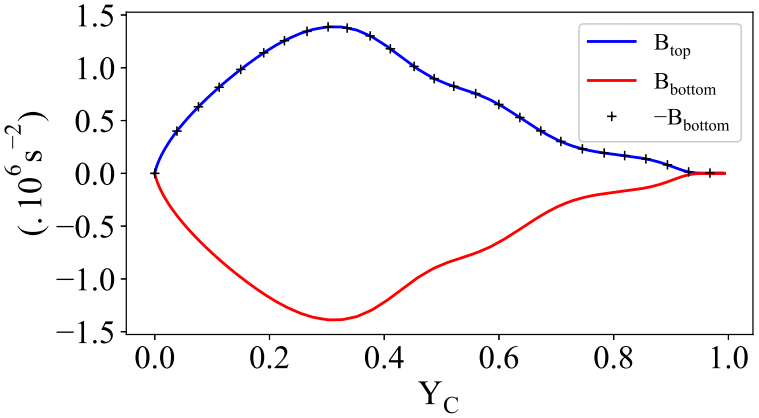

Figure 6.8: Baroclinic torque (iv) versus $Y_{\text{CO}_2}/Y^{\text{b}}_{\text{CO}_2}$ along the dashed-lines of figure 6.7(a).

All the terms contributing to the vorticity budget in equation (6.8) are shown in figure 6.9, along with the total budget, which sums up to zero as expected for both gravity and no-gravity steady cases. In the case without gravity, all terms change their sign between the upper and

bottom parts of the narrow channel, leading to a fully symmetric stable reaction zone (symbols in figures 6.9(a) and 6.9(b)). Accounting for the effect of gravity, the terms are not symmetric with respect to the channel axis. Because the density difference between fresh and burnt gases and flow acceleration are also very close with or without body forces, the amplitudes of the various terms of equation (6.8) are only slightly affected by gravity. Actually, to elucidate the mechanism that makes the flame to rotate when gravity is introduced, it is necessary to examine the transient when the body forced is added.

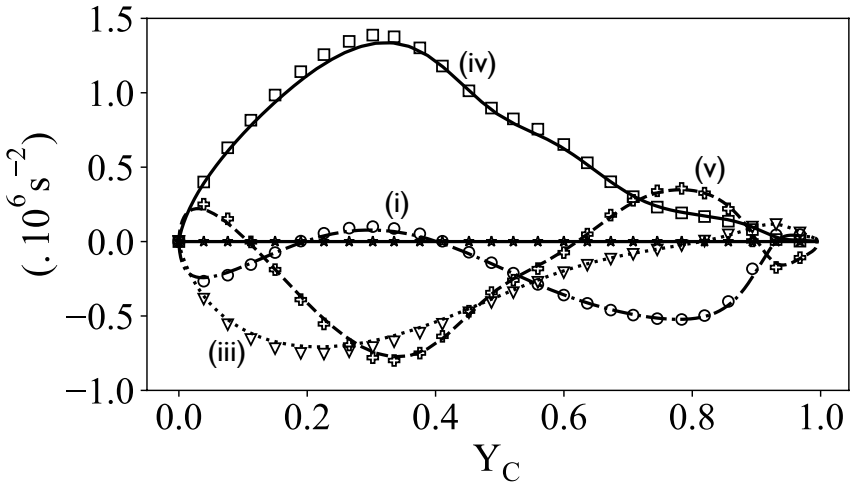

(a) Top line of figure 6.7(a)

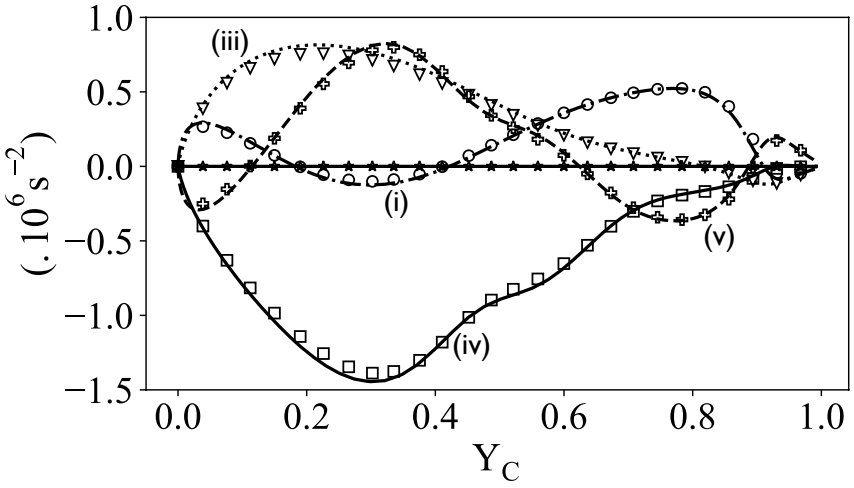

(b) Bottom line of figure 6.7(a)

Figure 6.9: Vorticity budget versus $Y_{CO_2}/Y^b_{CO_2}$ along the dashed-lines of figure 6.7. Lines: With gravity. Symbols: Without gravity. Circles: (i) of equation 6.8 . Triangles: (iii). Squares: baroclinic torque (iv). Crosses: (v). Stars: budget.

Starting from the converged simulation without gravity, the body force is added and the upper edge-flame rotation is completed in 16 ms, to reach the slanted flame steady state of figure 6.7(b). The introduction of gravity leads to an additional contribution to the baroclinic

torque (6.1), which may be approximated as

$$\frac{1}{\rho^2}\left[\frac{\partial\rho}{\partial x}\left(\frac{\partial P}{\partial y}\right)_{\mathrm{g}} - \left(\frac{\partial\rho}{\partial y}\right)_{\mathrm{g}}\frac{\partial P}{dx}\right] . \tag{6.10}$$

Isolating the effect of gravity, its premier impact is to promote flow stratification with negative density and pressure gradients in the vertical direction, $(\partial P/\partial y)_{\mathrm{g}} < 0$ and $(\partial\rho/\partial y)_{\mathrm{g}} < 0$. Considering an isentropic flow at rest subjected to gravity, the relative variation of pressure and density defines the speed of sound $c^2 = (\partial P/\partial\rho) > 1$. Therefore, the amplitudes of the density and pressure gradients in the vertical direction and due to gravity may be ranked as $(\partial P/\partial y)_{\mathrm{g}} < (\partial\rho/\partial y)_{\mathrm{g}} < 0$. Across the premixed reaction zone, $(\partial P/\partial x) < 0$, $(\partial\rho/\partial x) < 0$ and $(\partial T/\partial x) > 0$. The ranking in pressure and density gradient evolves across the flame front (figure 6.10). In the upstream part of the flame front $(\partial\rho/\partial x) < (\partial P/\partial x) < 0$, while further downstream $(\partial P/\partial x) < (\partial\rho/\partial x) < 0$. These gradients in the streamwise direction are orders of magnitudes larger than those in the vertical direction, therefore they may be assumed weakly affected by the addition of gravity. Combining these observations, the baroclinic torque induced by gravity (equation (6.10)) should be largely positive in the upstream part of the flame front and decrease after, yielding globally a positive enhancement of the baroclinic torque across the reaction zone.

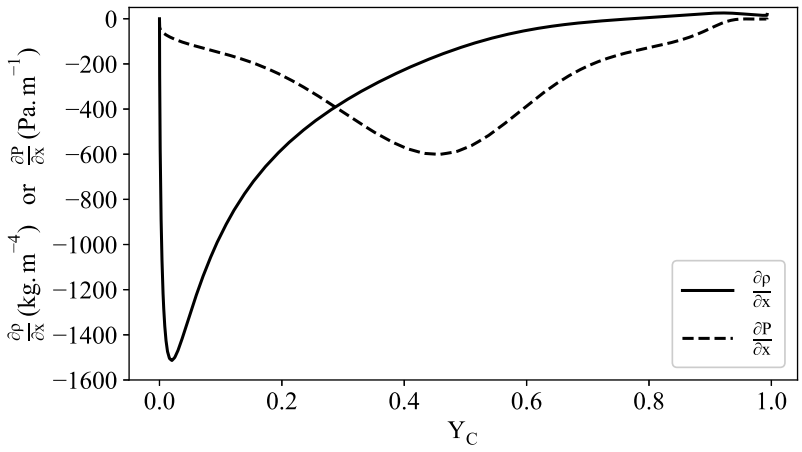

Figure 6.10: Pressure and density streamwise gradients versus $Y_{CO_2}/Y^{b}_{CO_2}$ along the dashed-lines of figure 6.7(a).

To verify this simple scaling, at the time $t = 18$ µs after adding gravity, the source of vorticity is analysed by computing the variation of all the terms of equation (6.8). This variation is measured in the simulation between their steady state value without gravity (figure 6.9) and their value at $t = 18$ µs after gravity addition. In both the upper and the bottom edge-flame close to wall, a positive source of baroclinic torque is indeed observed, corresponding to a positive source of vorticity (figure 6.11). This addition of vorticity represents a few percent of the overall baroclinic torque and is located across the reaction zones, where the longitudinal pressure and density gradients occur.

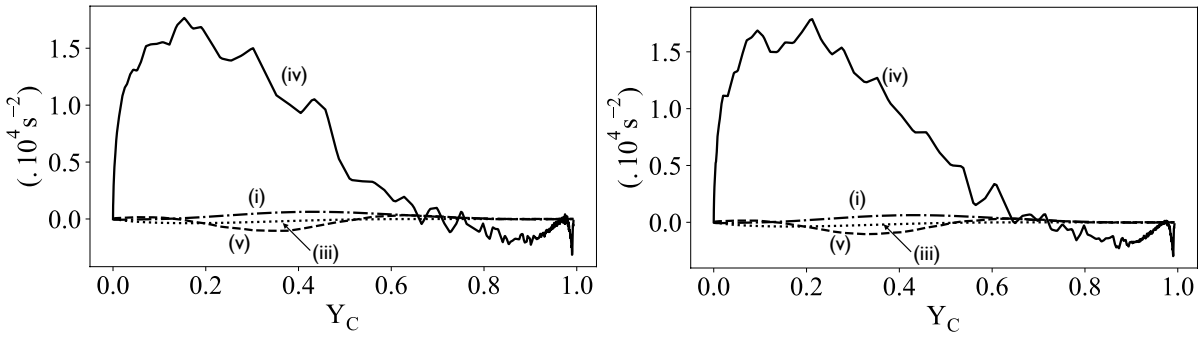

(a) Top line of figure 6.7(a)

(b) Bottom line of figure 6.7(a)

Figure 6.11: Deviation of vorticity balance versus $Y_{CO_2}/Y^b_{CO_2}$ along the dashed-lines of figure 6.7. Dashed-dot: (i) of equation 6.8. Dotted: (iii). Solid: baroclinic torque (iv). Dashed: (v).

In the top part of the channel, the streamlines are then less deviated toward the centreline with gravity when crossing the flame (figure 6.12), leading to their spreading upstream of the flame with a local flow deceleration, followed by an upstream flame movement (see figure 6.13, dashed line). In the bottom part of the channel, the opposite mechanism is found, with a highest concentration of the streamlines by the added vorticity (figure 6.12(b)), leading to local flow acceleration and a downstream flame movement (see figure 6.13, dotted line). The net result is a reaction zone that is pushed downstream at the bottom and pulled upstream at the top to evolve towards a slanted shape.

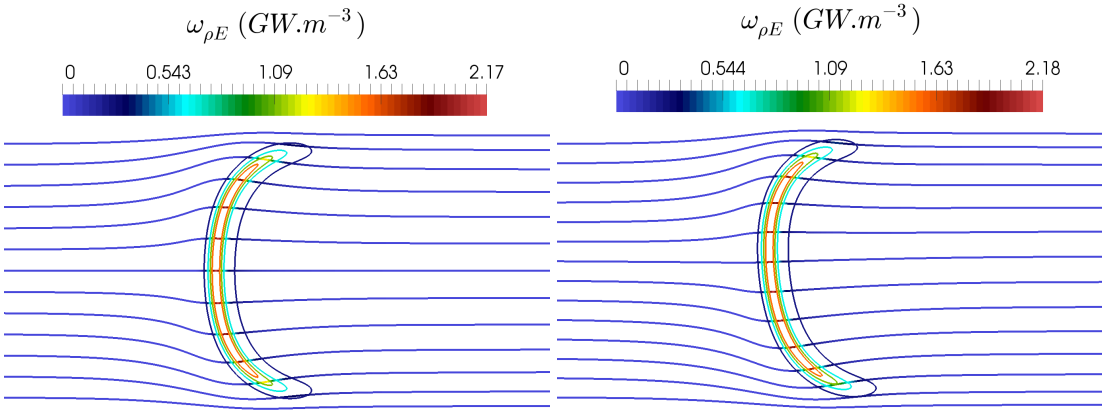

(a) Without gravity

(b) With gravity

Figure 6.12: Case (ii). Streamlines and flame contours of 10, 30, 50 and 70% of max heat release rate.

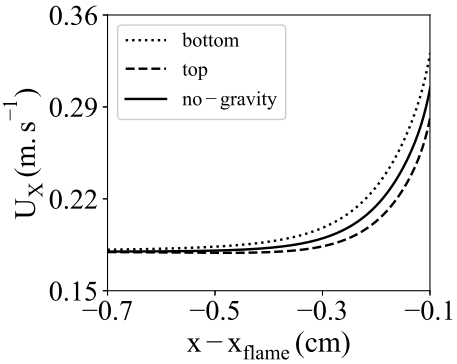

Figure 6.13: Velocity distribution at a distance of 0.7 mm to the top and bottom wall. x_{flame}: maximum of heat release on the probed line.

6.4 Influence of external heating and channel dimensions on the stability of symmetric flame topologies

In the previous section, a detailed analysis shows how the gravity field is associated to a generation of baroclinic torque, leading to flame shape asymmetry. A flame, thermally coupled with the channel walls, is found symmetrical and tulip-shaped (figure 6.3, top right) in the absence of gravity to take a strong tilting under the buoyant effects (figure 6.3, bottom right). Nevertheless, on-earth experiments show the possibility of observing stable symmetric tulip-shaped flames propagating in horizontal narrow channels [14, 29, 30], by providing an intense external heating of the channel walls. These observations point out the stabilizing effect, in term of symmetry, of external thermal enhancement.

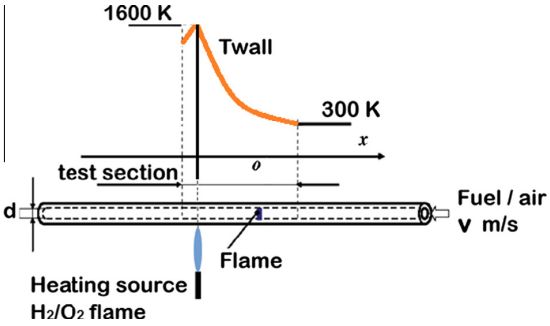

(a) Temperature profile along the tube

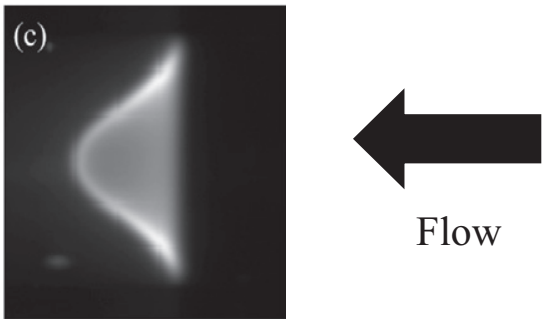

(b) Image of a stable tulip-shaped stoichiometric CH_4/air flame in a 2.15 mm inner diameter tube

Figure 6.14: Experimental set-up and observation extracted from [29].

Notably, Di Stazio *et al.* [29] studied the propagation of a stoichiometric methane/air flame in a narrow tube, of internal diameter $D_{\text{i}} = 2.15$ mm, heated by an external source (figure 6.14(a)). In the tube wall, a temperature profile peaking bellow 1600 K is imposed, and the inlet flow rate is varied to observe the flame response. Under an inlet flow rate of 1 m.s^{-1},

a stable tulip-shaped flame is observed (figure 6.14(b)).

Presently, numerical simulations are conducted in order to understand the mechanism permitting for the stablity of the symmetric flame topology. The objective is not to reproduce with fidelity the experiment in [29], but to obtain an analogous configuration for the flame propagation. Accordingly, the same equivalence ratio, $\phi = 1.0$ (thus employing the kinetic mechanism 17S-53R-1.0), and inlet bulk velocity, $S_L = 1$ m.s^{-1}, are used in the simulations. The wall temperature profile imposed (see figure 6.15) mimics the temperature profile obtained in the experiment from the external heat source (see [29], figure 8).

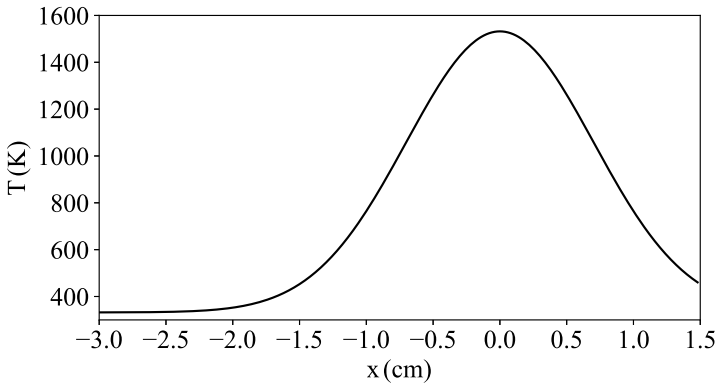

Figure 6.15: Temperature profile imposed within the channel walls, in the simulation. Peak located at $x = 0$.

Starting from the thermally coupled simulation without gravity (figure 6.3, top right), the wall temperature is progressively relaxed toward the experimental profile, while neglecting for buoyant effects. In this channel of internal height $\ell_i = 5$ mm, the subsequent introduction of gravity in the simulation still breaks the flame shape symmetry, although the imposition of the high wall temperature profile in figure 6.15. Considering the tube dimension in the experiments ($D_i = 2.15$ mm) and the promotion of flow/wall heat transfer with low characteristic length, smaller channels are tested numerically. The channel height is thus reduced step by step, until finding a dimension which yields a stable tulip-shaped flame, when introducing gravity in the simulation.

The cases $\ell_i = 1.8$ mm and $\ell_i = 1.6$ mm are reported in figures 6.16(a) and 6.16(b), respectively. The transition from a symmetric tulip to an asymmetric flame topology is observed for the case $\ell_i = 1.8$ mm (see figure 6.16(a)), and bigger dimensions. This transition is quickly initiated when applying gravity, exhibiting an asymmetric flame after 4 ms only. Focusing on the flame topology, the high temperature favours the flame propagation near the walls, leading to flame tails positioned upstream from the flame central inflection point (peak of heat release). For the case $\ell_i = 1.6$ mm and lower dimensions, the flame conserves its symmetric tulip shape when introducing gravity (see figure 6.16(b)), even after 80 ms of simulation. The combination of external heating and channel height reduction, permits thus to stabilize symmetric flames. At this dimension, the favoured flow/wall heat exchanges lead to auto-ignition of the incoming flow. On one hand, at the temperature of 1600 K, the auto-ignition delay of a stoichiometric

methane mixture is $\tau_{\text{ig}} \simeq 0.55$ ms (see chapter 3, figure 3.5). On the other hand, the residency time of particles in the flame thermal diffusion layer $t_{\text{res,th}}$, defined as the thermal diffusion layer thickness (taken as five times the flame thickness) over the flame burning rate S_{L}, is

$$t_{\text{res,th}} = \frac{5\delta_{\text{F}}}{S_{\text{L}}} \simeq 1 \text{ ms} \quad > \quad \tau_{\text{ig}} \,, \tag{6.11}$$

with $\delta_{\text{F}} = 194$ µm probed at the axis in the simulation.

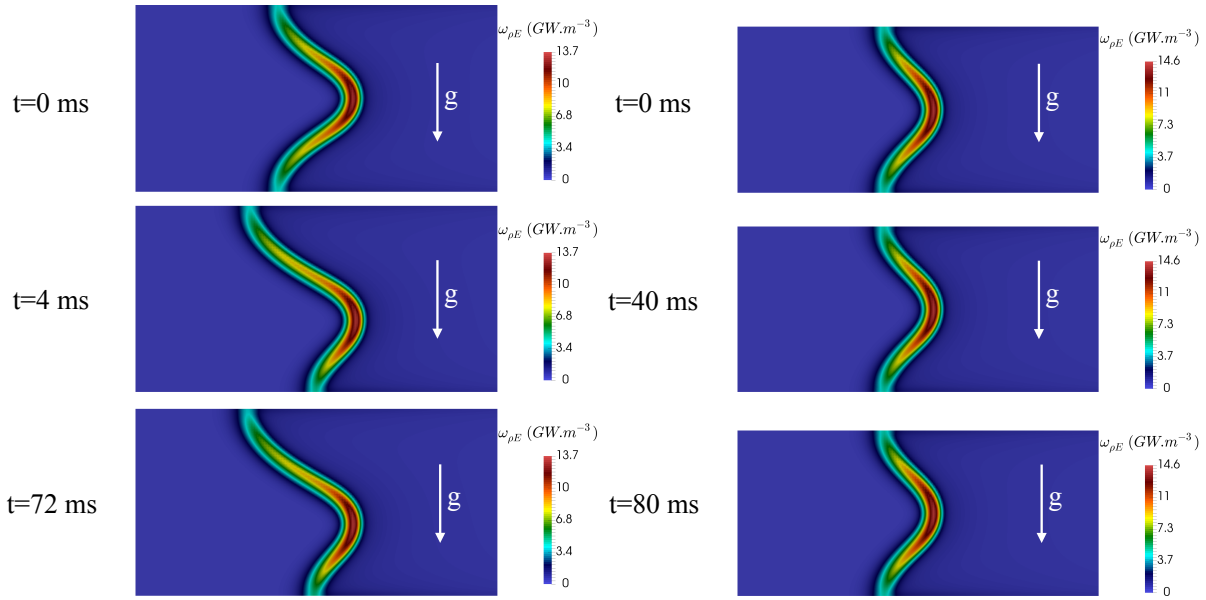

(a) $\ell_i = 1.8$ mm, $x_{\text{flame}} = -2.1$ mm (b) $\ell_i = 1.6$ mm, $x_{\text{flame}} = -2.3$ mm

Figure 6.16: Effect of channel dimension and external heating on small-scale channel flames when gravity is entered ($t = 0$). x_{flame}: position of the maximum of heat release.

Since based on auto-ignition, the nature of the present symmetric flame is quite different from the self-sustained flames studied in the previous sections. To the authors knowledge, the only experimental observations of stable tulip-shaped flames propagating in small-scale channel were performed while heating the tube [29] or the flat channel [14, 30]. The ability to recover numerically this behaviour, in the same framework as the one used to explain the stability of slanted flames, gives confidence in the overall validity of the numerics used in the present work.

In this chapter, experimental measurements and simulation reports similar trends for flames freely propagating above isothermal walls or stabilised by the incoming flow with strongly coupled heat exchanged with and within the wall. Both flames are asymmetrical, with an inclination that is less pronounced in the isothermal wall case. In the absence of modification by gravity of the convection on the outside channel wall, the flame is still tilted, with an anchoring at the upper wall. The heat-retrocession via conduction in the wall and the thermal boundary layer in the fresh gases upstream of the flame, increase the inclination of the slanted flames. Based on a previous theoretical study [72], the response of the baroclinic torque to gravity is explored to elucidate its responsibility on the flame tilting in such narrow combustion-systems. To finish,

based on numerical simulation, stable symmetric flame are shown to be sustainable under specific external heating and channel dimensions, as observed experimentally [29]. Characteristic times analysis points out that the topology of these flames is based on auto-ignition.

Chapter 7

Conclusion and perspectives

Contents

7.1 Chapter summary 137

7.2 Conclusion 137

7.2.1 Chemistry modelling 138

7.2.2 Flame/wall interactions 139

7.2.3 Flame response to upstream heating 140

7.2.4 Role of the gravity in the breaking of flame symmetry 140

7.3 Perspectives 141

7.3.1 On-earth intricate boundary layer, heat recirculation and flame coupling 141

7.3.2 Experimental comparisons 141

7.3.3 Low temperature chemistry 141

7.3.4 Thermally optimised and catalytic burners 142

7.1 Chapter summary

To conclude the manuscript, this chapter is organised as follows. First, section 7.2 quickly recalls the context and objectives of this study before summarizing the Ph. D. thesis main achievements. Then, from the observations gathered along this document, perspectives are opened in section 7.3. An emphasis is made on the improvements to be brought to the present work, along with the future studies of interest to further apprehend the physics of micro-combustion.

7.2 Conclusion

In the general context of miniaturization, the obstacles littering the path to weight and size reduction of electrical batteries now create a gap between the power sources and the powered

devices. From the high energy density of hydrocarbons compared to electrical batteries, small-scale combustion is believed to offer an adapted power source to small weight-constrained applications. Since last decades, researchers from the combustion community are pushed toward this new field. For example, prototypes of micro-propeller have been developed for the propulsion of micro-satellites, application well known for its mass constrains. Still, the physics controlling this young field quite differ from that of classical macro-scale combustion and need more understanding. Among the aspects calling for research efforts, this work intends to provide elements on two main points:

- First, a deeper comprehension of the physical parameters controlling or influencing the flame characteristics is valuable, requiring for complete physical analyses of the intricate phenomena occurring in small-scale burners. Physical analyses are the cornerstone of the present work as chapters 4, 5 and 6, are dedicated to them.

- Second, concerning the numerical simulations, the models employed to mimic this especial physics require a questioning to provide meaningful results. Some points are treated in chapter 3 through the study of the reduction methods for kinetic mechanisms, and in chapter 6 via the consideration of symmetry assumptions.

To conduct thorough analyses, DNS of methane/air flames propagating in a 5 mm high flat canal are conducted, with complex chemistry and transport modelling. Further the thermal coupling between the channel walls and the flow is considered. To do so, a numerical solver for the energy conservation in the solid was developed from scratch during this Ph. D. thesis.

7.2.1 Chemistry modelling

In chapter 3, the methods employed to derive reduced kinetic mechanisms from detailed schemes are questioned. It is shown that some reduction strategies, typically employed in the modelling of macro-scale combustion, are not fit to micro-combustion. In response, a reduction method tailored to our field of interest is derived. Accordingly, the detailed GRI-1.2 mechanism is reduced following different reference trajectories. From the absence of overwhelming heat losses in macro-combustion and the simplicity of the procedure, the reduction strategy based on adiabatic flames only is the most commonly employed. This general procedure is first tested:

- A 15 species and 26 reactions mechanism is obtained while reducing the GRI-1.2 based on an adiabatic flame only.

Still, in the case of small-scale combustion, the flame is subjected to quenching at the wall because of heat loss and may potentially undergo self ignition for an excess of enthalpy transferred to the fresh gases. To account for such small-scale phenomena, a second reduction is performed:

- A 17 species and 53 reactions mechanism is obtained based on auto-ignition and multiple 1D flames submitted to uniform heat loss, from adiabatic to quenching conditions.

Both mechanisms are tested, against the reference GRI-1.2, on a multi-dimensional simulation of a stabilised flame, thermally coupled with the small-scale channel walls. The second strategy is shown to provide far better, and quite accurate, results with the additional cost of two species only. In conclusion, the reduction of kinetic mechanisms, based on auto-ignition and multiple 1D flames submitted to uniform heat loss, is adapted to the modelling of small-scale combustion.

7.2.2 Flame/wall interactions

Few studies focus on stable, instead of moving, flames propagating in small-scale channels. The interest of such a configuration is nevertheless obvious, from most energy producing burners prototypes effectively exhibit stable flames. Presently, the difficulties arising from the numerical stabilisation of such flames, while accounting for the heat coupling with the wall, have been overcome to analyse the flame behaviour in a micro-burner.

The literature review points out that micro-combustion differs from macro-combustion, from the sheared flow and the heated channel walls interacting with the flame. In chapter 4, the impact of the boundary layer and heat recirculation on a stoichiometric flame dynamics and topology, is investigated. Notably, compared to an adiabatic flame, the flame speed increases with edge-flame quenching at an isothermal cold wall in the absence of a boundary layer, decreases with a boundary layer, to increase again with heat transfer coupling within a 1 mm thick quartz wall. A scaling low and additional budgets are applied on the simulations. It reveals that the flame speed depends on several parameters:

- The flame topology, both via an increase of the reaction zone surface and the deviation of the incoming wall-constrained flow, in this low-Mach configuration.
- The heat losses suffered by the flame from the proximity of a cold wall.
- The heat retrocession from the burnt to the fresh gases, via conduction within the wall.

To conduct a deeper analysis of the flame/wall thermal coupling, the wall conductivity and the external convective heat transfer coefficient are varied. Under a small level of convective heat transfer with the ambient air surrounding the channel, the larger the thermal conductivity in the solid, the faster the reaction zone propagates in the vicinity of the wall, leaving the centreline reaction zone behind. The premixed flame front is then concave towards the fresh gases on the axis of symmetry (so-called tulip flame) with a flame speed higher than in the adiabatic case. Increasing the heat loss at the wall through convection with ambient air, the flame shape becomes convex (mushroom flame) and the flame speed decreases below its adiabatic level.

This study shows both that the flame speed is directly related to its topology and that an intricate coupling exists between the channel thermal characteristics and the flame topology. Consideration of the flame/wall thermal coupling and multi-dimensional simulations are thus necessary to model properly the flame dynamics.

7.2.3 Flame response to upstream heating

Reaction zone propagation in a narrow channel, after introducing heat upstream of a premixed flame front, is studied numerically in chapter 5. Various heating intensities are considered and a minimum heating supply is found necessary to initiate a complete flame translation. Quite logically, the distance over which the flame proceeds and the speed of the flash back, both depend on the amount of heat brought to the system. Several observations are made, analysing the transient simulations:

- A specific attention is paid on the relative contributions of heat convection in the flow, and heat conduction in the solid, on the flash back triggering. The heat transfer mechanism triggering the flame movement is revealed to be mainly convective.
- The flame translation is found to be organised in two stages, with first a downstream movement due to fresh gases expansion because of their heating by the wall, followed by the upstream propagation due to the enhancement of the burning rate by the preheating of the mixture.
- During the translation, the speed of the flame and its shape are shown to result from the intricate coupling between the wall temperature at the flame edge and the flow temperature on the centreline of the channel. Thus conduction of heat in the solid and convection in the fluid are both at play during flash back.

Similarly to the experiments evoked in this chapter, a simulated flame is found to stabilise in the heated area, confirming the possibility to position the premixed flame at a desired position.

7.2.4 Role of the gravity in the breaking of flame symmetry

Concerning flames propagating in horizontal small-scale channels, previous on-earth experiments show the stability of a slanted flame with a preferential anchoring at the top in place of a symmetric flame. Although not based on complete analyses, these studies state that this observation might be related to a natural convection effect surrounding the channel, favouring the heating of the superior part of the channel external surface.

Based on experiments, theory and numerics, chapter 6 provides a comprehensible explanation for the observation of this breaking of flame symmetry. Along with the experimental team composed of A. Pieyre and F. Richecoeur (EM2C lab, UPR 288 CNRS), this observation is pointed out to be recovered both when the flame propagates along cold walls and when it is stabilized and thermally coupled with the channel walls. Numerically, the physical phenomena at play are incorporated progressively to finally show the preponderant role played by gravity in the symmetry breaking. A theoretical analysis of the configuration is developed, predicting that gravity acts on the flame topology via a positive enhancement of the baroclinic torque at the flame crossing. This modification of the vorticity budget results in a deviation of the incoming streamlines in a coherent manner with the experimental observations. The analysis is supported by the post-processing of a series of simulations. Both in experiments and numerical

simulations, the flame is shown to exhibit a stronger inclination when thermally coupled with the channel walls than when propagating along cold walls. The influence of heat retro-cession on the flames inclination is analysed and explained.

Finally, further investigations show and comment the stabilizing effect of the wall external heating and the flame/wall proximity on the flame symmetric form, as observed in previous experiments. The nature of these stable tulip-shaped flames is based on auto-ignition, and is consequently quite different from self-sustained combustion.

7.3 Perspectives

The work presented in this manuscript could be improved and continued regarding several points: (1) the extension of the observations made in microgravity to on-earth conditions, (2) the ability to compare the simulations to experimental data, (3) the selection of the reference kinetic mechanism in the reduction process, (4) the study of thermally optimised micro-burners and (5) the study of catalytic combustion at small-scale. These points are now further discussed.

7.3.1 On-earth intricate boundary layer, heat recirculation and flame coupling

In chapter 6, gravity is demonstrated to have a decisive effect on flame topology. Besides, chapters 4 and 5 are the occasion to stress the coupling between the flame topology and its dynamics. However, these two chapters analyse flames in a microgravity context, which is not without interest in the light of the possible applications of micro-combustion. Still, the study of the gravity effect during upstream flame propagation, or while varying the thermal properties driving the channel heat transfer to the ambient, would be of interest.

7.3.2 Experimental comparisons

A special attention is paid to provide data with precision along the various analyses proposed. Although consistent with the experimental observations highlighted, the present results are not built to reproduce a specific experimental set-up. Further attention could be brought to the building of a numerical framework matching precisely an experiment in order to provide quantitative comparisons. Efforts would need to be made on the modelling of heat losses from the channel walls, notably their variations with the channel temperature. Tabulating radiative and convective heat transfer coefficients from experimental data could provide thorough comparisons.

7.3.3 Low temperature chemistry

During chapter 3, it is evoked that the choice of the GRI-1.2 mechanism, as a reference mechanism, is made due to its applicability to a reference simulation and the absence of complex kinetic mechanisms perfectly fitted to the present application. Indeed, from the difficulties in conducting experimental measurements close to the walls, the chemistry driving the edge-flame

quenching is little known and complex kinetic mechanisms adapted to edge-flame quenching are not available yet. Joint efforts with experimental teams and chemistry specialists would be of great help to develop such detailed mechanisms, which may subsequently be employed as references for the work presented in chapter 3.

7.3.4 Thermally optimised and catalytic burners

In the introduction, two methods for managing small-scale combustion are presented, as they would extend the flammability limits impairing the flame stability. The design of thermally optimised burner, favouring the excess enthalpy of fresh gases is seriously envisaged in practice as it presents now little technological challenge in terms of fabrication. Still, few combustion research works have been presented in this direction and employing the present numerical framework to this problem would be valuable. Besides, catalytic combustion has been studied for some times and small-scale burners are good candidates to this technology as they yield a close relation between the flame and the walls. The transfer of this knowledge to the field of micro-combustion would also be a step toward the feasibility of micro-burners.

Appendix A

Reduced mechanisms for small-scale combustion at $\phi = 0.8$ and $\phi = 0.7$

Chapter 3 introduced a reduction strategy, employed to derive a skeleton kinetic mechanism, fitted to model small-scale combustion at stoichiometric conditions. During the reduction from the reference GRI-1.2 mechanism, the targeted species were CH_4, O_2, H_2O, CO_2 and CO. The fitness function, defined for optimisation, involved the evolution of these species (versus space or time) and the flame speed in the case of the one-dimensional propagating premixed flames. The canonical stoichiometric flames computed for this reduction procedure involved:

- A zero-dimensional homogeneous reactor, whose initial temperature is varied between 1000 K and 1600 K.
- A freely propagating adiabatic one-dimensional premixed flame.
- A set of freely propagating one-dimensional premixed flames subjected to an amount of heat loss increasing up to flame quenching.

The resulting scheme is referred as 17S-53R-1.0. Simultaneously, a second kinetic mechanism, 15S-26R, involving 15 species and 26 reactions, was reduced considering only the freely propagating adiabatic one-dimensional premixed flame. Finally, both skeleton schemes were compared to the reference GRI-1.2 mechanism, revealing the interest of considering the zero-dimensional homogeneous reactor and the set of freely propagating one-dimensional premixed flames subjected to heat loss in the reduction process. In this appendix, skeleton mechanisms are reduced following a method similar to the 17S-53R-1.0, for equivalence ratios of 0.8 (17S-53R-0.8 in table A.1) and 0.7 (17S-53R-0.7 in table A.2). Results on the canonical problems are displayed bellow for information, without reproducing the complete analysis of chapter 3. Globally, the performances of 17S-53R-0.8 and 17S-53R-0.7 against the GRI-1.2 mechanism, at the corresponding equivalence ratios, are comparable to the ones of 17S-53R-1.0 under stoichiometric conditions.

	Reaction	A	β	E_a
1	$O+H_2 \leftrightharpoons H+OH$	4.720E+04	2.600	6160
2	$O+HO_2 \leftrightharpoons OH+O_2$	2.220E+13	0	0
3	$O+H_2O_2 \leftrightharpoons OH+HO_2$	6.320E+06	1.955	3975
4	$O+CH_3 \leftrightharpoons H+CH_2O$	4.810E+14	0	0
5	$O+CH_4 \leftrightharpoons OH+CH_3$	1.330E+09	1.508	8621
6	$O+HCO \leftrightharpoons OH+CO$	3.400E+13	0	0
7	$O+HCO \leftrightharpoons H+CO_2$	4.710E+13	0	0
8	$O+CH_2O \leftrightharpoons OH+HCO$	5.190E+13	0	3471
9	$O+CH_3O \leftrightharpoons OH+CH_2O$	1.420E+13	0	0
10	$O_2+CH_2O \leftrightharpoons HO_2+HCO$	1.950E+14	0	39215
11	$H+O_2+M \leftrightharpoons HO_2+M$	5.630E+18	-0.716	0
12	$H+2O_2 \leftrightharpoons HO_2+O_2$	4.150E+20	-1.658	0
13	$H+O_2+H_2O \leftrightharpoons HO_2+H_2O$	4.180E+18	-0.723	0
14	$H+O_2+N_2 \leftrightharpoons HO_2+N_2$	1.090E+20	-1.626	0
15	$H+O_2 \leftrightharpoons O+OH$	8.520E+13	0	14100
16	$H+HO_2 \leftrightharpoons O+H_2O$	1.910E+12	0	698
17	$H+HO_2 \leftrightharpoons O_2+H_2$	3.270E+13	0	1085
18	$H+HO_2 \leftrightharpoons 2OH$	6.030E+13	0	635
19	$H+H_2O_2 \leftrightharpoons HO_2+H_2$	9.640E+06	2.086	5320
20	$H+CH_3+M \leftrightharpoons CH_4+M$	3.300E+16	-0.525	387
21	$H+CH_4 \leftrightharpoons CH_3+H_2$	1.030E+09	1.608	11033
22	$H+HCO+M \leftrightharpoons CH_2O+M$	5.300E+11	0.483	0
23	$H+HCO \leftrightharpoons H_2+CO$	7.680E+13	0	0
24	$H+CH_2O+M \leftrightharpoons CH_3O+M$	1.440E+12	0.444	2665
25	$H+CH_2O \leftrightharpoons HCO+H_2$	3.080E+10	1.044	3335
26	$H+CH_3O \leftrightharpoons H2+CH_2O$	2.130E+13	0	0
27	$H+CH_3O \leftrightharpoons OH+CH_3$	3.640E+13	0	0
28	$OH+H_2 \leftrightharpoons H+H_2O$	3.580E+08	1.555	3606
29	$2OH+M \leftrightharpoons H_2O_2+M$	7.800E+13	-0.272	0
30	$2OH \leftrightharpoons O+H_2O$	3.840E+04	2.553	0
31	$OH+HO_2 \leftrightharpoons O_2+H_2O$	1.410E+14	0	0
32	$OH+H_2O_2 \leftrightharpoons HO_2+H_2O$	9.360E+14	0	9243
33	$OH+CH_4 \leftrightharpoons CH_3+H_2O$	5.770E+07	1.591	3107
34	$OH+CO \leftrightharpoons H+CO_2$	4.160E+07	1.242	70
35	$OH+HCO \leftrightharpoons H_2O+CO$	5.480E+13	0	0
36	$OH+CH_2O \leftrightharpoons HCO+H_2O$	4.200E+09	1.214	0
37	$OH+CH_3O \leftrightharpoons H_2O+CH_2O$	2.200E+13	0	0
38	$2HO_2 \leftrightharpoons O_2+H_2O_2$	2.020E+11	0	0
39	$2HO_2 \leftrightharpoons O_2+H_2O_2$	5.110E+14	0	12090
40	$HO_2+CH_3 \leftrightharpoons O_2+CH_4$	1.870E+12	0	0
41	$HO_2+CH_3 \leftrightharpoons OH+CH_3O$	3.470E+13	0	0
42	$HO_2+CO \leftrightharpoons OH+CO_2$	3.530E+14	0	23896
43	$HO_2+CH_2O \leftrightharpoons HCO+H_2O_2$	8.980E+11	0	7858
44	$CH_3+O_2 \leftrightharpoons O+CH_3O$	2.470E+13	0	28850
45	$CH_3+O_2 \leftrightharpoons OH+CH_2O$	1.640E+10	0	9026
46	$CH_3+H_2O_2 \leftrightharpoons HO_2+CH_4$	2.620E+04	2.616	4950
47	$2CH_3+M \leftrightharpoons C_2H_6+M$	8.620E+15	-0.857	619
48	$CH_3+HCO \leftrightharpoons CH_4+CO$	4.340E+13	0	0
49	$CH_3+CH_2O \leftrightharpoons HCO+CH_4$	3.440E+03	2.669	6139
50	$HCO+H_2O \leftrightharpoons H+CO+H_2O$	6.480E+17	-0.903	17515
51	$HCO+M \leftrightharpoons H+CO+M$	1.420E+17	-0.881	16678
52	$HCO+O_2 \leftrightharpoons HO_2+CO$	8.030E+12	0	396
53	$CH_3O+O_2 \leftrightharpoons HO_2+CH_2O$	4.280E-13	7.874	0

Table A.1: 17S-53R-0.8 kinetic mechanism. Units are mol, s, cm^3, cal and K. Reduced CH_4/Air scheme for the modelling of small-scale combustion at an equivalence ratio of 0.8. The Chaperon efficiencies of the GRI-1.2 mechanism are preserved for both three-body and fall-off reactions.

	Reaction	A	β	E_a
1	O+H_2⇋H+OH	5.480E+04	2.615	6101
2	O+HO_2⇋OH+O_2	1.100E+13	0	0
3	O+H_2O_2⇋OH+HO_2	8.130E+06	2.062	4005
4	O+CH_3⇋H+CH_2O	1.570E+14	0	0
5	O+CH_4⇋OH+CH_3	6.030E+08	1.456	8628
6	O+HCO⇋OH+CO	2.440E+13	0	0
7	O+HCO⇋H+CO_2	2.030E+13	0	0
8	O+CH_2O⇋OH+HCO	2.400E+13	0	3519
9	O+CH_3O⇋OH+CH_2O	8.690E+12	0	0
10	O_2+CH_2O⇋HO_2+HCO	9.060E+13	0	40421
11	H+O_2+M⇋HO_2+M	3.600E+18	-0.866	0
12	H+2O_2⇋HO_2+O_2	4.880E+20	-1.721	0
13	H+O_2+H_2O⇋HO_2+H_2O	1.140E+19	-0.772	0
14	H+O_2+N_2⇋HO_2+N_2	5.130E+20	-1.772	0
15	H+O_2⇋O+OH	1.410E+14	0	14465
16	H+HO_2⇋O+H_2O	2.540E+12	0	656
17	H+HO_2⇋O_2+H_2	4.370E+13	0	1059
18	H+HO_2⇋2OH	9.310E+13	0	622
19	H+H_2O_2⇋HO_2+H_2	1.460E+07	2.027	5059
20	H+CH_3+M⇋CH_4+M	3.360E+16	-0.612	375
21	H+CH_4⇋CH_3+H_2	6.990E+08	1.637	10982
22	H+HCO+M⇋CH_2O+M	7.990E+11	0.465	0
23	H+HCO⇋H_2+CO	6.000E+13	0	0
24	H+CH_2O+M⇋CH_3O+M	3.870E+11	0.462	2519
25	H+CH_2O⇋HCO+H_2	2.080E+10	1.039	3239
26	H+CH_3O⇋H2+CH_2O	1.720E+13	0	0
27	H+CH_3O⇋OH+CH_3	2.620E+13	0	0
28	OH+H_2⇋H+H_2O	2.600E+08	1.543	3463
29	2OH+M⇋H_2O_2+M	8.170E+13	-0.371	0
30	2OH⇋O+H_2O	3.600E+04	2.359	0
31	OH+HO_2⇋O_2+H_2O	3.200E+13	0	0
32	OH+H_2O_2⇋HO_2+H_2O	8.460E+14	0	9579
33	OH+CH_4⇋CH_3+H_2O	7.740E+07	1.585	3117
34	OH+CO⇋H+CO_2	5.450E+07	1.209	71
35	OH+HCO⇋H_2O+CO	3.300E+13	0	0
36	OH+CH_2O⇋HCO+H_2O	3.650E+09	1.206	0
37	OH+CH_3O⇋H_2O+CH_2O	4.830E+12	0	0
38	2HO_2⇋O_2+H_2O_2	1.380E+11	0	0
39	2HO_2⇋O_2+H_2O_2	6.320E+14	0	11863
40	HO_2+CH_3⇋O_2+CH_4	1.180E+12	0	0
41	HO_2+CH_3⇋OH+CH_3O	1.490E+13	0	0
42	HO_2+CO⇋OH+CO_2	9.220E+13	0	23676
43	HO_2+CH_2O⇋HCO+H_2O_2	9.780E+11	0	8223
44	CH_3+O_2⇋O+CH_3O	2.660E+13	0	28673
45	CH_3+O_2⇋OH+CH_2O	3.180E+10	0	9067
46	CH_3+H_2O_2⇋HO_2+CH_4	2.330E+04	2.402	5121
47	2CH_3+M⇋C_2H_6+M	1.030E+16	-0.962	619
48	CH_3+HCO⇋CH_4+CO	3.800E+13	0	0
49	CH_3+CH_2O⇋HCO+CH_4	3.270E+03	2.760	5797
50	HCO+H_2O⇋H+CO+H_2O	2.690E+18	-0.975	17218
51	HCO+M⇋H+CO+M	1.140E+17	-1.027	17310
52	HCO+O_2⇋HO_2+CO	7.660E+12	0	398
53	CH_3O+O_2⇋HO_2+CH_2O	4.280E-13	7.901	0

Table A.2: 17S-53R-0.7 kinetic mechanism. Units are mol, s, cm^3, cal and K. Reduced CH_4/Air scheme for the modelling of small-scale combustion at $\phi = 0.7$. The Chaperon efficiencies of the GRI-1.2 mechanism are preserved for both three-body and fall-off reactions.

A.1 17S-53R-0.8 mechanism assessment

A.1.1 Flame speed

For $\phi = 0.8$ under SCTP , figure A.1 shows the flame speeds obtained with the skeletal mechanism and the detailed chemistry. The parameter α_{loss} is varied from the adiabatic condition ($\alpha_{\text{loss}} = 0$) up to flame quenching. Quenching is observed for $\alpha_{\text{loss}} = 38.5$ kW.m^{-3}.K^{-1} with the reference detailed mechanism and $\alpha_{\text{loss}} = 36.5$ kW.m^{-3}.K^{-1} with 17S-53R-0.8.

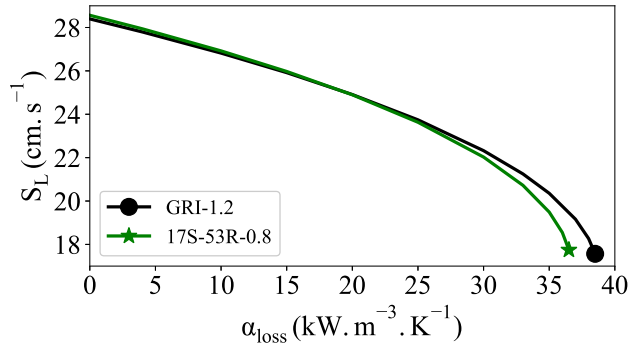

Figure A.1: Flame velocity value vs heat loss down to quenching conditions.

A.1.2 Auto-ignition delays

Auto-ignition delays are reproduced in a satisfactory manner by the 17S-53-0.8 mechanism (see figure A.2).

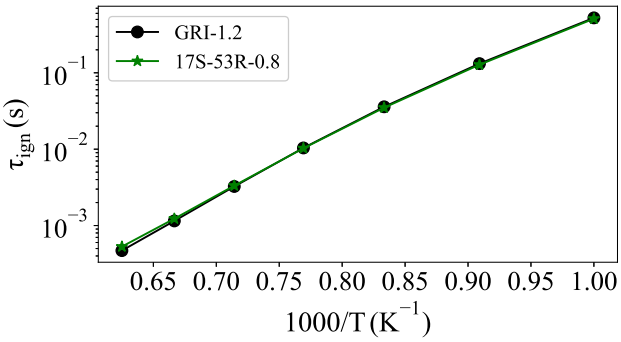

Figure A.2: Auto-ignition delays.

A.1.3 1D flame profiles

In figure A.3, the distributions of temperature, major target species and minor species obtained with the 17S-53R-0.8 chemical kinetics are compared to the detailed reference mechanism.

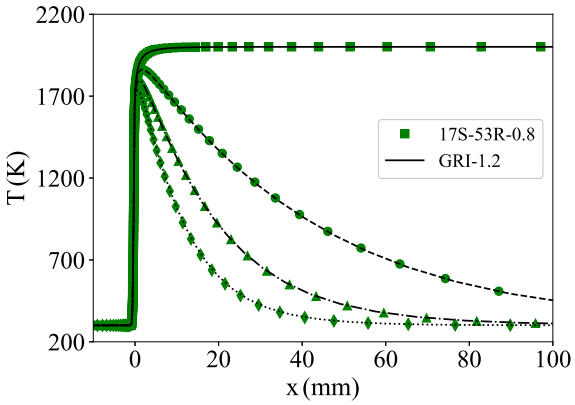

(a) T

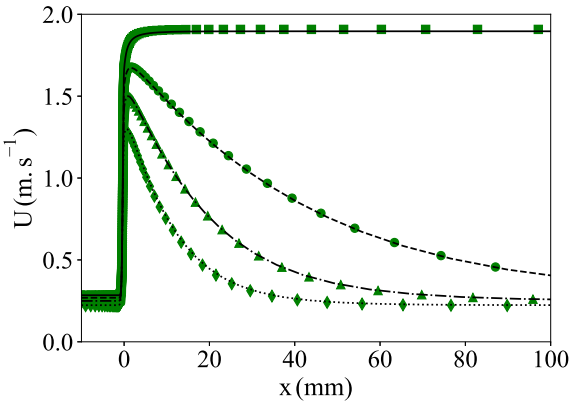

(b) U

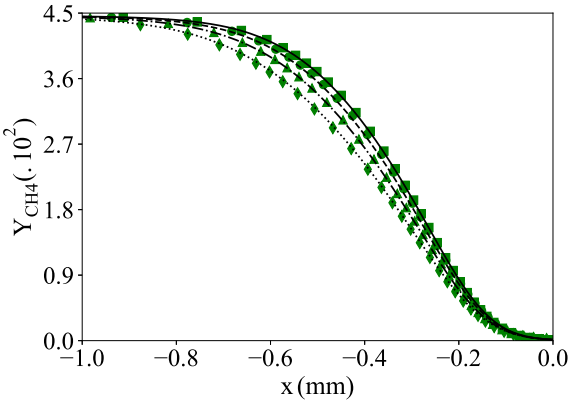

(c) CH_4

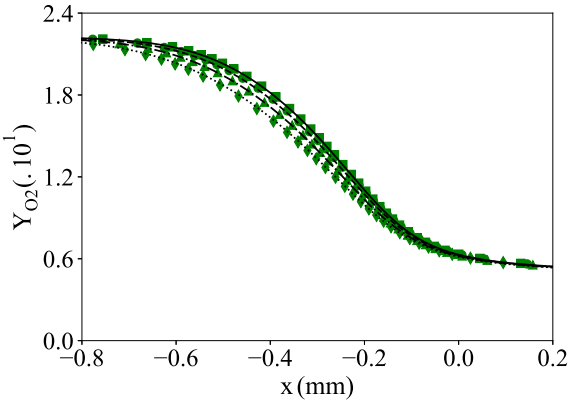

(d) O_2

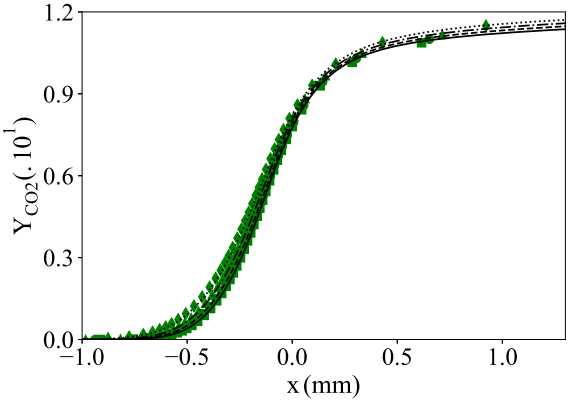

(e) CO_2

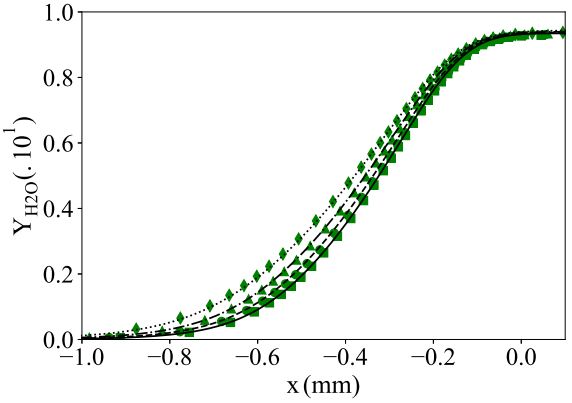

(f) H_2O

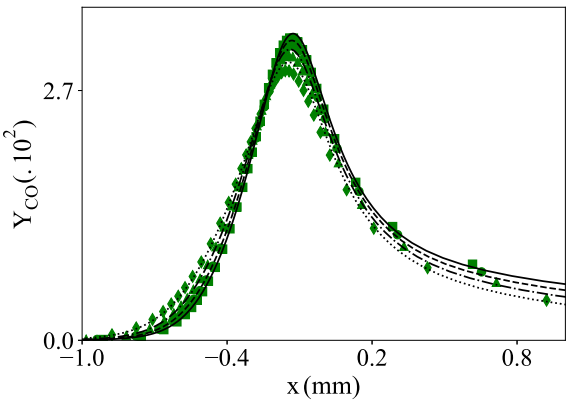

(g) CO

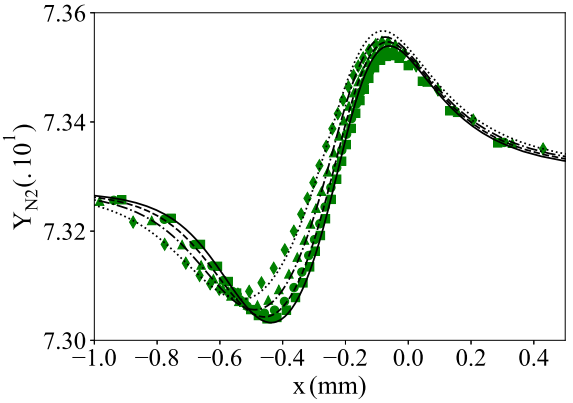

(h) N_2

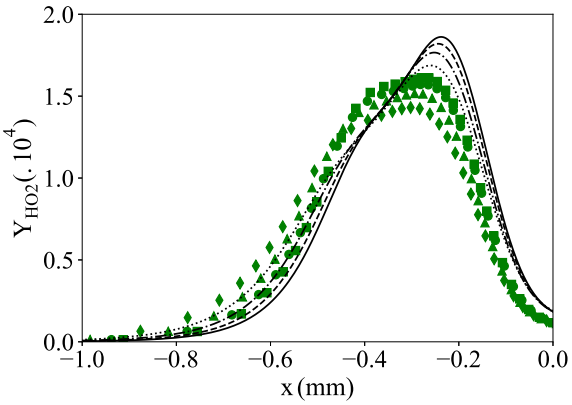

(i) HO_2

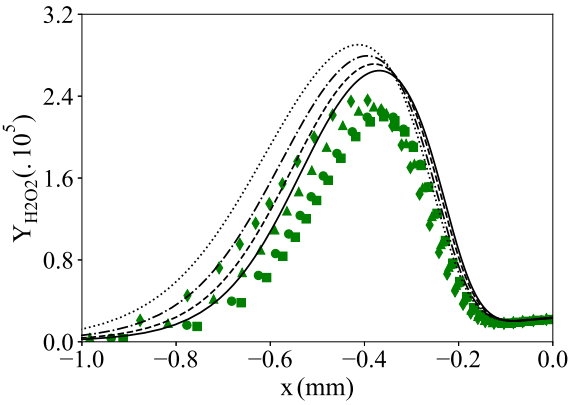

(j) H_2O_2

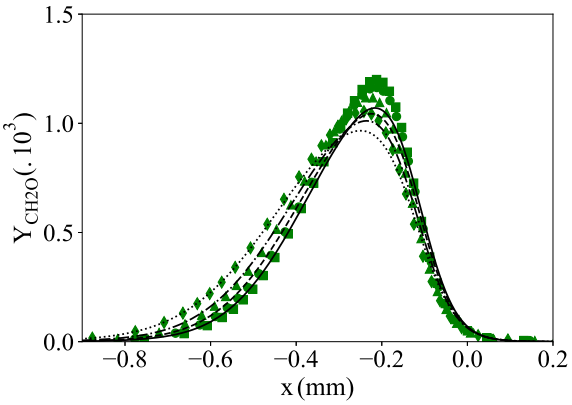

(k) CH_2O

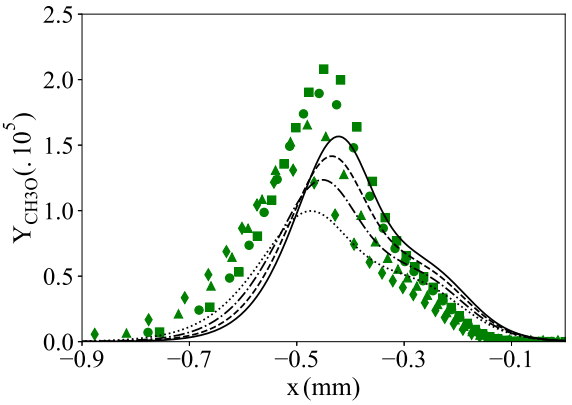

(l) CH_3O

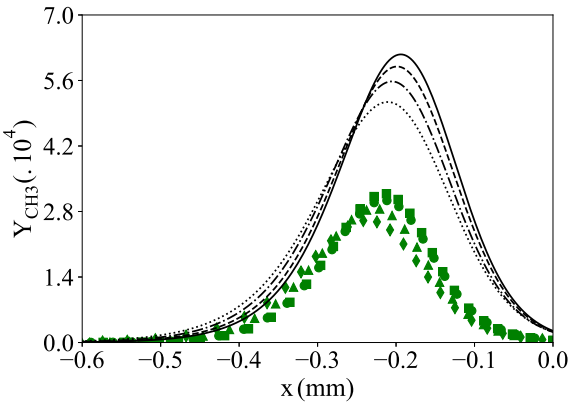

(m) CH_3

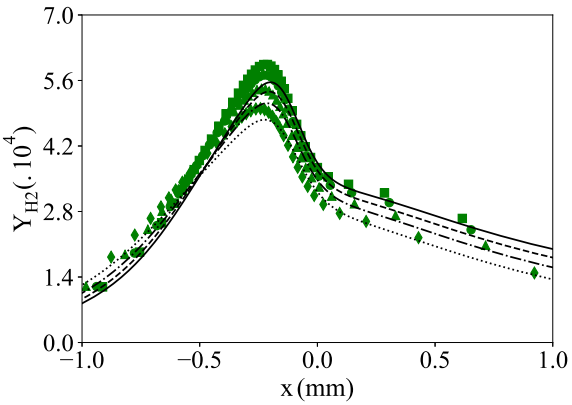

(n) H_2

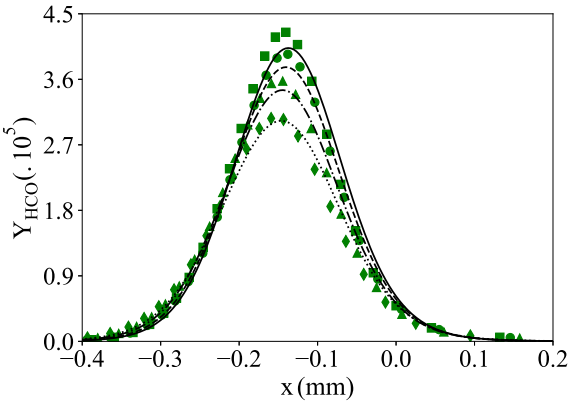

(o) HCO

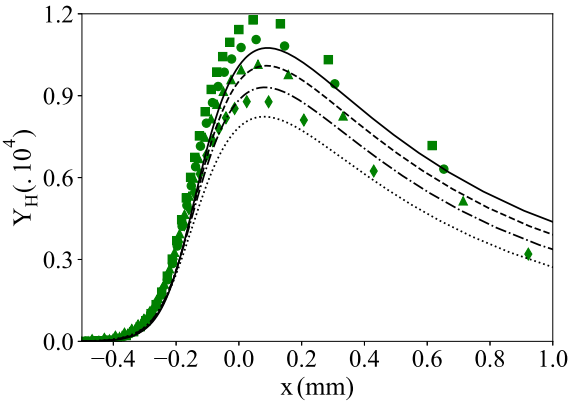

(p) H

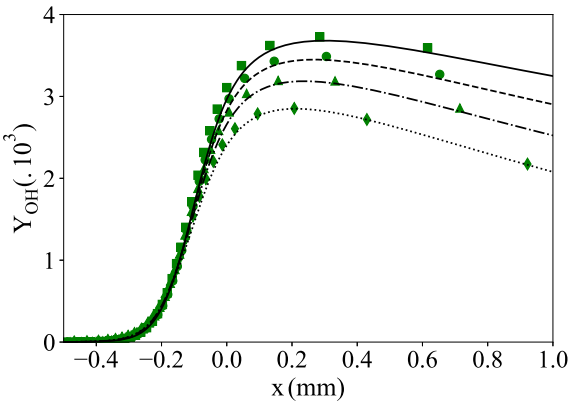

(q) OH

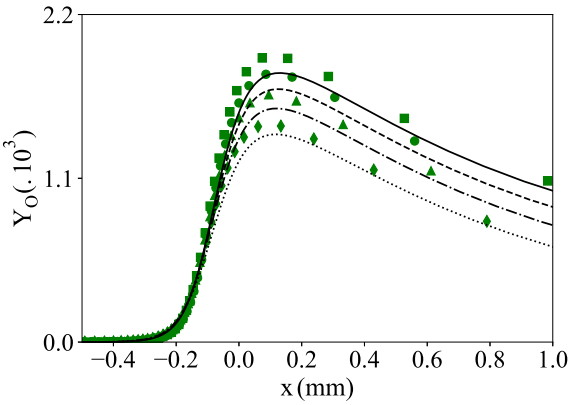

(r) O

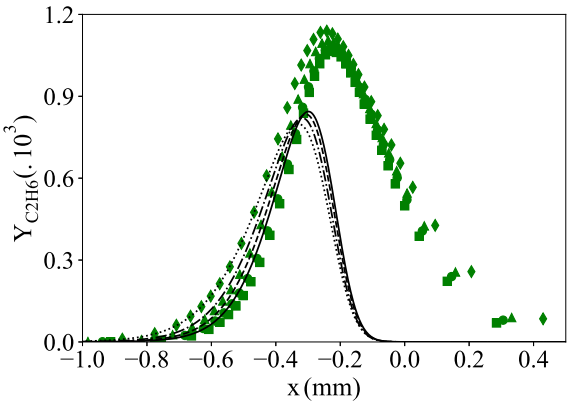

(s) C_2H_6

Figure A.3: Comparison between detailed (GRI-1.2 [41]) and 17S-53R-0.8 (table A.1) reduced chemistry. 1D profiles are provided for the four reference trajectories of the 17S-53R-0.8 scheme reduction. Lines: GRI-1.2. Full points: 17S-53R-0.8. $\alpha_{\text{loss}} = 0$ kW.m^{-3}.K^{-1}: full line and squares. $\alpha_{\text{loss}} = 10$ kW.m^{-3}.K^{-1}: dashed line and circles. $\alpha_{\text{loss}} = 20$ kW.m^{-3}.K^{-1}: dash-dotted line and triangles. $\alpha_{\text{loss}} = 30$ kW.m^{-3}.K^{-1}: dotted line and diamonds.

A.2 17S-53R-0.7 mechanism assessment

A.2.1 Flame speed

For $\phi = 0.7$ under SCTP (Standard Conditions for Temperature and Pressure), figure A.4 shows the flame speeds obtained with the skeletal mechanism and the detailed chemistry. The parameter α_{loss} is varied from the adiabatic condition ($\alpha_{\text{loss}} = 0$) up to flame quenching. Quenching is observed for $\alpha_{\text{loss}} = 16.7$ kW·m^{-3}·K^{-1} with the reference detailed mechanism and $\alpha_{\text{loss}} = 15.4$ kW.m^{-3}.K^{-1} with 17S-53R-0.7.

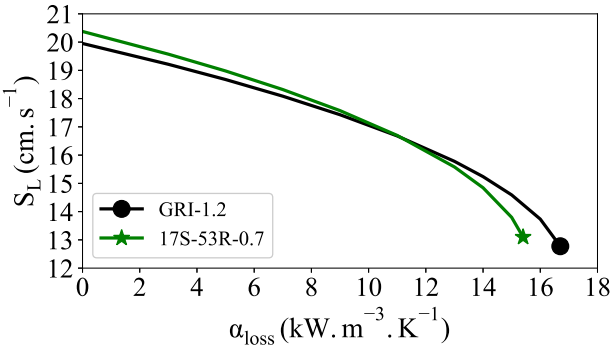

Figure A.4: Flame velocity value vs heat loss down to quenching conditions.

A.2.2 Auto-ignition delays

Now again, auto-ignition delays are reproduced in a satisfactory manner by the 17S-53-0.7 mechanism (see figure A.5).

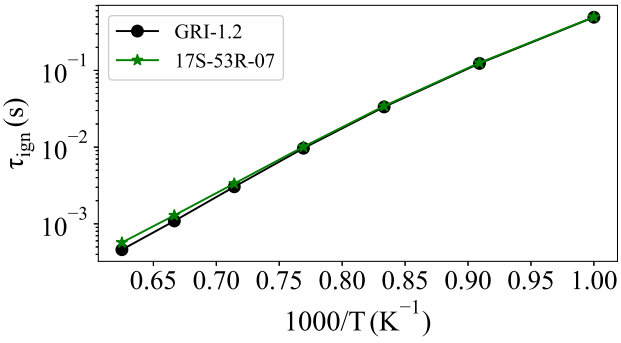

Figure A.5: Auto-ignition delays.

A.2.3 1D flame profiles

In figure A.6, the distributions of temperature, major target species and minor species obtained with the 17S-53R-0.7 chemical kinetics are compared to the detailed reference mechanism.

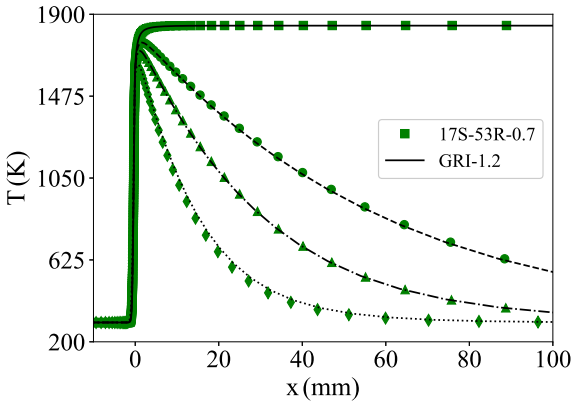

(a) T

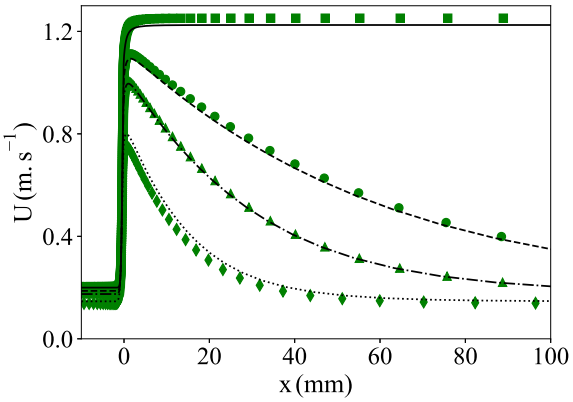

(b) U

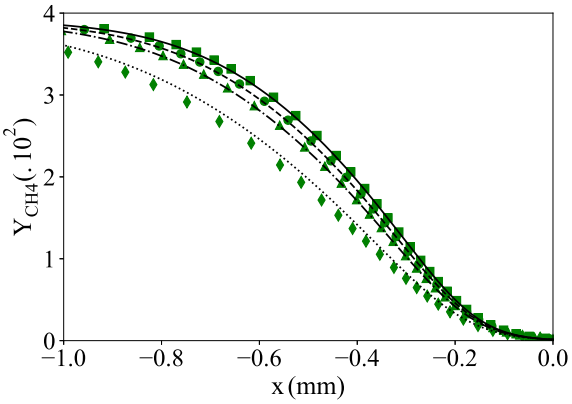

(c) CH_4

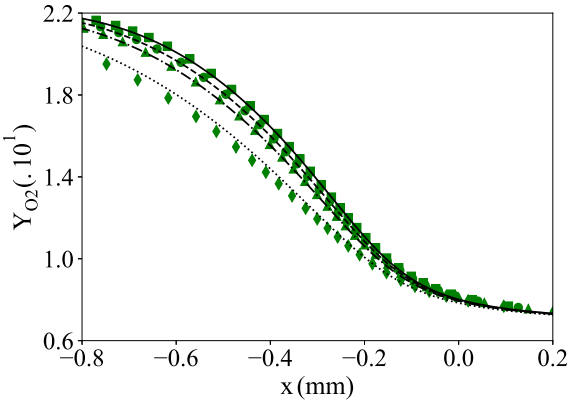

(d) O_2

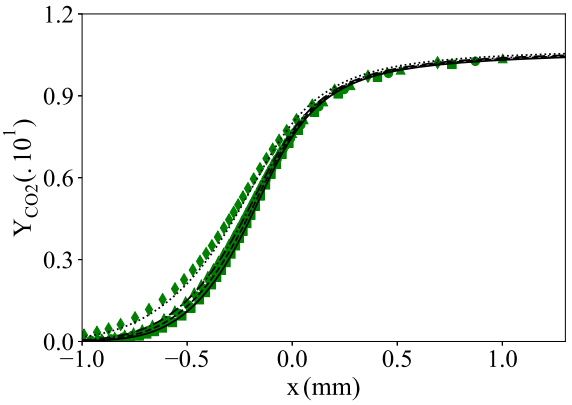

(e) CO_2

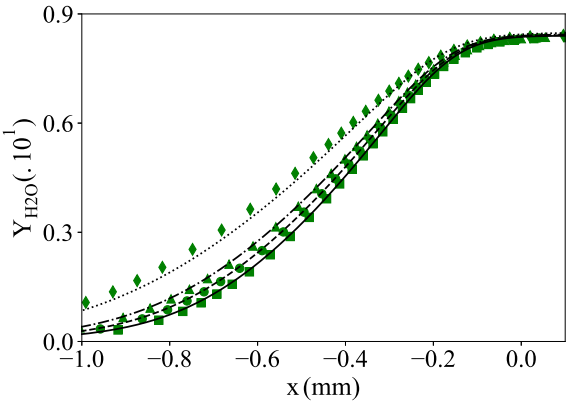

(f) H_2O

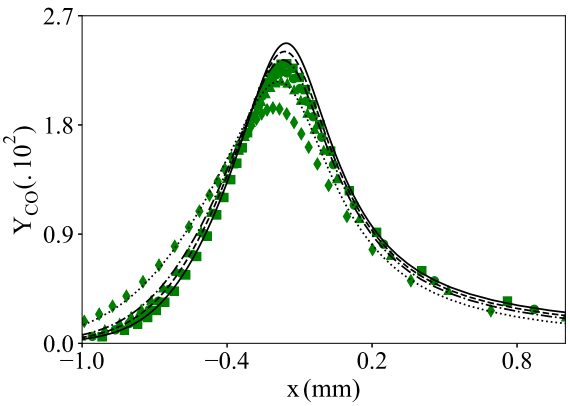

(g) CO

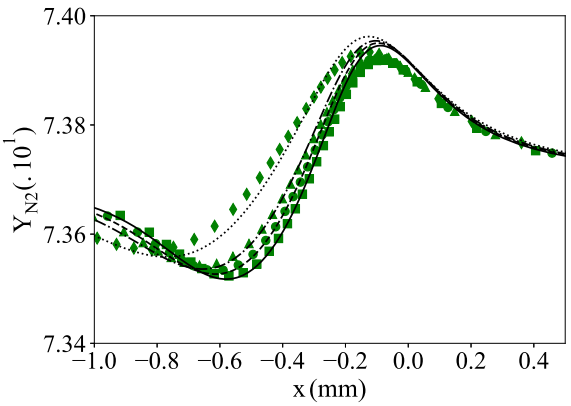

(h) N_2

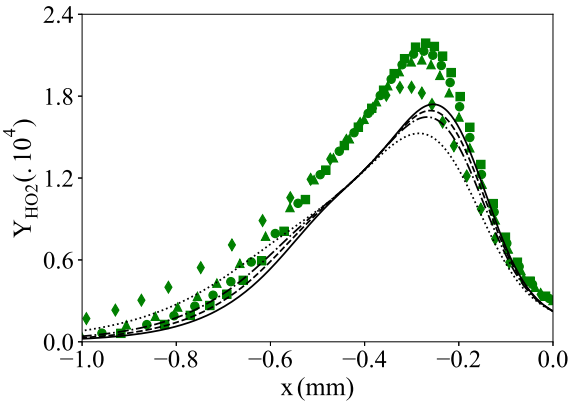

(i) HO_2

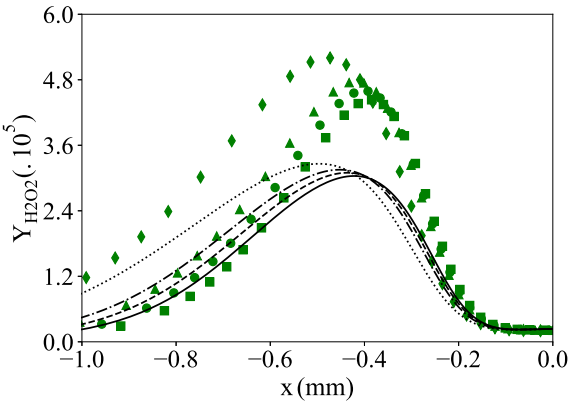

(j) H_2O_2

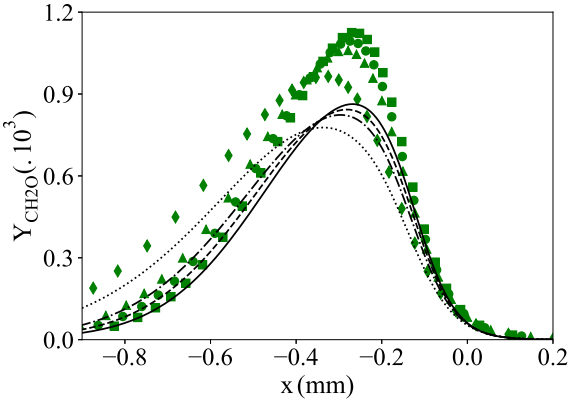

(k) CH_2O

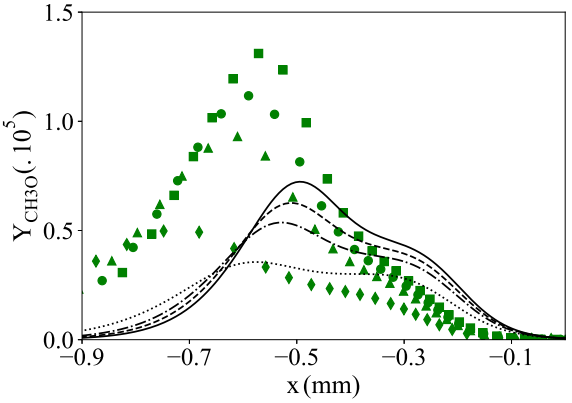

(l) CH_3O

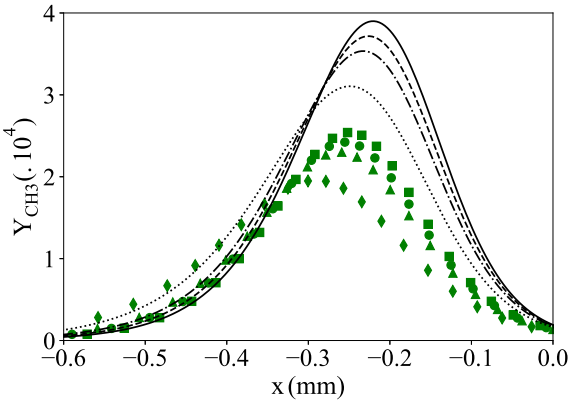

(m) CH_3

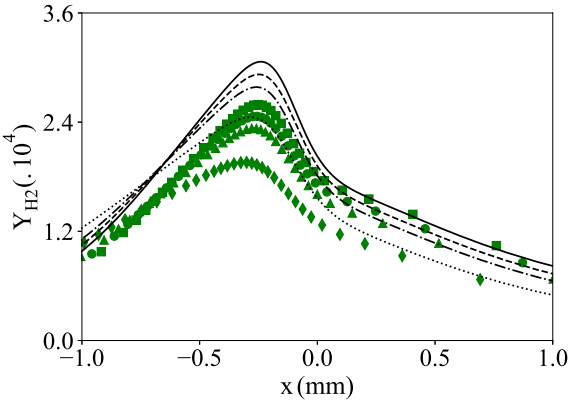

(n) H_2

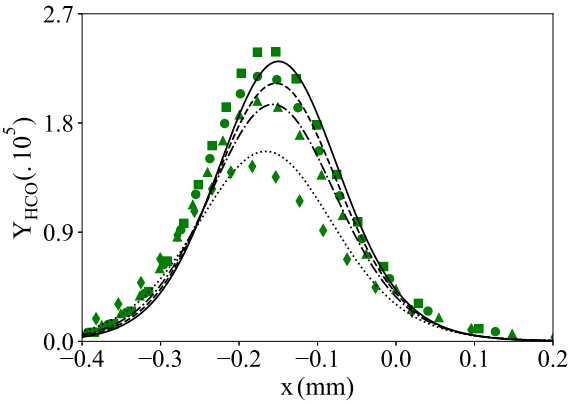

(o) HCO

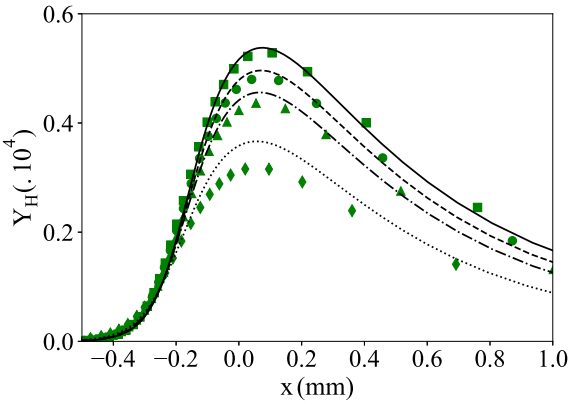

(p) H

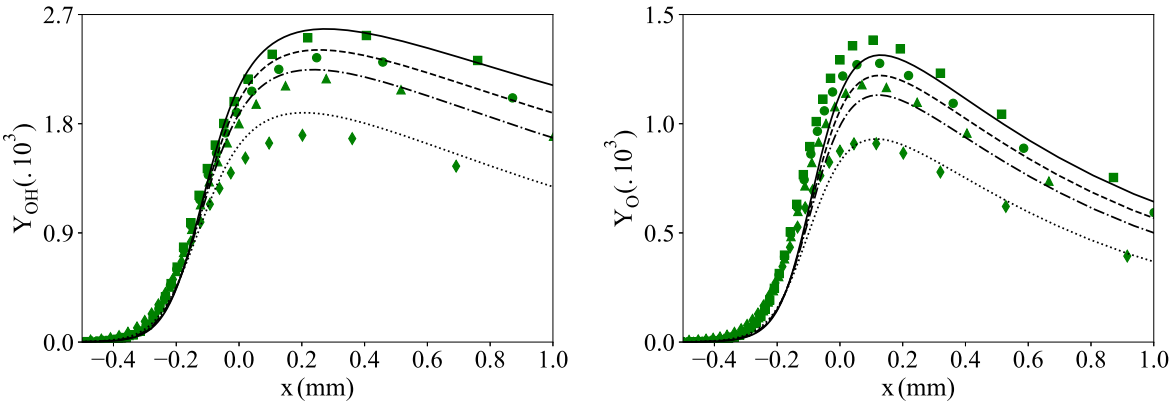

(q) OH (r) O

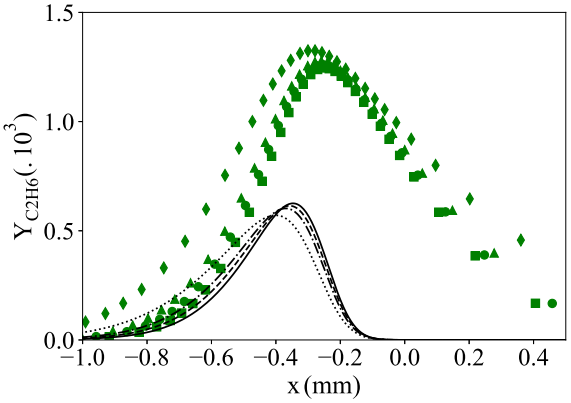

(s) C_2H_6

Figure A.6: Comparison between detailed (GRI-1.2 [41]) and 17S-53R-0.7 (table A.2) reduced chemistry. 1D profiles are provided for the four reference trajectories of the 17S-53R-0.7 scheme reduction. Lines: GRI-1.2. Full points: 17S-53R-0.7. $\alpha_{\text{loss}} = 0$ kW.m^{-3}.K^{-1}: full line and squares. $\alpha_{\text{loss}} = 5$ kW.m^{-3}.K^{-1}: dashed line and circles. $\alpha_{\text{loss}} = 9$ kW.m^{-3}.K^{-1}: dash-dotted line and triangles. $\alpha_{\text{loss}} = 15$ kW.m^{-3}.K^{-1}: dotted line and diamonds.

Appendix B

Meshing for DNS

In this appendix, the mesh refinement required in SiTCom-B to capture the flame front of a stoichiometric adiabatic flame, modelled with the schemes 15S-26R, 17S-53R-1.0 and GRI-1.2, is estimated. Results are compared to the ones furnished by Cantera simulations, whose automatic mesh refinement permits to capture perfectly the flame front. Various mesh resolutions are tested with SiTCom-B. The first mesh resolution tested is 50 µm, which is at the upper limit for the DNS of CH_4/air flames find in the litterature. Refer to the study of side wall quenching [42], where the 16 species and 25 reactions mechanism by Smooke and Giovangigli [138] was employed on a 50 µm mesh, based on the commonly-employed criterion requiring for the mesh resolution to be ten times finer than the flame thickness. Depending on the kinetic mechanism, finer mesh resolutions are tested until providing satisfactory results.

- For the skeleton schemes **15S-26R** and **17S-53R-1.0**, the **25 µm** mesh resolution is shown to improve significantly the results and is selected for future simulations.
- A mesh resolution of **12.5 µm** is found more appropriate in the case of the detailed **GRI-1.2** mechanism.

B.1 15S-26R

Figure B.1 gathers the comparison of the mass fraction and species source term profiles obtained with SiTCom-B (50 µm) and Cantera. Globally, results obtained from SiTCom-B with this mesh resolution yield a behaviour coherent with the reference. The mass fraction profiles of main and most intermediate species follow the Cantera solution. Although the H radical presents small discrepancies with the reference (figure B.1(e)), the mass fractions profiles seem satisfactory overall. Still, although they are not systematically mobilised when comparing kinetics across a flame, species source terms profiles offer a deeper sight of the flame resolution. When analysing figures B.1(b), B.1(d) and B.1(f), it is revealed that almost none of the source terms is properly seized with the 50 µm mesh resolution. The profiles do not capture accurately the peaks, compared to the perfectly resolved Cantera flame.

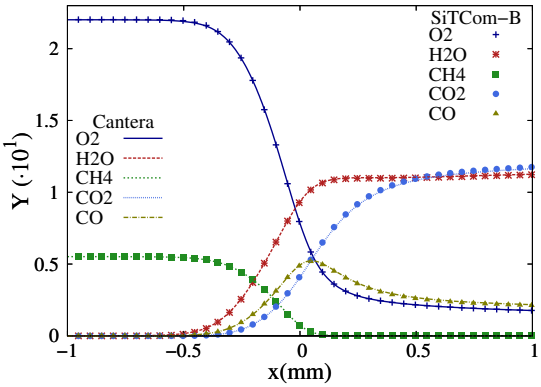

(a) Mass fraction profiles.

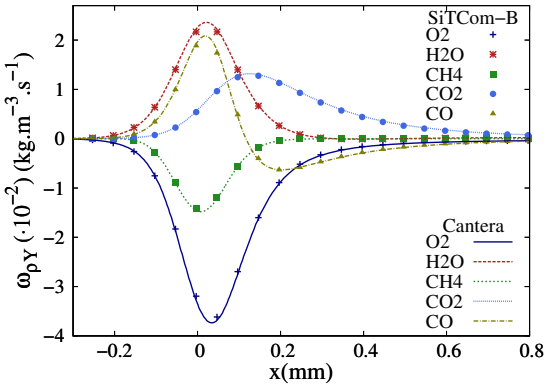

(b) Species source term profiles.

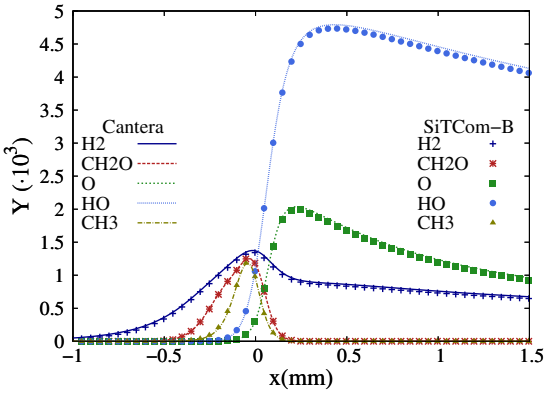

(c) Mass fraction profiles.

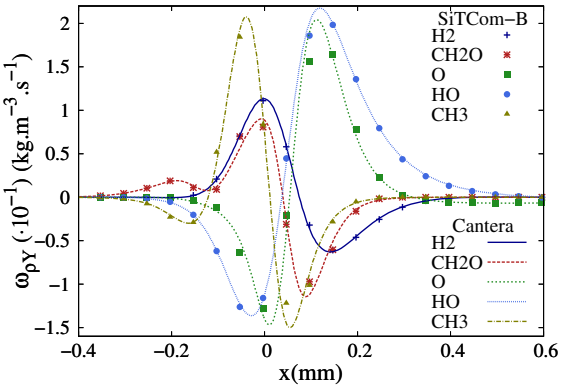

(d) Species source term profiles.

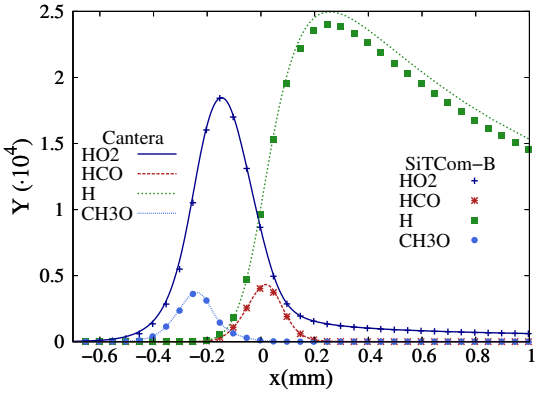

(e) Mass fraction profiles.

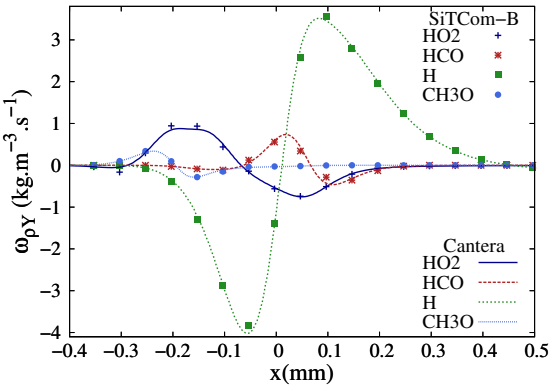

(f) Species source term profiles.

Figure B.1: Comparison of the mass fraction and species source term profiles, across an adiabatic stoichiometric methane/air flame, computed with different codes and mesh resolutions. Lines: Cantera (reference). Symbols : SiTCom-B (50 µm). 15S-26R scheme.

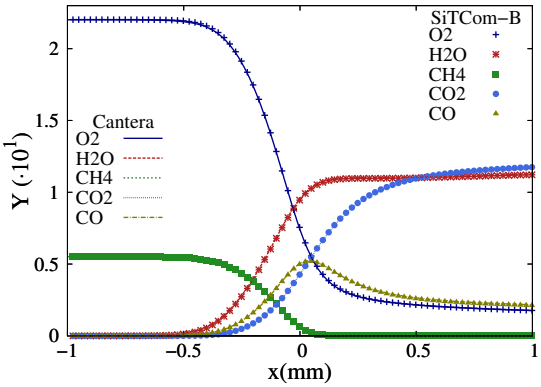

(a) Mass fraction profiles.

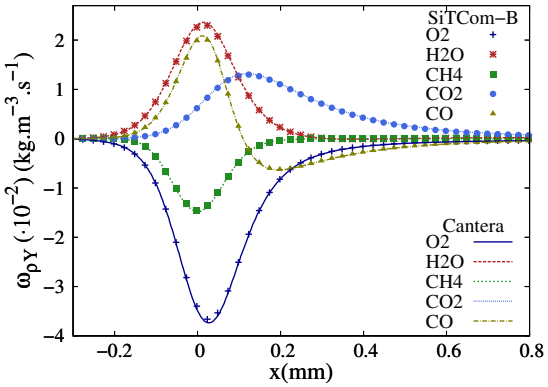

(b) Species source term profiles.

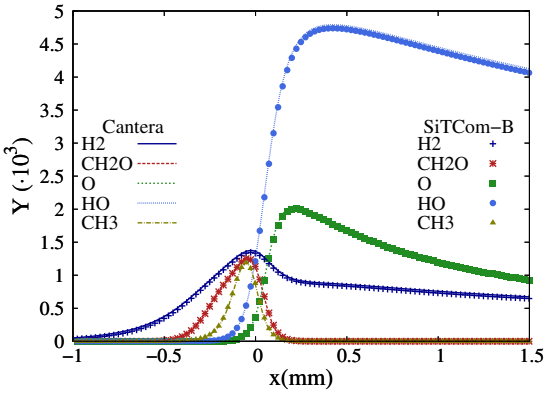

(c) Mass fraction profiles.

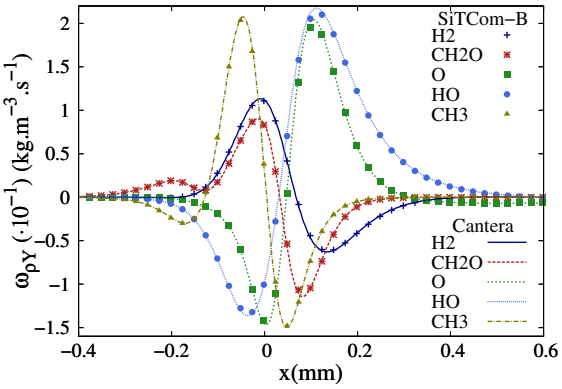

(d) Species source term profiles.

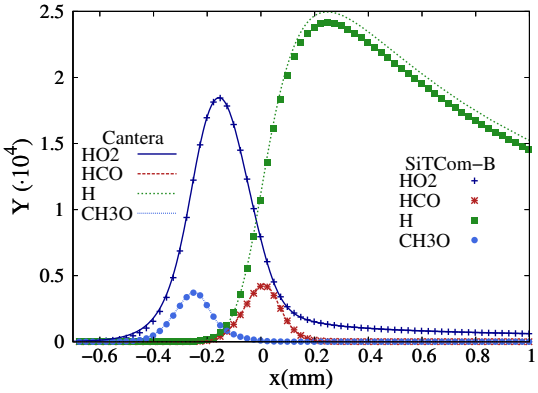

(e) Mass fraction profiles.

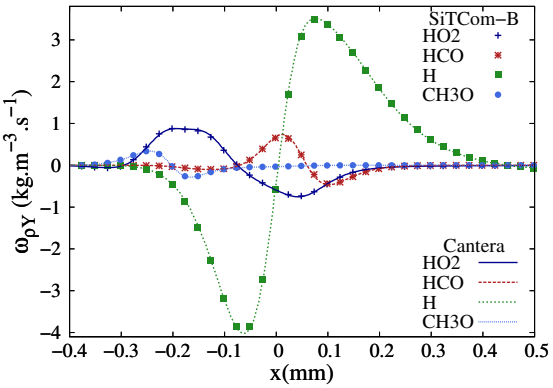

(f) Species source term profiles.

Figure B.2: Comparison of the mass fraction and species source term profiles, across an adiabatic stoichiometric methane/air flame, computed with different codes and mesh resolutions. Lines: Cantera (reference). Symbols : SiTCom-B (25 µm). 15S-26R scheme.

Figure B.2 displays the mass fraction and species source term profiles obtained with SiTCom-B (25 µm) and Cantera. By using a finer mesh, the gap present between Cantera and SiTCom-B simulations is strongly reduced. This achievement is especially visible on the species source term profiles which, although they are not perfect, yield far better results. In response, mass fraction profiles are also better respected, see HO_2 for example.

	Cantera	SiTCom-B (25 µm)	SiTCom-B (50 µm)	Units
S_L^o	38.47	38.03	37.71	$cm.s^{-1}$
T_F^o	2231	2231	2231	K
δ_F^o	448	451	453	µm

Table B.1: Adiabatic flame speed, temperature and thickness obtained with different codes and mesh refinement. 15S-26R scheme.

Finally, results of the three simulations on key flame characteristics are gathered in table B.1. With a mesh resolution of 50 µm, the errors on estimations are 1.5 % for the flame thickness, 2 % for the flame speed and minus than 1 ‰ for the burnt gas temperature. The mesh refinement to 25 µm improves the flame thickness and velocity predictions to 0.7 % and 1 %, respectively. As evoked in the literature, flame quenching requires a fine description of the kinetics. The peak values of main and intermediate species source terms are far better recovered with the finer mesh, making this resolution more reliable for the flame structure description. In consequence, for the 15S-26R kinetic mechanism, DNS will be secured with the finer mesh resolution all along the manuscript.

B.2 17S-53R-1.0

	Cantera	SiTCom-B (25 µm)	SiTCom-B (50 µm)	Units
S_L^o	39.46	39.06	38.72	$cm.s^{-1}$
T_F^o	2231	2231	2231	K
δ_F^o	437	439	446	µm

Table B.2: Adiabatic flame speed, temperature and thickness obtained with different codes and mesh refinement. 17S-53R-1.0 scheme.

The previous analysis is repeated here, for the 17S-53R-1.0 kinetic mechanism. Comparisons of mass fractions and species source terms profiles are provided in figures B.3 (50 µm) and B.4 (25 µm). Compared to the coarser, the 25 µm mesh resolution is again shown to improve the results, especially on the estimation of the species source terms peaks. Flame characteristics obtained from each solution are displayed in table B.2. Both the prediction of flame speed and the flame thickness are improved by the refinement. Accuracy on the flame speed passes from 1.9 % to 1 %, and on the flame thickness from 2.1 % to 0.5 %. In the light of the precision and

the time of return expected from the simulations, the mesh refinement 25 µm is selected for use in the whole manuscript.

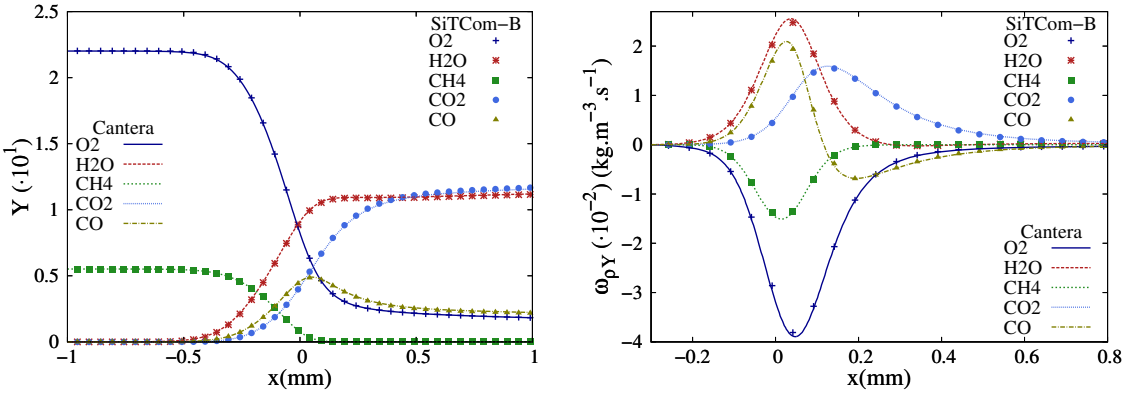

(a) Mass fraction profiles. (b) Species source term profiles.

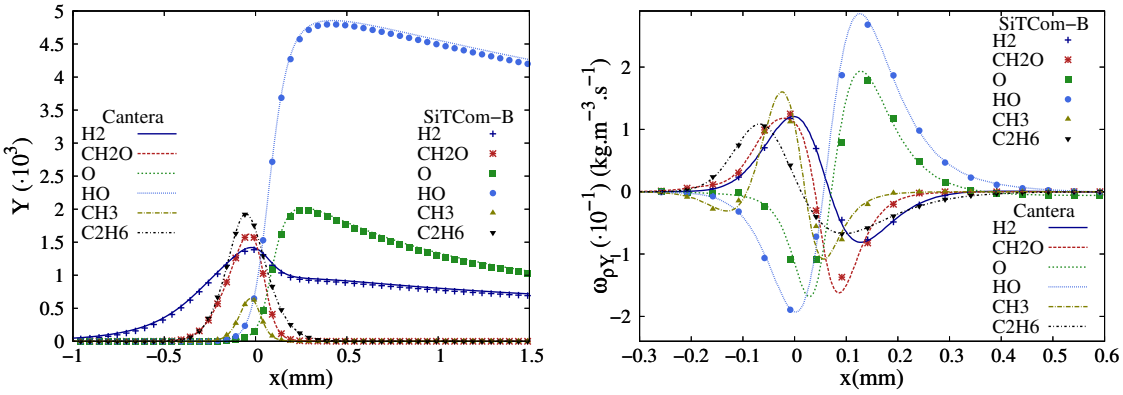

(c) Mass fraction profiles. (d) Species source term profiles.

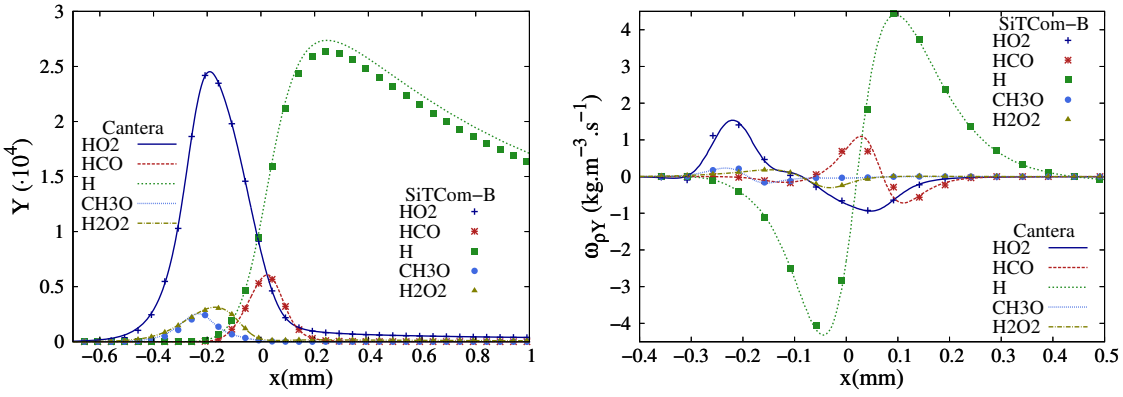

(e) Mass fraction profiles. (f) Species source term profiles.

Figure B.3: Comparison of the mass fraction and species source term profiles, across an adiabatic stoichiometric methane/air flame, computed with different codes and mesh resolutions. Lines: Cantera (reference). Symbols : SiTCom-B (50 µm). 17S-53R scheme.

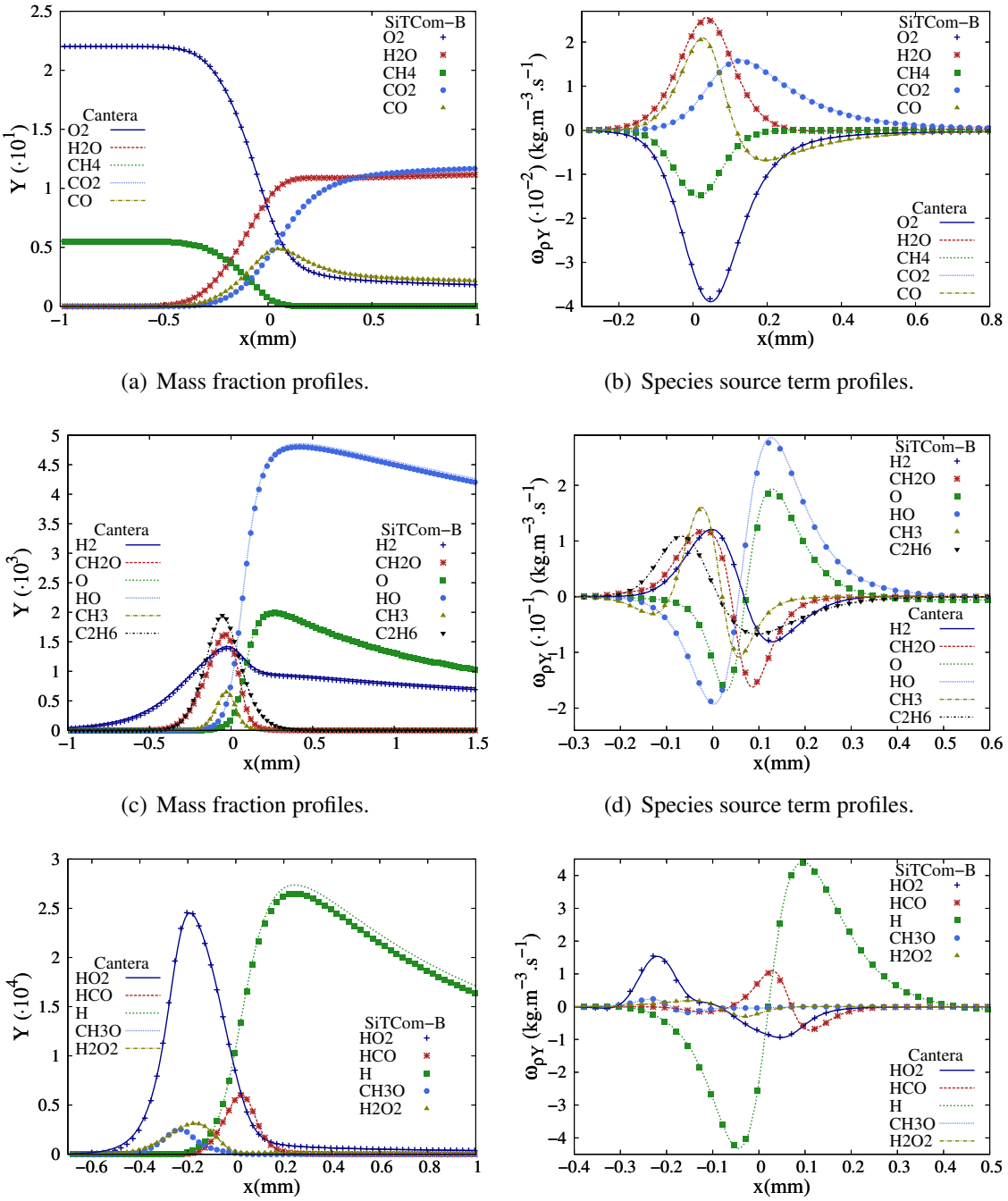

(a) Mass fraction profiles.

(b) Species source term profiles.

(c) Mass fraction profiles.

(d) Species source term profiles.

(e) Mass fraction profiles.

(f) Species source term profiles.

Figure B.4: Comparison of the mass fraction and species source term profiles, across an adiabatic stoichiometric methane/air flame, computed with different codes and mesh resolutions. Lines: Cantera (reference). Symbols : SiTCom-B (25 µm). 17S-53R scheme.

B.3 GRI-1.2

Concerning the detailed mechanism, convergence of 1D flames could not be achieved with the mesh resolutions of 50 and 25 µm. Indeed, when kinetic mechanisms rely on the description of numerous intermediate species, to coarse meshes can impair the convergence of solutions. This is directly due to an insufficient precision in the capture of these species evolution across the flame. To yield stable results, a finer resolution of 12.5 µm was found necessary. This resolution exhibits a loyal description of the flame structure, see figure B.5. The mass fractions profiles are almost perfectly seized, also when looking at intermediate species present over quite thin reaction layers such as HCCO (figure B.5(e)), CH_2OH (figure B.5(i)) or C_2H (figure B.5(k)). This quality of the mass fraction profiles description directly relates to the excellent resolution of the species source term profiles, from main (figure B.5(b)) to intermediate species (figures B.5(d), B.5(f), B.5(h), B.5(j) and B.5(l)), with this refinement. Table B.3 shows that the flame characteristics are also excellently replicated with this mesh resolution. Errors to the reference Cantera simulation are 0.3 % for the flame velocity, minus than 1 ‰ for the flame temperature and 0.2 % for the flame thickness. To secure the DNS and provide a reliable reference simulation, the mesh resolution of 12.5 µm is conserved for the detailed GRI-1.2 mechanism.

	Cantera	SiTCom-B (12.5 µm)	Units
S_L^o	39.02	38.91	$cm.s^{-1}$
T_F^o	2231	2231	K
δ_F^o	426	427	µm

Table B.3: Adiabatic flame speed, temperature and thickness obtained with different codes and mesh refinement. GRI-1.2 scheme.

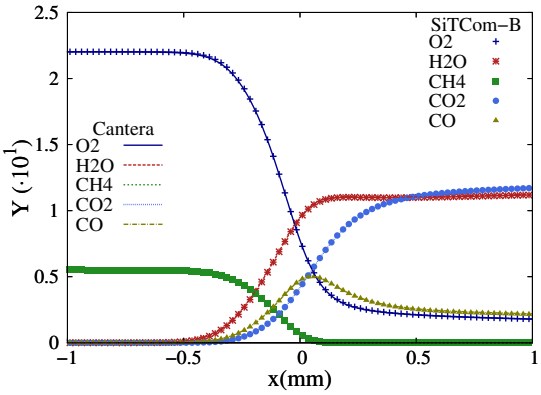

(a) Mass fraction profiles.

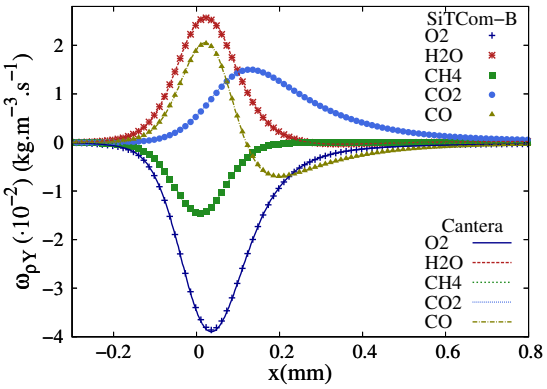

(b) Species source term profiles.

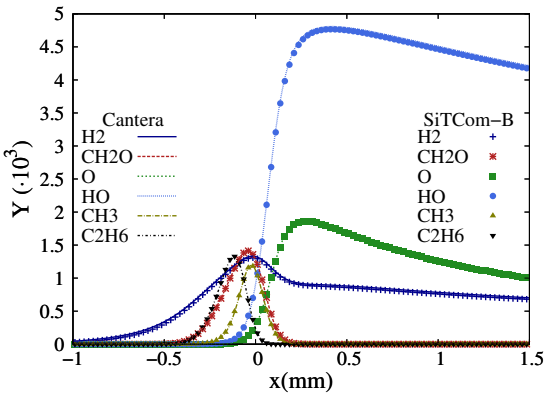

(c) Mass fraction profiles.

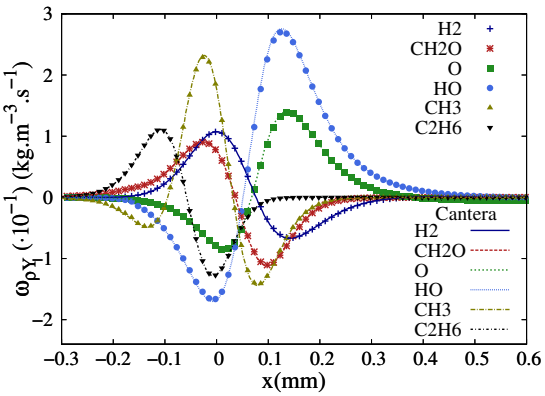

(d) Species source term profiles.

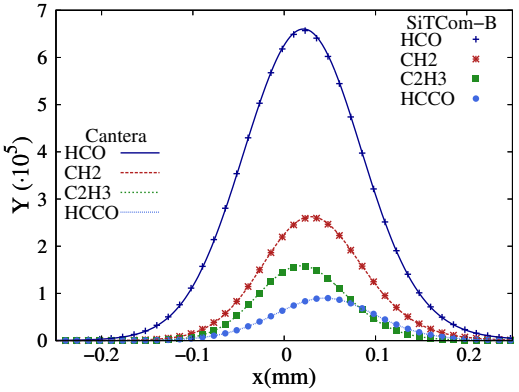

(e) Mass fraction profiles.

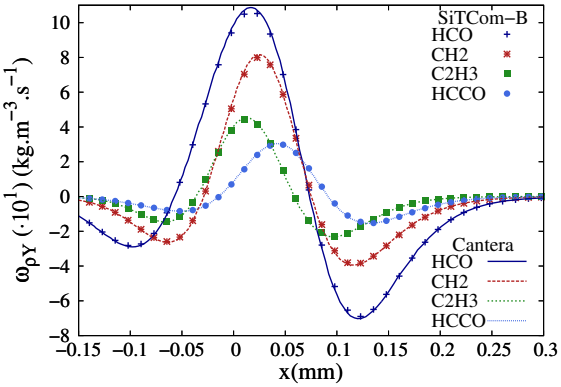

(f) Species source term profiles.

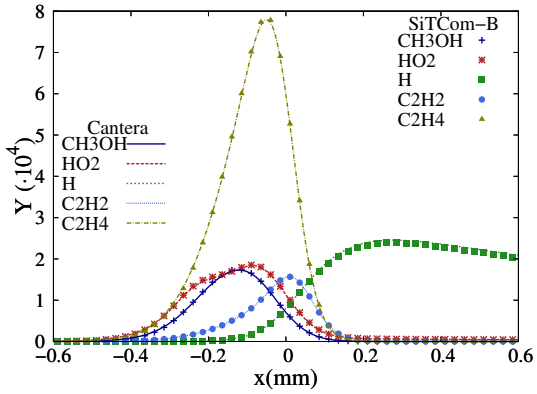

(g) Mass fraction profiles.

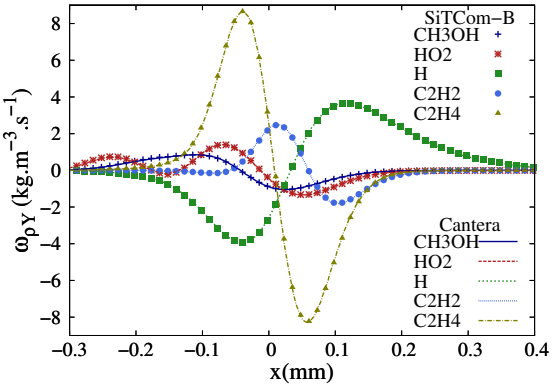

(h) Species source term profiles.

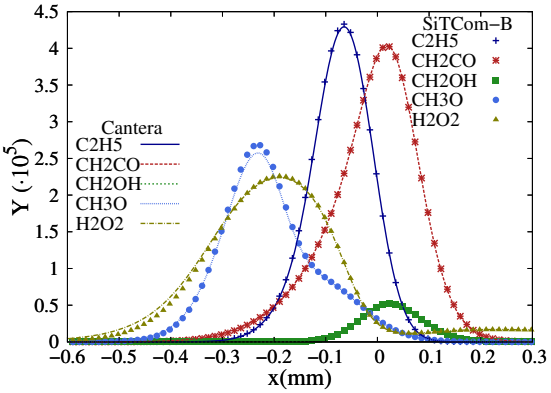

(i) Mass fraction profiles.

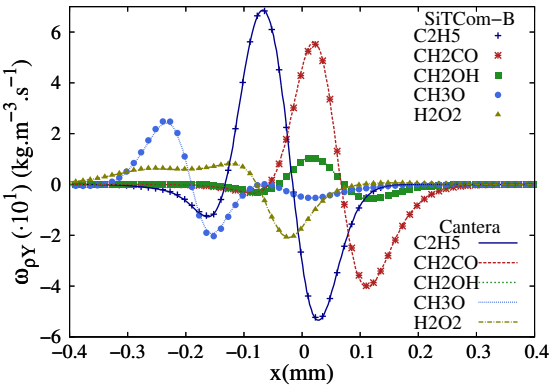

(j) Species source term profiles.

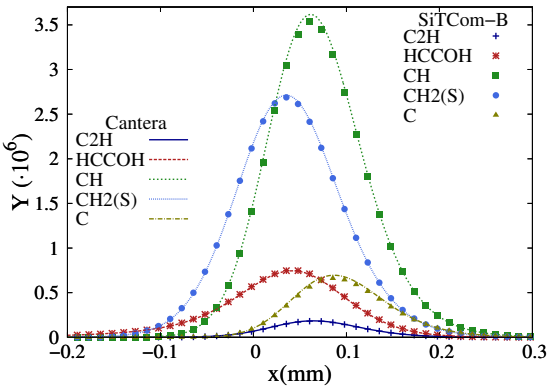

(k) Mass fraction profiles.

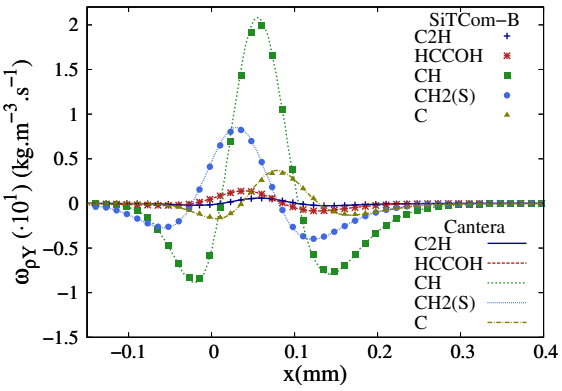

(l) Species source term profiles.

Figure B.5: Comparison of the mass fraction and species source term profiles, across an adiabatic stoichiometric methane/air flame, computed with different codes and mesh resolutions. Lines: Cantera (reference). Symbols : SiTCom-B (12.5 µm). GRI-1.2 scheme. To yield comprehensive results, subfigures (a), (c) and (g) display only one point over two for the SiTCom-B solution.

Appendix C

Equivalence ratio influence on the flame topology

This appendix gathers the reaction zone topologies, of flames stabilised and fully thermally coupled with the walls of the 5 mm high 2D channel, obtained for the equivalence ratios $\phi = 1.0$, $\phi = 0.8$ and $\phi = 0.7$. First, the results without accounting for gravity are given. Then the gravity field is added to the simulations to yield the flame topologies discussed in chapter 6.

C.1 Under microgravity

In the absence of gravity field, it is verified in chapter 3 (figure 3.6) that the assumption of symmetry with respect to the channel middle plan is valid. Under stoichiometric conditions (figure C.1, $\phi = 1.0$), chapter 4 exposes that the tulip flame shape relates to the heat retrocession from the burnt to the fresh gases, via conduction in the channel walls. In the same chapter, cold wall ($T = 300$ K) simulations exhibit mushroom flame shapes.

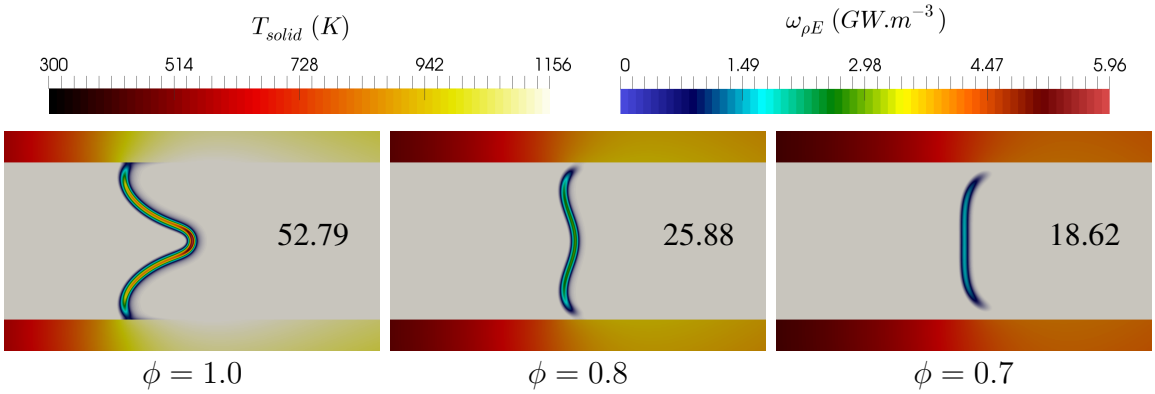

Figure C.1: Heat release rate distribution. Flame topology comparison between the various equivalence ratio employed along the manuscript, under microgravity. The corresponding flame velocity is given in black (cm.s^{-1}).

With the decrease of the equivalence ratio from 1.0 to 0.8 and 0.7 (figure C.1), the cooler burnt gases result in a weaker heat retrocession via the channel walls. Accordingly, the flame takes a less pronounced tulip shape for $\phi = 0.8$ and recovers a slight mushroom shape further at $\phi = 0.7$.

C.2 Under the gravitational field of the earth

Chapter 6 reveals that flames submitted to a gravity field lose their symmetric topology. In this case, slanted flames anchored at the upper walls are found, experimentally and numerically, to be the stable manifestation of combustion. When considering flames/wall thermal coupling at $\phi = 0.8$, the strong flame inclination is exposed to be due to the heat retro-cession and the incoming flow deviation. Indeed, the flow deviation results in a difference in residency time at the top and the bottom walls vicinity, where the fresh gases are preheated by the walls.

Still, when varying the equivalence ratio, the inclination of these slanted flames changes. Figure C.2 shows that the inclination diminishes when lowering the equivalence ratio. When operating with a leaner mixture, the diminution of the flame inclination results from the reduction of both preheating and flow deviation. Indeed, cooler burnt gases result into cooler walls and less heat retro-cession effect. It leads then to a weaker difference in the preheating of the fresh gases, between the top and the bottom channel walls. Further, with the lower mass flow rate stabilising the leaner flame, the variations of stream-wise flow velocities due to the flow deviation are reduced, ahead of the flame.

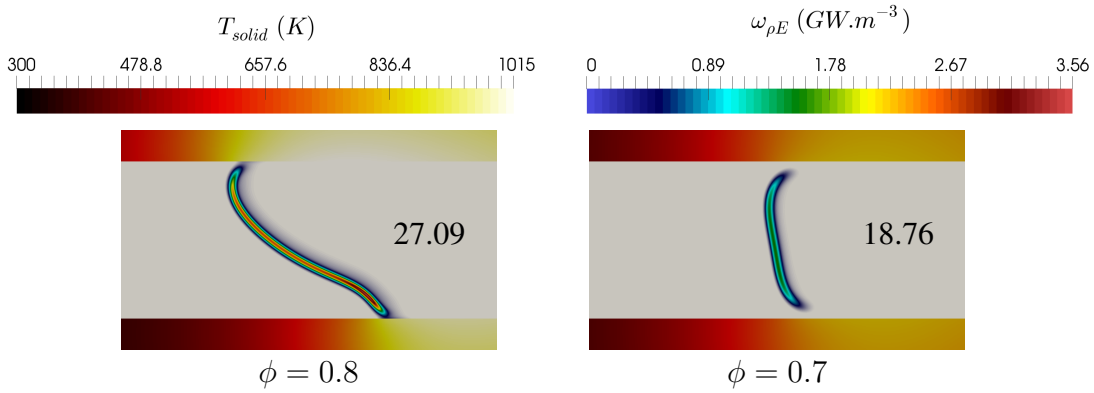

Figure C.2: Heat release rate distribution. Flame topology comparison, with a gravity field. The corresponding flame velocity is given in black (cm.s^{-1}).

Bibliography

[1] S. Acharya and S. K. Dash. Natural convection heat transfer from a short or long, solid or hollow horizontal cylinder suspended in air or placed on ground. *Journal of Heat Transfer*, 139(7):072501, 2017.

[2] J. Ahn, C. Eastwood, L. Sitzki, and P. D. Ronney. Gas-phase and catalytic combustion in heat-recirculating burners. *Proceedings of the Combustion Institute*, 30(2):2463–2472, 2005.

[3] H. T. Aichlmayr, D. B. Kittelson, and M. R. Zachariah. Micro-HCCI combustion: experimental characterization and development of a detailed chemical kinetic model with coupled piston motion. *Combustion and Flame*, 135(3):227–248, 2003.

[4] G. E. Andrews and D. Bradley. The burning velocity of methane-air mixtures. *Combustion and Flame*, 19(2):275–288, 1972.

[5] ArianeGroup. Présentation des lanceurs spatiaux, 2017. https://www.ariane.group/fr/lancement-spatial/ariane-6/.

[6] B. Bai, Z. Chen, H. Zhang, and S. Chen. Flame propagation in a tube with wall quenching of radicals. *Combustion and Flame*, 160(12):2810–2819, 2013.

[7] F. Bianco, S. Chibbaro, and G. Legros. Low-dimensional modeling of flame dynamics in heated microchannels. *Chemical Engineering Science*, 122:533–544, 2015.

[8] K. Bioche, A. Pieyre, G. Ribert, F. Richecoeur, and L. Vervisch. The role of gravity in the asymmetry of flames in narrow combustion chambers. *Combustion and Flame*, 203:238–246, 2019.

[9] K. Bioche, G. Ribert, and L. Vervisch. Simulating upstream flame propagation in a narrow channel after wall preheating: Flame analysis and chemistry reduction strategy. *Combustion and Flame*, 200:219–231, 2019.

[10] K. Bioche, L. Vervisch, and G. Ribert. Premixed flame-wall interaction in a narrow channel: Impact of wall thermal conductivity and heat losses. *Journal of Fluid Mechanics*, 856:5–35, 2018.

[11] S. B. Bird, W. E. Stewart, and E. N. Lightfoot. *Transport phenomena*. John Wiley & Sons, New York, 1960.

[12] A. L. Boehman. Radiation heat transfer in catalytic monoliths. *American Institute of Chemical Engineers Journal*, 44(12):2745–2755, 1998.

[13] L. Bouheraoua, P. Domingo, and G. Ribert. Large-eddy simulation of a supersonic lifted jet flame: Analysis of the turbulent flame base. *Combustion and Flame*, 179:199–218, 2017.

[14] A. Brambilla, M. Schultze, C. E. Frouzakis, J. Mantzaras, R. Bombach, and K. Boulouchos. An experimental and numerical investigation of premixed syngas combustion dynamics in mesoscale channels with controlled wall temperature profiles. *Proceedings of the Combustion Institute*, 35(3):3429–3437, 2015.

[15] M. Bucci, J.-M. Robinet, and S. Chibbaro. Global stability analysis of 3D micro-combustion model. *Combustion and Flame*, 167:132–148, 2016.

[16] S. Candel. *Mécanique des Fluides*. Dunod, Paris, 1995.

[17] S. Chakraborty, A. Mukhopadhyay, and S. Sen. Interaction of Lewis number and heat loss effects for a laminar premixed flame propagating in a channel. *International Journal of Thermal Sciences*, 47(1):84–92, 2008.

[18] J. Y. Chen. Development of reduced mechanisms for numerical modelling of turbulent combustion. In *Workshop on Numerical Aspects of Reduction in Chemical Kinetics, CERMICS-ENPC, Cite Descartes, Champus sur Marne, France*, 1997.

[19] N. Chigier and T. Gemci. A review of micro propulsion technology. In *41st Aerospace Sciences Meeting and Exhibit*, page 670, 2003.

[20] J.-H Cho, C. S. Lin, C. D. Richards, R. F. Richards, J. Ahn, and P. D. Ronney. Demonstration of an external combustion micro-heat engine. *Proceedings of the Combustion Institute*, 32(2):3099–3105, 2009.

[21] C. W. Choi and I. Puri. Response of flame speed to positively and negatively curved premixed flames. *Combustion Theory and Modelling*, 7:205–220, 2003.

[22] C. Clanet and G. Searby. On the tulip flame phenomenon. *Combustion and Flame*, 105(1-2):225–238, 1996.

[23] P. Clavin. Premixed combustion and gasdynamics. *Annual Review of Fluid Mechanics*, 26:321–52, 1994.

[24] P. Clavin, P. Pelcé, and L. He. One-dimensional vibratory instability of planar flames propagating in tubes. *Journal of Fluid Mechanics*, 216:299–322, 1990.

[25] P. Clavin and G. Searby. *Combustion Waves and Fronts in Flows*. Cambridge University Press, 2016.

[26] C. F. Curtiss and J. O. Hirschfelder. Transport properties of multicomponent gas mixtures. *The Journal of Chemical Physics*, 17(6):550–555, 1949.

[27] G. Darrieus. Propagation d'un front de flamme. *La Technique Moderne*, 30:18, 1938.

[28] H. Davy. Some researches on flame. *Philosophical Transactions of the Royal Society of London*, 107:45–76, 1817.

[29] A. Di Stazio, C. Chauveau, G. Dayma, and P. Dagaut. Combustion in micro-channels with a controlled temperature gradient. *Experimental Thermal and Fluid Science*, 73:79–86, 2016.

[30] U. Dogwiler, J. Mantzaras, P. Benz, B. Kaeppeli, R. Bombach, and A. Arnold. Homogeneous ignition of methane-air mixtures over platinum: Comparison of measurements and detailed numerical predictions. In *Symposium (International) on Combustion*, volume 27, pages 2275–2282. Elsevier, 1998.

[31] P. Domingo and L. Vervisch. DNS and approximate deconvolution as a tool to analyse one-dimensional filtered flame sub-grid scale modeling. *Combustion and Flame*, 177:109–122, 2017.

[32] P. Domingo, L. Vervisch, and D. Veynante. Large-eddy simulation of a lifted methane-air jet flame in a vitiated coflow. *Combustion and Flame*, 152(3):415–432, 2008.

[33] F. Duchaine, A. Corpron, L. Pons, V. Moureau, F. Nicoud, and T. Poinsot. Development and assessment of a coupled strategy for conjugate heat transfer with large eddy simulation: application to a cooled turbine blade. *International Journal of Heat and Fluid Flow*, 30(6):1129–1141, 2009.

[34] F. Ducros, V. Ferrand, F. Nicoud, C. Weber, D. Darracq, C. Gacherieu, and T. Poinsot. Large-eddy simulation of the shock/turbulence interaction. *Journal of Computational Physics*, 152(2):517–549, 1999.

[35] D. Dunn-Rankin, E. M. Leal, and D. C. Walther. Personal power systems. *Progress in Energy and Combustion Science*, 31(5):422–465, 2005.

[36] T. Echekki, B. L. Haroldsen, K. L. Krafcik, A. M. Morales, B. E. Mills, S. Liu, J. C. Lee, A. N. Karpetis, J. H. Chen, J. T. Ceremuga, et al. Design and fabrication of a meso-scale stirling engine and combustor. Technical report, Sandia National Laboratories, 2005.

[37] G. Emanuel. *Analytical Fluid Dynamics*. CRC Press, Boca Raton, USA, 1994.

[38] A. H. Epstein, S. D. Senturia, O. Al-Midani, G. Anathasuresh, A. Ayon, K. Breuer, K. S. Chen, P. P. Ehrich, E. Esteve, L. Frechette, et al. Micro-heat engines, gas turbines and rocket engines of the MIT microengine project. In *Proceedings of the 28th American Institute of Aeronautics and Astronautics Fluid Dynamics Conference*, 1997.

[39] G. H. Feng and S. C. Yen. Arch-shaped ionic polymer-metal composite actuator integratable with micromachined functional tools for micromanipulation. *Institute of Electrical and Electronics Engineers Sensors Journal*, 16(19):7109–7115, 2016.

[40] A. C. Fernandez-Pello. Micropower generation using combustion: issues and approaches. *Proceedings of the Combustion Institute*, 29(1):883–899, 2002.

[41] M. Frenklach, H. Wang, C.-L. Yu, M. Goldenberg, C. T. Bowman, R. K. Hanson, D. F. Davidson, E. J. Chang, G. P. Smith, D. M. Golden, W. C. Gardiner, and V. Lissianski. Grimech—an Optimized Detailed Chemical Reaction Mechanism for Methane Combustion. Technical report, Gas Research Institute, Chicago, IL, 1995. Report No. GRI-95/0058.

[42] S. Ganter, A. Heinrich, T. Meier, G. Kuenne, C. Jainski, M. Rissmann, A. Dreizler, and J. Janicka. Numerical analysis of laminar methane-air side-wall-quenching. *Combustion and Flame*, 186:299–310, 2017.

[43] G. P. Gauthier and J. M. Bergthorson. Effect of external heat loss on the propagation and quenching of flames in small heat-recirculating tubes. *Combustion and Flame*, 173:27–38, 2016.

[44] G. P. Gauthier, G. M. G. Watson, and J. M. Bergthorson. An evaluation of numerical models for temperature-stabilized CH4/air flames in a small channel. *Combustion Science and Technology*, 184(6):850–868, 2012.

[45] V. Giovangigli. *Multicomponent Flow Modeling*. Modeling and Simulation in Science, Engineering and Technology. Birkhäuser, 1999.

[46] M. U. Göktolga, J. A. van Oijen, and L. P. H. de Goey. 3D DNS of MILD combustion: a detailed analysis of heat loss effects, preferential diffusion, and flame formation mechanisms. *Fuel*, 159:784–795, 2015.

[47] M. Gonzalez, R. Borghi, and A. Saouab. Interaction of a flame front with its self-generated flow in an enclosure: The "tulip flame" phenomenon. *Combustion and Flame*, 88(2):201–220, 1992.

[48] D. Goodwin. Cantera: An object-oriented software toolkit for chemical kinetics, thermodynamics, and transport processes. http://code.google.com/p/cantera, 2009.

[49] D. G. Goodwin. An open-source, extensible software suite for CVD process simulation. *Chemical vapor deposition XVI and EUROCVD*, 14(40):2003–08, 2003.

[50] R. L. Gordon, A. R. Masri, S. B. Pope, and G. M. Goldin. Transport budgets in turbulent lifted flames of methane autoigniting in a vitiated co-flow. *Combustion and Flame*, 151(3):495–511, 2007.

[51] J. Guidez, F. X. Nicoul, P. Josso, and R. Valle. Development of a micro gas turbine engine at Onera. In *XIX International Symposium on Air Breathing Engines (ISABE 2009), Montreal, Canada, September*, pages 7–11, 2009.

[52] C. Hasse, M. Bollig, N. Peters, and H. A. Dwyer. Quenching of laminar iso-octane flames at cold walls. *Combustion and Flame*, 122(1-2):117–129, 2000.

[53] V. Hiremath, Z. Ren, and S. B. Pope. Combined dimension reduction and tabulation strategy using ISAT–RCCE–GALI for the efficient implementation of combustion chemistry. *Combustion and Flame*, 158(11):2113–2127, 2011.

[54] D. L. Hitt, C. M. Zakrzwski, and M. A. Thomas. MEMS-based satellite micropropulsion via catalyzed hydrogen peroxide decomposition. *Smart Materials and Structures*, 10(6):1163, 2001.

[55] K. Isomura, S. Tanaka, S. Togo, and M. Esashi. Development of high-speed micro-gas bearings for three-dimensional micro-turbo machines. *Journal of Micromechanics and Microengineering*, 15(9):S222, 2005.

[56] T. Iwaya, S. Akao, T. Sakamoto, T. Tsuji, N. Nakaso, and K. Yamanaka. Development of high precision metal micro-electro-mechanical-systems column for portable surface acoustic wave gas chromatograph. *Japanese Journal of Applied Physics*, 51(7S):07GC24, 2012.

[57] A. Jameson, W. Schmidt, and E. Turkel. Numerical solution of the euler equations by finite volume methods using runge kutta time stepping schemes. In *14th Fluid and Plasma Dynamics Conference*, page 1259, 1981.

[58] N. Jaouen, L. Vervisch, P. Domingo, and G. Ribert. Automatic reduction and optimisation of chemistry for turbulent combustion modelling: Impact of the canonical problem. *Combustion and Flame*, 175:60–79, 2017.

[59] J. Jarosinski. A survey of recent studies on flame extinction. *Progress in Energy and Combustion Science*, 12(2):81–116, 1986.

[60] C. Jiménez, D. Fernández-Galisteo, and V. N. Kurdyumov. DNS study of the propagation and flashback conditions of lean hydrogen-air flames in narrow channels: symmetric and non-symmetric solutions. *International Journal of Hydrogen Energy*, 40(36):12541–12549, 2015.

[61] G. Joulin and G. Sivashinsky. Influence of momentum and heat losses on the large-scale stability of quasi-2D premixed flames. *Combustion Science and Technology*, 98(1-3):11–23, 1994.

[62] Y. Ju and C. W. Choi. An analysis of sub-limit flame dynamics using opposite propagating flames in mesoscale channels. *Combustion and Flame*, 133(4):483–493, 2003.

[63] Y. Ju and K. Maruta. Microscale combustion: technology development and fundamental research. *Progress in Energy and Combustion Science*, 37(6):669–715, 2011.

[64] Y. Ju and B. Xu. Theoretical and experimental studies on mesoscale flame propagation and extinction. *Proceedings of the Combustion Institute*, 30(2):2445–2453, 2005.

[65] Y. Ju and B. Xu. Effects of channel width and lewis number on the multiple flame regimes and propagation limits in mesoscale. *Combustion Science and Technology*, 178(10-11):1723–1753, 2006.

[66] Y. Ju and B. Xu. Studies of the effects of radical quenching and flame stretch on mesoscale combustion. In *44th AIAA Aerospace Sciences Meeting and Exhibit*, page 1351, 2006.

[67] N. S. Kaisare, G. D. Stefanidis, and D. G. Vlachos. Transport phenomena in microscale reacting flows. *Micro Process Engineering: A Comprehensive Handbook, Volume 1, 2&3*, pages 283–302, 2013.

[68] N. S. Kaisare and D. G. Vlachos. A review on microcombustion: Fundamentals, devices and applications. *Progress in Energy and Combustion Science*, 38(3):321–359, 2012.

[69] S. H. Kang, S. W. Baek, and H. G. Im. Effects of heat and momentum losses on the stability of premixed flames in a narrow channel. *Combustion Theory and Modelling*, 10(4):659–681, 2006.

[70] T. Kania and A. Dreizler. Investigation of a micro combustion chamber for a thermoelectric energy converter. In *Proceedings of the European Combustion Meeting*, 2009.

[71] B. Karlovitz, D. W. Denniston, D. H. Knapschaefer, and F. E. Wells. Flame propagation across velocity gradients. In *4-th Symposium (Intl.) on Combustion, The Combustion Institute*, pages 613–620, 1953.

[72] K. A. Kazakov. Analytical study in the mechanism of flame movement in horizontal tubes. *Physics of Fluids*, 24(2):022108, 2012.

[73] R. J. Kee, F. M. Rupley, and J. A. Miller. Chemkin-ii: A fortran chemical kinetics package for the analysis of gas-phase chemical kinetics. Technical report, Sandia National Labs., Livermore, CA (USA), 1989.

[74] H. H. Kim, H. J. Jeon, H. K. Cho, J. H. Cheong, H. S. Moon, and J. S. Go. Highly sensitive microcantilever biosensors with enhanced sensitivity for detection of human papilloma virus infection. *Sensors and Actuators B: Chemical*, 221:1372–1383, 2015.

[75] K. T. Kim, D. H. Lee, and S. Kwon. Effects of thermal and chemical surface–flame interaction on flame quenching. *Combustion and Flame*, 146(1-2):19–28, 2006.

[76] N. I. Kim, S. Aizumi, T. Yokomori, S. Kato, T. Fujimori, and K. Maruta. Development and scale effects of small swiss-roll combustors. *Proceedings of the Combustion Institute*, 31(2):3243–3250, 2007.

[77] N. I. Kim, T. Kataoka, S. Maruyama, and K. Maruta. Flammability limits of stationary flames in tubes at low pressure. *Combustion and Flame*, 141(1):78–88, 2005.

[78] N. I. Kim and K. Maruta. A numerical study on propagation of premixed flames in small tubes. *Combustion and Flame*, 146(1):283–301, 2006.

[79] Y. Kizaki, H. Nakamura, T. Tezuka, S. Hasegawa, and K. Maruta. Effect of radical quenching on CH4/air flames in a micro flow reactor with a controlled temperature profile. *Proceedings of the Combustion Institute*, 35(3):3389–3396, 2015.

[80] P. Koniavitis, S. Rigopoulos, and W. P. Jones. A methodology for derivation of RCCE-reduced mechanisms via CSP. *Combustion and Flame*, 183:126 – 143, 2017.

[81] C. Koren. *Modélisation des transferts de chaleur couplés pour la simulation multi-physique des chambres de combustion*. PhD thesis, Université Paris-Saclay, 2016.

[82] C. H. Kuo and P. D. Ronney. Numerical modeling of non-adiabatic heat-recirculating combustors. *Proceedings of the Combustion Institute*, 31(2):3277–3284, 2007.

[83] V. N. Kurdyumov. Lewis number effect on the propagation of premixed flames in narrow adiabatic channels: Symmetric and non-symmetric flames and their linear stability analysis. *Combustion and Flame*, 158(7):1307–1317, 2011.

[84] V. N. Kurdyumov and E. Fernandez-Tarrazo. Lewis number effect on the propagation of premixed laminar flames in narrow open ducts. *Combustion and Flame*, 128(4):382–394, 2002.

[85] V. N. Kurdyumov and C. Jiménez. Propagation of symmetric and non-symmetric premixed flames in narrow channels: Influence of conductive heat-losses. *Combustion and Flame*, 161(4):927–936, 2014.

[86] L. D. Landau. On the theory of slow combustion. *Acta Physicochim*, 19:77–85, 1944.

[87] B. Lewis and G. Von Elbe. *Combustion, flames and explosions of gases*. Elsevier, 1987.

[88] D. H. Lewis Jr, S. W. Janson, R. B. Cohen, and E. K. Antonsson. Digital micropropulsion. *Sensors and Actuators A: Physical*, 80(2):143–154, 2000.

[89] J. Li, S. K. Chou, W. M. Yang, and Z. W. Li. A numerical study on premixed micro-combustion of CH 4–air mixture: Effects of combustor size, geometry and boundary conditions on flame temperature. *Chemical Engineering Journal*, 150(1):213–222, 2009.

[90] S. A. Lloyd and F. J. Weinberg. A burner for mixtures of very low heat content. *Nature*, 251(5470):47–49, 1974.

[91] G. Lodato, L. Vervisch, and P. Domingo. A compresssible wall-adapting similarity mixed model for large-eddy simulation of the impinging round jet. *Physics of Fluids*, 21:035102, 2009.

[92] G. Lodier, C. Merlin, P. Domingo, L. Vervisch, and F. Ravet. Self-ignition scenarios after rapid compression of a turbulent mixture weakly-stratified in temperature. *Combustion and Flame*, 159(11):3358–3371, 2012.

[93] T. Lovaas. Automatic generation of skeletal mechanisms for ignition combustion based on level of importance analysis. *Combustion and Flame*, 156:1348–1358, 2009.

[94] T. Lu and C. K. Law. A directed relation graph method for mechanism reduction. *Proceedings of the Combustion Institute*, 30(1):1333–1341, 2005.

[95] T. Lu and C. K. Law. Toward accommodating realistic fuel chemistry in large-scale computations. *Progress in Energy and Combustion Science*, 35(2):192–215, 2009.

[96] K. Maruta, T. Kataoka, N. I. Kim, S. Minaev, and R. Fursenko. Characteristics of combustion in a narrow channel with a temperature gradient. *Proceedings of the Combustion Institute*, 30(2):2429–2436, 2005.

[97] S. Mathur, P. K. Tondon, and S. C. Saxena. Thermal conductivity of binary, ternary and quaternary mixtures of rare gases. *Molecular physics*, 12(6):569–579, 1967.

[98] C. Merlin, P. Domingo, and L. Vervisch. Immersed boundaries in Large Eddy Simulation of compressible flows. *Flow Turbulence and Combustion*, 90(1):29–68, 2013.

[99] B. Michaelis and B. Rogg. FEM-simulation of laminar flame propagation. I: Two-dimensional flames. *Journal of Computational Physics*, 196(2):417–447, 2004.

[100] C. M. Miesse, R. I. Masel, C. D. Jensen, M. A. Shannon, and M. Short. Submillimeter-scale combustion. *American Institute of Chemical Engineers journal*, 50(12):3206–3214, 2004.

[101] S. Minaev, K. Maruta, and R. Fursenko. Nonlinear dynamics of flame in a narrow channel with a temperature gradient. *Combustion Theory and Modelling*, 11(2):187–203, 2007.

[102] Performance Materials Inc. Momentive. Thermal properties of fused quartz. 2017.

[103] H. Nakamura, A. Fan, S. Minaev, E. Sereshchenko, R. Fursenko, Y. Tsuboi, and K. Maruta. Bifurcations and negative propagation speeds of methane/air premixed flames with repetitive extinction and ignition in a heated microchannel. *Combustion and Flame*, 159(4):1631–1643, 2012.

[104] C. L. M. H. Navier. Mémoire sur les lois du mouvement des fluides. *Mémoires de l'Académie Royale des Sciences de l'Institut de France*, 6(1823):389–440, 1823.

[105] Z. Nikolaou and N. Swaminathan. Heat release rate markers for premixed combustion. *Combustion and Flame*, 161(12):3073–3084, 2014.

[106] D. G. Norton and D. G. Vlachos. Combustion characteristics and flame stability at the microscale: a CFD study of premixed methane/air mixtures. *Chemical Engineering Science*, 58(21):4871–4882, 2003.

[107] D. G. Norton and D. G. Vlachos. A CFD study of propane/air microflame stability. *Combustion and Flame*, 138(1-2):97–107, 2004.

[108] D. G. Norton, E. D. Wetzel, and D. G. Vlachos. Fabrication of single-channel catalytic microburners: effect of confinement on the oxidation of hydrogen/air mixtures. *Industrial & Engineering Chemistry Research*, 43(16):4833–4840, 2004.

[109] J. Peirs, P. Vleugels, T. Waumans, M. Verlinden, D. Reynaerts, and F. Verplaetsen. Development of high-speed bearings for micro gas turbines. In *Proceedings of the 15th MicroMechanics Europe Workshop*, pages 313–316, 2004.

[110] P. Pepiot and H. Pitsch. An efficient error propagation based reduction method for large chemical kinetic mechanisms. *Combustion and Flame*, 154(1-2):67 – 81, 2008.

[111] N. Peters. Systematic reduction of flame kinetics: Principles and details. *Progress in Astronautics and Aeronautics*, 113:67–86, 1988.

[112] X. Petit, G. Ribert, G. Lartigue, and P. Domingo. Large-eddy simulation of supercritical fluid injection. *The Journal of Supercritical Fluids*, 84:61–73, 2013.

[113] W. C. Pfefferle and L. D. Pfefferle. Catalytically stabilized combustion. *Progress in Energy and Combustion Science*, 12(1):25–41, 1986.

[114] G. Pizza, C. E. Frouzakis, J. Mantzaras, A. G. Tomboulides, and K. Boulouchos. Three-dimensional simulations of premixed hydrogen/air flames in microtubes. *Journal of Fluid Mechanics*, 658:463–491, 2010.

[115] G. Pizza, J. Mantzaras, C. E. Frouzakis, A. G. Tomboulides, and K. Boulouchos. Suppression of combustion instabilities of premixed hydrogen/air flames in microchannels using heterogeneous reactions. *Proceedings of the Combustion Institute*, 32(2):3051–3058, 2009.

[116] T. Poinsot and D. Veynante. *Theoretical and numerical combustion*. RT Edwards, Inc., 2005.

[117] T. J. Poinsot, D. C. Haworth, and G. Bruneaux. Direct simulation and modeling of flame-wall interaction for premixed turbulent combustion. *Combustion and Flame*, 95(1-2):118–132, 1993.

[118] T. J. Poinsot and S. K. Lele. Boundary conditions for direct simulations of compressible viscous flows. *Journal of Computational Physics*, 101(1):104–129, 1992.

[119] W. Polifke, W. Geng, and K. Döbbeling. Optimization of rate coefficients for simplified reaction mechanisms with genetic algorithms. *Combustion and Flame*, 113(1):119–134, 1998.

[120] P. Popp, M. Smooke, and M. Baum. Heterogeneous/homogeneous reaction and transport coupling during flame-wall interaction. In *Symposium (International) on Combustion*, volume 26, pages 2693–2700. Elsevier, 1996.

[121] S. Raimondeau, D. Norton, D. G. Vlachos, and R. I. Masel. Modeling of high-temperature microburners. *Proceedings of the Combustion Institute*, 29(1):901–907, 2002.

[122] F. Richecoeur and D. C. Kyritsis. Experimental study of flame stabilization in low reynolds and dean number flows in curved mesoscale ducts. *Proceedings of the Combustion Institute*, 30(2):2419–2427, 2005.

[123] P. D. Ronney. Analysis of non-adiabatic heat-recirculating combustors. *Combustion and Flame*, 135(4):421–439, 2003.

[124] R. N. Roy, S. Kumar, and S. Sreedhara. Predictions of lift-off height of turbulent methane and propane flames issuing in cold surroundings using conditional moment closure coupled with an extinction model. *Combustion and Flame*, 162(4):1164–1166, 2015.

[125] G. R. Ruetsch, L. Vervisch, and A. Liñán. Effects of heat release on triple flame. *Physics of Fluids*, 6(7):1447–1454, 1995.

[126] D. R. Sadoway and A. M. Mayes. Portable power: advanced rechargeable lithium batteries. *Material Research Society bulletin*, 27(8):590–596, 2002.

[127] P. G. Saffman and G. Taylor. The penetration of a fluid into a porous medium or hele-shaw cell containing a more viscous liquid. In *Dynamics of Curved Fronts*, pages 155–174. Elsevier, 1988.

[128] Y. Saiki and Y. Suzuki. Effect of wall surface reaction on a methane-air premixed flame in narrow channels with different wall materials. *Proceedings of the Combustion Institute*, 34(2):3395–3402, 2013.

[129] T. Saitoh, T. Sajiki, and K. Maruhara. Bench mark solutions to natural convection heat transfer problem around a horizontal circular cylinder. *International Journal of Heat and Mass Transfer*, 36(5):1251–1259, 1993.

[130] M. Sánchez-Sanz. Premixed flame extinction in narrow channels with and without heat recirculation. *Combustion and Flame*, 159(10):3158–3167, 2012.

[131] M. Sánchez-Sanz, D. Fernández-Galisteo, and V. N. Kurdyumov. Effect of the equivalence ratio, Damköhler number, Lewis number and heat release on the stability of laminar premixed flames in microchannels. *Combustion and Flame*, 161(5):1282–1293, may 2014.

[132] R. Sankaran, E. R. Hawkes, J. H. Chen, T. Lu, and C. K. Law. Direct numerical simulations of turbulent lean premixed combustion. In *Journal of Physics: conference series*, volume 46, page 38. IOP Publishing, 2006.

[133] R. Sankaran, E. R. Hawkes, J. H. Chen, T. Lu, and C. K. Law. Structure of a spatially developing turbulent lean methane–air bunsen flame. *Proceedings of the Combustion Institute*, 31(1):1291–1298, 2007.

[134] M. Short and D. A. Kessler. Asymptotic and numerical study of variable-density premixed flame propagation in a narrow channel. *Journal of Fluid Mechanics*, 638:305–337, 2009.

[135] C.-W. Shu and S. Osher. Efficient implementation of essentially non-oscillatory shock-capturing schemes. *Journal of Computational Physics*, 77(2):439–471, 1988.

[136] G. I. Sivashinsky. Diffusional-thermal theory of cellular flames. *Combustion Science and Technology*, 15(3-4):137–145, 1977.

[137] G. P. Smith, D. M. Golden, M. Frenklach, N. W. Moriarty, B. Eiteneer, M. Goldenberg, C. T. Bowman, R. K. Hanson, S. Song, W. C. Gardiner, V. V. Lissianski, and Z. Qin. Technical report, 1999. http://www.me.berkeley.edu/gri-mech/.

[138] M. D. Smooke and V. Giovangigli. Formulation of the premixed and nonpremixed test problems. In *Reduced Kinetic Mechanisms and Asymptotic Approximations for Methane-Air Flames*, pages 1–28. Springer, 1991.

[139] G. G. Stokes. On the theories of the internal friction of fluids in motion. *Transactions of the Cambridge Philosophical Society*, 8:287–305, 1845.

[140] J. W. Strutt and L. Rayleigh. Investigation of the character of the equilibrium of an incompressible heavy fluid of variable density. pages 170–177, 1883.

[141] V. Subramanian, P. Domingo, and L. Vervisch. Large-Eddy Simulation of forced ignition of an annular bluff-body burner. *Combustion and Flame*, 157(3):579–601, 2010.

[142] R. Swanson and E. Turkel. On central-difference and upwind schemes. *Journal of Computational Physics*, 101(2):292–306, 1992.

[143] S. Tatsumi, L. Martinelli, and A. Jameson. Flux-limited schemes for the compressible navier-stokes equations. *American Institute of Aeronautics and Astronautics Journal*, 33(2), 1995.

[144] G. I. Taylor. The instability of liquid surfaces when accelerated in a direction perpendicular to their planes. i. *Proceedings of the Royal Society of London. Series A, Mathematical and Physical Sciences*, 201(1065):192–196, 1950.

[145] L. H. Thomas. Elliptic problems in linear difference equations over a network. *Watson Scientific Computing Laboratory report, Columbia University, New York*, 1, 1949.

[146] C. H. Tsai. The asymmetric behavior of steady laminar flame propagation in ducts. *Combustion Science and Technology*, 180(3):533–545, 2008.

[147] Y. Tsuboi, T. Yokomori, and K. Maruta. Lower limit of weak flame in a heated channel. *Proceedings of the Combustion Institute*, 32(2):3075–3081, 2009.

[148] T. Turanyi and A. S. Tomlin. *Analysis of Kinetic Reaction Mechanisms*. Springer, Berlin, Germany, 2015.

[149] A. M. Turing. The chemical basis of morphogenesis. *Philosophical Transactions of the Royal Society B: Biological Sciences.*, 237(641):37–72, 1952.

[150] Z. Turkeli-Ramadan, R. N. Sharma, and K. Yamaguchi. Combustion characteristics of hex-combustor for ultra micro gas turbine. In *European Combustion Meeting (ECM)*, 2011.

[151] A. Veeraragavan and C. P. Cadou. Flame speed predictions in planar micro/mesoscale combustors with conjugate heat transfer. *Combustion and Flame*, 158(11):2178–2187, 2011.

[152] J. G. B. F. Vican, B. F. Gajdeczko, F. L. Dryer, D. L. Milius, I. A. Aksay, and R. A. Yetter. Development of a microreactor as a thermal source for microelectromechanical systems power generation. *Proceedings of the Combustion Institute*, 29(1):909–916, 2002.

[153] D. C. Walther and J. Ahn. Advances and challenges in the development of power-generation systems at small scales. *Progress in Energy and Combustion Science*, 37(5):583–610, 2011.

[154] P. Wang, R. Kahawita, and D. L. Nguyen. Transient laminar natural convection from horizontal cylinders. *International Journal of Heat and Mass Transfer*, 34(6):1429–1442, 1991.

[155] B. Warneke, M. Last, B. Liebowitz, and K. S. J. Pister. Smart dust: Communicating with a cubic-millimeter computer. *Computer*, 34(1):44–51, 2001.

[156] F. J. Weinberg, D. M. Rowe, G. Min, and P. D. Ronney. On thermoelectric power conversion from heat recirculating combustion systems. *Proceedings of the Combustion Institute*, 29(1):941–947, 2002.

[157] Wikipedia. Safety lamp, 2017. https://en.wikipedia.org/wiki/Safety_lamp.

[158] Z. Xie, Z. Yang, L. Zhang, and C. Liu. Effects of non-catalytic surface reactions on the CH4–air premixed flame within micro-channels. *Royal Society of Chemistry Advances*, 5(43):34272–34280, 2015.

[159] B. Xu and Y. Ju. Experimental study of spinning combustion in a mesoscale divergent channel. *Proceedings of the Combustion Institute*, 31(2):3285–3292, 2007.

[160] R. A. Yetter, V. Yang, M. H. Wu, Y. Wang, D. Milius, I. A. Aksay, and F. L. Dryer. Combustion issues and approaches for chemical microthrusters. *International Journal of Energetic Materials and Chemical Propulsion*, 6(4), 2007.

[161] V. V. Zamashchikov. Some features of gas-flame propagation in narrow tubes. *Combustion, Explosion and Shock Waves*, 40(5):545–552, 2004.